

DISS. ETH NO. 29918

**NEXT-GENERATION OFFSHORE WIND TURBINE FOUNDATIONS
UNDER SEISMIC AND ENVIRONMENTAL DYNAMIC LOADING**

A thesis submitted to attain the degree of
DOCTOR OF SCIENCES
(Dr. sc. ETH Zurich)

presented by
MARIA ANTONIOU

National Technical University of Athens
M.Sc., University of Dundee

born on 02.06.1989

accepted on the recommendation of:

Prof. Dr. Ioannis Anastasopoulos
Prof. Dr. Michael Brown
Prof. Dr. Amir Kaynia
Dr. Rallis Kourkoulis

2023

Abstract

This dissertation comprises five chapters summarising the work conducted on the seismic/dynamic performance of next-generation offshore wind turbine (OWT) foundations in transitional water depths. Beyond the prevalent (in shallow water) monopile solution, the seismic performance of alternative substructures has been scarcely addressed in the literature. At the same time, the effect of cyclic degradation during short-term transient loading for OWTs founded on soft soil deposits still raises uncertainties. Aiming to address this gap, the dissertation utilizes 3D finite element (FE) modelling to study the response of two state-of-the-art foundations in cohesive soils under adverse seismic and environmental cyclic loading: a guyed support system and a jacket structure, both founded on the seabed via suction caissons. To the best of the author's knowledge, this is the first detailed study on such foundations that offers a comprehensive exploration of the mechanisms governing the problem from a soil-foundation-superstructure (SFS) system perspective.

The behaviour of the guyed support system is initially examined (Chapter 2), considering a compliant OWT tower mounted on a central shallow footing and anchored to the seabed through an array of four pretensioned cables. For this purpose, a 3D FE model representing the SFS system is developed based on a reference 10 MW turbine installed at 50 m water depth. A validated kinematic hardening model with a Von Mises failure criterion is employed to describe the undrained nonlinear soil behaviour. The study demonstrates the efficacy of the proposed foundation by assessing its performance under Ultimate Limit State (ULS) and Serviceability Limit State (SLS) conditions and its resilience under combined environmental and earthquake loading. Design insights regarding the structural performance of the 'above-ground' system are provided, emphasizing the dynamic response of the cables and the potential of an unconventional design alternative where the system's frequency does not fall within the widely used 'soft-stiff' design range. The optimum position of the padeye is parametrically investigated, showcasing its effect on the pullout capacity and stiffness of the anchoring system. The impact of suction pressure developed and maintained below the caisson lid on foundation performance is discussed, along with the crucial role of the central foundation in controlling the cables' pretension during seismic shaking.

In the second part of the study, a simplified method for the performance-based seismic design of suction caissons supporting jacket OWTs is proposed, using an 8 MW turbine

installed in 60m water depth as a benchmark for the investigations (Chapter 3). An enhanced 'Caisson-on-Winkler-Soil' (CWS) model is developed, capturing the soil-suction caisson interaction via nonlinear hysteretic elements that allow the simulation of permanent caisson deformations (vertical and horizontal displacements, and rotations). Its performance is compared to a detailed 3D FE model of the entire SFS system (using the soil constitutive model of Chapter 2). The mechanics that govern the accumulation of nonlinear caisson deformations under concurrent environmental and earthquake loading are explored: it is revealed that under inertial and kinematic loading, the accumulation of co-seismic caisson settlements is driven by a dual-shearing mechanism that cannot be captured by the developed (or any other similar) Winkler-based model. To address the problem, a hybrid seismic assessment methodology is proposed, combining: (a) the CWS model for the estimation of Vertical-Horizontal-Moment loads and horizontal displacements/rotations at the jacket legs and (b) a set of linear regression equations (developed with the aid of parametric numerical analysis) for the estimation of co-seismic caisson settlements. The derived equations – provided in dimensionless form to allow broader applicability – correlate caisson settlements with characteristic dimensional variables of the problem at hand and the Arias Intensity (I_A) of the surface ground motion.

Finally, an extended kinematic hardening soil constitutive model is developed to study the influence of soil strength and stiffness degradation on the undrained cyclic performance of suction caissons in soft cohesive deposits (Chapter 4). The simplified – yet practical – model is encoded in Abaqus via a user subroutine and is calibrated using a targeted set of cyclic triaxial tests on normally consolidated Kaolin conducted at the ETH Zurich geotechnical laboratory as part of this study. The triaxial tests not only serve calibration purposes but also help identify the key parameters affecting the cyclic behaviour of the examined soil. A strong dependency of the cyclic degradation rate on the mean effective stress level and the applied cyclic strain amplitude is revealed. Following validation against published centrifuge tests, the model is exploited to numerically assess the performance of suction caisson foundations under short-term cyclic and seismic loading through a parametric study that provides insights on the mechanisms that drive permanent foundation deformations in fast-degrading soil and the influence of caisson aspect ratio on the dynamic foundation resistance.

Zusammenfassung

Diese Doktorarbeit erläutert in fünf Kapiteln das seismische/dynamische Verhalten von Offshore-Windenergieanlagen (OWT) der nächsten Generation in Übergangswassertiefen. Abgesehen von der in seichten Gewässern dominierenden Monopile-Gründung wurde das seismische Verhalten von OWT Gründungsstrukturen in der Fachliteratur kaum behandelt. Zudem ist die Auswirkung der zyklischen Degradation während kurzzeitiger transienter Belastungen für OWTs auf weichen Bodenablagerungen immer noch mit Unsicherheiten behaftet. Um diese Lücke zu schließen, untersucht diese Dissertation mittels 3D-Finite-Elementen (FE) Analysen die Reaktion auf seismische und zyklische Umweltbelastungen von zwei hochmodernen Gründungsstrukturen in bindigen Böden: ein abgespanntes Trägersystem und eine Jacket-Struktur, beide über Saug-Caissons auf dem Meeresboden gegründet. Soweit dem Autor bekannt, ist dies die erste detaillierte Studie zu solchen Gründungsstrukturen, welche eine umfassende Untersuchung der Mechanismen aus der Perspektive des Boden-Gründungs-Überbau (SFS) Systems bietet.

Zunächst wird das Verhalten des abgespannten Trägersystems untersucht (Kapitel 2), dabei wird ein nachgiebiger OWT-Turm, der auf einem zentralen Flachfundament montiert und über eine Anordnung von vier vorgespannten Seilen am Meeresboden verankert ist, betrachtet. Zu diesem Zweck wird ein 3D-FE-Modell des SFS-Systems einer 10-MW-Referenzturbinen in 50 m Wassertiefe entwickelt. Ein validiertes kinematisches Verfestigungsmodell mit einem Von-Mises-Bruchkriterium beschreibt das undrainierte nichtlineare Bodenverhalten. Die Studie demonstriert die Effizienz des abgespannten Trägersystems als OWT-Gründungsstruktur, indem seine Leistungsfähigkeit bezüglich den Grenzzuständen der Tragsicherheit (ULS) und der Gebrauchstauglichkeit (SLS) sowie seine Widerstandsfähigkeit unter kombinierter Umwelt- und Erdbebenbelastung bewertet wird. Es werden Einblicke in die strukturelle Leistungsfähigkeit des «oberirdischen» Systems gegeben, wobei die dynamische Reaktion der Kabel und das Potenzial einer unkonventionellen Entwurfsalternative hervorgehoben werden, bei der die Frequenz des Systems nicht in den weit verbreiteten "weich-steifen" Entwurfsbereich fällt. Die optimale Position des Pad-Eye wird parametrisch untersucht, um die Auswirkung auf die Auszugskapazität und Steifigkeit des Verankerungssystems aufzuzeigen. Die Auswirkung des Saugdrucks unterhalb des Caissons auf die Leistungsfähigkeit

des Fundaments wird ebenso erörtert wie die entscheidende Rolle des zentralen Fundaments bei der Kontrolle der Kabelvorspannung während seismischer Erschütterungen.

Der zweite Teil der Studie erarbeitet eine vereinfachte Methode für die leistungsbasierte seismische Bemessung von Caissons, die Jacket-OWTs tragen, wobei eine 8-MW-Turbine 60 m Wassertiefe, als Referenz für die Untersuchungen dient (Kapitel 3). Es wird ein verbessertes "Caisson-on-Winkler-Soil"-Modell (CWS) entwickelt, das die Boden-Saug-Caisson-Interaktion über nichtlineare hysteretische Elemente erfasst, welche die Simulation permanenter Caisson-Verformungen (vertikale und horizontale Verschiebungen und Rotationen) ermöglichen. Das Verhalten des Modells wird mit einem detaillierten 3D-FE-Modell des gesamten SFS-Systems verglichen (unter Verwendung des Bodenmodells aus Kapitel 2). Die Mechanismen, die für die Akkumulation nichtlinearer Senkkastenverformungen unter gleichzeitiger Umwelt- und Erdbebenbelastung verantwortlich sind, werden untersucht: Es zeigt sich, dass die Akkumulation koseismischer Caissonsetzungen unter Trägheitslasten und kinematischer Belastungen durch einen doppelten Schermechanismus angetrieben wird, der von dem entwickelten oder ähnlichen Winkler-basierten Modellen nicht erfasst werden kann. Zur Lösung des Problems wird eine hybride seismische Bewertungsmethode vorgeschlagen, die Folgendes kombiniert: (a) das CWS-Modell für die Abschätzung der kombinierten Vertikal-, Horizontal- und Momentbelastung und der horizontalen Verschiebungen/Drehungen an den Jacket-Beinen; und (b) eine Reihe linearer Regressionsgleichungen, welche mit Hilfe einer parametrischen numerischen Analyse entwickelt wurden, für die Abschätzung der koseismischen Caissonsetzungen. Die abgeleiteten Gleichungen - die in dimensionsloser Form bereitgestellt werden, um eine breitere Anwendbarkeit zu ermöglichen - korrelieren Caissonsetzungen mit charakteristischen Dimensionsvariablen des vorliegenden Problems und der Arias-Intensität (I_A) der Bodenbewegung an der Oberfläche.

Schließlich wird ein erweitertes kinematisches Bodenverfestigungsmodell entwickelt, um den Einfluss von Festigkeits- und Steifigkeitdegradation auf das undrainierte zyklische Verhalten von Saug-Caissons in weichen kohäsiven Böden zu untersuchen (Kapitel 4). Das vereinfachte und praktische Modell wird in Abaqus über eine Benutzer-Subroutine kodiert und mit Hilfe von zyklischen Triaxialversuchen an normal konsolidiertem Kaolin kalibriert, die im Rahmen dieser Studie am geotechnischen Labor der ETH Zürich durchgeführt wurden. Die Triaxialversuche dienen nicht nur der Kalibrierung, sondern helfen auch, die Schlüsselparameter zu identifizieren, die das zyklische Verhalten des untersuchten Bodens

beeinflussen. Es zeigt sich eine starke Abhängigkeit der zyklischen Degradationsrate vom mittleren effektiven Spannungsniveau und der aufgebrauchten zyklischen Dehnungsamplitude. Nach der Validierung anhand veröffentlichter Zentrifugenversuche wird das Modell zur numerischen Bewertung der Leistungsfähigkeit von Saug-Caissons unter kurzzeitiger zyklischer und seismischer Belastung durch eine parametrische Studie genutzt. Dies ermöglicht Einblicke in die Mechanismen, die permanente Caissonverformungen in schnell degradierenden Böden antreiben und zeigt den Einfluss des Caisson-Seitenverhältnisses auf den dynamischen Fundamentwiderstand auf.

Dedicated to my father, George

I will always miss you.

Acknowledgements

As my research journey reaches its conclusion, I would like to extend my heartfelt appreciation to everyone who has provided support, encouragement, and inspiration over the past six years.

I am especially grateful to my thesis supervisors, Prof. Dr. Ioannis Anastasopoulos and Dr. Rallis Kourkoulis (Grid Engineers, Greece), for their invaluable mentorship and guidance.

I also wish to express my thanks to the co-examiners of my thesis, Prof. Dr. Michael Brown and Prof. Dr. Amir Kaynia, for dedicating their time to review my work and for their insightful feedback.

A special acknowledgment goes to my closest collaborator, Dr. Fani Gelagoti from Grid Engineers. Her hands-on involvement, innovative ideas, and sage advice were essential for the successful culmination of this project.

Additionally, I would like to extend my gratitude to Ralf Herzog (Head of Laboratories at the Chair of Geotechnical Engineering, ETH Zurich) for his valuable support in the laboratory, Dr. Athanasios Agalianos (ETH Zurich) for our fruitful scientific discussions, and Max Sieber (ETH Zurich) for his assistance whenever German language skills were required.

I am profoundly thankful to my colleagues at Grid Engineers (Dr. Angelos Tsatsis, Dr. Marianna Loli, Elena Bouzoni) for their continuous support and inspiration, and for occasionally shouldering an extra workload to allow me to concentrate on my research. The supportive atmosphere and spirit of continuous improvement within the office significantly contributed to the successful completion of my doctoral thesis.

Finally, I would like to thank my family and friends for their support and encouragement throughout this journey, and express my deepest gratitude to Lazaros, my most wonderful friend and partner, whose patience, love, and understanding have been a pillar of strength through challenging times.

Zurich, December 2023

Maria Antoniou

Table of Contents

Abstract	i
Zusammenfassung	iii
Acknowledgements	vii
Table of Contents	ix
1. Introduction	1
Abstract.....	1
1.1. Motivation and problem statement	2
1.2. Background and state-of-art	6
1.3. Research gap and objectives.....	14
1.4. Structure of the dissertation.....	15
References	17
2. A compliant guyed system for deep-sea installations of offshore wind turbines: Concept, design insights & dynamic performance	25
Abstract.....	25
2.1. Introduction and problem statement	26
2.2. Proposed concept: 10 MW OWT in the Adriatic Sea	27
2.3. Structural performance of the ‘above-ground’ system	33
2.4. Foundation design and assessment	40
2.5. Earthquake performance of the guyed system	50
2.6. Conclusions	58
Notation	60
References	63
3. Simplified method for performance-based seismic design of suction caissons supporting jacket offshore wind turbines.....	67
Abstract.....	67
3.1. Introduction	68
3.2. Detailed 3D FE Modelling.....	70
3.3. ‘Caisson-on-Winkler-Soil’ (CWS) model.....	78
3.4. CWS vs. detailed 3D FE models: Comparison of performance	85
3.5. Co-seismic caisson settlements	92
3.6. Simplified approach for the preliminary assessment of permanent seismic settlements in SBJ OWTs.....	103

3.7. A hybrid approach for the seismic assessment of SBJ OWTs	109
3.8. Conclusions	110
Acknowledgement	113
Appendix 3A.....	113
Notation	114
References	117
4. Offshore foundations in low-plasticity cohesive soils: Cyclic degradation experimental evidence and simplified numerical analysis.....	122
Abstract.....	122
4.1. Introduction	123
4.2. Experimental cyclic response of normally consolidated kaolin	125
4.3. A practical-simplified model for cyclic degradation in fine-grained soils	133
4.4. Validation against cyclic centrifuge tests of a monopile	144
4.5. Suction caisson in sensitive cohesive soil: cyclic loading.....	149
4.6. Suction caisson in sensitive cohesive soil: seismic loading.....	158
4.7. Study Limitations	162
4.8. Conclusions	163
Acknowledgement	165
Appendix 4A.....	166
Notation	169
References	172
5. Conclusions & Outlook.....	176
Abstract.....	176
5.1. Synopsis and key conclusions	177
5.2. Limitations and outlook	183
References	185

1. Introduction

Abstract

This chapter provides a short introduction to the research detailed in this dissertation, which focuses on the effects of dynamic (seismic and environmental) loading on offshore wind turbine (OWT) foundations suitable for deep water environments and their impact on system performance and operations. The chapter begins by outlining the motivation for this study and then delves into essential background information about the problem under consideration. This aids in highlighting existing research gaps in the literature, which subsequently define the primary objectives of this work. The concluding section offers a brief overview of the dissertation structure.

1.1. Motivation and problem statement

The construction of offshore wind farms (OWFs) is experiencing a surge as countries globally invest more in wind power, aligning with their imperative goals of climate sustainability and energy autonomy. By the end of 2022, more than 60 GW of cumulative offshore wind capacity was recorded worldwide, with almost 9 GW installed in 2022 alone [GWEC, 2023]. For regions like Northern Europe and China, wind farms have already become mainstream power sources, making increasing economic sense, even compared to solar or nuclear power. Not surprisingly, the U.S. is also gearing up with the technology by setting a goal of 30 GW of offshore wind by 2030 and 110 GW or more by 2050 [U.S. Department of Energy, 2023]. Southern Europe also seeks to better exploit its offshore wind potential, while Japan and Taiwan have put in place ambitious Energy Plans that emphasize renewable energy as a 'major' component of their future electricity supply [ACP, 2023; Reuters, 2023]. Ember's Global Electricity Review [2023] identified 2022 as an 'accelerator year' for renewables, propelled by the recent energy crisis and significant policy initiatives, such as REPowerEU¹ (launched by the European Union) and the US Inflation Reduction Act². Wind power generation is anticipated to play a crucial role in this global energy transition.

Just as the offshore wind industry is unlocking its potential worldwide, developers are 'pushing the boundaries' of what is technically possible by increasing the turbines' size and capacity and going further out to the sea for more complex projects in deeper water. Naturally, such changes in turbine structures and installation depths cannot come without an effect on OWT foundations. The current state of practice features the monopile (**Fig. 1.1**) – a steel tubular pile with an outside diameter typically between 3-7 m³ and an embedded length of 25-40 m – as the prevailing foundation option for supporting OWTs [Jiang & Lin, 2022]. Up to 2019, monopiles accounted for 80% of the deployed OWT foundations in Europe [WindEurope, 2019]. Although significant efforts are being made to extend the use of this mature technology for larger capacity turbines in deeper water (e.g., up to 55 – 60m), the industry is increasingly investing in R&D for more suitable foundation schemes to harness the promising market potential in the deep water of Japan, USA, China, the Mediterranean and

¹ <https://eur-lex.europa.eu/legal-content/EN/TXT/?uri=COM%3A2022%3A230%3AFIN&qid=1653033742483>

² The White House (2023). Building A Clean Energy Economy: A Guidebook to the Inflation Reduction Act's Investments in Clean Energy and Climate Action. <https://www.whitehouse.gov/wp-content/uploads/2022/12/Inflation-Reduction-Act-Guidebook.pdf>.

³ Diameters may extend up to 11 m in the case of XXL monopile solutions.

the North Sea, and also to comply with the strict federal policies of limiting noise emissions during monopile driving. Efficient and easy-to-install alternatives for transitional water depths (40-60m) are already establishing their position in the market. Jacket substructures, comprising tubular steel frames founded on piles or suction caissons (**Fig. 1.1**), are currently the second most installed OWT foundation globally, with a percentage of 11.6% in 2022, which is expected to rise with the improvement and industrialization of manufacturing technology [U.S. Department of Energy, 2022]. Other alternatives, such as tethered monopole systems⁴, are currently undergoing large-scale feasibility testing.

From the point of view of investment per megawatt (MW), fixed-bottom offshore wind currently costs about 50% more than onshore wind [Stehly and Duffy, 2022]. Inventory data suggests that foundation expenses constitute 13–20% of a typical offshore wind farm's total cost [IEA, 2019; Stehly and Duffy, 2022]. This significantly contributes to the elevated costs of offshore wind turbines (OWTs) compared to their onshore counterparts, highlighting the importance of choosing appropriate foundation types as a potential avenue to lower energy costs for high-capacity turbines, paving the way for more efficient harnessing of offshore wind energy.

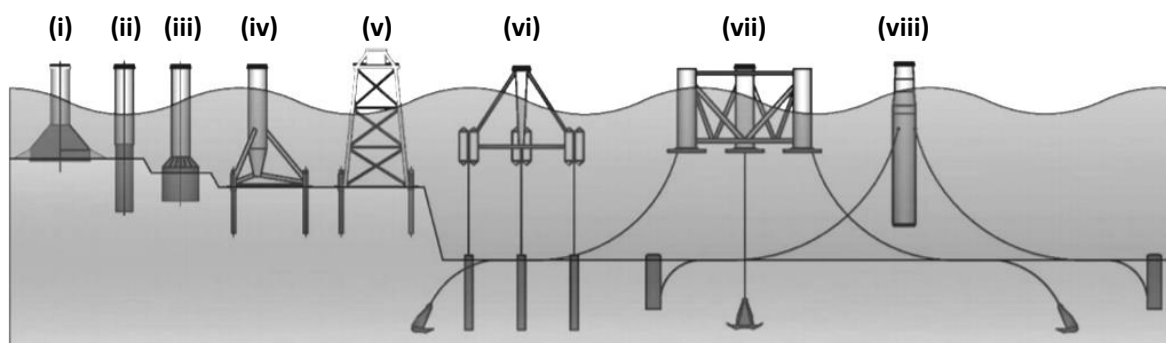


Figure 1.1. Common foundation types used to support offshore wind turbines. *Fixed-bottom systems:* (i) gravity base foundation; (ii) monopile foundation; (iii) monopod suction caisson foundation; (iv) tripod substructure supported on piles; (v) jacket structure supported on piles. *Floating systems:* (vi) tension leg platform anchored to piles; (vii) semi-submersible floating platform moored to drag anchors; (viii) ballast-stabilized floating spar platform anchored to suction caissons [after Bhattacharya et al., 2017].

In deep water (>60m), where fixed-bottom installations are not feasible, floating wind turbine concepts are gaining traction (**Fig. 1.1**), grasping the opportunity to access much larger ocean

⁴ Such as the FRP (fully restrained platform) foundation: <https://www.entrionwind.com/technology>.

areas with high-quality wind resources. Presently, a handful of floating projects are operating globally with a combined capacity of approximately 200 MW [U.S. Department of Energy, 2022]. Notable amongst them are Hywind Scotland (UK), Kincardine (UK), Windfloat Atlantic (Portugal), Hywind Tampen (Norway), and Goto (Japan). Hywind Tampen⁵, currently recognized as the world's largest floating OWF, features concrete spar-type foundations that support eleven 8MW turbines and are anchored at impressive depths of 260 - 300 m. Just 15km off the Aberdeen coast (Scotland) in water depths varying from 60 to 80 m, Kincardine offshore wind farm is the second largest, with five 9.5MW turbines mounted on triangular-shaped semi-submersible foundations⁶. While the prospects for floating offshore wind are indeed promising, it is currently at an earlier technological and commercial stage. Extensive research and development are essential to make it cost-competitive [U.S. Department of Energy, 2023], while the market forecasts its full commercialization after 2030 [GWEC, 2023].

With new foundation concepts in the pipeline and installations moving further into the sea, major issues regarding the entire OWT structure-foundation response need to be thoroughly addressed, from ongoing maintenance/inspection issues to better predictions of the foundation's lifetime performance and ensuring resilient design in view of unfavourable or unexpected loading situations (e.g., more extreme weather conditions than originally anticipated). Wind turbines are designed for a service life of 20 years and are thus subjected to $10^7 - 10^8$ loading cycles during their lifetime. The non-periodic and highly unpredictable nature of offshore cyclic loading may be responsible for significant changes in the soil-foundation response of more than an order of magnitude within the facility's service life. These changes, commonly described by the term 'cyclic degradation', may involve a reduction in both soil stiffness and strength with cyclic loading due to significant soil de-structuring and/or pore pressure accumulation. Considering the effect of cyclic degradation during OWT foundation design is important, as it can be detrimental to foundation capacity; however, it is not an easy task. According to Andersen & Jostad [1999], cyclic soil degradation is extremely stress-path specific, as it is controlled by the ratio of the cyclic shear stress to the average shear stress of a given soil element, as well as the absolute amplitude and frequency of the cyclic loading. As a result, the intensity of cyclic degradation is nonuniform along the foundation.

⁵ <https://www.equinor.com/energy/hywind-tampen>

⁶ <https://www.principlepower.com/projects/kincardine-offshore-wind-farm>

Furthermore, as the industry grows and offshore wind farm construction expands in coastal regions of high seismicity (e.g., Pacific Coast, Gulf of Mexico, Taiwan, Japan, China, and the Mediterranean), the earthquake vulnerability of OWTs should be revisited. Despite their massive dimensions (and hence their large fundamental period), wind turbines are not seismically insensitive [Kourkoulis et al., 2014]. During earthquake shaking, the tower experiences simultaneous unidirectional wind loading, which prevents the oscillation of the tower around its zero-rotation position. As a result, in each seismic cycle, the system accumulates rotation, which (although not disastrous) may risk the serviceability of the structure very early in its operational life. At the same time, the potential reduction of foundation capacity due to changes in soil stiffness and strength during seismic loading may have disastrous consequences: Ashford et al. [2011] offer compelling evidence of the severe impacts of strong earthquakes on wind turbine structures, exemplified by incidents of seismically triggered liquefaction causing tilting of turbine towers during the 2011 Tohoku earthquake in Japan.

Until recently, published offshore design standards [e.g., IEC 61400-1, 2005; GL, 2010; DNV-OS-J101, 2013; API, 2014] did not comprehensively address earthquake loading, either by suggesting the use of seismic specifications from local building codes or other relevant seismic design standards, or by only specifying loading scenarios relevant to seismic assessment/design and raising generic performance expectations without getting into details on the effects of seismic loading on OWTs, the required geotechnical considerations, and appropriate methods to solve the problem [Kaynia, 2019]. Recognizing that earlier design guidance and standards were insufficient for seismic design (or could be interpreted in different ways), DNV recently published the DNV-RP-0585 [2021] recommended practice, where emphasis is placed on best practices for designing OWFs against seismic loading. The standard provides instructions for conducting seismic hazard analysis at a particular OWF site, specifies the seismic design load cases that should be included in the assessment, recommends modelling approaches for analyzing OWT performance under seismic loads (i.e., time-domain analysis or frequency-domain analysis), and highlights critical geotechnical aspects associated with seismic shaking, such as the study of liquefaction phenomena and the consideration of soil-structure interaction and foundation damping in the analysis. Nevertheless, it does not tackle ‘cyclic degradation’ issues that may arise for installations in

weak cohesive soils, nor does it emphasize suitable substructure models for assessing the dynamic performance of OWT foundations (other than the monopile) in deeper water.

In conclusion, the need to reduce the uncertainty (and therefore the cost) in the performance of upcoming OWT foundation schemes for deeper water under cyclic and seismic loading, coupled with the necessity for methods to counter potential soil degradation impacts on their cyclic behaviour, are the primary drivers of the research presented in the present dissertation.

1.2. Background and state-of-art

The cyclic loading exerted on offshore wind turbine foundations ranges from a very large number of low-frequency cycles arising from wind and wave loads during normal operating conditions to a few critical cycles of higher frequency load generated by storms, hurricanes, or earthquakes. In the former case, water-saturated seabeds of relatively high permeability (cohesionless soil, such as sand or gravel) are typically expected to behave in a drained manner. On the contrary, materials of lower permeability (such as soils of high fine-grained content) are assumed to be partially drained, with the development and dissipation of excess pore water pressures alternating during each load cycle. In the case of high frequency, short-duration transient loading, excess pore water pressures do not usually have the time to dissipate, even in the case of sandy materials, forcing soils to behave in an undrained manner. The combination of pore pressure accumulation under undrained conditions and soil remoulding/de-structuring due to foundation deformations may lead to reductions in soil stiffness and strength, manifested in the form of increased accumulated foundation deformations and reduced post-cyclic foundation capacities [Andersen et al., 1993]. Generally acknowledged with the term 'cyclic degradation', the phenomenon may raise alarming concerns for the stability of OWT turbine foundations, especially when considering the strict deformation limits (maximum foundation rotation $\leq 0.5^\circ$) dictated by design standards [DNV-OS-J101, 2013].

The engineering community has invested significant effort over the past few decades in understanding the response of OWT structures under transient cyclic loading. Most studies focused on the response of monopiles subjected to dynamic environmental loading, with a significant portion dedicated to the behaviour of suction caissons, employing both experimental and numerical methods. Less attention has been paid to the response of OWTs

under seismic loading and the mechanics that govern the problem. This section offers a concise overview of the available studies, breaking down the literature into two components: (a) research related to numerical and experimental work on the seismic response of OWTs and (b) recent advances in experimental and computational methods regarding soil-foundation response under cyclic loading in the offshore environment. The present dissertation focuses on the less studied dynamic response of foundations supported on suction caissons, which may offer a cost-efficient alternative (reducing installation cost and underwater installation noise) for increasing water depths. To this end, a large part of the literature review below is dedicated to this foundation type.

Suction caisson foundation: a promising industry entry

Suction-installed foundations, referred to as suction caissons, suction buckets, or suction anchors, have been widely used in the offshore industry since the early 1980s for a wide range of applications, spanning from catenary mooring lines [Colliat et al., 1996] and tension leg platforms [Andersen et al., 1993; Clukey et al., 1995] to (recently) wind-turbine foundations. A suction caisson is essentially a skirt foundation (**Fig. 1.2a**), i.e., a cylindrical shell with an open bottom ('skirt') and a top slab ('lid'). Suction caissons are installed using the principle of suction, whereby the pressure difference between the inside of the bucket and the water surrounding it (at the seabed) leads to the structure being installed without any mechanical force (**Fig. 1.2b**). Negative pore pressures ('suction') are created inside the skirt compartment, pulling the foundation downwards until the internal soil plug is perfectly 'sealed' onto the caisson's lid, thus eliminating the need for driving.

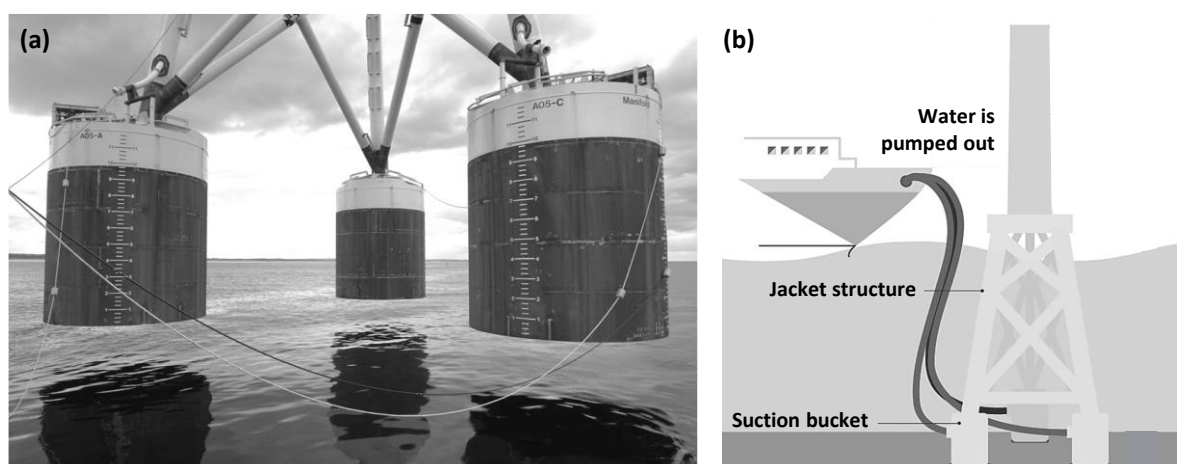


Figure 1.2. (a) Suction caissons as the foundation of a tripod jacket substructure (Image credits: [SPT Offshore](#)); and (b) schematic illustration of the suction caisson installation

procedure, where water is being pumped out of the caissons' interior, creating suction conditions (Image credits: [Vattenfall](#)).

A key difference between suction-installed foundations and other foundation types is that the installation design, which must consider the soil type, soil strength, installation-specific risks (e.g., the presence of boulders or other hard inclusions) and the installation process (e.g., the speed of installation), have a direct influence on foundation dimensions. As long as perfectly undrained conditions are assumed (i.e. when soil permeability is low or/and the application of the load is transient), the 'sealing' is safe. The negative excess pore water pressure generated between the bottom side of the foundation top plate and the soil prevents the caisson detachment from the surrounding soil, thus offering tensile resistance. In the case of a vertically pulled-up caisson, as the inner soil plug is uplifted due to suction, the outer soil is dragged beneath the bucket, mobilizing a 'reverse end bearing' mechanism of increased resistance [Senders, 2008]. Increased resistance values have also been reported for horizontally or rotationally displaced perfectly 'sealed' caissons. In the literature, one may find experimental data questioning the validity of the perfectly 'sealed' conditions assumption. Randolph et al. [1998] reported centrifuge model tests of suction caissons in normally consolidated silty clay with evidence of soil-caisson detachment in the form of a vertical crack along the skirt periphery, forming at very large displacement and causing an 18% drop in bearing capacity. On the other hand, the experiments of Clukey et al. [2003] and Coffman et al. [2004] in normally consolidated clay showed no detachment, even at large displacements.

OWTs under seismic loading

Ground shaking exerts inertial loading on the structure, while the propagation of seismic shear waves through the soil induces additional stressing to the foundation (kinematic loading) due to the vibration of the surrounding soil. Despite the decades of research into earthquake engineering, the topic only recently became of interest for OWTs following the expansion of the offshore wind industry into seismically active areas.

Most of the relevant research to date is related to monopile-supported OWTs. Through a series of 1g shaking table tests on the reference NREL-5MW turbine supported by a monopile foundation, Zheng et al. [2015] demonstrated that ignoring environmental actions in seismic analysis underestimates foundation deformations. Mo et al. [2017], De Risi et al. [2018], Wang et al. [2018] and Vacareanu et al. [2019] used numerical analysis to explore the sensitivity of

OWTs on monopile foundations to recorded seismic events, considering the combined effects of seismic and environmental (wind and wave) loading, while Kaynia [2021] highlighted the influence of soil-pile kinematic interaction in the seismic response of the system.

Despite the rise of jacket support structures in the offshore market, investigations of their dynamic response have received less attention in the recent literature. Alati et al. [2015] assessed the structural stability of the blades during earthquake events for OWTs on tripod or tetrapod structures. With a focus on structural OWT response, the study revealed that the seismic oscillation of the tower top significantly affects the rotor aerodynamics. Gelagoti et al. [2019] performed a direct comparison of the performance of a 10MW offshore wind turbine supported on either a large-diameter monopile or a 4-legged jacket on piles under combined environmental and seismic loading. The analysis revealed the superior performance of the lattice structure, which was found to accumulate less irrecoverable deformation under non-symmetric dynamic loading.

Similarly, few studies have been reported on the response of suction caissons in clay subjected to (undrained) seismic shaking, despite the extensive work on their undrained monotonic capacity, installation process, and short-term cyclic response⁷, by means of centrifuge tests [e.g., Mana et al., 2012; 2013; Bienen et al., 2018a], 1-g laboratory tests [e.g., Cauble 1998], limit equilibrium methods [e.g., Deng et al., 2002; Iskander et al., 2002; Randolph & House, 2002], and finite element (FE) modelling [e.g., Bransby & Yun, 2009; Gourvenec & Barnett, 2011; Vulpe 2015; Keawsawasvong & Ukritchon, 2016; Ukritchon & Keawsawasvong, 2016; Ukritchon et al., 2018; Zou et al., 2018]. In one of the few studies dealing with seismic response, Kourkoulis et al. [2014] provide insights into the role of soil-structure interaction (SSI) using coupled 3D numerical analyses to evaluate the effect of soil-sidewall interfaces on the response of OWTs founded on monopod suction caissons under combined environmental and earthquake loading.

For cohesionless soils, the effect of earthquake-induced liquefaction on system performance has gained significant attention. With the aid of centrifuge model testing, Yu et al. [2015], Wang et al. [2020], and Seong et al. [2023] investigated the phenomenon for monopile-supported OWTs under strong seismic shaking in terms of post-earthquake foundation deformations and remaining foundation capacity. Using the same physical

⁷ For studies relevant to the cyclic response of suction caissons refer to the next subsection.

modelling technique, Wang et al. [2017] examined the liquefaction potential of OWTs on monopod suction caissons, considering the effect of different aspect ratios in the caisson dynamic resistance. Esfeh & Kaynia [2020] and Gao et al. [2021] employed numerical analysis to investigate the seismic performance of OWTs supported on both monopiles and monopod suction caissons in liquefiable soils, indicating that both foundations may experience considerable rotation when liquefaction occurs. Finally, several researchers have proposed simplified methods for the estimation of liquefaction potential for OWTs on liquefiable soil [Geng et al., 2023], the effect on the fundamental frequency of the system [Demirci et al., 2022], or the liquefaction-induced foundation deformations [Farahani & Barari, 2023; Patra et al., 2022].

Long-term environmental cyclic loading

As the industry is focusing its interest on the lifetime performance assessment of OWTs, the long-term cyclic performance of dominant OWT foundations has been the subject of numerous experimental investigations. Most of them focus on the performance of monopile or suction caisson foundations in sand or clay, subjected to a large number of environmental load cycles.

Using small-scale 1g experiments [e.g., LeBlanc et al., 2010; Cuellar, 2011; Abadie et al., 2019] or centrifuge model testing [e.g., Bienen et al., 2012; Klinkvort & Hededal, 2013; Truong et al., 2019], empirical formulas (typically power or logarithmic laws) have been proposed to correlate the long-term accumulated deformations of monopiles in sand under lateral loading (rotation or lateral deflection at the pile head) and the change in soil-pile stiffness with the number of lateral load cycles N , considering the effects of load amplitude, symmetry and sequence, foundation rigidity and aspect ratio, strain rate, sand particle size and material density.

Unlike monopiles, where the principal loading direction is horizontal, suction caissons may sustain combined horizontal and moment loading when applied as monopod foundations or axial loading when part of a tripod or tetrapod jacket substructure. Based on experimental results, empirical expressions such as those mentioned above have also been derived for the accumulated rotation of suction caissons under cyclic lateral loading in sand [Zhu et al., 2013; Foglia et al., 2016; Cox et al., 2014], clay [Zhu et al., 2018; 2019; Zhou et al., 2022] and layered soil profiles [Zhu et al., 2018; 2019]. Using small-scale 1g model tests, Zhu et al. [2018]

quantified the effect of 1 million load cycles (corresponding to fully drained conditions for sand and initially undrained/partially drained after many cycles conditions for clay) on the post-cyclic foundation capacity and stiffness, reporting a significant increase in both due to densification effects in sand and consolidation in clay. Their results were coupled with the experimental campaign of Zhu et al. [2019], who repeated the same tests in the centrifuge to compare the response at correct stress levels⁸, where the suction caisson installation and drainage effects can be modelled appropriately. To date, limited experimental work has been conducted on the long-term behaviour of suction caissons under vertical cyclic loading (especially relevant to the design of multipod OWT foundations). To the author's knowledge, no experimental study exists for the prediction of the caisson long-term axial response, with the work conducted so far corresponding to a limited amount of loading cycles [e.g., Clukey et al., 1995; Byrne & Houlsby, 2002; Chen and Randolph, 2007; Villalobos et al., 2010; Kelly et al., 2006; Bienen et al., 2018] examining the effect of load characteristics, soil parameters, or installation method (jacked in place or installed with suction) on the caisson's cyclic response and post-cyclic foundation capacity.

Aiming to predict long-term cyclic foundation performance, the numerical methods proposed over the years broadly fall into two categories. *Implicit methods* employ advanced finite element, finite difference, or macro-element approaches [e.g., Taiebat & Dafalias, 2008; Cuellar et al., 2014; Masin, 2014; Tasiopoulou & Gerolymos, 2016; Liu et al., 2019; Elia & Rouainia, 2016; Shi et al., 2018; Skau et al., 2018; Fuentes et al., 2021] to describe soil cyclic response on an incremental stress-strain basis. However, their application is typically limited to a small number of cycles ($< 10^4$), not only due to prolonged computation times but also because the numerical error tends to accumulate with load cycles [Staubach et al., 2022]. *Explicit methods* have been developed to address this challenge, such as the high-cycle accumulation model for sand and clay [Niemunis et al., 2005; Staubach et al., 2022]. Rather than using stress-strain increments, these models model soil response through an explicit function that correlates the accumulated soil strain with the number of load cycles, the mechanical soil properties and the loading parameters. Explicit models are calibrated on the

⁸ Centrifuge modelling offers the ability to correctly reproduce the confining soil stresses to be consistent with those of the prototype, thus avoiding scale effects.

basis of long-term cyclic laboratory tests and are considered more accurate and efficient for computations involving a large number of load cycles [Skau et al., 2022].

Cyclic degradation phenomena in soft marine soils

The repeated undrained (or partially drained) cyclic shear loading induced on soft cohesive deposits underlying OWT structures degrades the soil structure, leads to the accumulation of pore water pressures, and decreases the stiffness and undrained shear strength of the soil [Vucetic & Dobry, 1988; Andersen, 2015]. On the other hand, the undrained strength of cohesive soils subjected to repeated cyclic loading has been shown to increase with a rise in strain rate [Lefebvre & Pfendler, 1996], raising questions on how these opposing mechanisms may eventually affect the response of an OWT foundation under high-frequency cyclic loading.

The influence of cyclic degradation on the response of cohesive soils has been evaluated extensively via laboratory testing [e.g., Procter & Khaffaf, 1984; Andersen et al., 1980; Hyde and Ward, 1985; Azzouz et al., 1989; Diaz-Rodriguez, 1989; Yasuhara et al., 1992; Andersen et al., 1992; Matasovic & Vucetic, 1995; Lefebvre & Pfendler, 1996; Mortezaie & Vucetic, 2013; Hanna & Javed, 2014; Wichtmann & Triantafyllidis, 2018; Thian et al., 2018, Zografou et al., 2019]. The relevant studies employed cyclic undrained triaxial or simple shear tests on different types of cohesive soils to explore dominant parameters affecting soil properties under repeated cyclic loading, such as the magnitude and number of load cycles, the over-consolidation ratio, the strain rate, the plasticity and sensitivity of the soil material, and the average shear stress to cyclic shear stress ratio. Einav & Randolph (2005) presented a simple physics-based model for the quantification of strain rate and strain softening effects on the undrained shear strength of cohesive soils based on the analysis of cyclic penetrometer tests.

Several studies have examined the phenomenon experimentally, using centrifuge tests to assess the performance of OWT foundation systems in soft soils under a limited number of cycles [e.g., Zhang et al., 2011; Lai et al., 2020; Hong et al., 2017; Zhu et al., 2020; 2021]. The experimental results of Zhu et al. [2020] on pile foundations indicate a clear degradation trend of lateral soil-pile resistance, which tends to stabilize after the first 20 load cycles. For the same foundation type, Zhang et al. [2011] and Lai et al. [2020] investigated the impact of alternating episodes of cycling and reconsolidation, reporting that the decrease in lateral soil-pile stiffness during cyclic loading is ultimately recovered (and even increased) during the intervening

periods of reconsolidation, due to dissipation of excess pore water pressures, leading to a local increase of shear strength. On the contrary, in their study on the vertical cyclic response of suction caissons in soft clay, Zhu et al. [2021] reported that several cycles of large-amplitude loading (equivalent to an extreme event, rather than normal operating conditions) were sufficient to dramatically reduce the foundation bearing capacity, leading to failure.

In terms of numerical methods, few studies have proposed implicit methods (involving advanced constitutive models based on an effective stress approach) to simulate the degradation of cyclically loaded undrained clay [e.g., Elia & Rouainia, 2016; Shi et al., 2018; Masin, 2014, also referenced in the previous section]. However, the application of such models for the assessment of foundation response at the system level is scarce and only related to pile foundations [e.g., Hong et al., 2017], while it does not extend to the assessment of the phenomenon during realistic irregular cyclic loading (stemming from a storm or an earthquake event). More recently, Huang et al. [2021] and Shi et al. [2023] proposed a less complex numerical approach based on total stress-based models that treat the soil as a single-phase medium with undrained shear strength properties (stiffness and strength) that may vary during cycling as a function of the cyclic degradation characteristics of the examined soil. The approach has not yet been employed to explore the deformation generation mechanisms in OWT foundations under extreme transient events.

Apart from the aforementioned methods, the cyclic degradation method developed by the Norwegian Geotechnical Institute (NGI) may also be used to predict cyclic degradation effects for foundations in undrained or partially drained soils [Andersen, 2015]. The method has been incorporated in two user-defined material models in the finite element (FE) code PLAXIS [Jostad et al., 2014; 2015] and accounts for the effect of cyclic loading on soils based on strain contour diagrams derived from cyclic and monotonic laboratory tests. For the calculations, the original loading history (e.g., storm loading) should be replaced with an equivalent number of constant amplitude load cycles. However, such idealisation of the actual load history cannot be ensured to be efficiently applied in simulations of earthquake events due to the highly variable – in terms of frequency and amplitude – nature of seismic excitations. Furthermore, although it allows the calculation of post-cyclic foundation resistance in the aftermath of a cyclic event and, therefore, may be used to assist foundation design, it does not allow monitoring of the evolution of the event, thereby hindering the detection of the nonlinear mechanisms involved in the generation of accumulated foundation deformations.

1.3. Research gap and objectives

As highlighted by the literature review, the seismic performance of alternative OWT foundations – beyond the prevalent monopile solution – has been sparingly addressed in the literature. At the same time, the effect of cyclic degradation during short-term transient loading for OWTs founded on very soft soil deposits remains ambiguous.

Aiming to address this gap, the dissertation utilizes nonlinear 3D FE modelling techniques to comprehensively study the response of emerging fixed-bottom OWT foundation schemes in cohesive soils under adverse seismic and environmental cyclic loading: namely, a tethered monopile structure and a jacket structure, both founded through suction caissons. The presented work examines the issue from the soil-foundation-superstructure (SFS) perspective, offering a comprehensive exploration of the seismic interplay between foundation-wind turbine systems and their response to adverse environmental loading. Furthermore, to meet the pressing requirement of current OWT design standards for special studies considering seismic loading, a simplified method for the performance-based assessment of OWTs supported on Suction Bucket Jackets (SBJs) is proposed. The methodology enables the preliminary evaluation of co-seismic foundation deformations without necessitating a 3D FE analysis of the entire system. The potential impact of cyclic degradation on the undrained dynamic response of the examined systems in very soft soils is also explored using a practical numerical method. The proposed constitutive model is calibrated through cyclic laboratory tests conducted at the ETHZ geotechnical laboratory and validated against published centrifuge model test results.

The dissertation makes an original contribution towards maintaining the operability of offshore foundations during extreme events by proposing a shift in the design philosophy for next-generation offshore wind turbines: from merely fortifying the superstructure to enhancing the agility of the entire structure-foundation system. Herein, the foundation is recognized not just as a boundary condition but as a pivotal element in maintaining operability and prolonging the lifespan of OWTs. As new foundation concepts are envisioned and constructed at a prototype level to fulfil installation requirements at a reasonable cost, the outcomes of the present research offer valuable insights into their dynamic performance, which could remove the barriers to investment in offshore wind energy resources in areas of intense weather conditions and/or seismic activity, and lead to substantial reductions in

design and construction costs, as well as potential disaster losses (e.g., loss in energy production from a wind farm shutdown).

1.4. Structure of the dissertation

This dissertation comprises five chapters in total that summarise the conducted work. Chapter 1 briefly introduces the studied problem, while Chapters 2 and 3 explore the dynamic/seismic performance of two easily installable substructure alternatives for OWTs founded in intermediate water depths, where the monopile no longer constitutes a viable option. More specifically, Chapter 2 describes the behaviour of a compliant OWT tower mounted on a central shallow footing anchored to the seabed via an array of pretensioned cables (at a 45° angle). This novel foundation scheme aims to bridge the gap between traditional fixed-bottom systems and floating substructures, offering a cost-efficient solution for transitional water depths. Utilizing Abaqus, a 3D FE model representing the soil-foundation-superstructure system is developed based on a reference 10 MW turbine installed at a 50 m water depth. The study demonstrates the effectiveness of the proposed solution by assessing its performance under Ultimate Limit State (ULS) and Serviceability Limit State (SLS) environmental conditions and its resilience to combined environmental and seismic loading. A rigorously validated kinematic hardening model with a Von Mises failure criterion is employed to describe the undrained nonlinear soil behaviour. Design insights regarding the structural performance of the 'above-ground' system are provided, emphasizing the dynamic response of the cables and the potential of an unconventional design alternative where the system's frequency does not fall within the widely used 'soft-stiff' design range. The optimum location for the padeye (i.e., the connection point between the suction caissons and the mooring lines) is parametrically investigated, revealing its effect on the pullout capacity and stiffness of the anchoring system. The impact of caisson 'sealing' (i.e., the ability of caissons to resist tensile stresses due to the suction developed and maintained below the lid) in the overall foundation response is explored, along with the pivotal role of the central foundation in controlling the pretension of the mooring lines during seismic shaking.

Chapter 3 delves into the response of the commercially available – yet less studied – Suction Bucket Jacket (SBJ) foundation under concurrent environmental and seismic loading. An 8 MW OWT installed at 60m depth is used as a benchmark. In an effort to increase computational efficiency, an enhanced 'Caisson-on-Winkler-Soil' (CWS) model is developed,

where soil-suction caisson interaction is captured by nonlinear hysteretic (vertical, horizontal, and rotational) elements that allow simulation of permanent caisson deformations. The performance of the simplified model is compared to that of a comprehensive 3D FE model of the entire soil–foundation–structure (SFS) system (using the same soil constitutive model employed in Chapter 2) to explore its limitations and shed light on the mechanics that govern the accumulation of nonlinear caisson deformations (settlement, horizontal displacement, and rotation) under combined environmental and earthquake loading. The 3D analyses reveal a coupled shearing mechanism occurring due to inertial and kinematic loading at the caisson-soil interfaces, which drives the accumulation of co-seismic caisson settlements and cannot be captured by the proposed (or any similar) Winkler-based model. A hybrid method is introduced for performance-based seismic assessment of OWTs on Suction Bucket Jackets, combining the CWS model for the estimation of Vertical-Horizontal-Moment (VHM) loads and horizontal displacements/rotations at the jacket legs with a regression model (developed with the aid of an extensive numerical campaign) for the assessment of co-seismic caisson settlements. The derived regression equations, formulated in dimensionless terms to allow broader applicability, correlate caisson settlements with the Arias Intensity (I_A) of the surface ground motion and a set of dimensional variables related to load characteristics, soil properties, and foundation geometry.

Chapter 4 extends the formulation of the total stress-based soil constitutive model employed in Chapters 2 and 3 to study the influence of soil strength and stiffness degradation on the undrained cyclic performance of offshore foundations in soft cohesive deposits. The developed ‘VM-CD’ model is encoded in Abaqus via a user subroutine and is calibrated using a targeted series of cyclic triaxial tests on normally consolidated Kaolin conducted as part of this study at the ETHZ geotechnical laboratory. The triaxial tests not only serve calibration purposes but also help identify the key parameters affecting the cyclic behaviour of the examined soil – a low plasticity material that remains largely unaffected by strain rate effects. Following validation against published centrifuge model tests, the model is exploited to assess the performance of suction caisson foundations under short-term cyclic and seismic loading. The load combinations applied to the 3D soil-caisson models are relevant to those anticipated for suction caissons supporting the substructure types discussed in Chapters 2 and 3. Through a parametric study, the chapter provides insights into the mechanisms driving permanent

foundation deformations in fast-degrading soil and the influence of the caisson aspect ratio on the caisson dynamic resistance.

Finally, Chapter 5 summarizes the key findings and contributions of this dissertation and provides an outlook with suggestions for future research on the studied problem.

References

- Abadie, C. N., Byrne, B. W., & Houlsby, G. T. (2019). Rigid pile response to cyclic lateral loading: laboratory tests. *Géotechnique*, 69(10), 863-876.
- ACP (2023). Offshore Wind Market Report. May 2023. *American Clean Power*. Available at: <https://cleanpower.org/resources/offshore-wind-market-report-2023/>
- Alati, N., Failla, G., & Arena, F. (2015). Seismic analysis of offshore wind turbines on bottom-fixed support structures. *Philosophical Transactions of the Royal Society A: Mathematical, Physical and Engineering Sciences*, 373(2035), 20140086.
- Andersen, K. H. (2015). Cyclic soil parameters for offshore foundation design. *Frontiers in offshore geotechnics III*, 5.
- Andersen, K. H., Dyvik, R., Yoshiaki, Y. & Skomedal, E. (1992). Clay behaviour under irregular cyclic loading. In *Proceedings of the 6th international conference on the behaviour of offshore structures (BOSS 92)* (eds M. H. Patel and R. Gibbins), vol. 2, pp. 937–950. London, UK: BPP Technical Services.
- Andersen, K. H., Rosenbrand, W. F., Brown, S. F., & Pool, J. H. (1980). Cyclic and static laboratory tests on Drammen clay. *Journal of the Soil Mechanics and Foundations Division*, 106(5), 499-529.
- Andersen, K., Dyvik, H.R., Schroder, K., Hansteen, O.E, Bysveen, S. (1993). Field test of anchors in clay II predictions and interpretation. *Journal of Geotechnical and Geoenvironmental Engineering* 119, 1532–1549.
- Andersen, K.H. and Jostad, H.P. (1999). Foundation design of skirted foundations and anchors in clay, *Proc. Annual Offshore Technology Conf.*, Houston, Paper OTC 10824.
- API (2014). API Recommended Practice 2A-WSD - Planning, Designing, and Constructing Fixed Offshore Platforms. API recommended practice 2A-WSD (RP2A-WSD), 22nd Ed., *American Petroleum Institute*, Washington DC.
- Ashford, S. A., Boulanger, R. W., Donahue, J. L., & Stewart, J. P. (2011). Geotechnical quick report on the Kanto Plain region during the March 11, 2011, Off Pacific Coast of Tohoku earthquake, Japan. *GEER Association Report No GEER-025a*, Geotechnical Extreme Events Reconnaissance (GEER).
- Azzouz, A. S., Malek, A. M., & Baligh, M. M. (1989). Cyclic behavior of clays in undrained simple shear. *Journal of Geotechnical Engineering*, 115(5), 637-657.
- Bhattacharya, S., Nikitas, G., Arany, L., & Nikitas, N. (2017). Soil-Structure Interactions (SSI) for Offshore Wind Turbines. *IET Engineering and Technology Reference*, 24(16).

- Bienen, B., Dührkop, J., Grabe, J., Randolph, M. F., & White, D. J. (2012). Response of piles with wings to monotonic and cyclic lateral loading in sand. *Journal of Geotechnical and Geoenvironmental Engineering*, 138(3), 364-375.
- Bienen, B., Klinkvort, R. T., O'loughlin, C. D., Zhu, F., & Byrne, B. W. (2018a). Suction caissons in dense sand, part I: installation, limiting capacity and drainage. *Géotechnique*, 68(11), 937-952.
- Bienen, B., Klinkvort, R. T., O'Loughlin, C. D., Zhu, F., & Byrne, B. W. (2018). Suction caissons in dense sand, part II: vertical cyclic loading into tension. *Géotechnique*, 68(11), 953-967.
- Bransby M.F., Yun G. (2009). The undrained capacity of skirted strip foundations under combined loading. *Géotechnique* 59 (2), 115–125.
- Byrne, B. W., & Houlsby, G. T. (2002). Experimental investigations of response of suction caissons to transient vertical loading. *Journal of Geotechnical and Geoenvironmental Engineering*, 128(11), 926-939.
- Cauble, D. F. (1998). An experimental investigation of the behavior of a model suction caisson in a cohesive soil.
- Chen, W., & Randolph, M. F. (2007). Uplift capacity of suction caissons under sustained and cyclic loading in soft clay. *Journal of Geotechnical and Geoenvironmental Engineering*, 133(11), 1352-1363.
- Clukey, E.C., Aubeny C.P. and Murff J., (2003). Comparison of Analytical and Centrifuge Model Tests for Suction Caissons Subjected to Combined Loads. *International Conference on Offshore Mechanics and Arctic Engineering*, Volume 3: Materials Technology; Ocean Engineering; Polar and Arctic Sciences and Technology; Workshops, pp. 889-894, Cancun, Mexico.
- Clukey, E.C., Morrison, M.J., Garnier, J., and Corte, J.F. (1995). The response of suction caissons in normally consolidated clays to cyclic TLP loading conditions. *Offshore Technology Conference*, Houston, Texas, OTC 7796.
- Coffman, R.A., El-Sherbiny, R.M., Rauch, A.F., Olson, R.E., (2004). Measured Horizontal Capacity of Suction Caissons. *Proc., Offshore Tech. Conf.*, Houston, Paper 16161.
- Colliat, J.L., Boisard, P., Gramet, J.C., Sparrevik, P., (1996). Design and installation of suction anchor piles at a soft clay site in the Gulf of Guinea. Paper OTC 8150, *Offshore Technology Conference*, Houston, Texas.
- Cox, J. A., O'Loughlin, C. D., Cassidy, M., Bhattacharya, S., Gaudin, C., & Bienen, B. (2014). Centrifuge study on the cyclic performance of caissons in sand. *International Journal of Physical Modelling in Geotechnics*, 14(4), 99-115.
- Cuéllar, P. (2011). Pile foundations for offshore wind turbines: numerical and experimental investigations on the behaviour under short-term and long-term cyclic loading. PhD Thesis. TU Berlin.
- Cuéllar, P., Mira, P., Pastor, M., Merodo, J. A. F., Baeßler, M., & Rücker, W. (2014). A numerical model for the transient analysis of offshore foundations under cyclic loading. *Computers and Geotechnics*, 59, 75-86.

- De Risi, R., Bhattacharya, S., & Goda, K. (2018). Seismic performance assessment of monopile-supported offshore wind turbines using unscaled natural earthquake records. *Soil Dynamics and Earthquake Engineering*, 109, 154-172.
- Demirci, H. E., Jalbi, S., & Bhattacharya, S. (2022). Liquefaction effects on the fundamental frequency of monopile supported offshore wind turbines (OWTs). *Bulletin of Earthquake Engineering*, 20(7), 3359-3384.
- Deng, W., Carter, J.P. (2002). A theoretical study of the vertical uplift capacity of suction caissons. *Int. J. Offshore Polar* 12 (2), 89–97.
- Diaz-Rodriguez, J. A. (1989). Behavior of Mexico City clay subjected to undrained repeated loading. *Canadian Geotechnical Journal*, 26(1), 159-162.
- DNV-OS-J101 (2013). Design of offshore wind turbine structures. *Det Norske Veritas*.
- DNV-RP-0585 (2021). Seismic design of wind power plants. *Det Norske Veritas*.
- Einav, I., & Randolph, M. F. (2005). Combining upper bound and strain path methods for evaluating penetration resistance. *International journal for numerical methods in engineering*, 63(14), 1991-2016.
- Elia, G., & Rouainia, M. (2016). Investigating the cyclic behaviour of clays using a kinematic hardening soil model. *Soil Dynamics and Earthquake Engineering*, 88, 399-411.
- Esfeh, P. K., & Kaynia, A. M. (2020). Earthquake response of monopiles and caissons for Offshore Wind Turbines founded in liquefiable soil. *Soil Dynamics and Earthquake Engineering*, 136, 106213.
- Farahani, S., and Barari, M. (2023). A simplified procedure for the prediction of liquefaction-induced settlement of offshore wind turbines supported by suction caisson foundation based on effective stress analyses and an ML-based group method of data handling. *Earthquake Engineering & Structural Dynamics*.
- Foglia, A., & Ibsen, L. B. (2016). Monopod bucket foundations under cyclic lateral loading. *International Journal of Offshore and Polar Engineering*, 26(02), 109-115.
- Fuentes, W., Masin, D., Duque, J. (2021) Constitutive model for monotonic and cyclic loading on anisotropic clays. *Geotechnique* 71(8):657–673.
- Gelagoti, F. M., Kourkoulis, R. S., Georgiou, I. A., & Karamanos, S. A. (2019). Soil–structure interaction effects in offshore wind support structures under seismic loading. *Journal of Offshore Mechanics and Arctic Engineering*, 141(6), 061903.
- Geng, F., Yang, W., Nadimi, S., Han, B., & Huang, G. (2023). Study for predicting the earthquake-induced liquefaction around the monopile foundation of offshore wind turbines. *Ocean Engineering*, 268, 113421.
- GL (2010). Guideline for the certification of wind turbines. *Germanischer Lloyd*, Hamburg.
- Gourvenec S., Barnett S. (2011). Undrained failure envelope for skirted foundations under general loading. *Géotechnique*, 261(3), 263–270.
- GWEC (2023). Global Offshore Wind Report 2023. *Global Wind Energy Council*. Available at: <https://gwec.net/wp-content/uploads/2023/08/GWEC-Global-Offshore-Wind-Report-2023.pdf>

- Hanna, A. M., & Javed, K. (2014). Experimental investigation of foundations on sensitive clay subjected to cyclic loading. *Journal of Geotechnical and Geoenvironmental engineering*, 140(11), 04014065.
- Hong, Y., He, B., Wang, L. Z., Wang, Z., Ng, C. W. W., & Mašín, D. (2017). Cyclic lateral response and failure mechanisms of semi-rigid pile in soft clay: centrifuge tests and numerical modelling. *Canadian Geotechnical Journal*, 54(6), 806-824.
- Huang, M., Liu, L., Shi, Z., & Li, S. (2021). Modeling of laterally cyclic loaded monopile foundation by anisotropic undrained clay model. *Ocean Engineering*, 228, 108915.
- Hyde, A. F. L., & Ward, S. J. (1985). A pore pressure and stability model for a silty clay under repeated loading. *Geotechnique*, 35(2), 113-125.
- IEA (2019). Offshore Wind Outlook 2019. *International Energy Agency*.
- IEC 61400-1 (2005). Wind turbines – Part 1: design requirements, Ed. 3. *International Electrotechnical Commission*, Geneva.
- Iskander, M., El-Gharbawy, S., Olson, R. (2002). Performance of suction caissons in sand and clay. *Can. Geotech. J.* 39 (3), 576–584.
- Jiang, W., & Lin, C. (2022). Lateral responses of monopile-supported offshore wind turbines in sands under combined effects of scour and earthquakes. *Soil Dynamics and Earthquake Engineering*, 155, 107193.
- Jostad, H.P., Grimstad, G., Andersen, K.H. & Sivasithamparam, N. (2015). A FE procedure for calculation of cyclic behaviour of offshore foundations under partly drained conditions. *Proc., Int. Symp. on Frontiers in Offshore Geotechnics*, ISFOG, Oslo, Norway.
- Jostad, H.P., Grimstad, G., Andersen, K.H., Saue, M., Shin, Y. & You, D. (2014). A FE procedure for foundation design of offshore structures – applied to study a potential OWT monopile foundation in the Korean Western Sea. *Geotech. Engrg. J. of SEAGS & AGSSEA*, Vol. 45 (4), Dec 2014.
- Kaynia, A. M. (2019). Seismic considerations in design of offshore wind turbines. *Soil Dynamics and Earthquake Engineering*, 124, 399-407.
- Kaynia, A. M. (2021). Effect of kinematic interaction on seismic response of offshore wind turbines on monopiles. *Earthquake Engineering & Structural Dynamics*, 50(3), 777-790.
- Keawsawasvong S., Ukritchon B. (2016). Finite element limit analysis of pullout capacity of planar caissons in clay. *Comput. Geotech.* 75, 12–17.
- Kelly, R. B., Houlsby, G. T., & Byrne, B. W. (2006). Transient vertical loading of model suction caissons in a pressure chamber. *Géotechnique*, 56(10), 665-675.
- Klinkvort, R. T., & Hededal, O. (2013). Lateral response of monopile supporting an offshore wind turbine. *Proceedings of the Institution of Civil Engineers-Geotechnical Engineering*, 166(2), 147-158.
- Kourkoulis, R., Lekakakis, P.C., Gelagoti, F.M. and Kaynia, A. (2014). Suction Caisson foundations for offshore wind turbines subjected to wave and earthquake loading: effect of soil-foundation interface. *Géotechnique*, 64, No. 3, 171-185.

- Lai, Y., Wang, L., Hong, Y., & He, B. (2020). Centrifuge modeling of the cyclic lateral behavior of large-diameter monopiles in soft clay: Effects of episodic cycling and reconsolidation. *Ocean Engineering*, 200, 107048.
- LeBlanc, C., Houlsby, G. T., & Byrne, B. W. (2010). Response of stiff piles in sand to long-term cyclic lateral loading. *Géotechnique*, 60(2), 79-90.
- Lefebvre, G., and Pfendler, P. (1996). Strain rate and preshear, effects in cyclic resistance of soft clay. *Journal of Geotechnical Engineering*, ASCE, 22(1): 21–26.
- Liu, H. Y., Abell, J. A., Diambra, A. & Pisanò, F. (2019). Modelling the cyclic ratcheting of sands through memory-enhanced bounding surface plasticity. *Géotechnique* 69, No. 9, 783–800, <https://doi.org/10.1680/jgeot.17.P.307>
- Mana, D.S.K., Gourvenec, S., Randolph, M., Hossain, M.S. (2012). Failure mechanisms of skirted foundations in uplift and compression. *Int. J. Phys. Modell. Geotech.*12 (2), 47–62.
- Mana, D.S.K., Gourvenec, S., Randolph, M.F. (2013). Experimental investigation of reverse end bearing of offshore shallow foundations. *Can. Geotech. J.* 50, 1022–1033.
- Mašín, D. (2014). Clay hypoplasticity model including stiffness anisotropy. *Géotechnique* 64(3): 232-238.
- Matasović, N., & Vucetic, M. (1995). Generalized cyclic-degradation-pore-pressure generation model for clays. *Journal of geotechnical engineering*, 121(1), 33-42.
- Mo, R., Kang, H., Li, M., & Zhao, X. (2017). Seismic fragility analysis of monopile offshore wind turbines under different operational conditions. *Energies*, 10(7), 1037.
- Mortezaie, A. R., & Vucetic, M. (2013). Effect of frequency and vertical stress on cyclic degradation and pore water pressure in clay in the NGI simple shear device. *Journal of Geotechnical and Geoenvironmental Engineering*, 139(10), 1727-1737.
- Niemunis, A., Wichtmann, T. & Triantafyllidis, T. (2005). A high-cycle accumulation model for sand. *Comput. Geotech.* 32, No. 4, 245–263
- Patra, S. K., Haldar, S., & Bhattacharya, S. (2022). Predicting tilting of monopile supported wind turbines during seismic liquefaction. *Ocean Engineering*, 252, 111145.
- Procter, D. C., & Khaffaf, J. H. (1984). Cyclic triaxial tests on remoulded clays. *Journal of Geotechnical Engineering*, 110(10), 1431-1445.
- Randolph, M. F., & House, A. R. (2002). Analysis of suction caisson capacity in clay. Offshore technology conference. *Offshore Technology Conference*, Houston, Texas.
- Randolph, M., O'Neill, M., Stewart, D., Erbich, C., (1998). Performance of suction anchors in fine-grained calcareous soils. Proceedings of the 30th *Offshore Technology Conference*, Houston, Texas.
- Reuters (2023). Factbox: Japan aims to become major offshore wind energy producer. Online article, published on June 30, 2023. <https://www.reuters.com/business/energy/japan-aims-become-major-offshore-wind-energy-producer-2023-06-30/>
- Seidel, M. (2007). Jacket Substructures for the REpower 5M Wind Turbine. *European Offshore Wind Conference and Exhibition*, Berlin, Germany, Dec. 4–6, 2007.

- Senders, M. (2008). Suction Caissons in Sand as Tripod Foundations for Offshore Wind Turbines, PhD Thesis, *University of Western Australia*, Perth, Australia.
- Seong, J., Abadie, C. N., Madabhushi, G. S., & Haigh, S. K. (2023). Dynamic and monotonic response of Monopile Foundations for Offshore wind turbines using centrifuge testing. *Bulletin of Earthquake Engineering*, 21(2), 1303-1323.
- Shi, Z., Buscarnera, G., & Finno, R. J. (2018). Simulation of cyclic strength degradation of natural clays via bounding surface model with hybrid flow rule. *International Journal for Numerical and Analytical Methods in Geomechanics*, 42(14), 1719-1740.
- Shi, Z., Liu, L., Huang, M., Shen, K., & Wang, B. (2023). Simulation of cyclic laterally-loaded piles in undrained clays accounting for soil small-strain characteristics. *Ocean Engineering*, 267, 113268.
- Skau, K. S., Dahl, B. M., Jostad, H. P., Suzuki, Y., De Sordi, J., & Havmøller, O. (2022). Response of lightly overconsolidated clay under irregular cyclic loading and comparison with predictions from the strain accumulation procedure. *Géotechnique*, 1-13.
- Skau, K. S., Grimstad, G., Page, A. M., Eiksund, G. R., & Jostad, H. P. (2018). A macro-element for integrated time domain analyses representing bucket foundations for offshore wind turbines. *Marine Structures*, 59, 158-178.
- Staubach, P., Machaček, J., Tafili, M., & Wichtmann, T. (2022). A high-cycle accumulation model for clay and its application to monopile foundations. *Acta Geotechnica*, 17(3), 677-698.
- Stehly, T., and Duffy, P. (2022). 2021 Cost of Wind Energy Review. *National Renewable Energy Laboratory (NREL)*. Available at: <https://www.nrel.gov/docs/fy23osti/84774.pdf>.
- Taiebat, M. & Dafalias, Y. F. (2008). SANISAND: simple anisotropic sand plasticity model. *Int. J. Numer. Analyt. Methods Geomech.* 32, No. 8, 915–948.
- Tasiopoulou, P., & Gerolymos, N. (2016). Constitutive modeling of sand: Formulation of a new plasticity approach. *Soil Dynamics and Earthquake Engineering*, 82, 205-221.
- Thian, S. Y., & Lee, C. Y. (2018). Shear Strength Degradation Behavior of Offshore Clay Under Cyclic Loading. *Soil Mechanics & Foundation Engineering*, 54(6).
- Truong, P., Lehane, B. M., Zania, V., & Klinkvort, R. T. (2019). Empirical approach based on centrifuge testing for cyclic deformations of laterally loaded piles in sand. *Géotechnique*, 69(2), 133-145.
- U.S. Department of Energy (2022). Offshore Wind Market Report: 2022 Edition. *Office of Energy Efficiency & Renewable Energy*. https://www.energy.gov/sites/default/files/2022-08/offshore_wind_market_report_2022.pdf
- U.S. Department of Energy (2023). Advancing Offshore Wind Energy in the United States: U.S. Department of Energy Strategic Contributions Toward 30 Gigawatts and Beyond. *Highlights*.
- Ukritchon B., Keawsawasvong, S. (2016). Undrained pullout capacity of cylindrical suction caissons by finite element limit analysis. *Comput. Geotech.* 80, 301–311.

- Vacareanu, V., Kementzetzidis, E., & Pisano, F. (2019, June). 3D FE seismic analysis of a monopile-supported offshore wind turbine in a non-liquefiable soil deposit. In *Proc. of 2nd Int. Conf. on Natural Hazards & Infrastructure (ICONHIC2019)* (pp. 23-26).
- Villalobos, F. A., Byrne, B. W., & Houlsby, G. T. (2010). Model testing of suction caissons in clay subjected to vertical loading. *Applied Ocean Research*, 32(4), 414-424.
- Vucetic, M., & Dobry, R. (1988). Degradation of marine clays under cyclic loading. *Journal of Geotechnical Engineering*, 114(2), 133-149.
- Vulpe, C. (2015). Design method for the undrained capacity of skirted circular foundations under combined loading: effect of deformable soil plug. *Géotechnique*, 65, No. 8, 669–683.
- Wagner, H., Baack, C., Eickelkamp, T., Epe, A., Lohmann, J., and Troy, S. (2011). Life Cycle Assessment of the Offshore Wind Farm Alpha Ventus. *Energy*, 36(5), pp. 2459–2464.
- Wang X, Zeng X, Li X, Li J (2020) Liquefaction characteristics of offshore wind turbine with hybrid monopile foundation via centrifuge modelling. *Renewable Energy* 145:2358–2372.
- Wang, P., Zhao, M., Du, X., Liu, J., & Xu, C. (2018). Wind, wave and earthquake responses of offshore wind turbine on monopile foundation in clay. *Soil Dynamics and Earthquake Engineering*, 113, 47-57.
- Wang, X, Yang, X, Zeng, X (2017). Seismic centrifuge modelling of suction bucket foundation for offshore wind turbine. *Renewable Energy* 114.
- Wichtmann, T., & Triantafyllidis, T. (2018). Monotonic and cyclic tests on Kaolin: a database for the development, calibration and verification of constitutive models for cohesive soils with focus to cyclic loading. *Acta Geotechnica*, 13(5), 1103-1128.
- WindEurope (2019). Offshore Wind in Europe: Key Trends and Statistics 2018. Available at: <https://windeurope.org/about-wind/statistics/offshore/european-offshore-wind-industry-key-trends-statistics-2018/> , Brussels.
- Yasuhara, K., Hirao, K., & Hyde, A. F. (1992). Effects of cyclic loading on undrained strength and compressibility of clay. *Soils and Foundations*, 32(1), 100-116.
- Yu, H., Zeng, X., Li, B., Lian, J. (2015) Centrifuge modeling of offshore wind foundations under earthquake loading. *Soil Dynamics and Earthquake Engineering*, 77, 402–4.
- Zhang, C., White, D., & Randolph, M. (2011). Centrifuge modeling of the cyclic lateral response of a rigid pile in soft clay. *Journal of Geotechnical and Geoenvironmental Engineering*, 137(7), 717-729.
- Zheng, X. Y., Li, H., Rong, W., & Li, W. (2015). Joint earthquake and wave action on the monopile wind turbine foundation: An experimental study. *Marine Structures*, 44, 125-141.
- Zhou, N., Kou, H. L., & Chen, Q. (2022). Horizontal cyclic response of bucket caisson for offshore wind turbines in over-consolidated clay. *Applied Ocean Research*, 118, 102973.
- Zhu, B., Byrne, B. W., & Houlsby, G. T. (2013). Long-term lateral cyclic response of suction caisson foundations in sand. *Journal of geotechnical and geoenvironmental engineering*, 139(1), 73-83.
- Zhu, B., Dai, J. L., Kong, D. Q., Feng, L. Y., & Chen, Y. M. (2020). Centrifuge modelling of uplift response of suction caisson groups in soft clay. *Canadian Geotechnical Journal*, 57(9), 1294-1303.

- Zhu, F. Y., Bienen, B., O'Loughlin, C., Cassidy, M. J., & Morgan, N. (2019). Suction caisson foundations for offshore wind energy: cyclic response in sand and sand over clay. *Géotechnique*, 69(10), 924-931.
- Zhu, F. Y., O'Loughlin, C. D., Bienen, B., Cassidy, M. J., & Morgan, N. (2018). The response of suction caissons to long-term lateral cyclic loading in single-layer and layered seabeds. *Géotechnique*, 68(8), 729-741.
- Zhu, S., Chen, R. P., & Kang, X. (2021). Centrifuge modelling of a tetrapod jacket foundation under lateral cyclic and monotonic loading in soft soil. *Canadian Geotechnical Journal*, 58(5), 637-649.
- Zografou, D., Gourvenec, S. & O'Loughlin, C. D. (2019). Response of normally consolidated kaolin clay under irregular cyclic loading and comparison with predictions from the accumulation procedure. *Géotechnique*, 69(2), 106–121.
- Zou, X., Hu, Y., Hossain, M. S., & Zhou, M. (2018). Capacity of skirted foundations in sand-over-clay under combined VHM loading. *Ocean Engineering*, 159, 201-218.

2. A compliant guyed system for deep-sea installations of offshore wind turbines: Concept, design insights & dynamic performance

This chapter consists of the post-print version of the following published article, differing from the original only in terms of layout and formatting:

Antoniou, M., Gelagoti, F., & Anastasopoulos, I. (2019). A compliant guyed system for deep-sea installations of offshore wind turbines: Concept, design insights and dynamic performance. *Soil Dynamics and Earthquake Engineering*, 119, 235-252.

Available at <https://doi.org/10.1016/j.soildyn.2018.11.030>

Abstract

The paper explores the potential of a cost-efficient and easy-to-install foundation scheme for Mega-Turbines in seismic regions. The envisioned system comprises a compliant tower, tethered to the ground with an array of four pretensioned cables moored to the seabed by suction anchors. To facilitate installation, a single pinned connection is implemented at the tower base, which is founded on a circular shallow footing. Compared to conventional solutions, the studied scheme offers the necessary support without resource to massive and difficult to construct foundations. By eliminating the moment transfer at the tower foundation, its design requirements are substantially reduced. The efficacy of the proposed solution is demonstrated by investigating the performance of the NOWITECH 10 MW reference turbine installed at 50 m water depth, in the seismically active region of North-Western Adriatic. The entire soil–foundation–structure system is modelled in 3D, employing the finite element method. After confirming the acceptable performance of the guyed system against ULS and SLS conditions (even when allowing 3P mechanical vibrations to resonate with the oscillation of the turbine tower), its seismic response is evaluated. Under seismic loading, the guyed system is shown to be resilient, sustaining the seismically induced loading with controlled displacements at the cable connection point, protecting the tower from excessive distress and undesirable inelastic deformations. The anchoring is also shown to have acceptable performance, with the maximum attained tension being much lower than the pullout capacity of the suction caisson; the seismically induced deformations are negligible. Finally, the seismic performance of the taut mooring lines is also shown to be satisfactory. Although a condition of ‘complete slack’ may arise momentarily at the leeward cable, structural stability is not compromised.

2.1. Introduction and problem statement

Dictated by the world's escalating energy demands, offshore wind engineering is transforming. In order to unlock the promising offshore market potential in the deep water of the Atlantic Ocean, the Mediterranean and the North Sea, where the wind blows more strongly and steadily, windfarms are now moving beyond the immediate continental shelf while increasing the turbine size. Naturally, this 'new' deep-water world comes with major challenges in the field of offshore geotechnics. Traditional foundations (i.e., large gravity-based foundations and monopiles) are gradually being abandoned in favor of more flexible anchoring systems, while lately, the offshore industry is stepping up work in novel ideas, including floating or semi-floating concepts. Over the past 15 years or so, many design concepts of floating wind turbines have been proposed [Henderson & Patel, 1998; Bulder et al., 2002], but it was not until 2008 that the first prototype, Blue H, was installed offshore of Italy at a water depth of 113 m [Bastick, 2009]. This was followed by the Spar-type Hywind prototype off the island of Karmøy in Norway [Bratland, 2009] and the Semi-submersible 3-legged floating foundation of WindFloat [Weinstein, 2009]. Statoil, the developer/owner of Hywind technology, recently launched the world's biggest 30 MW floating wind turbine farm offshore Peterhead (in Scotland), while off the coast of Fukushima, Japan is demonstrating the flagship project 'FORWARD' carrying a total capacity of 13 MW mounted on semi-submerged and SPAR structures. Despite being very promising, floating wind technology is still nascent and has yet to be demonstrated at a large scale. Of the 40 concepts currently under development, only five have been demonstrated at full scale in an offshore environment. Moreover, there is a critical need to find ways to reduce the costs of elaborative floating concepts before moving to a commercialization phase.

Motivated by this reality, the objective of this paper is to explore the potential of a transitional supporting scheme for offshore wind turbines (OWT) that may be best exploited for intermediate water depths. Unlike floating concepts, the proposed system comprises a compliant tower founded on the seabed. Instead of a massive foundation (as in the case of fixed-base installations), the lateral stability of the tower is provided by a taut mooring system comprising four prestressed tendons anchored to the seabed by suction caissons (**Fig. 2.1**). After investigating the highly nonlinear mechanics of the guyed support system (stemming from the nonlinear force–deflection relationship of the cable supports), the paper performs

an in-depth analysis on the decisive role of foundation stiffness and capacity on system performance. To this end, a significant part of the research presented herein is dedicated to the pullout behavior of suction foundations subjected to relatively steep inclined loads (as those imposed by a taut mooring line). The last part of the paper analyses the performance of the guyed OWT subjected to environmental (wind and wave) and earthquake loading.

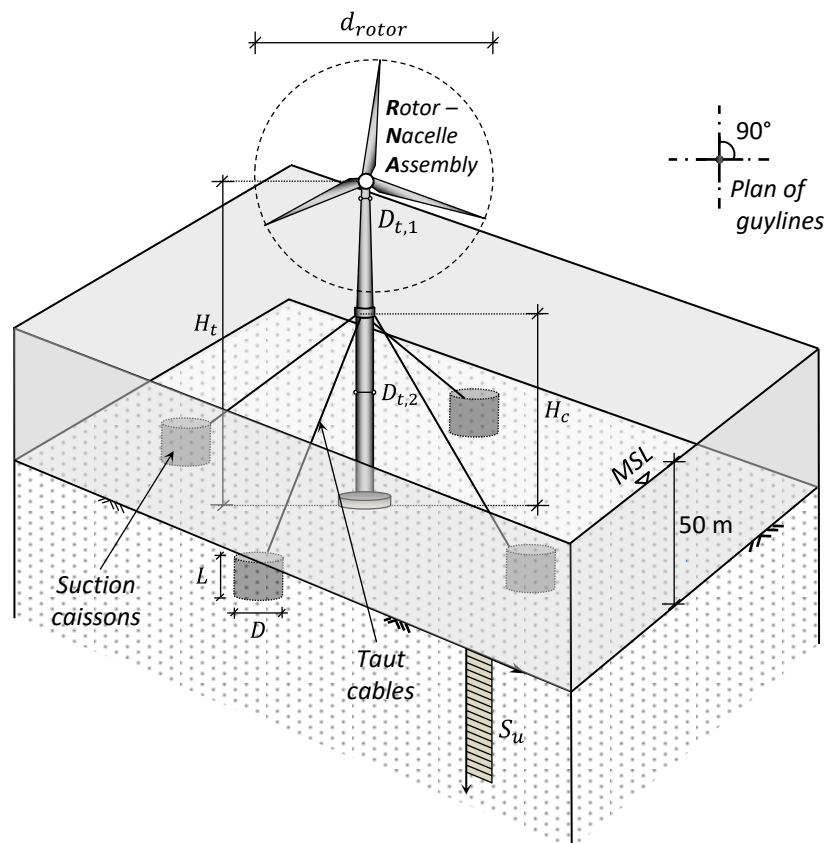


Figure 2.1. The 10 MW offshore wind turbine under consideration founded on a guyed support structure in a homogeneous clay stratum.

2.2. Proposed concept: 10 MW OWT in the Adriatic Sea

Guyed tower: key structural components

In the examined case study, the NOWITECH 10 MW reference turbine is assumed to be installed at 50 m water depth in the seismically active region of the North-Western Adriatic. The seabed at the wind farm location is covered by an almost uniform clay stratum with undrained shear strength $S_u = 100 \text{ kPa}$ [Tonni et al., 2016]. The dimensions of the reference turbine, as well as the structural and soil parameters of the investigated system, are summarized in **Table 2.1** and **Table 2.2**, respectively.

Table 2.1. Geometric Properties of the 10MW wind turbine.

	$D_{t,1}$ (m)	$t_{t,1}$ (m)	$D_{t,2}$ (m)	$t_{t,2}$ (m)	H_t (m)	d_{rotor} (m)	Nacelle & Rotor Mass : (ton)
10MW	3.6	0.021	6	0.05	150	140.4	400

Table 2.2. Structural and soil parameters of the examined system.

OWT Tower				Taut Cables		
ρ_t (t/m ³)	$EI_{t,1}$ (MNm ²)	$EI_{t,2}$ (MNm ²)	W_t (MN)	ρ_c (t/m ³)	EI_c (MNm ²)	W_c (MN)
8.5 (Upper part) / 7.85 (Bottom part)	79396	868622	7.9	7.85	29.51	0.35

Caissons		Shallow Footing		Soil		
ρ_{sc} (t/m ³)	W'_{sc} (MN)	ρ_f (t/m ³)	W_f (MN)	S_u (kPa)	ρ (t/m ³)	E_o/S_u
7.85	0.23	2.5	3.6	100	2.0	1800

The studied concept is considered a cost-efficient and easy-to-install scheme, ideal for the support of Mega-Turbines in intermediate sea depths (i.e., $d > 30$ m) where the mainstay of offshore foundations, the monopile, is practically becoming impractical. The turbine tower is tethered to the ground with an array of four cables, equally spaced around the tower at 90° intervals (**Fig. 2.1**). Each cable is moored to the seabed by means of a suction anchor. Each mooring line comprises four galvanized steel spiral strands (each of area $A = 11677$ mm², elasticity modulus $E = 170$ GPa, and ultimate breaking strength $T_{ult} = 17.5$ MN) pretensioned at $T_0 = 6$ MN, which yields an initial pretension over breaking strength ratio $T_0/T_{ult} = 8.6\%$, in compliance with the 8–15% range proposed by the TIA/EIA-222-G standards [Telecommunications Industry Association, 2005].

Similar to the concept introduced by Bunce & Carey [2001a; 2001b], a single pier-pin connection is implemented at the tower base (**Fig. 2.2a**) sitting on top of a base plate. As such, no overturning moment is transmitted to the tower foundation, while most importantly, the bending at the lower tower sections is significantly reduced, allowing for material savings. Moreover, the pin-connection facilitates the installation process by offering an easy-to-erect system (described in detail in the Global Energy Concepts report [2001]). Alternatively, by fixing the base connection (dotted black line in **Fig. 2.2a**), some bending moment is expected

to develop close to the tower base, still though, far lower than the one expected for a monopile installation (loosely dashed line).

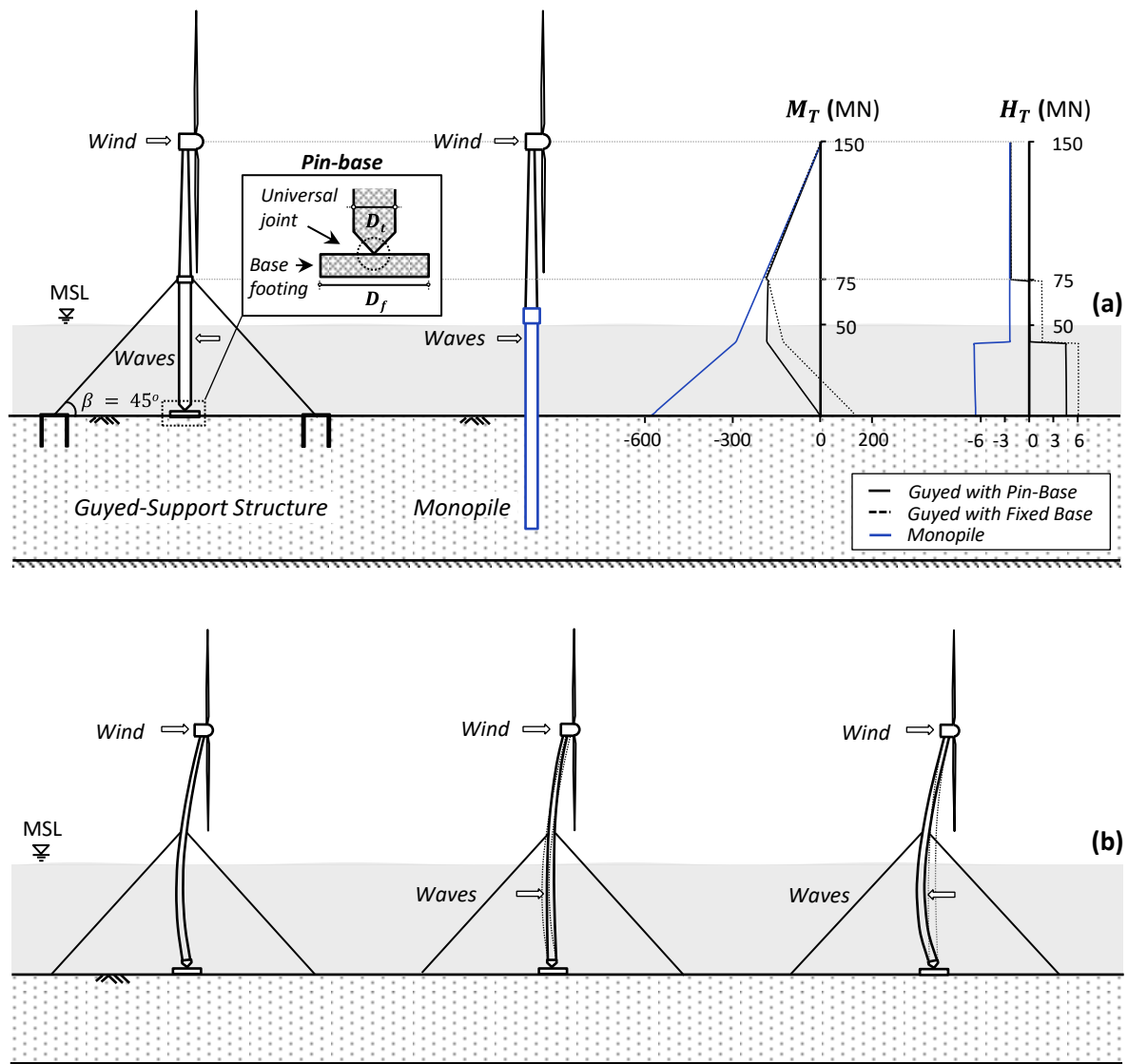


Figure 2.2. Load-carrying mechanism of the gyped support structure: (a) moment (M_T) and lateral force (H_T) distributions along the tower height (black dashed and continuous line correspond to fixed or pinned tower base, respectively) compared to the conventional monopile solution (blue line); and (b) tower deformations under environmental loading.

Excessive lateral deformations of the compliant tower (induced by wind and wave loads) are controlled by adjusting the design tension of the prestressed tendons. In the proposed scheme, a single mooring connection is assumed, just beneath the rotor blades and a few meters above the MSL (mean sea level). On the other hand, the anchoring system should be adequately designed to safely sustain the pullout loading from the taut moorings without

excessive deformation. If not, the cable might go slack, endangering the stability of the guyed structure.

Once the turbine tower is erected, the mooring lines are pre-stressed and safely tethered at the anchor padeye. At that instant, the central footing of the installation is subjected to purely vertical loading (stemming from the dead loads of the structure and the vertical component of the initial pretension). Application of steady wind loading at the nacelle level introduces an overturning moment on the simply supported tower, which is maximized at the level of the mooring connection, while the corresponding shear force is assumed by axial loading of the tendons: the tension on the 'windward' cable increases, while the one of the 'leeward' cable decreases by the same amount. If the leeward cable loses its initial pretension, it will go slack, and the overall structural stability may be compromised.

The same load-carrying mechanism also applies to wave loading (represented here by a concentrated force acting a few meters below the mooring connection). It is interesting to note that the most adverse loading combination corresponds to wind and wave loads acting in opposite directions, as schematically illustrated in **Fig. 2.2b**. The wind loading-induced tower deformation is counteracted by the application of wind-ward wave loading. On the contrary, wave loading acting in the opposite direction leads to further deformation and stressing of the tower (close to the point of maximum curvature). A non-negligible part of the combined wind-wave action is transmitted to the central footing by means of a shear force. For the sake of simplicity, all environmental loads are assumed to act collinearly on the exact same plane. As such, the out-of-plane cable lines are not contributing to the system's lateral resistance, a fairly conservative assumption.

Numerical modelling of the 'above-ground' system

The problem is analyzed employing the finite element (FE) method. The OWT tower is modelled with 3D elastic beam elements of variable diameter D_t and thickness t_t to account for the tapered tower-section. The steel density of the upper part of the tower (above the connection point) is increased to $\rho_t = 8.5 \text{ t/m}^3$, in order to take account of the extra weight due to welds and other tower equipment. The rotor-nacelle assembly is modelled as a concentrated mass at the top of the tower, while elastic 3D truss elements (i.e., zero bending and torsional stiffness) are employed for the prestressed cables. According to a preliminary sensitivity analysis, a minimum of 75 truss elements per cable are necessary to capture

nonlinear cable response (described in detail in Section 2.3). Hydrodynamic masses associated with the submerged parts of the cables and the turbine tower are calculated according to Chen and Chung [1976] and incorporated in the FE model as concentrated masses distributed along the length of the submerged elements.

The effect of pretension on the load-carrying mechanism

A key design parameter of the guyed system is the prescribed tension T_0 on the prestressed moorings. This should be large enough to guarantee no-slack conditions throughout the service life of the OWT but low enough to avoid the need for massive anchoring systems. Moreover, the mechanics of the individual cable, as well as the overall stiffness of the installation, is expected to be controlled by the initial amount of pretension applied to the system.

To highlight the nonlinear mechanics governing the response of a taut cable, let's consider a simply supported cable (**Fig. 2.3a**) subjected to a uniform initial tension load T_0 . The numerical example refers to an inclined cable ($\beta = 45^\circ$), with cross-section $A = 0.047 \text{ m}^2$, $E = 170 \text{ MPa}$ and length $L = 106 \text{ m}$. Under a load q_y acting perpendicular to its axis, the cable deforms, acquiring a sag y_{max} . In the case of taut cables, i.e., cables with small sag-to-span ratios ($y_{max} \leq 1/8$) as those considered herein, the deformed shape at static equilibrium may be approximated by a parabola, while the sag amplitude y_{max} is controlled by the level of tension:

$$y_{max} = 1/8 (q_y L^2) / T_{st} \quad (2.1)$$

where: T_{st} is the cable tension under static equilibrium. This is also consistent with the FE calculation presented in **Fig. 2.3b**. After equilibrium is attained, a monotonically increasing horizontal displacement u_c is applied at the top end of the cable. By dividing the cable horizontal reaction force $T_{c,h}$ by the imposed displacement u_c , the evolution of horizontal cable stiffness K_c with u_c is estimated. The results of the nonlinear analysis of the cable are displayed in **Fig. 2.3c**, where the initial pretension T_0 is parametrically varied.

At zero horizontal displacement ($u_c = 0$), the initial cable stiffness at static equilibrium $K_{c,st}$ can be analytically expressed using the formula of Davenport [1959]:

$$K_{c,st} = \frac{1}{\frac{1}{K_e} + \frac{1}{K_i}} = \frac{K_e K_i}{K_e + K_i} \quad (2.2)$$

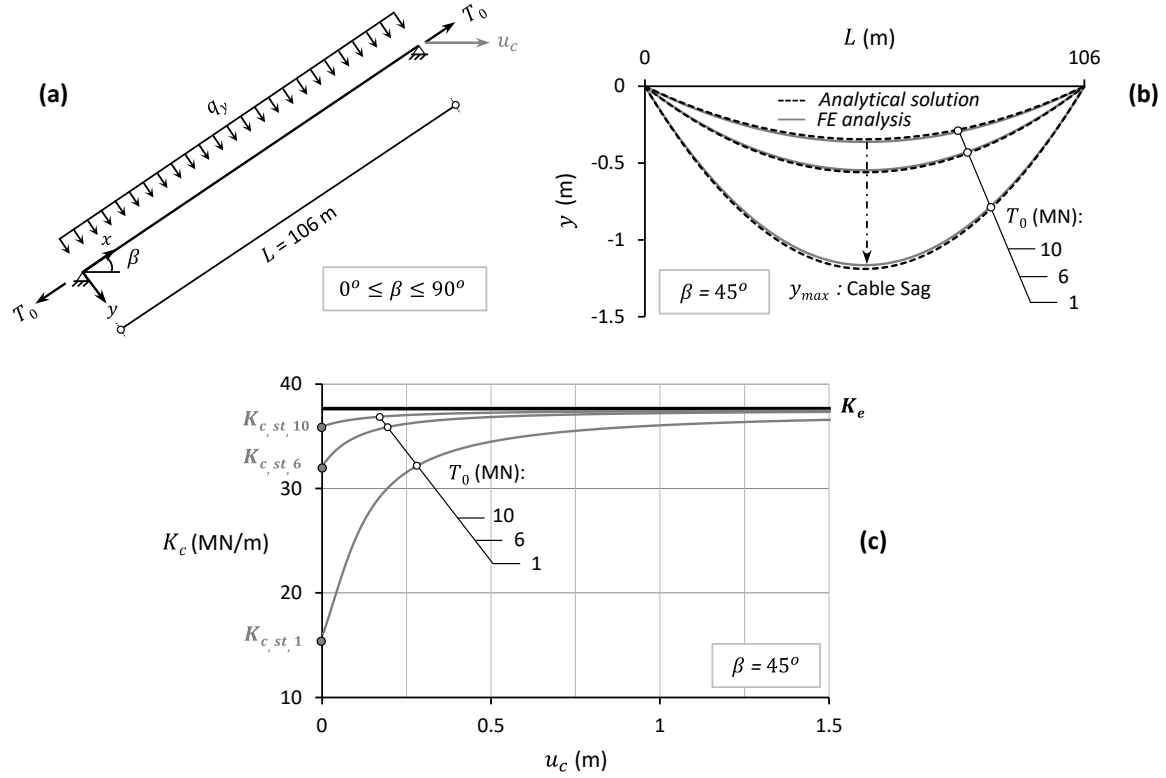


Figure 2.3. FE simulation of a pretensioned taut cable: (a) problem definition; (b) cable sag y_{max} at static equilibrium (for $\beta = 45^\circ$): FE analysis results compared to analytical solutions for different T_0 ; and, (c) evolution of cable horizontal stiffness K_c with imposed horizontal displacement u .

in which K_e is the elastic axial stiffness:

$$K_e = \frac{AE}{L_e} \cos^2 \beta \quad (2.3)$$

and K_i is the stiffness component representing the contribution of the cable sag:

$$K_i = 12 \frac{T_{st}}{L} \left(\frac{T_{st}}{q_y L} \right)^2 \cos^2 \beta \quad (2.4)$$

In the above expressions, β is the cable inclination and L_e its effective length:

$$L_e = L \left[1 + 8 \left(\frac{y_{max}}{L} \right) \right] \quad (2.5)$$

With the increase of u_c , the cable moves from the sagged static equilibrium to a more stretched profile; $K_{c,st}$ increases, asymptotically approximating the elastic axial stiffness K_e

of an elastic rod. The increase of T_0 leads to suppression of nonlinearities and stabilization of cable response.

2.3. Structural performance of the ‘above-ground’ system

Wind turbines are exposed structures subjected to severely variable environmental loads caused predominantly by the non-stationary action of wind and waves. For design purposes, external loads are distinguished as normal when the probability of exceedance is higher than once a year or extreme for a recurrence period higher than 50 years. Under extreme loading conditions (EC), an ultimate limit state (ULS) analysis of the OWT is performed to ensure that structural strength and stability requirements are fulfilled, while on the contrary, serviceability limit state (SLS) criteria are relevant under Normal Conditions (NC). The latter are defined as deformation tolerances that cannot be exceeded. These refer to permanent tower deformations (typically specified by the wind-turbine manufacturer) associated with installation malfunctions, permanent displacements of the foundation elements or plastic deformations of the structural components.

Whereas specific deformation tolerances are not provided, the DNV-OS-J101[25] standard suggests that the permanent rotation at the top of the foundation (θ_{SLS}) should not exceed 0.25° (i.e., 0.0044 rad). Although this criterion is appropriate for conventional wind-turbines (where the tower is practically fixed to the ground), it cannot be considered applicable to the guyed system where the tower response is intentionally isolated from foundation rotations (at the anchoring system or the central footing) by introducing pinned connections. In this specific case, the entire mooring system (from the seabed up to the connection point) could be treated as the foundation system, allowing the application of the θ_{SLS} criterion at the level of the connection point.

Code-specified frequency intervals

A preliminary set of modal FE analyses is conducted to assess the natural frequencies of the guyed OWT assuming fixed-base conditions, i.e., ignoring foundation and anchor compliance and soil–structure interaction (SSI) effects (which will be incorporated subsequently). A key concern is to ensure that the first natural frequency of the system is far from that of external (wind and wave) loading to avoid (or minimize) the risk of resonance. In addition, mechanical vibrations at the hub level (due to mass and aerodynamic imbalances of the rotor) may also interact with the OWT, and resonance should be avoided. To avoid such undesirable frequency

crossings, DNV [2002] proposes certain intervals of safe operation, graphically illustrated in the power spectral density plot of **Fig. 2.4**. Three regions can be distinguished: (i) the ‘soft–soft’ region, lying on the left of the commonly referred 1P frequency (which corresponds to rotor operation); (ii) the ‘soft–stiff’ region, between 1P and 3P (which corresponds to the blade passing frequency, for 3-bladed turbines); and (iii) the ‘stiff–stiff’ region at frequencies higher than the 3P.

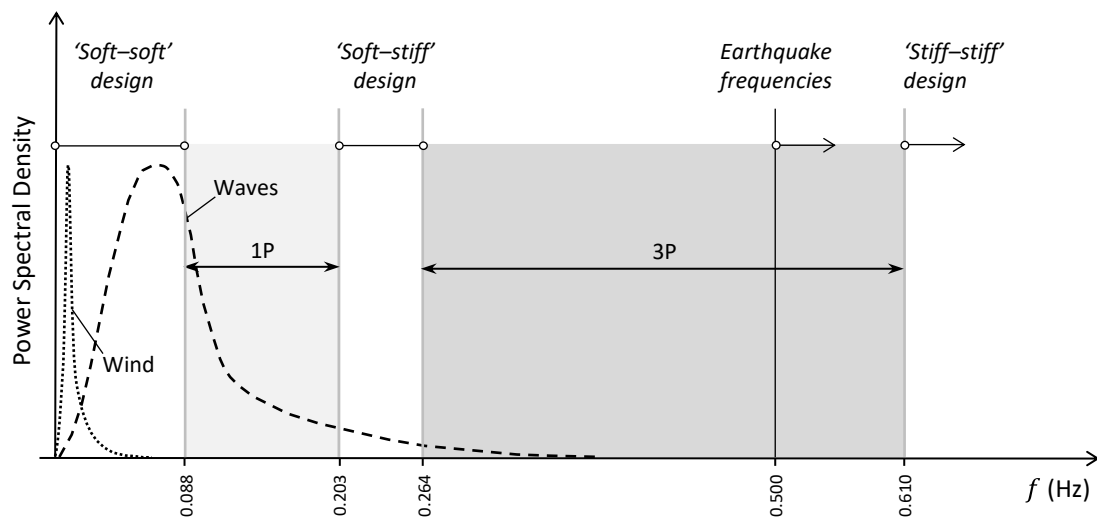


Figure 2.4. Suitable design intervals for the examined OWT. Power spectral density as a function of frequency f for environmental (wind and wave) and seismic loading, compared to the rotor (1P) and blade passing (3P) frequency bands.

The example 10MW turbine has a rotational operating interval of 5.27 – 12.19 RPM [Crozier, 2011], which results in a 1P frequency band $0.088 \text{ Hz} < f_{1P} < 0.203 \text{ Hz}$, and a 3P frequency band $0.264 \text{ Hz} < f_{3P} < 0.61 \text{ Hz}$. Therefore, for a resonance-free design, the natural frequency of the guyed turbine should either fall within the ‘soft-stiff’ frequency range of $0.203 \text{ Hz} < f_o < 0.264 \text{ Hz}$ or should go beyond 0.61 Hz, aiming at a ‘stiff-stiff’ design approach. The latter would require designing a very stiff structural system which does not comply with the current quest of the OWT industry for reduction of material and installation costs. This essentially leaves us with only one viable option: to fine-tune the system’s first natural frequency within the code-favored but extremely narrow ‘soft-stiff’ frequency range. As if this particular code restriction was not difficult enough to comply with, the effective natural frequency of the OWT may dynamically change with time [Lombardi et al., 2013; Arany et al., 2016] due to the millions of loading cycles and phenomena associated with

fatigue of structural elements or stiffness-degradation of the foundation. To handle the above uncertainties, an unconventional design alternative is explored herein: an OWT with a first natural frequency at $f_{n,1} = 0.32$ Hz, which evidently falls within the ‘not recommended’ 3P frequency band. The appropriateness of this selection is justified in the ensuing, considering the turbine’s optimum tip speed ratio and employing dynamic time history analyses, where the rotor vibrations are simulated in detail.

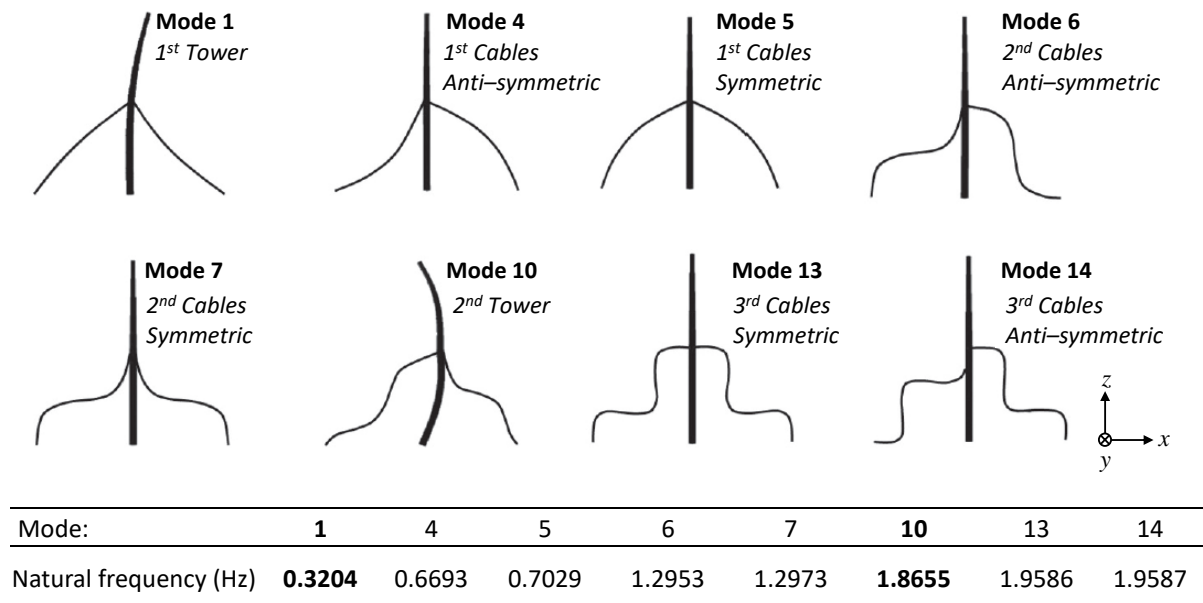


Figure 2.5. Modal analysis of the OWT assuming fixed-base conditions: in-plane eigenmodes and corresponding natural frequencies of the tower and the pretensioned cables.

Modal analysis of the examined OWT is conducted, assuming initial pretension $T_o = 6$ MN for the taut guylines. An overview of all in-plane vibration modes is portrayed in **Fig. 2.5** (the missing modes refer to out-of-plane vibrations). The turbine tower participates in the 1st ($f_{n,1} \approx 0.32$ Hz) and 10th mode of vibration ($f_{n,10} \approx 1.87$ Hz); the remaining eigenmodes are associated with the cables. Each symmetric mode pairs with an anti-symmetric of almost the same eigen-frequency: an interesting pattern first shown by Triantafyllou [1984]. The cable eigenmodes are clearly above the f_{3P} frequency band, and therefore, resonance at the taut mooring system due to mechanical loads should not be expected. However, the risk of resonance is not ruled out for seismic loading, which typically lies within the range of 0.5 – 5 Hz.

Performance under ULS and SLS

The performance of the guyed OWT system is explored for ULS (Ultimate Limit State) and SLS (Serviceability Limit State) design considerations.

ULS Design

The design for ULS is performed considering Consequence Class 2, as defined by API RP 2A-WSD [2000], DNV-OS-E301 [2010] and ISO-19901-7 Annex B.2 [2013] guidelines. Environmental load calculations (**Table 2.3**) are based on a site-specific metocean study of the Adriatic Sea, reported by the EU Funded Research Program JABACO [Mavrakos, 2016]. These refer to a maximum significant wave height of $H_{s,ULS} = 12.1$ m (and fundamental period $T_{p,ULS} = 14.4$ sec) and an ocean current of constant velocity $U_c = 1.3$ m/s. Using Morison's [1950] equation, this extreme sea state may be translated into hydrodynamic loading of $F_{wave,ULS} = 4.5$ MN, acting at $h_w \approx 42$ m above mudline. In addition, the OWT is subjected to a maximum wind speed of 25 m/s (which corresponds to the cut-out speed of the turbine), which translates to a concentrated wind thrust $F_{wind,ULS} = 2.4$ MN on the rotor (i.e., acting at $H_t \approx 150$ m) and a distributed wind drag force along the tower. To derive design loads, the operational environmental load values are multiplied by a γ factor (**Table 2.3**). For ULS design purposes, environmental loads are simulated as pseudo-static – a reasonable assumption given their extremely low-frequency range compared to the eigenmodes of the OWT.

Under these extreme loads (**Fig. 2.6**), the maximum developed tension on the wind-ward guy cable reaches 12.2MN, which is 5.7 times lower than the ultimate breaking strength of the tendon, while the leeward guy cable remains always in tension ($T_{c,min} = 3$ MN). The maximum bending moment of the tower (attained at the connection point, $H_c \approx 75$ m) reaches 185 MNm, being sufficiently lower than its bending moment capacity ($M_{T,ult} = 445$ MNm).

Table 2.3. ULS and SLS environmental actions.

Limit State	Wind Loading, F_{wind} (MN)	Wave Loading, F_{wave} (MN)
ULS [$\gamma = 1.35$]	2.4	4.5
SLS [$\gamma = 1.2$]	1.1	1.0

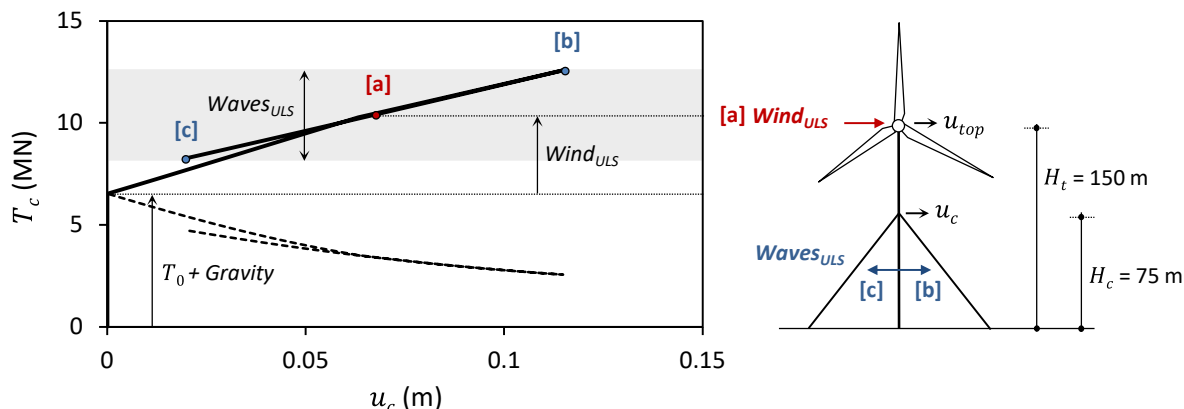


Figure 2.6. ULS Design of the ‘above-ground’ system: cable tension T_c as a function of horizontal displacement u_c at the cable connection point.

SLS Design

In order to assess the OWT compliance with SLS requirements, dynamic time-history analyses are performed, accounting for combined mechanical and environmental loading (**Fig. 2.7a**). The adopted normal wind loads correspond to a significant wave height of $H_{s,SLS} = 2.6$ m [Mavrakos, 2016], which introduces a hydrodynamic sinusoidal force of amplitude $F_{wave,SLS} = 1$ MN acting at frequency $f_{p,SLS} = 0.11$ Hz. The applied loading protocol involves ten cycles of a sinusoidal wave, yielding 91.2 s of total dynamic loading time. The aerodynamic load, on the other hand (referring to wind speed $V_{hub} = 13.25$ m/s), is approximated as the combination of a permanent static wind thrust $F_{wind,SLS}$ (justified by the large period of wind loading $T_{wind} \sim 10$ minutes compared to the waves) and a harmonic excitation $F_{drag,d}$ introduced by the blade. Every time one of the blades passes in front of the tower, the drag force is reduced at length L_b (the length of the blade), with the magnitude of load loss $F_{drag,d}$ computed as the total drag force multiplied by the ratio of the face area of the blade to the face area of the top part of the tower, which, in this example, equals $F_{drag,d} = 0.019$ MN. This dynamically applied reduction ($F_{drag,d}$) is typically simulated as a sinusoidal time-history of 3P frequency, acting at the middle of the blade.

Concurrently with the wind and wave loads, the OWT is also subjected to mechanical loads (stemming from the vibration of the rotor). The rotor mass imbalance I_m (assumed to be located on one of the turbine blades) is modeled as a concentrated mass m at radial distance R from the center of the hub [Arany et al., 2015]:

$$I_m = m R \quad (2.6)$$

This yields a centrifugal force:

$$F_C = ma = mR\Omega^2 = I_m\Omega^2 = 4\pi^2 I_m f_{1P}^2 \quad (2.7)$$

where: $a = R\Omega^2$ the centrifugal acceleration, Ω the angular frequency, and f_{1P} the rotational frequency. This centrifugal force F_C acts with a level arm equal to the rotor overhang b with respect to the z-axis. Hence, it may be analyzed in two sinusoidal forces: $F_{C,z} = F_C \sin \varphi$ acting in-plane, and $F_{C,y} = F_C \cos \varphi$ acting out-of-plane (where φ is the angle between the vertical z-axis and the position of the blade where the mass imbalance is located). Simulation of non-harmonic periodic loading or non-periodic random loading (induced by turbulence or random waves) is beyond the scope of this preliminary study.

In order to harvest as much power as possible from the wind stream, turbines are tuned to operate at their optimal wind tip speed ratio. The tip speed ratio λ is a non-dimensional factor correlating the wind speed and the rate of rotation of the rotor, defined as:

$$\lambda = \frac{\omega r}{V} \quad (2.8)$$

where: V the wind speed, ω the angular speed of the rotor, and r the rotor radius. Optimal operation of a 3-bladed turbine is achieved for λ values between 5 to 8 [Cetin et al., 2005]. This suggests that for the SLS wind speed of $V_{hub} = 13.25$ m/s, and in order to maximize performance, the 10MW turbine would operate at 9 – 12.19 RPM. For this speed range, the 3P region becomes smaller (i.e., 0.46 – 0.61 Hz), leaving outside the natural frequency of the OWT tower $f_{n,1} = 0.32$ Hz. Hence, no resonance is expected at SLS conditions, although resonance is possible at lower wind speeds.

Nevertheless, aiming at evaluating the code recommendation for ‘resonance-free’ design, a highly improbable but rather insightful loading scenario is examined herein (**Fig. 2.7**). It is assumed that the 10MW turbine at SLS conditions (i.e., when the wind and waves loads are quite large) operates exactly at $\Omega = 6.4$ RPM yielding $3P = 0.32$ Hz – which is very close to the 1st natural frequency of the system. The amplitude of the ‘1P-induced’ centrifugal force in this case equals: $F_{C,z} = 0.0085$ MN.

The dynamic performance of the OWT is summarized in **Fig. 2.7**. The beat-shaped signal of the recorded acceleration at the nacelle (**Fig. 2.7b**) simply confirms the fact that the OWT has been forced into a resonating oscillation. Of course, such an unfavorable loading introduces

amplified (with respect to the amplitude of the input signal) accelerations and displacements at the nacelle.

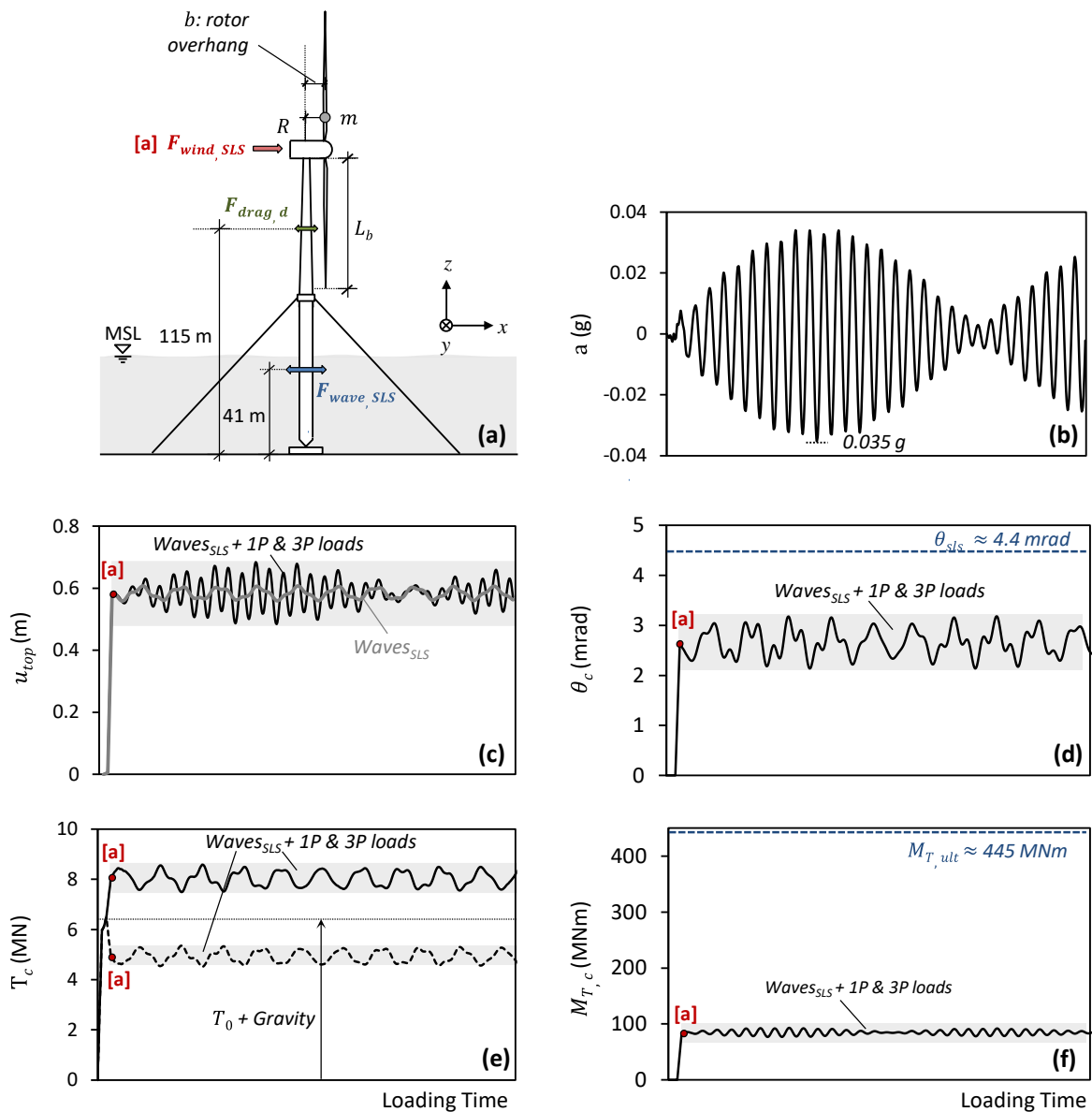


Figure 2.7. SLS Design for the “above-ground” system: (a) normal operational loads; system response in terms of time-histories of: (b) horizontal acceleration at the tower top, (c) horizontal displacement at the tower top, (d) cable tension, (e) rotation at the cables connection point; and (f) tower bending moment at the cables connection point.

It is interesting to observe, for example, that the amplitude of horizontal displacement generated exclusively by the wave loading (grey line in **Fig. 2.7c**), which is an order of magnitude greater than 3P loading, is comparable to the amplitude associated with the ‘3P’ oscillation. In any case, and despite resonance, the overall performance of the turbine is acceptable. The accelerations do not exceed the value of 0.035g, while the maximum

horizontal displacement at the tower top and the dynamically attained rotation at the connection point are within the prescribed code limits (**Fig. 2.7c** and **2.7d**). Moreover, the stressing of the tower remains well below the yield point: the maximum bending moment does not exceed 86 MNm (**Fig. 2.7f**), which is more than four times lower than $M_{T,ult}$ (justifying the elastic simulation of the tower). The performance of the pretensioned cables is also well within design limits: the maximum tension on the windward cable is only 8.5 MN, while the tension on the leeward cable does not drop below 4.5 MN (**Fig. 2.7e**).

2.4. Foundation design and assessment

The viability of the guyed OWT has so far been assessed assuming fixed-base conditions. The key objective of this section is to explore the effects of SSI and the role of anchoring on the overall performance of the unconventional compliant system. To this end, rigorous 3D FE models are developed to simulate the stiffness and capacity of the mooring anchors. In the envisioned system, anchoring is achieved by means of suction caissons [Andersen et al., 2005]. The latter are essentially skirted foundations supplemented with a valve in their top lid. The caisson is installed taking advantage of its self-weight. By pumping the water trapped within the caisson, an under-pressure develops inside the skirt compartment, ‘sucking’ the caisson into the seabed until the internal soil plug is perfectly ‘sealed’ against the underside of the caisson's lid. On the other hand, the OWT tower is founded on a circular shallow footing that will facilitate the envisaged easy and cost-effective ‘one-piece’ installation process, i.e., lowering of the pinned-connected tower to the seabed along with the solid footing and subsequent erection of the tower in place with a single lift. The surface foundation is designed to sustain vertical loading (stemming from the structure's dead load and the vertical component of initial pretension T_0), combined with a limited amount of horizontal loading (due to the environmental loads).

For the specific numerical example, a footing of diameter $D_f = 11$ m and height $h_f = 2.5$ m is considered, with bearing and sliding capacities of $V_{ult} = 6.17AS_u = 58.64$ MN and $H_{ult} = AS_u = 9.50$ MN, respectively [API RP 2A-WSD, 2000]. These correspond to safety factors of $SF_v = 2.4$ and $SF_h = 2.1$ against vertical and horizontal ULS loading. The latter are higher than the minimum safety factors proposed by API RP 2A-WSD [2000] against bearing and sliding failure of shallow foundations, namely $SF_{v,min} = 2.0$ and $SF_{h,min} = 1.5$ to accommodate for the consequences of a mildly evolving soil creep on the long-term stability of the central

footing. Other than that, in cases of high-plasticity clays (where the rate and magnitude of creep deformations are expected to be larger), higher safety factors (of the order of 3-4) may be more appropriate for the central footing.

The problem is analyzed employing the FE code ABAQUS [Dassault Systèmes, 2013]. As illustrated in **Fig. 2.8**, the entire soil-structure system is modelled in 3D. The soil stratum is modelled with nonlinear 8-noded hexahedral continuum elements. The same applies to the central tower footing, which is, however, elastic (reinforced concrete), and a tensionless soil-footing interface is used to allow sliding and detachment. The suction caisson anchors are crucial for system performance and are described in more detail in the following section. In addition to the global model, smaller local models are also developed and used to analyze specific aspects of foundation response.

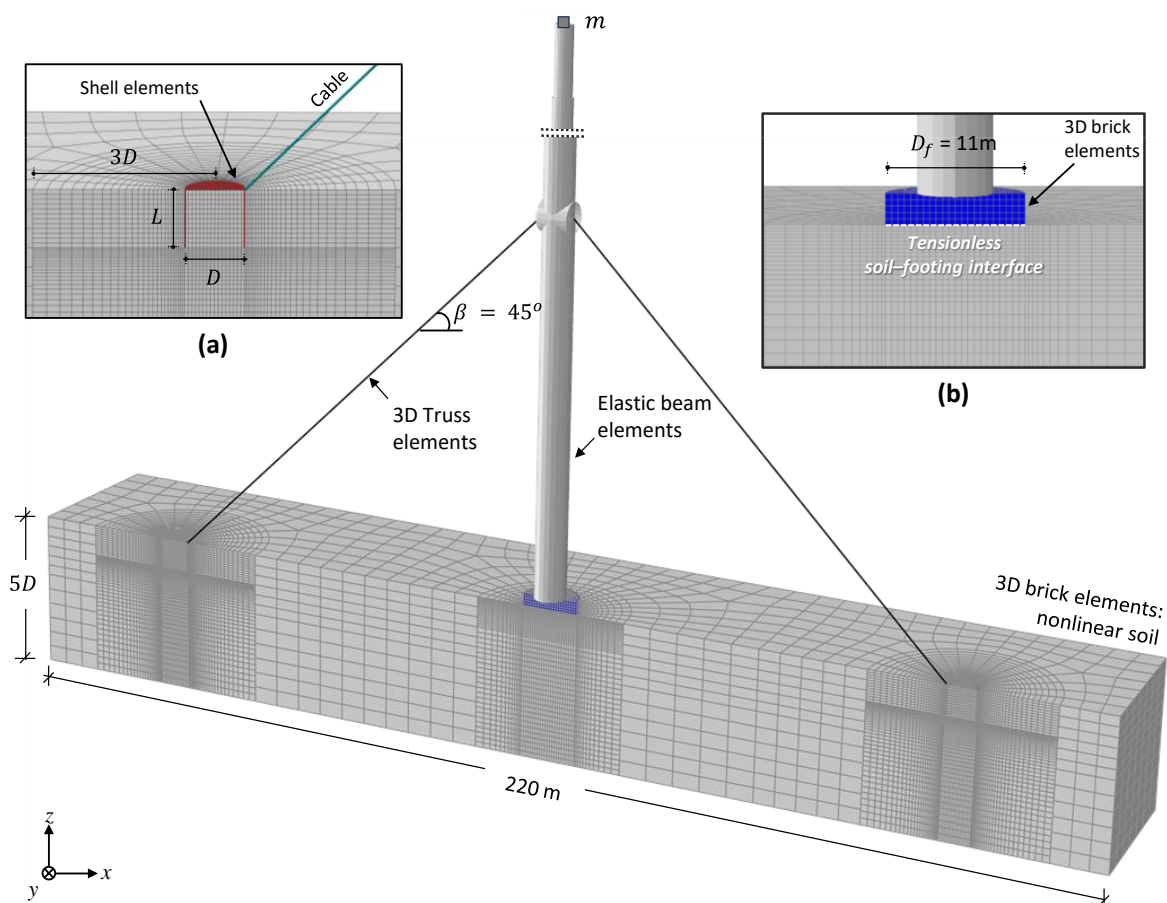


Figure 2.8. Finite element mesh of the global soil–foundation–structure system. Modelling details of:(a) suction caisson anchors; and (b) central tower footing.

Suction caisson anchors

Although suction caissons have been the preferred solution for a number of mooring applications since the mid 90s [Tjelta, 2001], there is still uncertainty over the magnitude of uplift resistance (even under purely vertical loading). Randolph & House [2002] suggest that the uplift capacity critically depends on assumptions regarding the degree of suction that can be relied upon. Under perfectly ‘sealed’ conditions (i.e., when suction develops under the lid), a ‘reverse end bearing’ mechanism is mobilized (**Fig. 2.9a**) where the inner soil plug is uplifted, and the outer soil is dragged beneath the bucket – *Type A Mechanism* [Cho & Bang, 2002; Deng & Carter, 2000; McCarron & Sukumaran 2000; Senders & Kay, 2002; Sukumaran et al, 1999; Supachawarote et al., 2004]. If the ‘sealing’ is inefficient (i.e., in case of improper installation or when the soil permeability is very high to sustain suction), failure will occur in the form of sliding along the caisson sidewall – *Type B Mechanism* (**Fig. 2.9b**). In intermediate cases, when a hydraulic short-circuit may prevent the development of full suction at the caisson base, the uplift capacity relies on the external friction, the caisson weight, the weight of the inner soil plug and any amount of tensile capacity available at the base of the caisson. In this mode, described by Randolph & House [2002] as a ‘sealed (base-vented)’ failure mechanism, the load–displacement response is a time–dependent problem controlled by seepage flow mechanics [Zdrakovic et al., 2001; Cao et al. 2002; Mana et al., 2014; Achmus & Thieken, 2014; Clukey et al., 2004].

The present study focuses on the upper and lower bound caisson failure modes and thus, examines the performance of the OWT structure-foundation system under ‘sealed’ (Type A) and ‘unsealed’ (Type B) caisson conditions. To simulate Type A or B failure mechanisms, the soil is modelled as a one-phase medium of undrained shear strength S_u . A circular suction caisson of diameter D and skirt length L is considered, embedded in a uniform deposit of over-consolidated clay (G, S_u). The lid and skirts of the steel caisson foundation are simulated by linear elastic shell elements. As illustrated in **Fig. 2.8**, model boundaries are positioned far enough to avoid undesired boundary effects. The mesh is adequately fine at a radius of $3D$ around the caisson, becoming sparser further away. The distance to the bottom boundary is $5D$, so that the vertical bearing capacity is not affected. A pinned connection at the top plate of the caisson is implemented to simulate the mooring connection.

Nonlinear soil behavior is described by a simplified kinematic hardening model that follows a Von Mises failure criterion with an associated flow rule. The formulation is available in

Abaqus and has been parameterized by Anastasopoulos et al. [2011] to simulate the monotonic and cyclic response of clays. Despite its simplicity, the implemented constitutive model has been extensively validated against physical model tests of surface and embedded foundations [Anastasopoulos et al., 2011], piles and caissons [Giannakos et al., 2012; Zafeirakos et al., 2013], proving its efficiency in capturing the soil–foundation response.

To account for either ‘sealed’ or ‘un-sealed’ conditions, special-purpose contact elements of zero thickness (available in ABAQUS) are introduced between the soil and the caisson. By appropriately adjusting their properties, different failure mechanisms can be triggered:

- For perfectly ‘sealed’ conditions (**Fig. 2.9a**), an unlimited tension interface is introduced under the caisson lid and along the caisson sidewalls.
- For ‘unsealed’ conditions (**Fig. 2.9b**), a tensionless interface is assumed, allowing sliding (when the prescribed shearing capacity is exhausted) and separation.

In both cases, the maximum available shearing capacity at the soil–foundation interface equals αS_u to account for possible soil remoulding during installation. Following the API RP 2A-WSD [2000] recommendations for stiff clays, an adhesion factor $\alpha = 0.5$ is adopted.

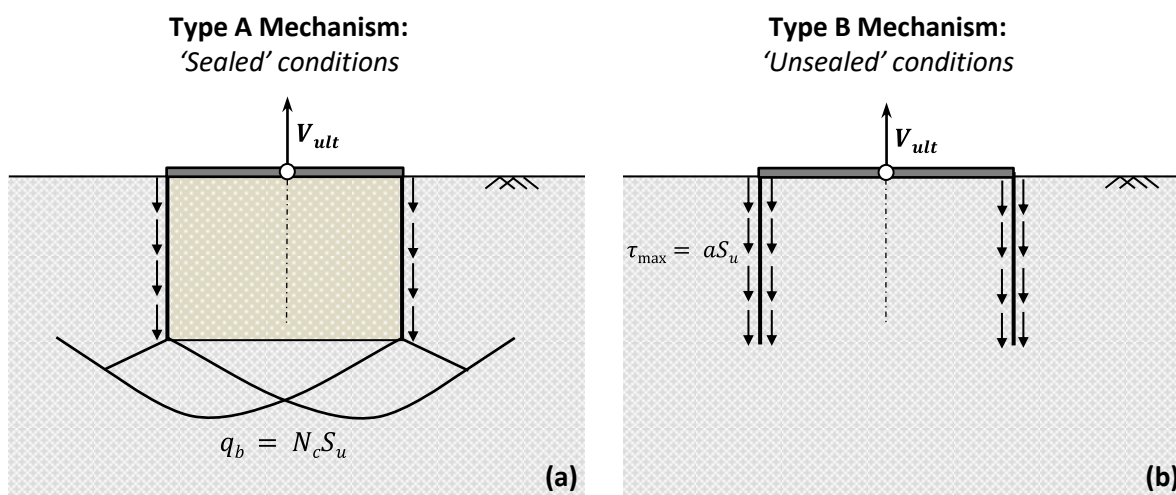


Figure 2.9. Suction caisson subjected to vertical pullout loading: (a) Type A mechanism for perfectly ‘sealed’ conditions; and (b) Type B mechanism for ‘unsealed’ conditions.

Model Validation

Before proceeding to the design of the anchoring system, the efficiency of the numerical model to simulate the pullout capacity of suction caissons is validated. An idealized circular suction caisson of diameter $D = 17$ m and embedment ratio $L/D = 12/17 = 0.7$, solved

numerically by Zdravkovic et al. [2001], is used as a benchmark (**Fig. 2.10a**). In the examined case, the caisson is resting on an isotropic normally consolidated clay stratum of linearly variable S_u . At mudline, the undrained shear strength under triaxial compression equals S_{uc} 10.8kPa, while it increases with depth z with a gradient $S_{uc}/\sigma'_v = 0.36$ (where $\sigma'_v = 30 + 10z$ the vertical effective stress profile). At this point, it should be noted that a purely isotropic behavior (i.e., $S_{uc} = S_{ue} = S_{uss}$) cannot be achieved by the Von Mises failure criterion. The latter inherently yields a slightly reduced capacity, both in triaxial tension (S_{ue}) and compression (S_{uc}), with respect to simple shear (S_{uss}): $S_{uc} = S_{ue} = 0.866 S_{uss}$ [Randolph & House, 2002]. The ABAQUS kinematic hardening model utilized in this study uses as input the undrained shear strength value in simple shear (S_{uss}). Therefore, in order to have the desired S_{uc} at the mudline and be compatible with Zdravkovic et al. [2001], an equivalent $S'_{uss} = (1/0.866)S_{uss}$ is adopted. Perfectly 'sealed' conditions and full skirt adhesion ($\alpha = 1$) are assumed, and the loading is applied at the center of the cap with inclination angle β until failure. By parametrically varying β ($0^\circ \leq \beta \leq 90^\circ$), the Horizontal-Vertical (H - V) failure envelope can be constructed, representing the pullout capacity of the caisson for all possible β . As shown in **Fig. 2.10b**, the FE analyses results compare well with the benchmark [Zdravkovic et al., 2001], and therefore, the developed modelling technique can be considered adequately validated.

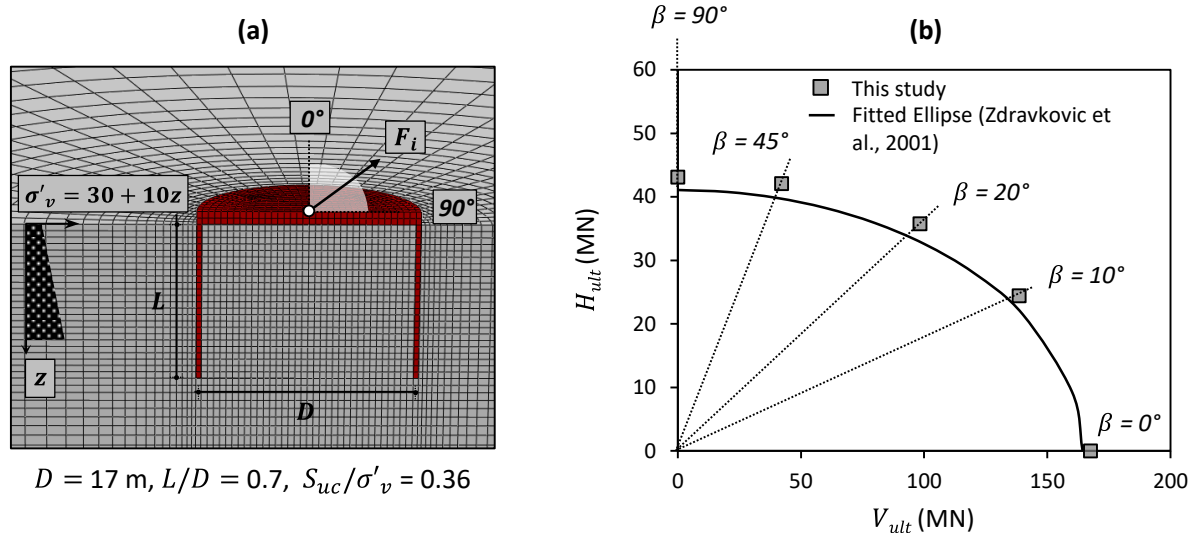


Figure 2.10. Suction caisson subjected to inclined pullout loading: (a) FE configuration, and (b) validation against Zdravkovic et al. [2001], in terms of H - V failure envelopes. The results refer to isotropic conditions, linearly increasing shear strength with depth, and perfectly 'sealed' conditions.

Foundation design: Assumptions and performance objectives

The primary function of an anchor is to hold the mooring line in place under all environmental conditions. Since extreme conditions lead to the highest mooring line tension, anchor design is typically performed for the ULS. Except for the general deformation requirement (the maximum, permanent rotation under normal loads should not exceed a prescribed value), no specific guidance is provided for the SLS. In order to address this issue – also in view of the ambiguity covering the ultimate pullout response of a suction caisson – the previously identified failure modes (Type A or B) are paired to specific loading scenarios and performance criteria as follows:

- **ULS design for Extreme Loads (e.g., severe storms or earthquakes):** loading is fast enough so that drainage cannot take place. Hence, negative pore water pressures are expected to develop below the lid (even in the case of leaking seals), and thus an augmented pullout capacity can be mobilized (corresponding to Type A mechanism). The primary ULS design objective is to ensure that the mooring system will remain intact, thus, a minimum Factor of Safety $SF = 1.5$ against pullout actions is advisable [API RP 2A-WSD, 2000].
- **SLS design for Normal Loads:** suction is conservatively ignored, and the pullout capacity of the caissons is provided by Type B failure mechanism. The primary SLS design objective is to prevent excessive deformation of the anchoring system, which may endanger the serviceability of the OWT. To this end, following the previously discussed rationale and the DNV-OS-J101 deformation criteria for OWTs, it should be ensured that the accumulated (permanent) displacements at the foundation level (under the action of normal loading) will not lead to rotation exceeding 0.25° (i.e., 4.4 mrad) at the top of the supporting system (i.e., at the level of the connection point).

A special reference in Code provisions is reserved for the optimal location of the padeye (i.e., the connection point between the tensioned cable and the suction caisson). It is generally advised to place the padeye (off the center) at a location that generates a translational mode of failure, without rotation of the anchor, to best exploit the capacity/stiffness reserves of the mooring system. Based on the ULS design loads (**Table 2.4**), a suction caisson of diameter $D = 6$ m, embedment length $L = 1$ m ($L/D = 1$), and thickness $t_w = 0.024$ m (which satisfies the $100 < D/t_w < 250$ range reported by Supachawarote et al. [2004] and Andersen et al. [2005])

was found to best comply with the aforementioned requirements. Its performance at ULS and SLS conditions is analyzed in the ensuing (**Figs. 2.11–1.13**).

Table 2.4. Design loads for the suction caissons are derived from the tension loads at ULS and SLS amplified by a γ_d factor [API RP 2A-WSD, 2000]. Capacity checks are performed for the higher $T_{c,design}$ value (in this case 18.3 MN).

<i>Windward Cable</i>	T_c (MN)	$T_{c,design}$ (MN)
ULS [$\gamma_d = 1.5$]	12.2	18.3
SLS [$\gamma_d = 2.0$]	8.0	16.0

ULS Performance

Figure 2.11 compares the pullout response of the suction caisson for two different padeye locations (edge and centerline). The beneficial role of mobilizing ‘passive’ resistance is depicted in the augmented values of pullout capacity (**Fig. 2.11a**). For a centrally-applied load, the pullout capacity reaches $F_{i,ult} = 22$ MN, which provides $SF = 1.8$ against extreme environmental loads. By shifting the padeye to the right, the pullout capacity $F_{i,ult}$ increases measurably. When the padeye is at the edge of the caisson (i.e., $x = 3$ m), $F_{i,ult}$ is increased by 55%; the initial (small-strain) foundation stiffness is also amplified by 35% (**Fig. 2.11b**). It is interesting to note that compared to usual caisson configurations (where the padeye is buried within the soil to maximize performance) – this configuration is definitely preferable in terms of installation and maintenance since the cable remains accessible over its entire length. This is accommodated by the – deliberately chosen – low caisson embedment (L/D) ratio, which allows for a sufficiently large level arm for the ‘necessary’ counterclockwise moment to develop.

Further insight into the role of padeye location is provided by the mobilized (Type A) failure mechanisms of **Fig. 2.11c**. In the case of centerline loading, an asymmetric deep scoop failure mechanism develops, similar to that observed for shallow foundations and low aspect ratio caissons subjected to moment loading at their cap center [Bransby & Yun, 2009]. In contrast, when the pullout force is applied at the edge, an – almost – purely translational mechanism develops. The 45° cable load at the edge of the $L/D = 1$ caisson results in a centerline loading depth of $0.5L$, i.e., close to the $\sim 0.55L$ value reported by Bang & Cho [2002] as the ideal loading depth to obtain the maximum ultimate horizontal loading capacity of a suction pile in

a uniform strength clay stratum. In the following analyses, the padeye is always assumed to be at the edge of the caisson.

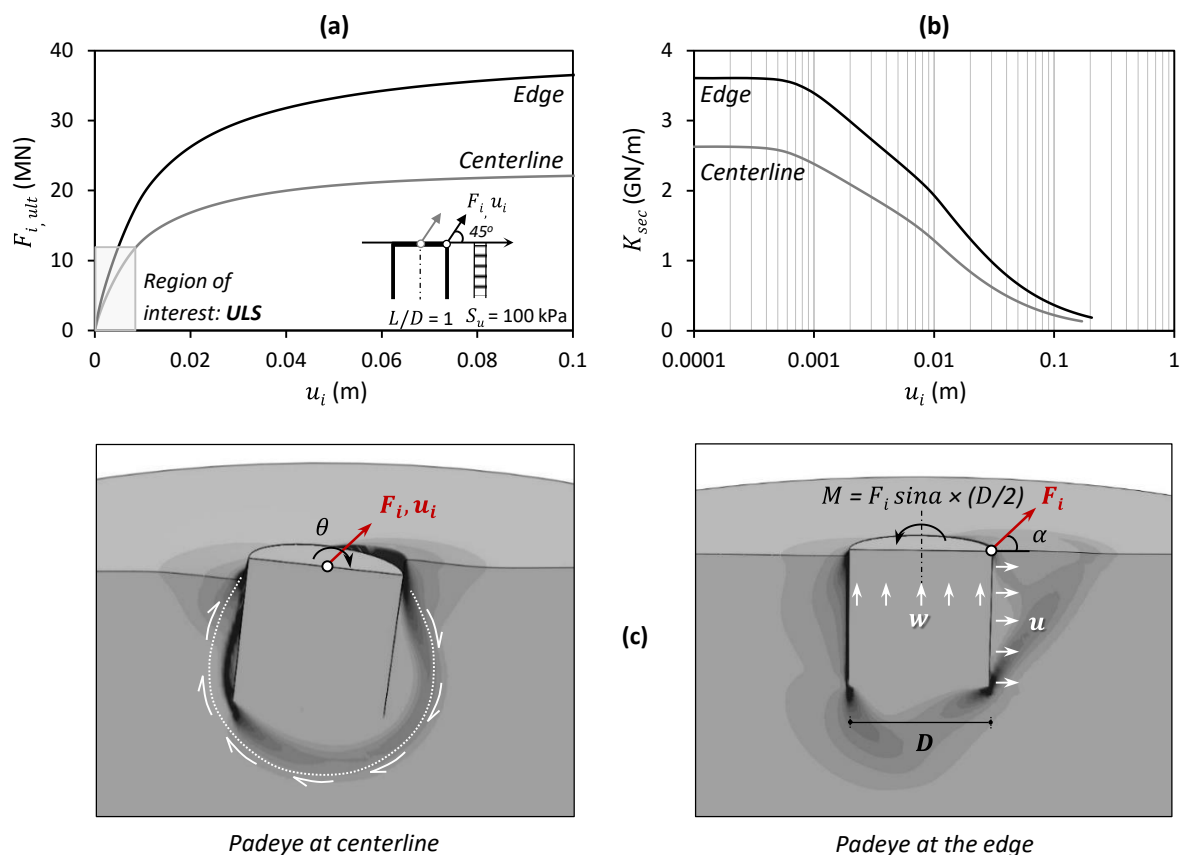


Figure 2.11. Performance of ‘perfectly sealed’ caisson. The effect of padeye location on: (a) inclined pullout capacity $F_{i,ult}$; (b) secant stiffness K_{sec} ; and (c) failure mechanism.

SLS Performance

When the beneficial role of suction is ignored, both the inclined pullout capacity and the stiffness of the caisson decrease substantially (**Figs. 2.12a,b**): $F_{i,ult}$ does not exceed 12 MN (compared to 34 MN with ‘sealed’ ULS conditions), and the initial stiffness is reduced by almost 1 GN/m (2.5 GN/m instead of 3.5 GN/m). Nonetheless, the ‘unsealed’ caisson may safely undertake the environmental loading under normal conditions, maintaining $SF = 1.5$. It is clarified that these values refer to the padeye located at the edge, which, although being optimum for ULS, is not necessarily associated with maximized performance for unsealed caissons.

As shown in **Fig. 2.12c**, under ‘unsealed’ conditions, two inherently different failure mechanisms develop. The first one (left) is associated with the mobilization of shaft friction along the caisson skirt and is responsible for the vertical resistance R_z . As revealed by **Fig.**

2.12d, this frictional mechanism mobilizes its maximum resistance R_z almost instantaneously ($u_{sc,z} = 8$ mm). Note also that the maximum developed $R_z \approx 8.3$ MN is lower than the purely vertical shaft caisson capacity $Q_{sf} = Q_{sf,int} + Q_{sf,ext} = 11.3$ MN. This is explained by the formation of a tensile gap between the outer caisson shaft and the soil, opposite to the direction of loading, at a very early stage. As indicated by the developed shear stresses at the soil-caisson interface (refer to the small snapshot in **Fig. 2.12c**, left) at $u_z \approx 0.01$ m (when the maximum vertical resistance has been reached), half of the caisson periphery is inactive, thus resulting in the mobilization of a lower value of shaft capacity. The horizontal resistance R_x is associated with the second failure mechanism (**Fig. 2.12c**, right), which is in the form of a passive failure wedge on the caisson sidewall. As such, R_x evolves more gradually and reaches its maximum value (which is bound to be equal to the vertical capacity R_z Due to the 45° loading direction) at a much higher displacement $u_{sc,x} = 0.03$ m; that is more than four times $u_{sc,z}$. As a result, for small values of applied deformation ($u_{sc} < 0.005$ m), R_z (acting at the edge) develops a counterclockwise moment M_z , which counterbalances the resisting moment offered by lateral soil resistance, thus inhibiting the increase of θ_{sc} (**Fig. 2.12d**). With increasing u_{sc} , the resisting moment M_x (offered by R_x) raises with an increasing rate, eventually overtopping the counter-balancing moment M_z (offered by R_z). This moment imbalance is responsible for some non-trivial (linearly evolving) caisson rotations for $u_{sc} > 0.005$ m.

An overview of the amplitude of accumulated caisson displacement for different limit states and simulation assumptions is provided in **Fig. 2.13**, where the OWT of **Fig. 2.8** is subjected to monotonically increasing wind and wave loading. The performance of the caisson assuming ‘sealed’ and ‘unsealed’ conditions is compared in terms of rotation θ_{sc} at the caisson head (**Fig. 2.13a**), horizontal translation $u_{sc,x}$ (**Fig. 2.13b**), and vertical displacement $u_{sc,z}$ (**Fig. 2.13c**) at padeye location. The dashed lines depict highly infrequent combinations. Note that the accumulated displacements (and the rate of accumulation) during ULS loading (when the beneficial effect of suction is taken into consideration) are systematically lower than those recorded during SLS loading. However, for all analyzed scenarios (excluding the improbable combination of ‘unsealed’ conditions with extreme actions), the displacements increase linearly with the applied pullout load, which means that the foundation response is essentially elastic. Even in the unlikely scenario of ‘unsealed’ ULS

loading (grey dashed line), where caissons have reached their pull – out capacity and displacements start to increase exponentially, the maximum pull-out displacement does not exceed 0.06 m.

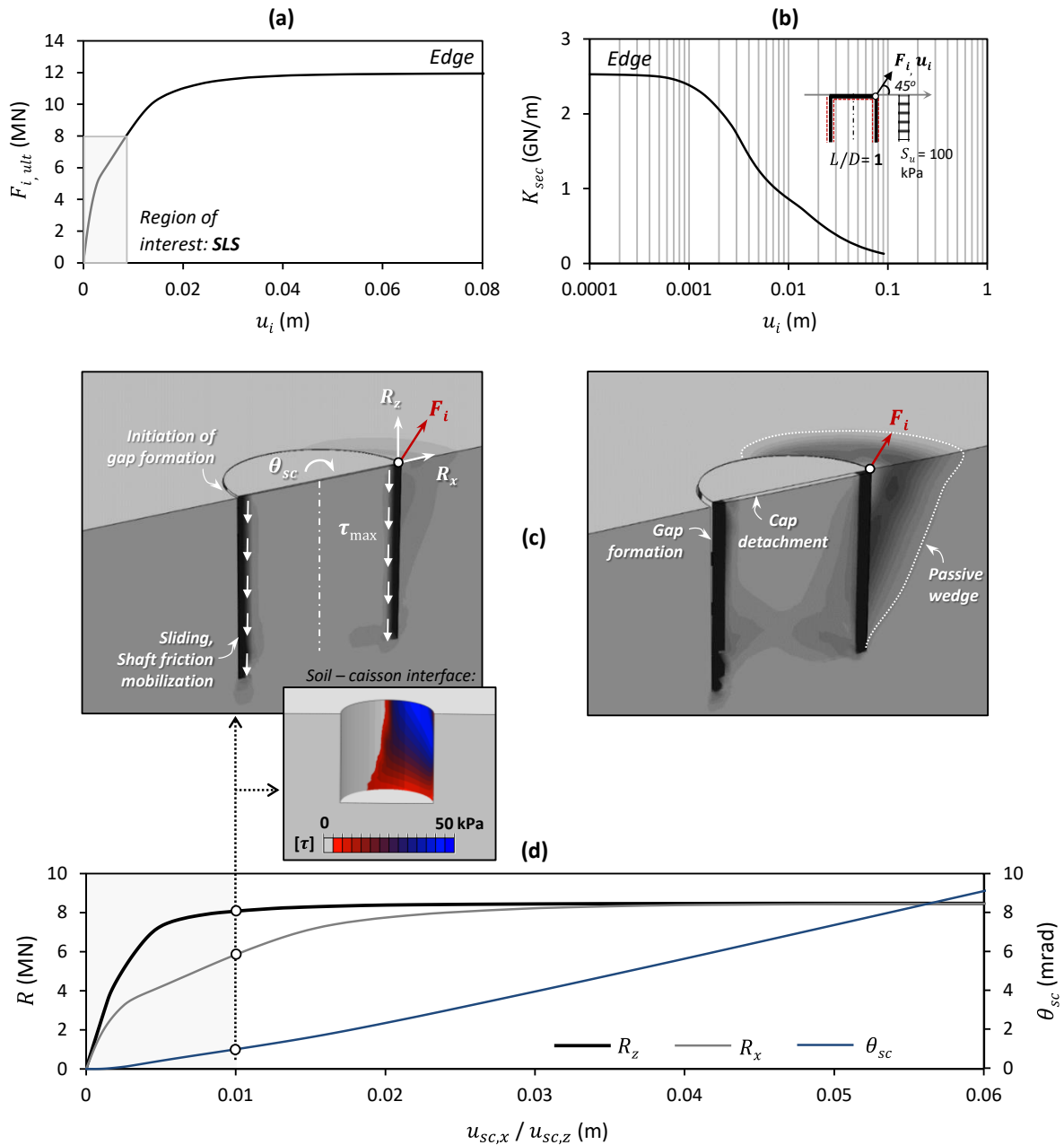


Figure 2.12. Performance of ‘unsealed’ caisson, with the padeye at the edge: (a) inclined pullout capacity $F_{i,ult}$; (b) secant stiffness K_{sec} ; (c) development of Type-B failure mechanism in terms of plastic strain contours at low (left) and large (right) deformation; and (d) evolution of vertical (R_z) and horizontal (R_x) caisson resistance, and caisson rotation (θ_{sc}), with imposed displacement u .

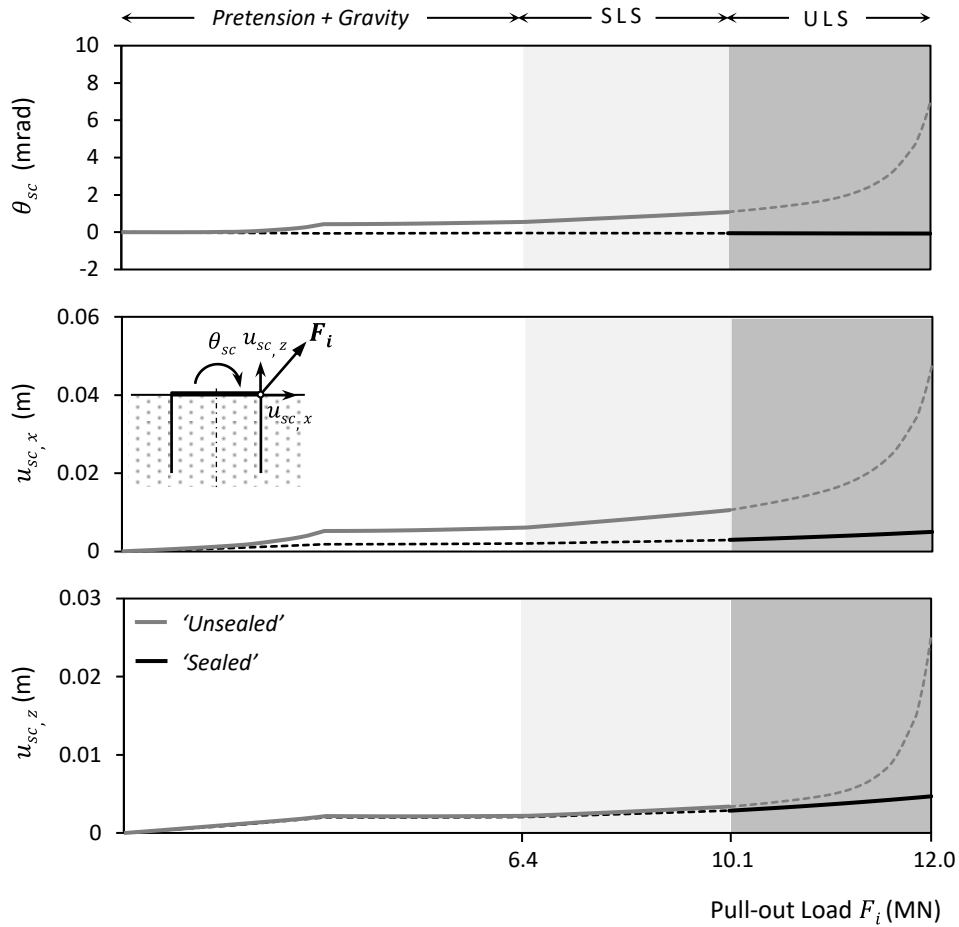


Figure 2.13. Windward caisson response under subsequent SLS and ULS monotonic loading, considering ‘sealed’ or ‘unsealed’ conditions. Comparison in terms of: (a) rotation θ_{sc} at the center of the cap; (b) horizontal displacement $u_{sc,x}$ at padeye; and (c) vertical displacement $u_{sc,z}$ at padeye. The dashed lines depict infrequent combinations: ‘unsealed’ conditions under ULS loads (grey line) and ‘sealed’ conditions under SLS loads (black line).

2.5. Earthquake performance of the guyed system

Although the (long-period) OWT is expected to be relatively insensitive to seismic shaking [Witcher, 2005; Haenler et al., 2006; Zhao & Maisser, 2006], the performance of individual components may be challenging. These may involve local resonance of the taut mooring lines (generating high-amplitude dynamic tension waves) or seismically induced deformations at the anchoring system that may threaten system stability. To address such issues, the seismic performance of the entire soil-structure model is investigated. Wherever appropriate, the performance of the fixed-base system (i.e., ignoring SSI) is also provided for comparison. In the ensuing simulations, the OWT is subjected simultaneously to seismic shaking and metocean loading (applied as a quasi-static load), a loading combination which was found to be the most adverse for monopod installations [Kourkoulis et al., 2014].

Seismic environment and numerical modelling

An example case-study is analyzed, referring to the studied guyed OWT installed in the Adriatic Sea – one of the most seismically active regions of the Mediterranean. According to the Seismic Zonation Map of **Fig. 2.14a**, the design ground acceleration is $a_d = 0.3g$. To comply with regional seismicity, input motions from nearby seismic events are selected:

- The 6.3 M_w L' Aquila earthquake in the Abruzzi region of central Italy (2009) [Station: IT.ACIV, E-W component]; and
- The 5.9 M_w Emilia Romagna earthquake (2012) [Station: IT.MRN, N-S component].

Each seismic motion is treated in a different way. The L' Aquila record is modified to match the EC8 spectrum, whilst the Emilia Romagna record is used without any modification (**Figs. 2.14b,c**). The elastic response spectra (SA) of the two records are plotted in **Fig. 2.14b**, along with the EC8 design spectrum at the OWT site (corresponding to stiff clay profile, Category C).

The previously discussed global FE model of **Fig. 2.8** is slightly modified for the dynamic analyses. Radiation damping is taken into account by introducing appropriate absorbing boundaries (C) at the base of the model:

$$C = \rho V_s A \quad (2.9)$$

where $\rho = 2 \text{ t/m}^3$ the material density, $V_s = 173.2 \text{ m/s}$ the shear wave velocity (assuming half-space), and $A \text{ (m}^2\text{)}$ the effective area of each dashpot. Appropriate kinematic constraints are imposed at the lateral boundaries of the FE model to simulate free-field response of a soil-column subjected to in-plane vertically incident SV waves. The analysis is conducted in five consecutive steps: (a) static gravity loading on the soil and foundations; (b) static pretension of guy lines, along with dead loads on the OWT tower (concentrated mass at the nacelle level and tower weight); (c) static application of gravity loading on the taut mooring system; (d) static application of wind load at the nacelle level (representing the 70% of wind loading under NC); and (e) dynamic time history analysis for the seismic loading. Due to the short-duration and transient nature of seismic loading, *perfectly sealed* conditions are assumed.

Figure 2.14d depicts the free-field elastic response spectra for damping ratio $\xi = 2\%$, which is consistent with the prescribed damping of the superstructure elements. The first two eigenperiods of the OWT are also plotted in the graph. It is no surprise that the fundamental period

of the flexible OWT lies in the descending branch, at a period range of low SA (0.15-0.2g, depending on the excitation). In contrast, the second eigenmode (at $T = 0.56$ s) is at a period range associated with significantly higher accelerations: 0.8g for the modified L'Aquila and as high as 1g for the Emilia Romagna record. The objective of the next sections is to explore the resulting deformation and distress of the OWT, offering a better understanding of the dynamic response of the guyed system.

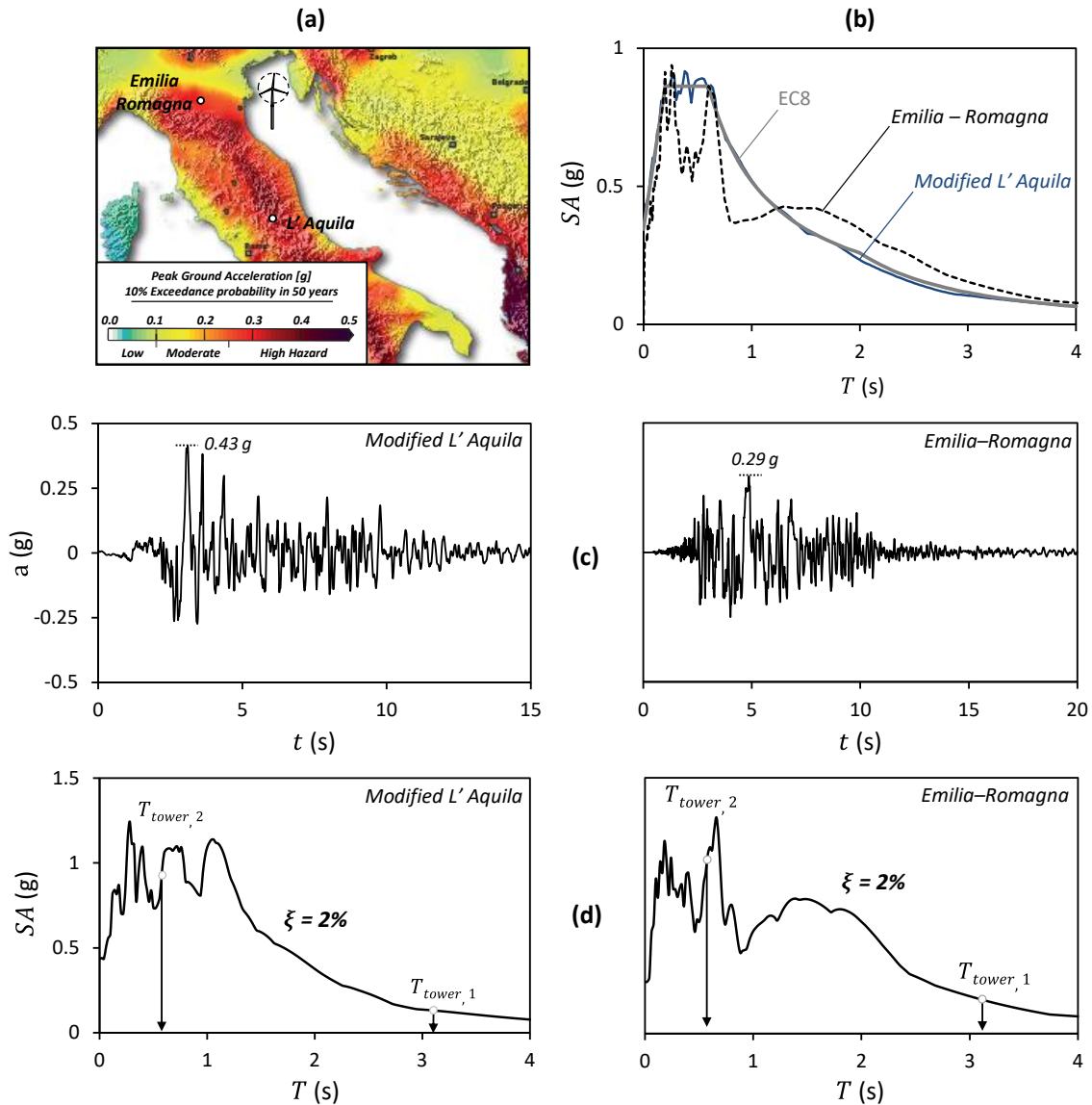


Figure 2.14. Seismic analysis of the guyed OWT: (a) Seismic Hazard Map (SHARE, 2009–2013) of the Adriatic Region; (b) acceleration elastic response spectra of the selected input seismic motions compared to the EC8 design spectrum; (c) acceleration time-histories of the modified L'Aquila and the Emilia Romagna records; and (d) free-field acceleration response spectra.

Tower and foundation response

Figures 2.15 and **2.16** summarize the seismic response of the tower in terms of acceleration and displacement time histories at characteristic locations: (a) at the tower head; (b) at the top of the support structure (i.e., at the connection point of the mooring lines); and (c) at the foundation (i.e., at the top of the caisson). The plotted displacements are relative to the movement of the ground surface, computed by subtracting the free-field displacement.

The seismic response of the OWT can be seen to be decomposed in two different components: the response of the very flexible upper sub-system, as revealed by the long-period oscillation of the tower top (**Fig. 2.15a**), and that of the stiffer sub-system, which is revealed by the oscillation of the connection point (**Fig. 2.15b**). The latter consists of a high-frequency oscillation dominated by the 2nd mode of vibration; despite the large accelerations, the corresponding displacements are limited (**Fig. 2.16b**) exactly because of the high frequencies involved. The opposite is observed for the flexible upper system, which experiences lower accelerations, as the response is dominated by the 1st mode, but much larger displacements exactly due to its flexibility (**Fig. 2.16a**). The interaction of the two oscillating sub-systems is reflected in the acceleration time-history of the tower head (**Fig. 2.15a**): high-frequency wrinkles (triggered by the oscillation of the cable point) are superimposed on the low-frequency and low-amplitude oscillation of the tower (which is governed by the 1st mode).

The seismic performance of the suction caisson foundations (i.e., the anchors) is expressed in terms of time histories of relative horizontal and vertical displacements of the caisson lid (**Fig. 2.17**). Foundation rotations are not relevant, as they cannot be transmitted to the upper system. Both anchors perform 'quasi-elastically', being subjected to minor seismically induced pullout displacements. The latter is added to the wind-induced deformation of the first step, resulting in an ultimate anchor displacement of the order of 1 cm – considered minor in view of the severity of the shaking. This 'quasi-elastic' foundation performance is also confirmed by the acceleration time histories of **Figs. 2.15a,b**, where the response of the fixed-base system is almost identical to that of the soil-structure system. Some slight differences are observed in the free-oscillation part of the motion, where the foundation-structure system oscillates at a somehow prolonged eigenperiod (3.3 sec instead of the initial 3.1 sec), something that can be attributed to some limited soil inelasticity.

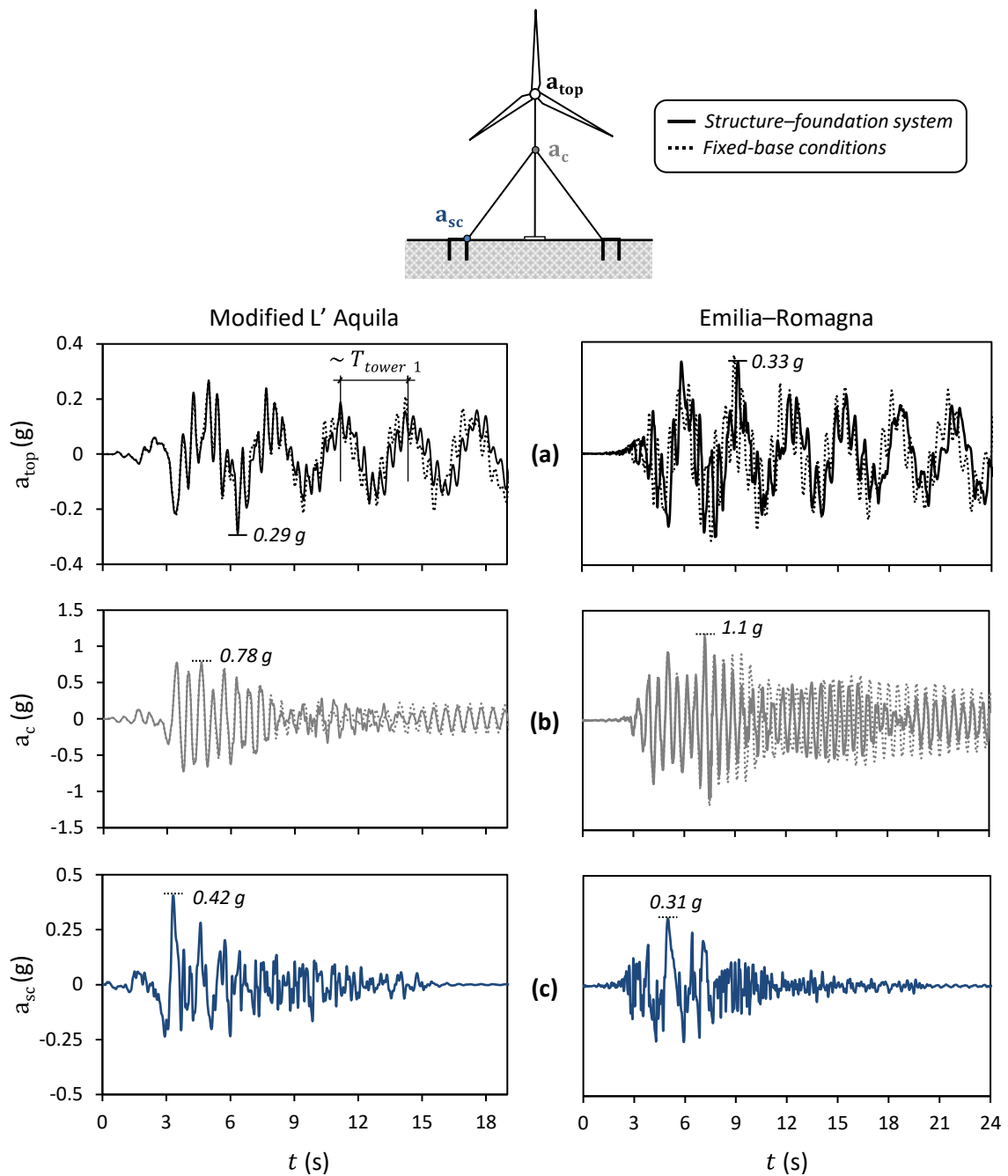


Figure 2.15. Tower response to combined wind and seismic loading, subjected to the modified L' Aquila record (left) and the Emilia–Romagna record (right). Acceleration time-histories at: (a) the tower top; (b) the guylines connection point; and (c) the foundation top.

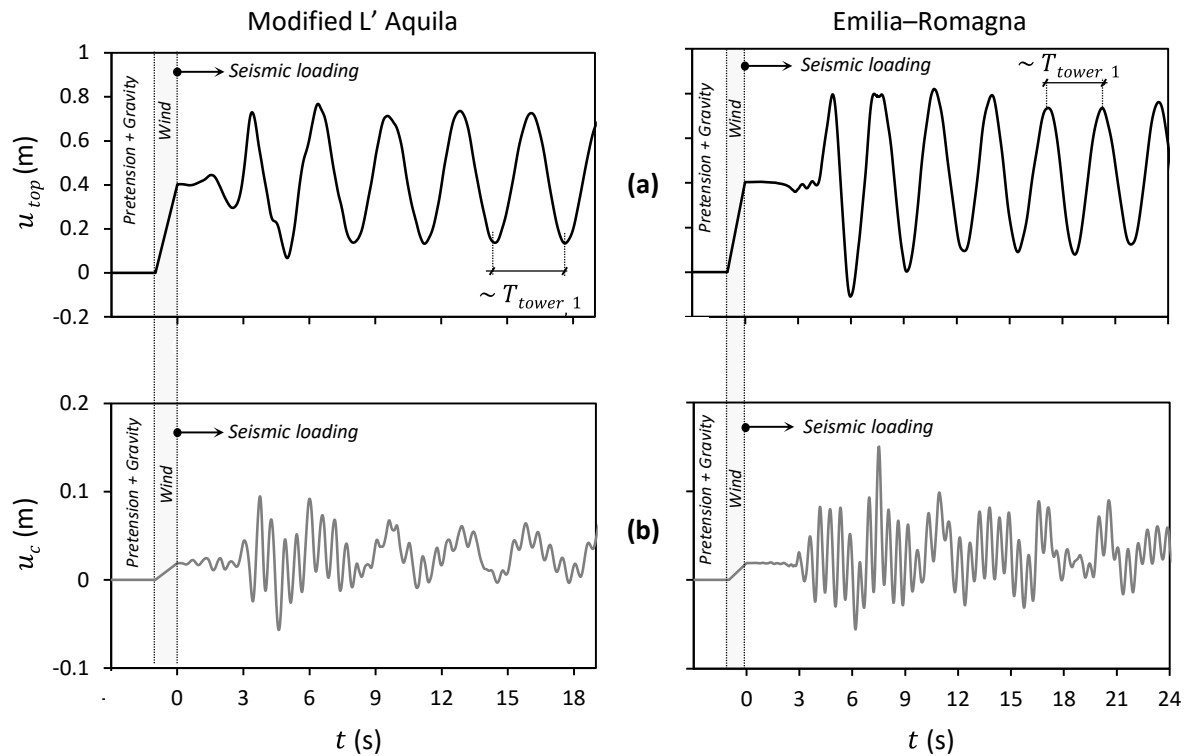


Figure 2.16. Tower response to combined wind and seismic loading, subjected to the modified L' Aquila (left) and the Emilia–Romagna records (right). Relative (to the free-field) hor. displacement time-histories at: (a) the tower top; (b) the guylines connection point.

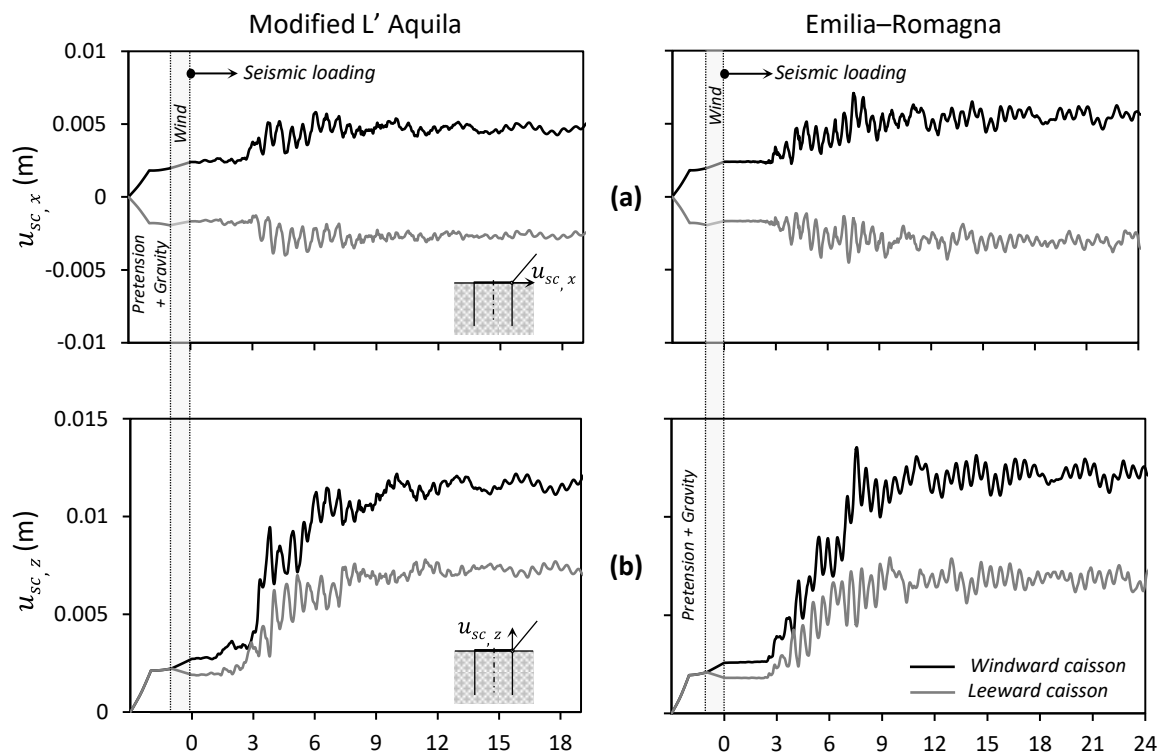


Figure 2.17. Foundation response to combined wind and seismic loading, subjected to the modified L' Aquila record (left) and the Emilia–Romagna record (right). Time histories of: (a) horizontal caisson displacement; and (b) vertical caisson displacement.

Cable Response

Figure 2.18 summarizes cable response in terms of time histories of cable tension. The response can be seen as the superposition of: (a) an almost steady-state vibration at the 1st eigen-frequency of the cables; and (b) a transient component induced by late arrivals of dispersive perturbations, which propagate at non-constant velocities along the cable length, resulting in an asynchronous spatially variable oscillation. The resulting horizontal (relative) displacements (u_c) at the cable connection point are essentially controlling the dynamic variations in the amplitude of the cable tension forces shown in **Fig. 2.18**. The cable forces start oscillating around their initial pretension values, $T_{0,l} \approx 5.5$ MN for the leeward cable and $T_{0,w} \approx 7.5$ MN for the windward one (the difference is due to the preceding wind loading), but with the progression of seismic shaking, the mean tension gradually decreases on both cable lines. At the end of shaking, equilibrium is attained with substantially lower cable tension: $T_{c,res} = 4.5$ MN and 5 MN in the case of Modified L' Aquila and Emilia–Romagna, respectively.

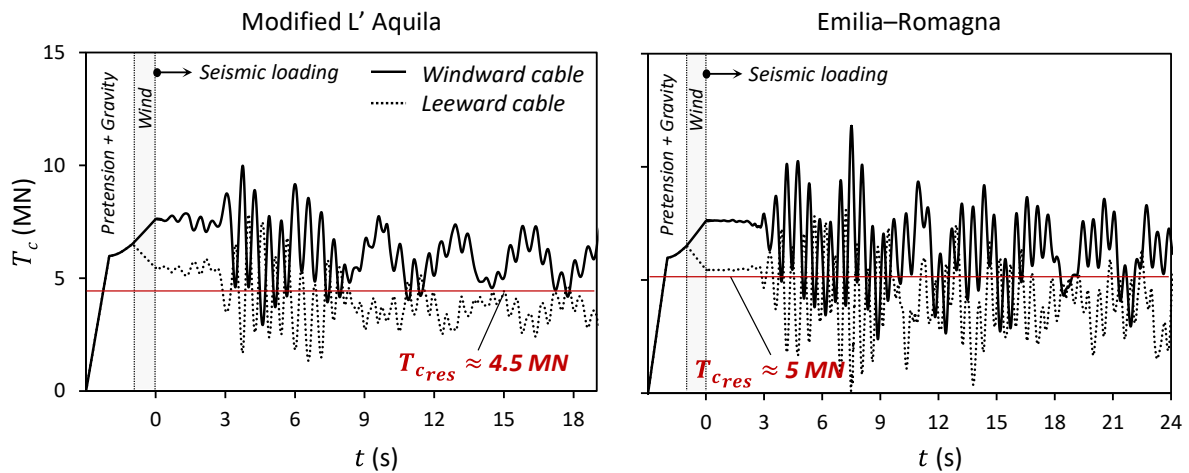


Figure 2.18. Cable response to combined wind and seismic loading, subjected to the modified L' Aquila record (left) and the Emilia–Romagna record (right). Time histories of cable tension.

As revealed by the time-histories of **Fig. 2.19** (Emilia - Romagna excitation, zoomed in the first 12s of response), the decrease in mean cable tension values occurs mainly due to the accumulation of plastic deformations at the central tower foundation. Evidently, the footing is subjected to non-symmetric shearing, oscillating around a (non-zero) $H_{f,o} = 0.8$ MN, which

is due to the preceding wind loading (**Fig. 2.19a**). This initial shear loading leads to an initial footing rotation $\theta_{f,0} = 0.08$ mrad, which is trivial but non-zero.

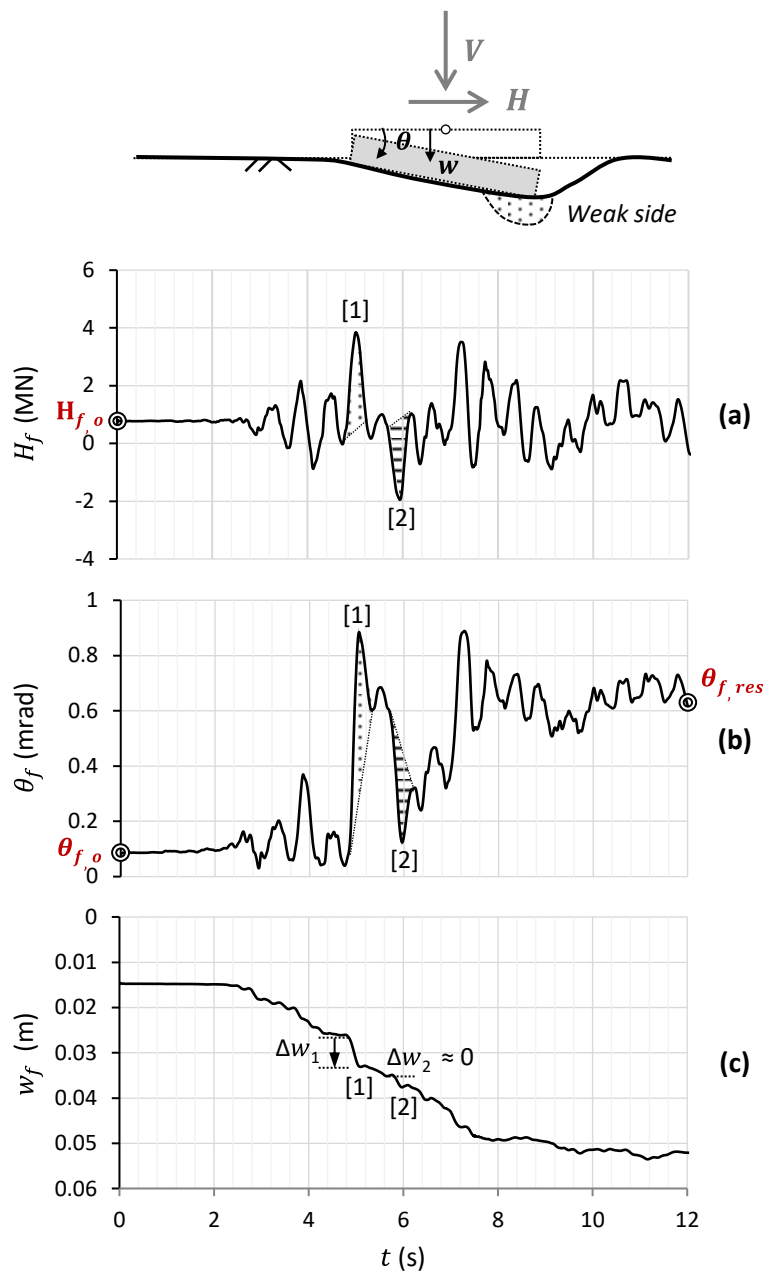


Figure 2.19. Response of the central tower footing subjected to combined wind and seismic loading (Emilia–Romagna record). Time histories of: (a) lateral load; (b) rotation; and (c) settlement.

Due to the introduced asymmetry, when the footing is subjected to subsequent seismic loading, it tends to accumulate rotation towards the same direction (denoted as the ‘weak side’). For example, seismic pulse [1] that induces dynamic lateral force H_f in the same

direction with $H_{f,0}$, leads to further accumulation of θ_f towards the ‘weak side. (Fig. 2.19b). A subsequent pulse [2], acting in the opposite direction, leads to rotation θ_f towards the opposite direction but not below $\theta_{f,0}$ as the wind load that introduced the asymmetry is always present. As a result, the footing keeps accumulating rotation towards the ‘weak side’, and for the same reason, settlement is also accumulated for loading in this direction (Fig 2.19c). At the end of shaking ($t > 12$ sec), the residual rotation $\theta_{f,res} \approx 0.7$ mrad is an order of magnitude higher, but thanks to the pinned connection, this does not affect system response.

This is not the case for the accumulated settlement, which reaches $w_f \approx 0.05$ m for the specific seismic excitation (Emilia–Romagna). Although this is not particularly high in absolute terms, its consequences are worth discussing. This settlement is, in fact, responsible for the previously discussed 1.5 MN decrease of the cable pretension, which almost led to a condition of ‘complete slack’ on the lee-ward cable during the Emilia-Romagna event (Fig. 2.18). To avoid such an alarming situation, the settlements of the central footing should be minimized, something that calls for moderate over-design. Still, though, since the zeroing of cable tension is only momentary, it may actually not be that critical. At least for the load cases examined, the analysis did not reveal any issues of structural stability.

2.6. Conclusions

The paper has explored the potential of a cost-efficient and easy-to-install scheme for the support of Mega-Turbines in intermediate sea depths (i.e., $30 \text{ m} < d \leq 60 \text{ m}$), with the scope to investigate the system’s response and derive a deeper understanding of its key mechanisms. The proposed system comprises a compliant tower, tethered to the ground with an array of four pretensioned cables, which are moored to the seabed by means of suction caisson anchors. The efficacy of the envisioned solution is demonstrated numerically by studying the performance of an example case study, but the key conclusions can be extended (at least quantitatively) to Mega-sized turbines installed in similar offshore environments.

The envisioned scheme has been shown to comply with the ULS and SLS design requirements. It is demonstrated that even in the ‘code-prohibited’ case of 3P-Resonance (i.e., when the frequency of the mechanical vibrations of the turbine rotor coincides with the OWT eigenfrequency), the dynamic performance of the turbine remains satisfactory. This finding is of general interest for the offshore industry if we consider the large rotational operating

intervals of current OWTs and the very narrow ‘soft-stiff’ frequency range, which codes dictate for the design.

Under concurrent wind and seismic loading, the guyed OWT proved to be resilient, in contrast to monopile alternatives that are shown to be more sensitive to deformation accumulation under the exact same loading combination [Kourkoulis et al., 2014]. Although the rotation at the connection point repeatedly crossed the SLS limit, the residual rotation at the end of shaking was found to be equal to the wind-induced θ_o . This is positive for the envisioned guyed system, which sustains the seismically induced loading with controlled displacements at the cable connection point, protecting the tower from excessive structural distress and undesirable inelastic deformations.

The anchoring of the turbine was shown to have excellent performance; the maximum attained tension is much lower than the pullout capacity of the suction caisson, while the seismically induced foundation deformations are negligible. The observed exceptional performance highlights the degree of conservatism of current codes on the design of suction caissons. By completely ignoring the beneficial effect of suction (for NC conditions), we are ending up with oversized foundations that perform ‘quasi-elastically’ even when subjected to Extreme Loads. If code recommendations could be relaxed, smaller caissons could be selected, allowing for better exploitation of the anchoring mechanism. This would essentially allow cost reduction in the foundation, which constitutes an important fraction of the overall construction cost. In contrast, stricter criteria (i.e., higher factors of safety) are necessary for the design of the central footing in order to control the seismically accumulated (permanent) displacements, as these were shown to produce a significant decrease in the tension of the mooring lines. Apart from that, a surface foundation solution may also be confronted with two other practical challenges: the costs associated with ensuring a reasonably flat surface for installation and creep-related issues in the case of soft clay stratum. In this context, a suction caisson alternative could also be considered for the tower foundation.

Finally, the seismic performance of the taut mooring lines was also satisfactory. Although conditions of ‘complete slack’ (i.e., zeroing of tension loading) may occur during seismic shaking, due to their dynamic and momentary nature, they are not expected to pose a risk to the overall stability of the OWT. This is of particular importance in view of recent advances in mooring offshore technology. Despite the scepticism, it is believed that mooring concepts

applied to ground-based or semi-floated OWTs may efficiently replace traditional solutions, especially in areas of high seismicity.

Notation

α	Adhesion factor
β	Cable inclination angle
γ	Design environmental load factor
γ_d	Caissons design factor
θ_c	Rotation at the cables' connection point
θ_f	Rotation of shallow footing
θ_{sc}	Rotation at the caisson head
θ_{SLS}	Serviceability Limit of foundation rotation
λ	Wind tip speed ratio
ρ	Material density
σ'_v	Vertical effective stress
τ_{max}	Soil unit shaft resistance
φ	Angle between the z-axis and the position of the blade where the rotor mass imbalance is located
ω	Angular speed of the rotor
Ω	Angular frequency
a	Acceleration
$a_{c/sc/top}$	Acceleration at the cables' connection point/caisson head/tower top
a_d	Design ground acceleration
A	Area
b	Rotor overhang
C	Dashpot coefficient
D	Suction caisson diameter
D_f	Shallow footing diameter
d_{rotor}	Rotor diameter
D_t	Wind turbine tower diameter
E	Young's Modulus
$EI_{t,1}$	Tower Rigidity (top cross-section)
$EI_{t,2}$	Tower Rigidity (connection point cross-section)
EI_c	Cables Rigidity
f	Frequency

$f_{1P/3P}$	1P/3P frequency
f_n	Natural frequency
$f_{p,SLS/ULS}$	Fundamental wave frequency at SLS/ULS
F_c	Centrifugal force due to the rotor mass imbalance
F_i	Inclined pull-out load
$F_{i,ult}$	Inclined pull-out caisson capacity
$F_{wave,SLS/ULS}$	Wave load acting at SLS/ULS
$F_{wind,SLS/ULS}$	Wind thrust acting at SLS/ULS
$F_{wind,d}$	Dynamic wind drag force
G	Soil shear modulus
h_f	Height of shallow footing
h_w	Height (from seabed) of the wave load acting point
H_c	Height (from seabed) of the cables connection point
H_f	Footing horizontal load in x-axis
H_t	Hub height
H_T	Tower horizontal load in x-axis
$H_{s,SLS/ULS}$	Significant wave height at SLS/ULS
H_{ult}	Horizontal footing capacity
I_m	Rotor mass imbalance
k'	Reduction factor
K_c	Horizontal cable stiffness
$K_{c,st}$	Horizontal cable stiffness at static equilibrium
K_e	Cable elastic axial stiffness
K_i	Cable stiffness component representing the contribution of cable sag
L	Length
L_b	Blade length
L_e	Cable effective length
m	Concentrated mass
M_T	Tower bending moment about y-axis
N_c	Cohesion factor
q_b	Soil unit end bearing resistance
Q_{sf}	Suction caisson total shaft resistance
$Q_{sf,int}$	Suction caisson internal shaft resistance
$Q_{sf,ext}$	Suction caisson external shaft resistance
q_y	Distributed load acting on y-axis

R	Radial distance
S_u	Soil undrained shear strength
$S_{uc}/S_{ue}/S_{uss}$	Soil undrained shear strength under compression/tension/simple shear
SF	Safety Factor
t	Time
t_w	Caisson thickness
t_t	Tower thickness
T	Period
T_c	Cable tension load
$T_{c,h}$	Cable horizontal reaction force
T_0	Cable pretension load
$T_{p,SLS/ULS}$	Fundamental wave period at SLS/ULS
T_{st}	Cable tension at static equilibrium
T_{ult}	Cable ultimate breaking strength
T_{wind}	Period of wind loading
u_c	Horizontal displacement at the cables connection point
u_i	Inclined caisson displacement
$u_{sc,x}$	Horizontal displacement at caisson padeye
$u_{sc,z}$	Vertical displacement at caisson padeye
u_{top}	Horizontal displacement at the tower top
U_c	Current velocity
V	Wind speed
V_{hub}	Wind speed at hub height
V_s	Soil shear wave velocity
V_{ult}	Vertical footing capacity
W_t	Tower weight (partially submerged)
W_c	Taut cable weight (partially submerged)
W_f	Submerged shallow foundation weight
W'_{sc}	Submerged caisson weight
y_{max}	Cable sag

References

- ABAQUS 6.13. (2013). *Standard user's manual*. Dassault Systèmes Simulia Corp., Providence, RI, USA.
- Achmus, M., and Thieken, K. (2014). Numerical simulation of the tensile resistance of suction buckets in sand. *The Twenty-fourth International Ocean and Polar Engineering Conference*. International Society of Offshore and Polar Engineers.
- Anastasopoulos, I., Gelagoti, F., Kourkoulis, R. and Gazetas, G. (2011). Simplified Constitutive Model for Simulation of Cyclic Response of Shallow Foundations: Validation against Laboratory Tests, *Journal of Geotechnical and Geoenvironmental Engineering*, ASCE, **137** (12): 1154-1168.
- Andersen, K. H., Murff, J. D., Randolph, M. F., Clukey, E. C., Erbrich, C. T., Jostad, H. P., Hansen, B., Aubeny, C., Supachawarote, C. (2005, September). Suction anchors for deepwater applications. In *Proceedings of the 1st International Symposium on Frontiers in Offshore Geotechnics, ISFOG, Perth*.
- API. (2000). Recommended practice for planning, designing and constructing fixed offshore platforms—working stress design. *API recommended practice 2A-WSD (RP2A-WSD)*, 21st Ed, American Petroleum Institute, Washington DC.
- Arany, L., Bhattacharya, S., Macdonald, J., & Hogan, S. J. (2015). Simplified critical mudline bending moment spectra of offshore wind turbine support structures. *Wind Energy*, 18(12), 2171-2197.
- Arany, L., Bhattacharya, S., Macdonald, J. H., & Hogan, S. J. (2016). Closed form solution of Eigen frequency of monopile supported offshore wind turbines in deeper waters incorporating stiffness of substructure and SSI. *Soil Dynamics and Earthquake Engineering*, 83, 18-32.
- Bang, S., & Cho, Y. (2002). Ultimate horizontal loading capacity of suction piles. *International Journal of Offshore and Polar Engineering*. International Society of Offshore and Polar Engineers.
- Bastick, N. (2009). Blue H - The World's First Floating Wind Turbine. *The First Dutch Offshore Wind Energy Conference*, "Essential Innovations", November 12 -13, 2009, Den Helder, The Netherlands. (Presentation)
- Bratland, S. (2009). Hywind - The World First Full-scale Floating Wind turbine. *Seminar and B2B meetings "Powering the Future – Marine Energy Opportunities"*, November 5, 2009, Lisbon, Portugal. (Presentation)
- Bransby, M. F. and Yun, G. J. (2009). The undrained capacity of skirted strip foundations under combined loading. *Géotechnique*, **59**(2), 115-125.
- Bulder, B. H., Van Hees, M. T., Henderson, A., Huijsmans, R. H. M., Pierik, J. T. G., Snijders, E. J. B., Wijnants, G. H. and Wolf, M. J. (2002). Study to feasibility of and boundary conditions for floating offshore wind turbines. *ECN, MARIN, Lagerway the Windmaster, TNO, TUD, Technical Report*, (2002-CMC), R43.
- Bunce, J. W., & Carey, J. M. (2001a). A guyed OWEC support structure design. In *Proceeding European Wind Energy Conference (EWEC 2001)*. Copenhagen, July.

- Bunce, J. W., & Carey, J. M. (2001b). A guyed support structure design for large megawatt offshore wind turbines in deep waters. *In Proc. EWEA Special Topic Conference on Offshore Wind Energy*. Brussels.
- Cao, J., Audibert, J. M. E., Al-Khafaji, Z., Phillips, R. and Popescu, R. (2002). Penetration resistance of suction caissons in clay. *The Twelfth International Offshore and Polar Engineering Conference*. International Society of Offshore and Polar Engineers.
- Cetin, N. S., Yurdusev, M. A., Ata, R., & Özdamar, A. (2005). Assessment of optimum tip speed ratio of wind turbines. *Mathematical and Computational Applications*, 10(1), 147-154.
- Chen, S.S. and Chung, H. (1976). Design guide for calculating hydrodynamic mass. Part I: Circular Cylindrical Structures. *Components Technology Division, Argonne National Laboratory*, Argonne, Illinois.
- Cho, Y. and Bang, S. (2002). Inclined loading capacity of suction piles. *The Twelfth International Offshore and Polar Engineering Conference*. International Society of Offshore and Polar Engineers.
- Clukey, E. C., Templeton III, J. S., Randolph, M. F., & Phillips, R. (2004). Suction caisson response under sustained loop current loads. *In Offshore Technology Conference*. Offshore Technology Conference.
- Crozier, A. (2011). Design and dynamic modelling of the Support Structure for a 10 MW Offshore Wind Turbine. MSc Thesis, *Dept. Energy and Process Eng., Norwegian University of Science and Technology*, Norway.
- Davenport, A. G. (1959). The wind-induced vibration of guyed and self-supporting cylindrical columns. *Transaction of the Engineering Institution of Canada*, 3, 119-141.
- Deng, W., & Carter, J. P. (2000). A theoretical study of the vertical uplift capacity of suction caissons. *The Tenth International Offshore and Polar Engineering Conference*. International Society of Offshore and Polar Engineers.
- Det Norske Veritas. (2005). Offshore Standard DNV-RP-E303, *Geotechnical Design and Installation of Suction Anchors in Clay*. Det Norske Veritas, Høvik.
- Det Norske Veritas. (2010). Offshore Standard DNV-OS-E301, *Position Mooring*. Det Norske Veritas, Høvik.
- Det Norske Veritas. (2014). Offshore Standard DNV-OS-J101, *Design of Offshore Wind Turbine Structures*. Det Norske Veritas, Høvik.
- Giannakos, S., Gerolymos, N., and Gazetas, G. (2012). Cyclic Lateral Response of Piles in Dry Sand: Finite Element Modelling and Validation, *Computers and Geotechnics*, 14, 116-131.
- Global Energy Concepts (2001). WindPACT Turbine Design Scaling Studies Technical Area 3. Self-Erecting Tower and Nacelle Feasibility. *National Renewable Energy Laboratory. Golden, CO. NREL/SR-500-29493*.
- Haenler, M., Ritschel, U., and Warnke, I. (2006). Systematic modelling of wind turbine dynamics and earthquake loads on wind turbines. *European Wind Energy Conference and Exhibition*, Athens, Greece, European Wind Energy Association.
- Henderson, A., Patel, M. (1998). Rigid-body motion of a floating offshore windfarm. *International journal of ambient energy*, 19(3), 127-134.

- ISO 19901-7. (2013). Specific Requirements for Offshore Structures – Part 7: Stationkeeping Systems for Floating Offshore Structures and Mobile Offshore Units. *Petroleum and Natural Gas Industries*, 2nd edition.
- Kourkoulis, R., Lekakakis, P.C., Gelagoti, F.M. and Kaynia, A. (2014). Suction Caisson foundations for offshore wind turbines subjected to wave and earthquake loading: effect of soil-foundation interface. *Géotechnique*, **64**, No. 3, 171-185.
- Lombardi, D., Bhattacharya, S. and Muir Wood, D. (2013). Dynamic soil–structure interaction of monopile supported wind turbines in cohesive soil. *Soil Dynamics and Earthquake Engineering*, Vol. 49, pp. 165–180.
- Mana, D. S., Gourvenec, S., & Randolph, M. F. (2014). Numerical modelling of seepage beneath skirted foundations subjected to vertical uplift. *Computers and Geotechnics*, 55, 150-157.
- Mavrakos, S., (2016). Med-Ocean data and hydrodynamic loading for the North Sea and the Mediterranean Sea location. *JABACO Development of Modular Steel Jacket for Offshore Windfarms*, Deliverable 1.1.
- McCarron, W. O. and Sukumaran, B. (2000). Ultimate capacities of suction caissons and pile elements for deepwater applications. *The Tenth International Offshore and Polar Engineering Conference*. International Society of Offshore and Polar Engineers.
- Morison, J. R., Johnson, J. W. and Schaaf, S. A. (1950). The force exerted by surface waves on piles. *Journal of Petroleum Technology*, **2(05)**, 149-154.
- Randolph, M. F., & House, A. R. (2002). Analysis of suction caisson capacity in clay. *Offshore technology conference*. Offshore Technology Conference.
- Risø, D. N. V. (2002). Guidelines for design of wind turbines. *Det Norske Veritas*.
- Senders, M., & Kay, S. (2002). Geotechnical suction pile anchor design in deep water soft clays. In *Conference Deepwater Risers Mooring and Anchorings, London*.
- Sukumaran, B., McCarron, W. O., Jeanjean, P. and Abouseeda, H. (1999). Efficient finite element techniques for limit analysis of suction caissons under lateral loads. *Computers and Geotechnics*, **24(2)**, 89-107.
- Supachawarote, C., Randolph, M., & Gourvenec, S. (2004, January). Inclined pull-out capacity of suction caissons. *The Fourteenth International Offshore and Polar Engineering Conference*. International Society of Offshore and Polar Engineers.
- Telecommunications Industry Association. (2005). Structural standards for Steel Antenna Towers and Antenna Supporting Structures. *TIA/EIA-222-G*, EUA.
- Tjelta, T. I. (2001). Suction piles: Their position and application today. *The Eleventh International Offshore and Polar Engineering Conference*. International Society of Offshore and Polar Engineers.
- Tonni, L., Rocchi, I., Cruciano, N. P., Martinez, M. F. G., Martelli, L., and Calabrese, L. (2016). A multidisciplinary tool for the development of a regional-scale geotechnical model: a case study in the North-Western Adriatic coastal area. *Procedia Engineering*, **158**, 546-551. DOI: 10.1016/j.proeng.2016.08.487.
- Triantafyllou, M. S. (1984). The dynamics of taut inclined cables. *The Quarterly Journal of Mechanics and Applied Mathematics*, **37(3)**, 421-440.

- Weinstein, A. (2009). WindFloat: A Floating Support Structure for Offshore Wind Turbines. *Seminar and B2B meetings "Powering the Future – Marine Energy Opportunities"*, November 5, 2009, Lisbon, Portugal. (Presentation)
- Witcher, D. (2005). Seismic analysis of wind turbines in the time domain. *Wind Energy*, **8(1)**, 81-91.
- Zafeirakos, A., Gerolymos, N., and Drosos, V. (2013). Incremental Dynamic Analysis of Caisson–Pier Interaction, *Soil Dynamics and Earthquake Engineering*, **48**, 71–88.
- Zhao, X., and Maisser, P. (2006). Seismic response analysis of wind turbine towers including soil-structure interaction. *Proceedings of the Institution of Mechanical Engineers, Part K: Journal of Multi-body Dynamics*, **220(1)**, 53-61.
- Zdravković, L., Potts, D. M., & Jardine, R. J. (2001). A parametric study of the pull-out capacity of bucket foundations in soft clay. *Geotechnique*, **51(1)**, 55-67.

3. Simplified method for performance-based seismic design of suction caissons supporting jacket offshore wind turbines

This chapter consists of the post-print version of the following published article, differing from the original only in terms of layout and formatting:

Antoniou, M., Kourkoulis, R., Gelagoti, F., & Anastasopoulos, I. (2022). Simplified method for performance-based seismic design of suction caissons supporting jacket offshore wind turbines. *Soil Dynamics and Earthquake Engineering*, 155, 107169.

Available at <https://doi.org/10.1016/j.soildyn.2022.107169>

Abstract

The paper studies the performance of Offshore Wind Turbines (OWTs) founded on Suction Bucket Jackets (SBJs) in clay under combined wind and seismic loading. A detailed 3D finite element (FE) model of the soil–foundation–structure (SFS) system is developed and used as a benchmark to assess the efficiency of an enhanced Winkler-based ‘Caisson-on-Winkler-Soil’ (CWS) model, where the soil is replaced by nonlinear hysteretic elements. The proposed CWS model captures residual deformations and hysteresis and offers physical coupling between vertical and moment loading. It allows excellent prediction of the H – M failure envelope in the most relevant first quadrant of H – M space, where the loads act in the same direction. Despite its successful application for the simulation of inertial loading, the CWS model fails to reproduce the dual shearing mechanism that develops at the caisson shaft during shaking, stemming from the combination of kinematic soil shearing due to the vertically propagating shear waves and shearing due to the superstructure inertial response, thus underpredicting the co-seismic caisson settlements. For the prediction of the latter, the research utilizes spectrum-compatible input motions and 3D FE models of varying geometric and material properties to derive linear regression equations that correlate the co-seismic dimensionless settlement of caissons (w_E/D) with characteristic dimensional variables of the problem under investigation and the Arias Intensity (I_A) of the surface ground motion. As a final step, the paper proposes a hybrid method for performance-based assessment of SBJ OWTs. The proposed method employs the simplified CWS model to calculate the VHM loads and approximately estimate horizontal displacements and rotations at the jacket legs, followed by a preliminary assessment of caisson settlements using the correlations of w_E/D with I_A , on the basis of spectrum-compatible input motions.

3.1. Introduction

Following the ambitious energy targets set by countries worldwide, the offshore wind sector has seen impressive growth over the last decade, transforming from niche technology to a global industry. As of 2019, Europe alone has 22 GW of installed offshore wind capacity – enough to cover 2.3% of its electricity consumption [WindEurope, 2020], while similar or even more potent growth is observed in many countries around the world, such as China, the USA, and India. Part of this energy transition is led by technology-driven innovation, with offshore wind turbines reaching new heights and larger capacities while wind farms are moving deeper into the sea to harness the increased energy potential. Given this new ‘deep-water’ environment, traditional OWT support structures are gradually being replaced by more cost-effective and agile foundation systems in a quest for reduction of investment costs.

Despite their obvious attractiveness, floating concepts require further development before commercialisation. Thanks to substantial progress towards standardized manufacturing and mass production of tubular joints using automatic welding, jackets are gradually establishing their position in the offshore industry [Seidel, 2007; Wagner et al., 2011; Shaumann et al., 2005]. They are currently the second most installed OWT foundation in Europe. Suction caissons (or buckets) were recently deployed as the foundation of jacket OWTs, including installations at the Borkum Riffgrund 1 (2014), Borkum Riffgrund 2 (2018), and Aberdeen Bay (2018) offshore windfarms. Suction caissons are decisively entering the market; their cost-efficient and low-noise installation (facilitated by water pumping between the caisson and the soil, with the hydraulic pressure difference driving the caisson into the soil) offers a major comparative advantage.

At the same time, the spread of such installations has broadened the hazard spectrum faced by OWTs [Katsanos et al., 2016; Swiss Re, 2017; Kaynia, 2019]. In recent years, a large number of wind turbines have been installed (or are planned to be installed) in high-seismicity areas, including China, Taiwan, India, and South Korea, as well as the USA, Mexico, and several seismically active zones in Southern Europe and the Middle East. According to Swiss Re [2017], a 50-year seismic event could trigger losses of millions of USD in vulnerable offshore wind markets by 2030. Amid persisting concerns on the structural robustness of OWTs in

earthquake-prone areas, DNV GL recently launched the ACE (Alleviating Cyclone and Earthquake Challenges for Wind farms) Joint Industry Project⁹.

Despite the growing literature on the seismic performance of OWTs [Mardfekri & Gardoni, 2013; Kim et al., 2014; Anastasopoulos & Theofilou, 2016; Mo et al., 2017; De Risi et al., 2018], several crucial issues remain. For example, the coupling of aerodynamic, hydrodynamic, and seismic loading was only recently explored for fixed-base OWTs (numerically and experimentally), confirming the non-trivial effect of tower seismic oscillation on rotor aerodynamics and the developing wind thrust [Alati et al.; 2005, Zheng et al., 2015; Wang et al. 2017a]. The effects of the combined action of wind and earthquake loading have been discussed by Gelagoti et al. [2019], focusing on foundation performance. The study analyzed a 10 MW OWT, supported on a large diameter monopile and a 4-legged jacket founded on piles. They observed a considerable accumulation of permanent deformations for both foundation systems when subjected to large-amplitude non-symmetric cyclic loading (due to the combined action of wind and seismic loading).

Significant research effort has been devoted to the response of suction caisson as an alternative foundation for OWTs, with the vast majority of the literature focusing on monopod installations [Bransby & Yun, 2009; Byrne & Houlsby, 2004; Gourvenec & Barnett, 2011; Vulpe 2015; Keawsawasvong & Ukritchon, 2016; Mana et al., 2012; Ukritchon & Keawsawasvong, 2016; Ukritchon et al., 2018]. To the best of our knowledge, only limited studies have addressed the dynamic performance of suction caissons. Suryasentana et al. [2018] presented an elastoplastic 1D Winkler-based model for suction caissons under *VHM* loading. By combining Winkler-type elastic soil reactions with local plastic yield surfaces, the model captured the monotonic and symmetric cyclic foundation response. A macro-element approach was proposed by Skau et al. [2018; 2019] to capture the nonlinear behaviour of flexible or rigid suction caissons in clay under irregular cyclic loading. Wang et al. [2017b] analyzed the lateral seismic response of monopod suction buckets in sand through centrifuge model testing. Esfeh & Kaynia [2020] investigated numerically the effect of liquefaction on the performance of monopod caisson foundations in sand under the combined actions of ground shaking and static/cyclic wind loading. Employing 3D finite element (FE) modelling, Kourkoulis et al. [2014] evaluated the effect of soil-sidewall interfaces on the response of wind turbines

⁹ [Alleviating cyclone and earthquake challenges for wind farms \(dnv.com\)](https://www.dnv.com/ace)

founded on monopod suction caissons in clay under lateral monotonic, cyclic, and seismic loading. Despite the recent advances and the valuable insights offered by sophisticated numerical and physical models, practice calls for efficient performance-based design techniques. To this end, this paper develops a simplified performance-based methodology for OWTs founded on Suction Bucket Jackets (SBJ) in clay, subjected to combined environmental and seismic loading. An enhanced Winkler-based ‘Caisson-on-Winkler-Soil’ (CWS) model is developed for this purpose, where soil–suction caisson interaction is represented by nonlinear hysteretic elements allowing the simulation of residual deformations. Moreover, the proposed CWS model captures the coupling between vertical and moment loading, using distributed vertical hysteretic elements on the caisson shaft, which contribute simultaneously to the axial and moment shaft resistance under combined *VHM* loading. A detailed 3D FE model of the entire soil–foundation–structure (SFS) system is developed and used as a benchmark to assess the efficiency of the simplified analysis technique. While the detailed 3D FE model is certainly more robust, the unavoidably less precise simplified CWS model offers the advantage of computational efficiency. The two modelling approaches are comparatively discussed to: (a) understand the mechanics governing the nonlinear deformation (displacement, rotation, settlement) of suction caissons under combined wind and earthquake loading; (b) explore the limitations of the CWS model; and (c) develop a simplified hybrid methodology to facilitate a performance-based assessment of the foundation of SBJ OWTs. The latter combines the CWS model for the estimation of VHM loads and horizontal displacements/rotations at the jacket legs with a regression model for the assessment of settlements (based on 3D FE analyses).

3.2. Detailed 3D FE Modelling

This section presents the detailed 3D FE modelling of the entire soil–foundation–structure (SFS) system, which is used as a benchmark to assess the efficiency of the simplified CWS model. Before diving into the full SFS system of the SBJ OWT, the numerical modelling of a single suction caisson is discussed in detail.

Single suction caisson

A single suction caisson of length to diameter ratio $L/D = 1$ is analysed, embedded in a uniform clay stratum. The problem is solved numerically, employing 3D FE modelling using ABAQUS [Dassault Systemes, 2013]. As shown in the FE mesh of **Fig. 3.1a**, half of the caisson

is modelled, taking advantage of problem symmetry. Model boundaries are at a sufficiently large distance to avoid boundary effects: $2.5D$ at either side of the foundation for the lateral boundaries and $1.5L$ beneath its tip for the bottom boundary. For static loading, the lateral displacements (x and y) are restrained at the lateral model boundaries, as well as the out-of-plane displacement (y) for the planes of symmetry and the vertical displacement (z) at the model base.

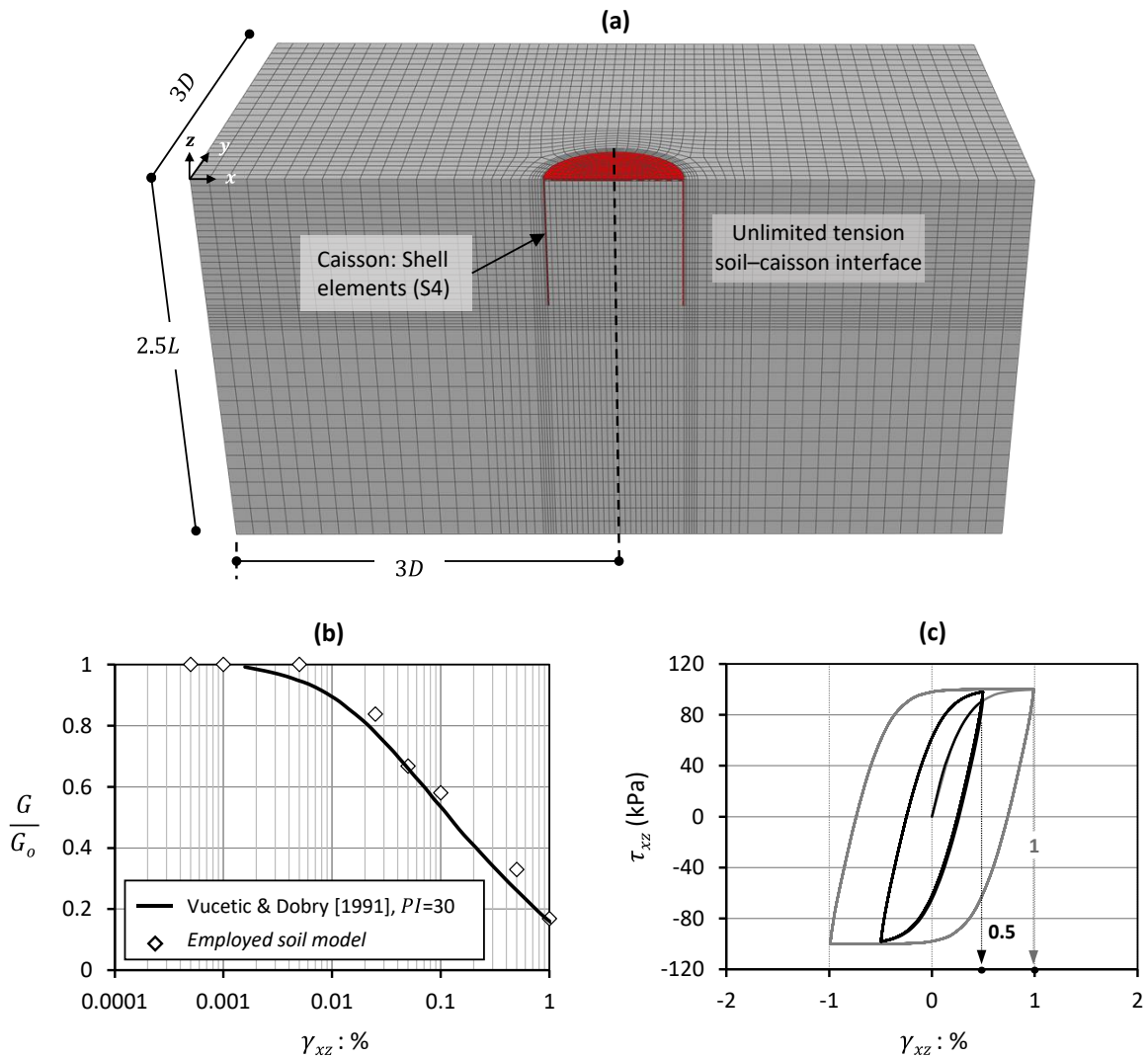


Figure 3.1. Single suction caisson: (a) FE mesh; (b) Comparison of the $G-\gamma_{xz}$ curve predicted numerically by the calibrated soil model ($S_u = 100$ kPa, $E_o = 180$ MPa) to the experimentally measured curve of Vucetic & Dobry [1991] for high plasticity clays ($PI = 30$); (c) Hysteresis loops of example clay specimen subjected to cyclic simple shear loading at two characteristic shear strain levels (5×10^{-3} and 10^{-2}).

The steel suction caisson is simulated with linear shell elements (S4) of Young's modulus $E = 210$ GPa, Poisson's ratio $\nu = 0.2$, and density $\rho = 7.85$ t/m³, while the soil is modeled as a one-phase medium of uniform undrained shear strength (S_u) described by 8-noded hexahedral continuum elements (C3D8). Rough interface conditions (no separation or detachment) are assumed between the soil and the caisson. The nonlinear hysteretic behavior of clay under undrained conditions is modelled with a kinematic hardening constitutive model with Von Mises failure criterion. Gerolymos & Gazetas [2005] and Anastasopoulos et al. [2011] provide more details on the model and its calibration. Herein, it is briefly described for completeness. The yield surface is defined by:

$$F = f(\underline{\mathbf{s}} - \mathbf{a}) - \sigma_o = 0 \quad (3.1)$$

where: σ_o corresponds to the maximum stress at zero plastic strain and $f(\underline{\mathbf{s}} - \mathbf{a})$ is the equivalent Mises stress with respect to the deviatoric stress $\underline{\mathbf{s}}$ and the backstress \mathbf{a} . The center of the yield surface is determined by the evolution law:

$$\dot{\mathbf{a}} = C \frac{1}{\sigma_o} (\underline{\mathbf{s}} - \mathbf{a}) \dot{\epsilon}^{Pl} - \gamma \mathbf{a} \dot{\epsilon}^{Pl} \quad (3.2)$$

In Eq. (3.2), C is the initial kinematic hardening modulus, and γ is a scalar coefficient that determines the rate of decrease of kinematic hardening with increasing plastic deformation. According to this evolution law, all stress points should lie within a cylinder of radius $\sqrt{2/3} \sigma_y$, where σ_y is the maximum yield stress at saturation. For uniaxial conditions at large plastic strains, when $\underline{\mathbf{s}}$ approaches σ_y , \mathbf{a} becomes equal to C/γ , $\dot{\mathbf{a}}$ tends to zero and

$$\sigma_y = C/\gamma + \sigma_o \quad (3.3)$$

For clays, the maximum yield stress σ_y is controlled by the undrained shear strength S_u according to:

$$\sigma_y = \sqrt{3} S_u \quad (3.4)$$

Consequently, the value of γ can be defined as:

$$\gamma = \frac{C}{\sqrt{3} S_u - \sigma_o} \quad (3.5)$$

Therefore, for the full description of nonlinear clay response, only three parameters need to be determined: the strength S_u , the ratio E_o/S_u (where E_o is the small-strain soil stiffness), and γ . The model is calibrated against the experimental $G - \gamma_{xz}$ curves of Vucetic & Dobry [1991] for high plasticity clays, yielding $E_o/S_u = 1800$ and $\gamma = 1154$ (**Fig. 3.1b**). **Figure 3.1c** displays typical shear stress – shear strain ($\tau_{xz} - \gamma_{xz}$) loops generated by the calibrated model under quasi-static simple shear loading.

Despite its simplicity, the 3-parameter constitutive model has been extensively validated against physical model tests, demonstrating its effectiveness in describing the overall soil-foundation system response under cyclic loading. Indicative such examples relevant to the present study involve surface and embedded foundations subjected to cyclic loading and seismic shaking [Anastasopoulos et al., 2011] and the cyclic response of piles and caissons subjected to horizontal/moment loading [Giannakos et al., 2012].

The suction caisson model is further validated herein against bearing capacity and small-strain stiffness calculations by comparing numerical predictions with available published data. As summarized in **Table 3.1**, the computed uniaxial capacity factors compare well to the numerical studies of Hung & Kim [2012], Suryasentana et al. [2018], and Fu et al. [2017], all of which are referring to 3D circular ($L/D = 1$) caisson foundations in homogeneous clay. The vertical capacity factor ($N_{CV} = V_o/AS_u$, where $A = \pi D^2/4$) is 9% lower (maximum deviation) compared to the numerical results of Hung & Kim [2012], while the horizontal capacity factor ($N_{cH} = H_o/AS_u$) displays a 6% difference (maximum deviation) against the solution of Suryasentana et al. [2018]. The uniaxial moment capacity factor ($N_{cM} = M_o/ADS_u$) compares well to the study of Suryasentana et al. [2018], displaying a mere 4% difference.

Furthermore, the elastic lateral (K_{HH}), rocking (K_{MM}) and coupled swaying-rocking (K_{HM}) stiffness coefficients compare well with the solutions of Gelagoti et al. [2018] for a relative soil-caisson rigidity ratio equal to $J = \left(\frac{E_{steel} t_w}{E_o D}\right) = 4.67$, where E_{steel} is the Young's modulus of the steel caisson, t_w is the skirt thickness, and D is the caisson diameter.

Table 3.1. Comparison of numerical predictions with published data for undrained uniaxial capacity factors N_{cV} , N_{cH} , N_{cM} and elastic stiffness coefficients K_{HH} , K_{MM} , K_{HM} for flexible caissons of $L/D = 1$ and rough interface conditions.

Uniaxial Capacity Factors			
	N_{cV}	N_{cH}	N_{cM}
This study	12.73	6.15	3.95
Suryasentana et al. [2018] $L/D=1$	13.00	5.80	3.80
Fu et al. [2017] $L/D=1$	13.65	-	-
Hung & Kim [2012] $L/D=1$	14.00	6.00	-
Elastic Stiffness Coefficients ($t_w = 0.024\text{m}$)			
	K_{HH} (MN)	K_{HM} (MN)	K_{MM} (MNm)
This study	2453.3	5585.9	50839.1
Gelagoti et al. [2018]	2381.18	5429.1	45347.6

Soil-Foundation-Structure (SFS) system

An 8MW jacket-supported OWT, installed at a water depth of 60 m in the Adriatic Sea, is used as an illustrative example. The wind turbine and jacket structure characteristics and the environmental load combinations for *Normal* and *Extreme* Sea states were provided by the EU Funded Research Program JABACO [Mavrakos, 2016; Von Borstel & Vobeck, 2016]. The foundation soil corresponds to a clay layer of undrained shear strength $S_u = 100$ kPa, while the suction caissons are of $D = L = 6$ m ($L/D = 1$). **Table 3.2** summarizes the turbine tower characteristics, while **Fig. 3.2** illustrates the 3D FE mesh of the soil–foundation–structure (SFS) system. Details on the geometric properties of the simulated jacket structure are provided in **Appendix 3A**.

Table 3.2. Geometric properties of the 8MW turbine.

	D_{tower} (m)	t_{tower} (m)	H_{tower} (m)	d_{rotor} (m)	Nacelle & Rotor Mass (ton)
8^{MW}	6	0.03	107	164	480

By taking advantage of the problem symmetry, half of the system is modelled. The turbine tower is modelled as an SDOF system, consisting of elastic 3D beam elements (B31) and a concentrated mass at the rotor-nacelle level. The tower is rigidly connected to the top of the jacket, which is also modelled with elastic beam elements (B31). Typical steel material

properties are assumed for both the tower and the jacket structure, i.e., $E = 210 \text{ GPa}$, $\nu = 0.2$, and $\rho = 7.85 \text{ t/m}^3$. Effective density values are considered for the submerged jacket parts.

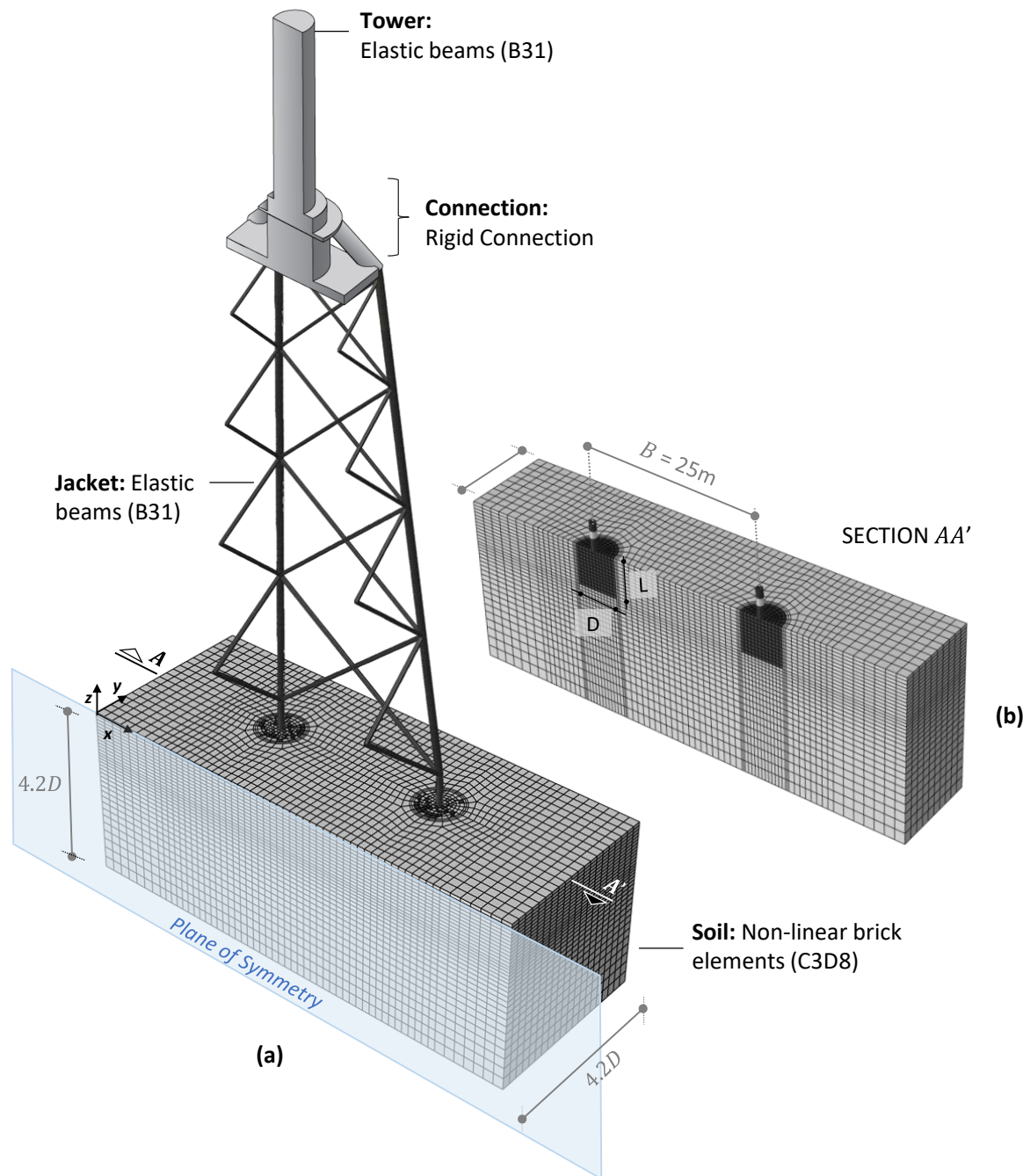


Figure 3.2. (a) FE mesh of the global soil–foundation–jacket structure system, and (b) section AA' cut view (caissons & inner soil plug are highlighted with black).

The suction caissons are modelled as previously described and are assumed to be fully bonded to the foundation soil (i.e., no separation or detachment is allowed). The assumption is justified by the rapid nature of seismic loading, during which full suction conditions can be

assumed beneath the caisson lid (excess pore water pressures cannot dissipate, and passive suction is maintained throughout the shaking).

Compared to the previously discussed static analysis of the single suction caisson, the boundary conditions are modified for the dynamic analyses. Radiation damping is taken into account by introducing dashpots at the base of the model (defined as $C_{dash} = \rho V_s A$, where: $\rho = 2 \text{ t/m}^3$ is the material density, $V_s = 350 \text{ m/s}$ the shear wave velocity at the FE model's base, and A the effective area that corresponds to each dashpot). Appropriate kinematic (MPC) constraints are imposed at the lateral model boundaries to replicate free-field soil response.

Benchmark simulation: SBJ OWT subjected to combined seismic and wind loading

For the benchmark simulation, wind loading is approximated by a static wind thrust at the nacelle level – a reasonable assumption, given the low-frequency range of wind loading compared to the eigenmodes of the turbine. The analysis is performed in two steps. The structure is initially subjected to a constant horizontal force $W = 872.2 \text{ kN}$ (corresponding to 70% of the SLS wind load) that generates an overturning moment M at the jacket base. The jacket provides resistance to this large-amplitude M through its frame structure; the two leeward legs undergo increased vertical load while the opposite (windward) legs are unloaded. All jacket legs are also subjected to bi-directional $H-M$ loading of much smaller amplitude. W is maintained throughout the second analysis step, during which the model is excited by an acceleration time history (IT.AC.V record from the 2009 L'Aquila earthquake).

Indicative analysis results are summarized in **Fig. 3.3**. Acceleration time-histories (**Fig. 3.3a**) are plotted for the nacelle level (a_{tower}) and at the ground surface ($a_{surface}$). The long-period superstructure (with its first natural period $T_{1,n} = 4.0 \text{ s}$ away from the dominant earthquake period $T_E = 0.5 \text{ s}$) leads to the motion's de-attenuation and a resulting peak acceleration $a = 0.31g$ at the nacelle level. At the time of maximum loading, the Mises stress at the tower and jacket structure is well below the yield point ($\sigma_{Mises} = 125 \text{ MPa}$ is observed at the right jacket leg at $t = 3.7s$, compared to $f_{yield} = 355 \text{ MPa}$), confirming the assumption of elastic jacket response. Foundation performance is described by the time histories of vertical (w) and horizontal (u) caisson displacements (**Fig. 3.3b**), the rotations at the jacket legs (θ_t and θ_c for the tensile and compressive leg, respectively) and the rotation (θ_j) of the jacket structure (**Fig. 3.3c**).

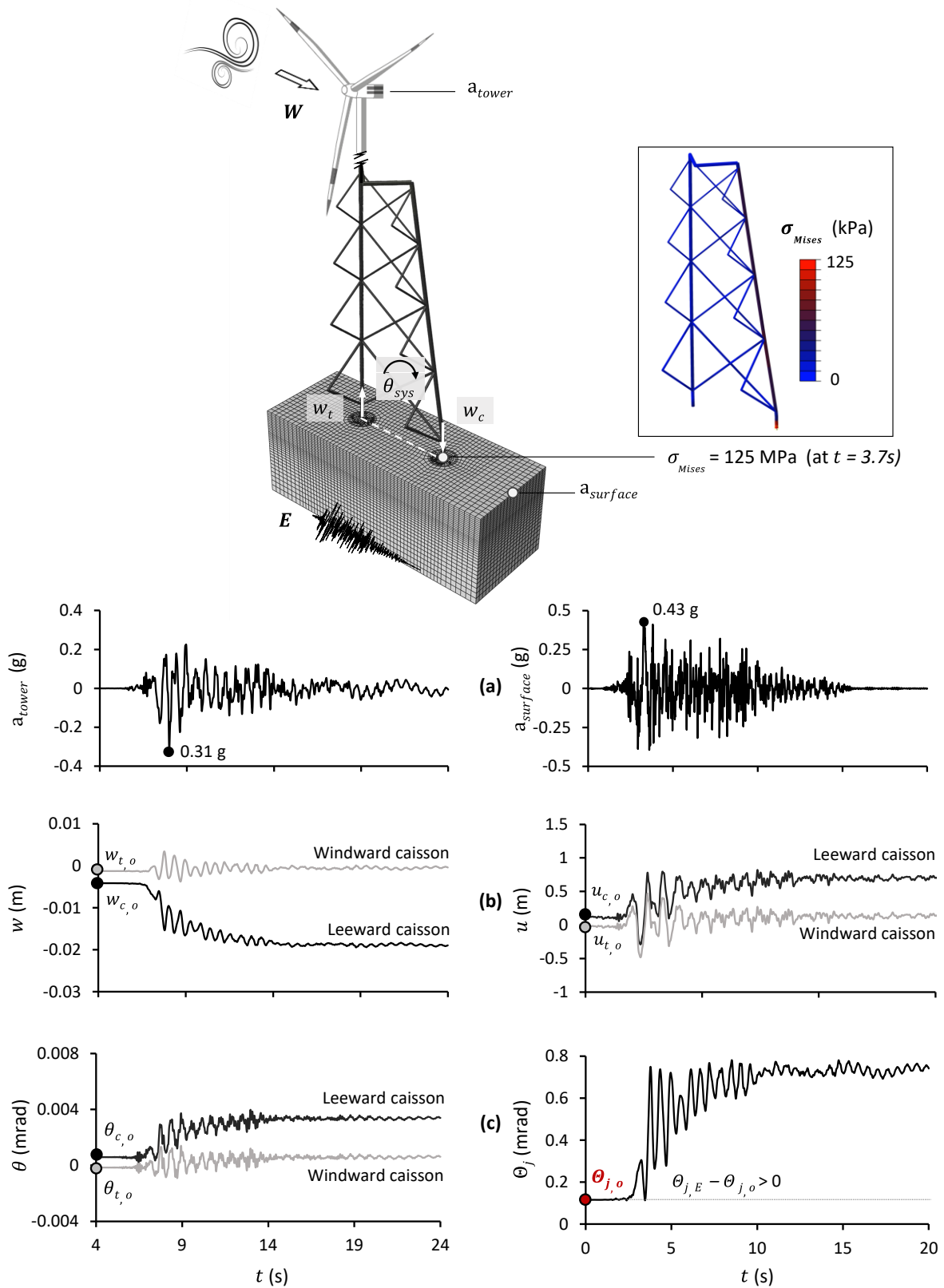


Figure 3.3. Performance of the 3D SFS system subjected to combined wind and seismic loading (L' Aquila record). Time histories of: (a) acceleration at tower top (a_{tower}) and soil surface ($a_{surface}$); (b) caissons' settlement (w) and horizontal displacement (u); (c) caissons' rotation (θ) and jacket rotation (θ_j).

The latter is defined as $(w_c - w_t)/B$, where w_t and w_c are the vertical displacements of the tensile (windward) and compressive (leeward) leg, respectively, and B is the width of the jacket. The leeward caisson carries a larger initial vertical load compared to the windward caisson due to the initially applied wind load. This initial load asymmetry leads to an imbalance in the rate of seismic settlement accumulation between the two legs: the compressed (leeward) caisson sustains $w_c = 0.02$ m, as opposed to zero settlement of the tensile (windward) caisson, leading to non-trivial residual jacket rotation $\theta_j = 0.7$ mrad. Note that, according to DNV-OS-J101 [2014], the operational limit for the specific configuration is $\theta_{lim,SLS} = 4.4$ mrad. The leeward caisson also accumulates larger horizontal displacement u_c and rotation θ_c (**Fig. 3.3b**), which are, however, not large enough to constitute a threat.

3.3. 'Caisson-on-Winkler-Soil' (CWS) model

Winkler-based models simplify the problem by replacing the soil with a series of uniformly distributed independent springs and dashpots. Such models have been widely used for the design and performance assessment of laterally and axially loaded piles [e.g., Novak, 1978; Randolph & Wroth, 1978; O'Rourke & Dobry, 1982; Pender, 1993; Guo, 2000; API, 2010; Anoyatis & Mylonakis, 2012]. Gerolymos & Gazetas [2006a; 2006b; 2006c] and Assimaki et al. [2009] proposed an extension for cylindrical embedded foundations. A 4-spring model was introduced (including four sets of springs and dashpots) to account for the coupled swaying-rocking response of rigid caisson foundations in multi-layered soils. A similar model was employed by Tsigginos et al. [2008] to study the seismic response of a caisson-bridge pier system.

A fundamental limitation of existing models is their inability to account for deformation accumulation. Even when nonlinear spring relations are employed (e.g., the $p - y$, $t - z$ methods proposed by API [2010]), these are still elastic and, therefore, limited to monotonic loading. Modelling permanent deformation accumulation requires introducing nonlinear hysteretic elements, which is the scope of this study.

General Description

The proposed 'Caisson-on-Winkler-soil' (CWS) model is essentially a nonlinear hysteretic variation of the 4-spring Winkler model, extended to incorporate the coupling of vertical –

horizontal – moment (VHM) loading, as well as permanent deformations under dynamic loading. As shown in the schematic of **Fig. 3.4a**, a rigid body motion is assumed for the suction caisson and the inner soil plug. This is a reasonable simplification for seismic loading, during which the soil-caisson interface is expected to maintain full contact, thanks to the development of negative pore pressures below the lid. Based on this assumption, the caisson and the inner soil plug are modelled as a rigid body of equivalent density, the response of which under combined $V-H_x - M_y$ loading is schematically shown in **Fig. 3.4b**. The caisson head is used as a reference, with the vertical and horizontal displacement and rotation denoted by u , and θ , respectively.

The CWS model comprises an assembly of distributed and concentrated hysteretic elements: (i) vertical distributed elements (k_z) along the caisson shaft; (ii) horizontal distributed elements that represent the normal ($k_{x,n}$) and frictional ($k_{x,s}$) resistance of the sides to lateral loading; (iii) a concentrated vertical element at the caisson base (K_{bz}), linked to the base axial resistance; (iv) a concentrated horizontal element (K_{bx}) at the base, which represents the base contribution to the lateral resistance mechanism; and (v) a concentrated rotational element at the base ($K_{b\theta}$), which provides the base resisting moment due to normal stresses. The distributed vertical elements on the sides serve a dual purpose, simultaneously contributing to both the axial shaft resistance and the rotational resisting mechanism. The latter is captured by the overturning moment $M_y = \sum m_y = \sum k_z w D$ (**Fig. 3.4b**), generated by the differential vertical movement w between the caisson sides. Such modelling allows the physical coupling between the axial and rotational response of the shaft. Since spring elements cannot incorporate hysteresis, nonlinear 1D hysteretic truss elements (T3D2) are employed instead. A considerable length (e.g., $L = 10$ m) is necessary to minimize the error related to second-order effects during large deformations. Their nonlinear response follows a kinematic hardening constitutive model with Von Mises failure criterion and associated flow rule (similar to the one previously described for the detailed 3D model). For the hysteretic truss elements, the model is defined by a small-strain stiffness modulus ($E_{o,ns}$), a yield point (σ_y), and hardening parameters that describe the post-yield response. As shown in **Fig. 3.4c**, their uniaxial behaviour follows a backbone curve, while the unloading/reloading response satisfies the Masing rule, which implies that the unloading–reloading modulus ($E_{ur,ns}$) is equal to the small-strain modulus ($E_{o,ns}$).

The small-strain stiffness modulus ($E_{o,ns}$) is calculated based on the uniaxial elastic stiffness (k_e) of each hysteretic element:

$$E_{o,ns} = k_e L / A \quad (3.6)$$

where: L, A are the element length and area, respectively. The maximum yield stress is equal to the ultimate soil reaction force of the element ($\sigma_y = f_{max}$).

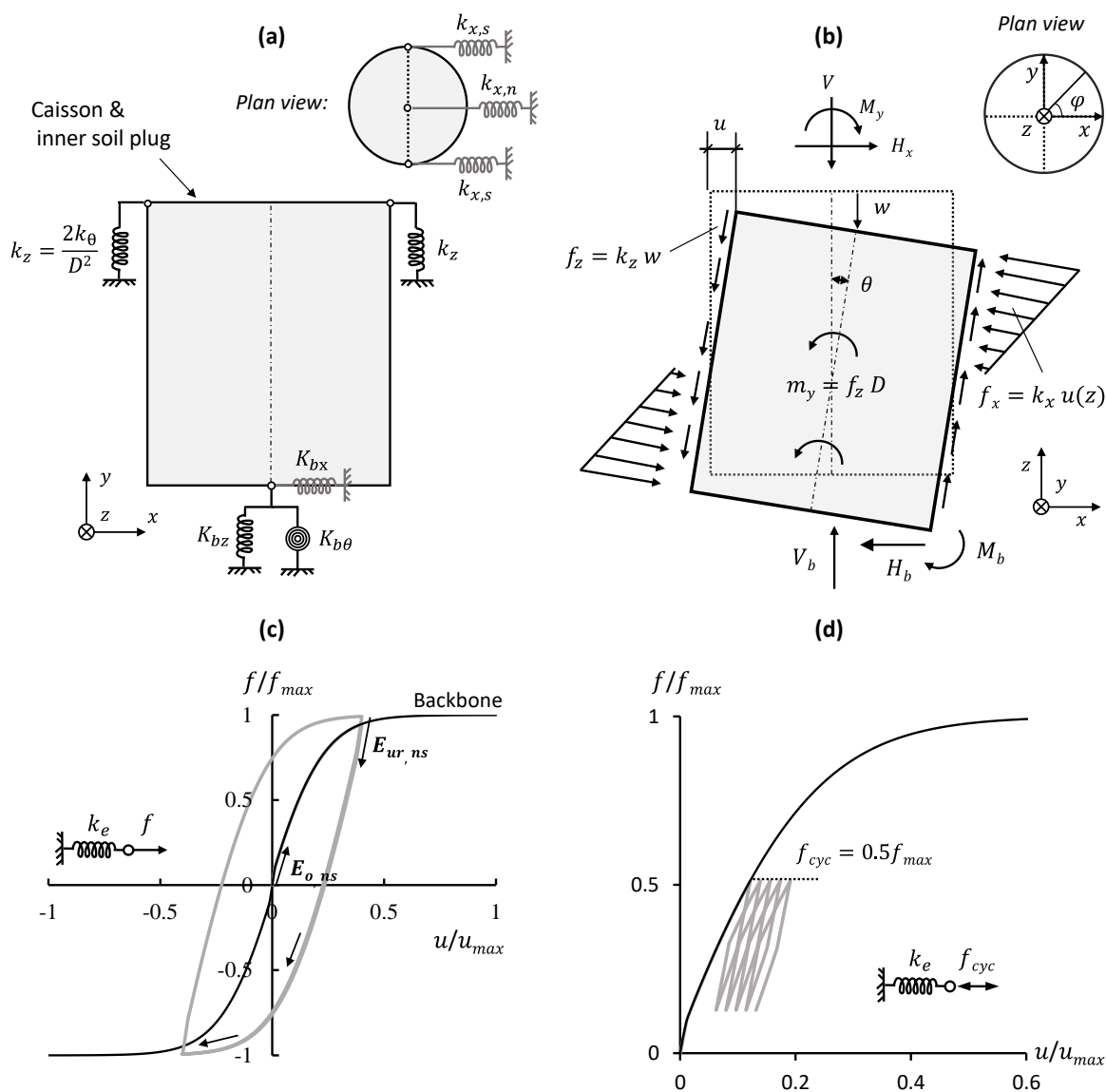


Figure 3.4. ‘Caisson-on-Winkler-Soil’ model: (a) schematic illustration of the model; (b) rigid body response of the caisson subjected to VHM loading at the top. Nonlinear hysteretic element response: (c) backbone curve and two-way cycling loading at $0.4u_{max}$; and (d) one-way cyclic loading at half of the maximum yield stress.

Figures 3.4c and 3.4d display indicative examples of force-displacement time-histories of a caisson experiencing two-way symmetric and one-way asymmetric cyclic loading. Under asymmetric loading ($f_{cyc} = 0.5f_{max}$), the element captures the accumulation of plastic strains with subsequent loading cycles without exhibiting signs of ratcheting (Fig. 3.4d).

CWS Model Calibration

Small strain stiffness

The calibration of the small-strain stiffness of the hysteretic elements is based on 3D FE calculations, following the flexibility approach of Assimaki et al. [2009]. A unit lateral force and a unit overturning moment are applied at the top of the 3D caisson model, allowing the computation of the lateral (K_{HH}), rocking (K_{MM}), and cross-lateral rocking (K_{HM}) stiffnesses. 3D FE modelling for calibration purposes may be avoided, using the previously discussed readily available closed-form solutions. Via horizontal force and moment equilibrium at the top of the caisson, the values of distributed (k_x, k_z) and concentrated base ($K_{bx}, K_{b\theta}$) horizontal and rotational stiffnesses are deduced as follows:

$$k_x = 2 \left(\frac{K_{HH}L + K_{HM}}{L^2} \right) \quad (3.7)$$

$$K_{bx} = - \frac{K_{HH}L + 2K_{HM}}{L} \quad (3.8)$$

$$K_{MM} = (k_z D^2 / 2)L + K_{b\theta} + \left(k_x \frac{L^3}{3} + K_{bx} L^2 \right) \quad (3.9)$$

In order to calculate the distributed k_z based on Eq. (3.9), $K_{b\theta}$ may be defined by evaluating the rotational stiffness of a diameter D surface foundation founded on a 6 m deep open trench (for the case examined), applying unitary overturning moment at the top (seabed). The closed-form solution of Gazetas [1991] can be used:

$$K_{b\theta} = \frac{1}{3} \frac{GD^3}{(1-\nu)} \quad (3.10)$$

where: G and ν are the soil shear modulus and Poisson's ratio. The same rationale applies to the vertical base coefficient K_{bz} , which may be calculated as [Gazetas et al., 1985]:

$$K_{bz} = \frac{2.01 GD}{(1 - \nu)} \left(1 + 0.195 \frac{L}{D}\right) \quad (3.11)$$

Nevertheless, K_{bz} and $K_{b\theta}$ are computed herein based on the 3D FE model to allow their direct comparison. For the studied problem, the computed k_x , k_z , K_{bx} , $K_{b\theta}$ and K_{bz} are summarized in **Table 3.3**.

The *dynamic* stiffnesses of the 1D hysteretic elements are calculated as products of the above *static* stiffnesses and a dynamic stiffness coefficient $\Delta(\omega)$. The latter is a function of the dimensionless frequency $a_0 = \omega D/V_s$, where ω is the angular frequency of the excitation, and V_s the shear wave velocity of the soil profile. They are derived according to the formulas proposed by Assimaki et al. [2009], based on the value of α_0 of each studied scenario. For the cases examined herein, the dynamic coefficient $\Delta(\omega)$ ranges between 0.9 and 1.0, and, therefore, the *dynamic* stiffnesses are very close to the *static* stiffnesses of **Table 3.3**.

Table 3.3. Computed stiffnesses of the CWS model for the studied problem.

Hysteretic element	Type	Static Stiffness
Horizontal / Shaft	Distributed	$k_x = 507.4 \text{ MN/m}^2$
Vertical / Shaft	Distributed	$k_z = 227.2 \text{ MN/m}^2$
Horizontal / Base	Concentrated	$K_{bx} = 591.3 \text{ MN}$
Rotational / Base	Concentrated	$K_{b\theta} = 11051.2 \text{ MNm}$
Vertical / Base	Concentrated	$K_{bz} = 1367.3 \text{ MN}$

Ultimate strength (f_{max})

The ultimate strength of the hysteretic elements is calibrated through the following three steps: (1) estimation of global (uniaxial) caisson capacities (V_o , H_o , M_o); (2) estimation of local capacity factors (i.e., the contribution of the shaft and base resistance); and (3) distribution of local capacities to individual hysteretic elements (i.e., assignment of f_{max}). The purely vertical resistance V_o can be calculated on the basis of 3D FE push-down analyses (assuming that the capacity is reached at $w = 0.01D$), which also allow to distinguish between base (V_b) and shaft (V_{shaft}) resistance. Readily available global and local capacity factors (N_{cv}) from the literature [e.g., Fu et al., 2017] can also be used, or experimental results (if available). The analysis conducted herein is based on the 3D FE analysis employing the kinematic hardening

model, but more sophisticated constitutive models can also employ the same calibration procedure.

As summarized in **Table 3.4**, the computed base resistance V_b is assigned to the vertical hysteretic element at the base of the caisson, while the ultimate shaft capacity $V_{shaft} = N_{cV,shaft} A S_u = 11.3$ MN is equally distributed to the vertical peripheral elements of the shaft, such that:

$$V_{shaft} = \int_0^L \int_0^{2\pi} \left(f_{max,kz} \frac{D}{2} \right) d\varphi dz = N_{cV,shaft} A S_u \quad (3.12)$$

where: $f_{max,kz}$ is the unit soil reaction of the vertically distributed elements expressed in kN/m², and the angle φ is defined in **Fig. 3.4b**. It should be noted that the vertical truss elements are assigned equal resistance for pull-out and push-down loading, justified by the assumption of full suction beneath the caisson lid. Under pure moment loading (M_o), the failure mechanism is a combination of scoop and wedge-sliding mechanisms, primarily driven by shear and normal stresses at the caisson shaft and the normal stresses developed at the caisson base. The contribution of the base to moment resistance (M_b) is calculated according to Suryasentana et al. [2018], yielding a local moment capacity factor equal to $N_{cM,base} = 0.72$. The shaft resisting moment (M_{shaft}) involves the aggregation of two stress distributions: (i) the moment generated by the vertical shear stresses developed on the shaft ($M_{shaft,y}$); and (ii) the moment generated by the horizontal stresses ($M_{shaft,x}$), which also contribute to the horizontal soil reaction. With $M_{shaft,y} = (\sum f_z) D$ (where $\sum f_z = V_{shaft}/2$) the capacity of the vertically distributed hysteretic elements ($f_{max,kz}$) is computed so that:

$$M_{shaft,y} = \int_0^L \int_0^{2\pi} \left(f_{max,kz} \frac{D^2}{4} \right) d\varphi dz = N_{cM,shaft,y} A D S_u \quad (3.13)$$

The remaining shaft moment capacity ($M_{shaft,x} = M_{shaft} - M_{shaft,y}$) is provided by the horizontally distributed hysteretic elements ($f_{max,kx,n}$ and $f_{max,kx,s}$).

Under pure lateral loading (H_o), the failure mechanism is the combination of a (broader) wedge-sliding mechanism above the skirt-tip level and a scoop mechanism beneath the skirt-tip level. Following the study of Suryasentana et al. [2018], similar values of lateral resistance per meter of length are assigned to the base (H_b) and shaft (H_{shaft}) elements. The horizontal shaft reaction is the resultant of two stress distributions: the passive and active pressures developed on the two sides perpendicular to the loading direction ($H_{shaft,n}$), and the

horizontal shear tractions on the sides parallel to the loading direction ($H_{shaft,s}$). Activation of 70% of the lateral frictional resistance ($H_{shaft,s} = S_u \times \pi DL/2$) is assumed in the case of pure horizontal loading, based on the results of the 3D FE analyses. The remaining lateral capacity is assigned to the distributed horizontal hysteretic elements of the shaft and the concentrated base element in a uniform manner so that:

$$H_{shaft,n} = \int_0^L \int_0^\pi \left(f_{max,kx,n} \frac{D}{2} \right) d\varphi dz = N_{cH,shaft,n} AS_u \quad (3.14)$$

$$H_{shaft,s} = \int_0^L \int_0^\pi \left(0.70 f_{max,kx,s} \frac{D}{2} \right) d\varphi dz = N_{cH,shaft,s} AS_u \quad (3.15)$$

where: $f_{max,kx,n}$ and $f_{max,kx,s}$ are the sought values of ultimate soil reactions of the horizontally distributed hysteretic elements (normal and frictional, respectively), expressed in kN/m².

The computed local capacity factors for all model elements for the problem studied herein are summarized in **Table 3.4**. It should be noted that for $L/D > 1$, the failure mechanisms for H_o or M_o are expected to change [Fu et al., 2017], and therefore, the local capacity factors presented herein will no longer be valid. Moreover, the pure horizontal and moment capacities are affected by the presence of vertical load V : the larger the vertical capacity ratio (V/V_o), the lower the resulting H_o and M_o capacities. However, the values of H_o , M_o corresponding to $V = 0$ remain approximately valid for $V/V_o \leq 40\%$, as indicated by Yun & Bransby [2006], and Gouvernec & Barnett [2011]. In the current study of combined wind and earthquake (W+E) loading, the static wind action leads to $V/V_o = 0.25$ for the critical leeward caisson, and therefore, the effect of V can be ignored in $H - M$ calculations. In the case of $V/V_o > 40\%$, readers are referred to Gouvernec & Barnett [2011] to quantify the effect of V on H_o , M_o .

Table 3.4. Best-fit local capacity factors assigned to the CWS model elements.

Global	Local Uniaxial Capacity Factors		
N_{cV}	$N_{cV,base} (V_b)$	$N_{cV,shaft} (V_{shaft})$	
10.32*	6.32	4.00	
N_{cH}	$N_{cH,shaft,s} (H_{shaft,s})$	$N_{cH,shaft,n} (H_{shaft,n})$	$N_{cH,base} (H_b)$
6.15	1.41	4.37	0.37
N_{cM}	$N_{cM,base} (M_b)$	$N_{cM,shaft,x} (M_x)$	$N_{cM,shaft,y} (M_y)$
3.95	0.72	1.23	2.00

* at $w = 0.01D$.

3.4. CWS vs. detailed 3D FE models: Comparison of performance

This section aims to assess the performance of the proposed CWS model, using the rigorous 3D FE model as a benchmark. The models are initially compared in terms of uniaxial and coupled monotonic horizontal–moment response, being subsequently tested in terms of seismic deformation predictions. The section offers below an overview of the ensemble of FE models employed in the analyses to assist the readers' understanding. More specifically, four models are utilized (two spring models and two rigorous 3D FE models), hereafter termed as:

- a. Single CWS model (**Fig. 3.5a**)
- b. Global CWS model (**Fig. 3.5b**)
- c. Single 3D FE model (**Fig. 3.1a**)
- d. Global 3D FE model (**Fig. 3.2a**)

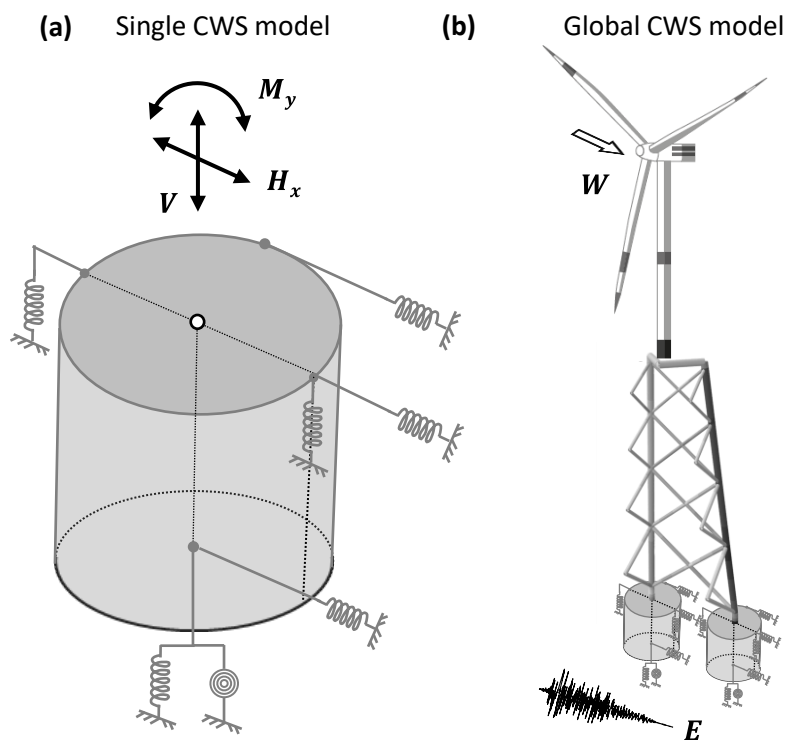


Figure 3.5. Simplified model configurations used in the comparison of the CWS model to the rigorous 3D FE model: (a) the single CWS model, and (b) the global CWS model.

Uniaxial capacities & H–M failure envelope

Figure 3.6 compares the single CWS model to the single 3D FE model (used as a benchmark) under (a) vertical, (b) horizontal, and (c) moment loading, confirming the efficiency of the

calibration procedure in terms of uniaxial capacities. **Figure 3.7** extends the comparison in the $H-M$ space. The displacement-controlled probe tests conducted with the 3D model match very well the normalised $H-M$ failure envelope ($V/V_o = 0$) of Suryasentana et al. [2018], further confirming its validity (**Fig. 3.7a**). The CWS model predictions are excellent in the first quadrant of the $H-M$ space, where the applied H, M loads share the same sign. However, the model fails to reproduce the failure envelope on the second quadrant, exhibiting a clear cut-off of the horizontal caisson capacity at H_o . This is hardly a surprise, as the model was calibrated based on H_o, M_o capacities, aiming to realistically capture the response on the 1st quadrant, where the examined ($W+E$) loading scenarios occur. Finally, **Figs. 3.7c** and **3.7d** present the good comparison of the single CWS model to the single 3D FE model for three $H-M$ load paths, corresponding to M/H ratios expected for the leeward suction caisson of the examined jacket OWT, due to environmental loading.

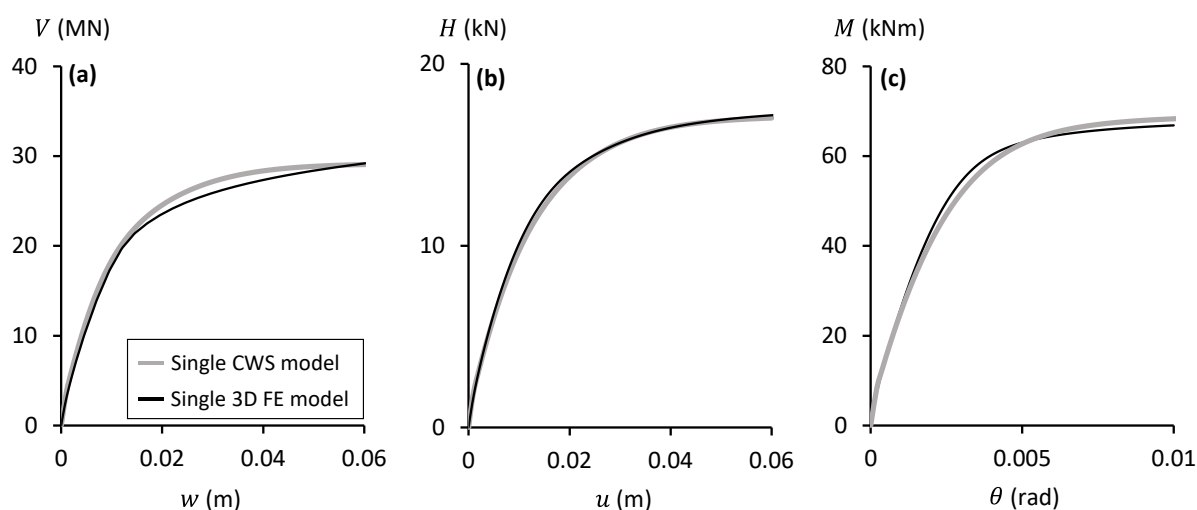


Figure 3.6. Simplified model configurations used in the comparison of the CWS model to the rigorous 3D FE model: (a) the single CWS model, and (b) the global CWS model.

Seismic deformation predictions

The proposed CWS model is tested herein for its ability to reproduce the foundation deformations of a jacket OWT under transient irregular VHM loading. The latter is generated by the combined action of a steady wind force at the nacelle level (70% of the SLS wind thrust at Normal Sea state) and seismic excitation. The IT.AC.V record (2009 L'Aquila earthquake) and

the Tabas-LN record (1978 Tabas earthquake) are used as seismic excitation, referred to hereafter as Scenarios 1 and 2, respectively (Fig. 3.8).

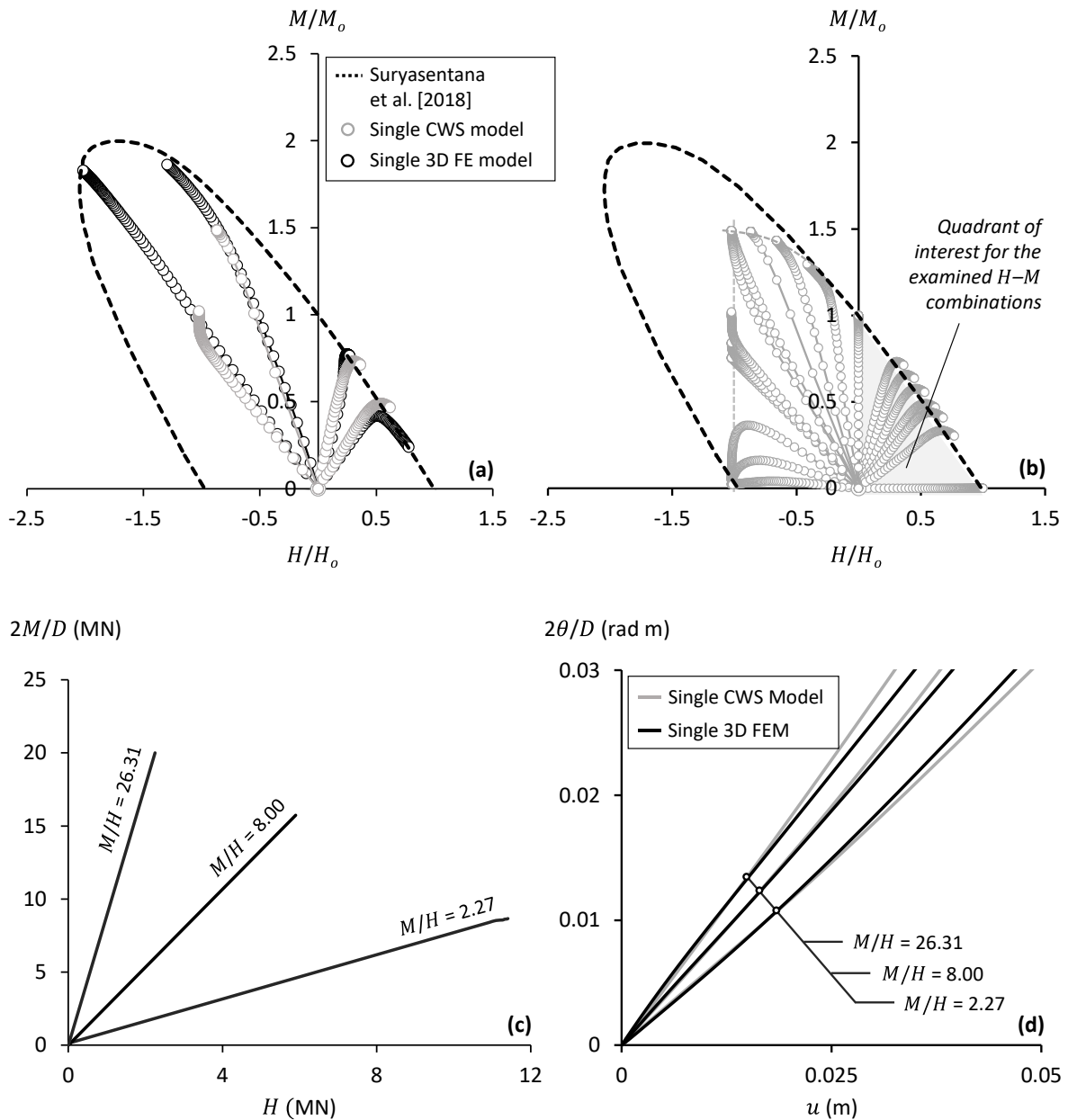


Figure 3.7. Comparison of the single CWS model against the single 3D FE model in the $H-M$ space: (a) displacement-controlled probe tests ($V/V_o = 0$), compared to the $H-M$ failure envelope of Suryasentana et al. [2018]; (b) CWS model failure envelope ($V/V_o = 0$), (c) examined $M-H$ load-controlled paths; and (d) single CWS vs. 3D FE model response for the examined load-controlled probe tests.

Two comparisons are performed, and the results are presented in **Fig. 3.9** and **Fig. 3.10**:

- Two caissons, represented by the single CWS model and the single 3D FE model, are subjected to identical $V - H_x - M_y$ time histories at their heads. The applied loads correspond to the inertial forces acting at the leeward leg of the jacket, calculated through structural analysis of the above-ground system under wind and earthquake loading.
- The global CWS and 3D FE systems of the SBJ wind turbine are subjected to combined wind and earthquake loading.

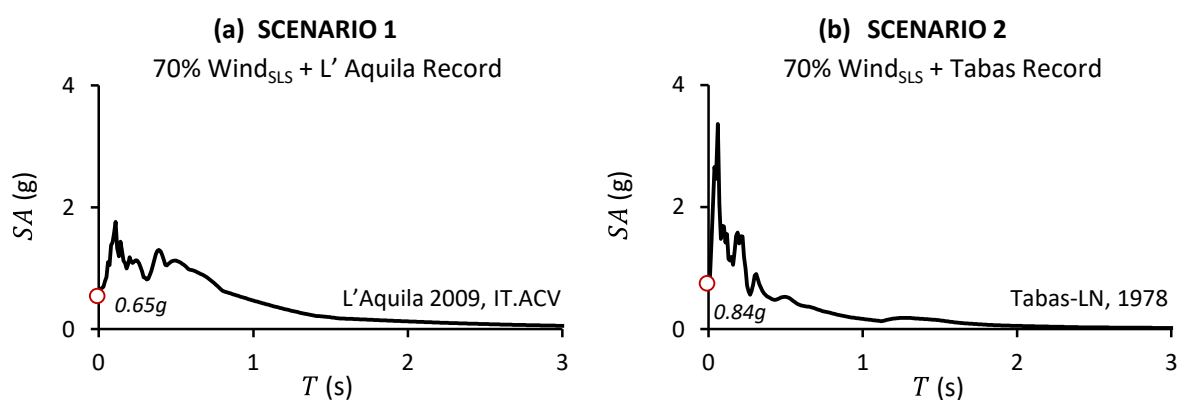


Figure 3.8. Seismic excitation scenarios for the comparison of the CWS models to the detailed 3D FE models in terms of seismic deformation predictions.

The following observations are worthy of note:

- When the single caisson is subjected to external loading (attributed to the inertial loading of the jacket), the performance of the CWS model (against the rigorous single 3D FE model) is excellent, both in terms of accumulation rate and permanent deformation (**Fig. 3.9**). The CWS model successfully reproduces all the key nonlinear and dynamic characteristics of the simulated caisson in both scenarios, while effectively reducing the average computational time by almost two orders of magnitude (80 times). The strong coupling between settlement and accumulation of rotation is worth noting: large vertical loads (V) push the sidewall k_z elements into their post-yield regime, leading to plastic deformations along the shaft. These are ultimately responsible for a non-trivial accumulation of caisson rotation (θ) during strong earthquake shaking. Under inertial VHM loading, the single 3D FE model produces significantly lower caisson deformations

compared to the global 3D FE model under combined wind and earthquake loading (benchmark simulation). The reasons behind such discrepancy are revisited later on in Section 5.

- ii. The global CWS model underpredicts the seismically accumulated settlements of the leeward leg for both earthquake scenarios. For example, the CWS model predicts a 20 mm residual settlement at the leeward leg after the Tabas (1978) earthquake when the actual value (derived by the global 3D FE model) is 50 mm. The reason behind this poor performance is the distinctive stressing combination generated by the concurrent action of wind and earthquake loading (which was not present in the previous comparison, where the loading was externally applied). Here, the foundation of the jacket is subjected to combined loading, stemming on the one hand from soil shearing due to the propagating earthquake waves (*kinematic* loading) and shearing due to the *inertial* loading of the superstructure. Not surprisingly, such a dual-shearing mechanism cannot be captured by the global CWS model, where the stressing of the horizontal k_x elements (due to the seismic excitation) is entirely uncorrelated to the stressing of vertical k_z elements. The subsequent section will provide a detailed presentation of this distinctive accumulation mechanism. On the other hand, the rotation and displacement predictions of the global CWS model are satisfactory. The CWS simulation competently captures the settlement-rotation coupling (as already discussed) while being sensitive to the seismic wave propagation effects responsible for non-uniform acceleration distribution along the caisson skirt, which also affects the ultimately developing deformations. In the specific example, due to this very effect, the rotation θ_c of the leeward caisson is increased to 1.2 mrad, while the horizontal displacement u_c to 4 mm during the Tabas 1978 event (compared to the 0.65mrad and 2.4 mm of **Fig. 3.9**, respectively).

In a nutshell, the proposed CWS model is shown to be appropriate for analysing the foundation response of SBJ OWTs under any combination of externally applied environmental loading (wind/waves time-histories applicable to power production or idling load cases of OWTs). When it comes to the seismic performance of SBJ OWTs, the CWS may be used for estimating rotations and displacements at the caisson level. However, it is not recommended for assessing the co-seismic settlements of the caissons (and hence the global rotation of the

jacket frame). In this regard, the following section explores in greater detail the mechanism of co-seismic settlement accumulation and proposes an engineering-based methodology for diagnosing the severity of its impact on OWT performance.

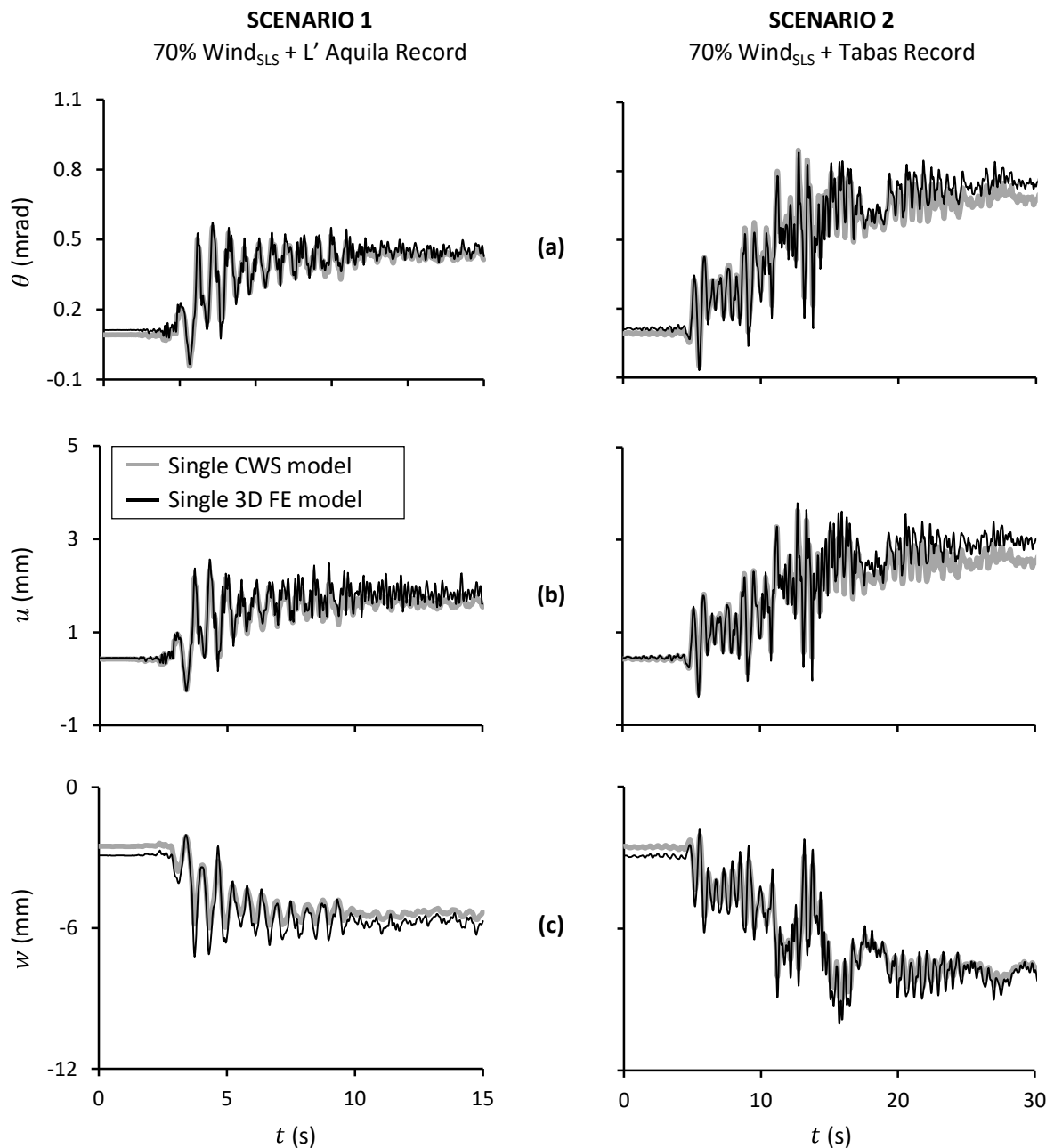


Figure 3.9. Comparison of the single CWS and 3D FE models for Scenarios 1 and 2. Time histories of: (a) caisson rotation θ ; (b) caisson horizontal displacement u ; and (c) caisson settlement w .

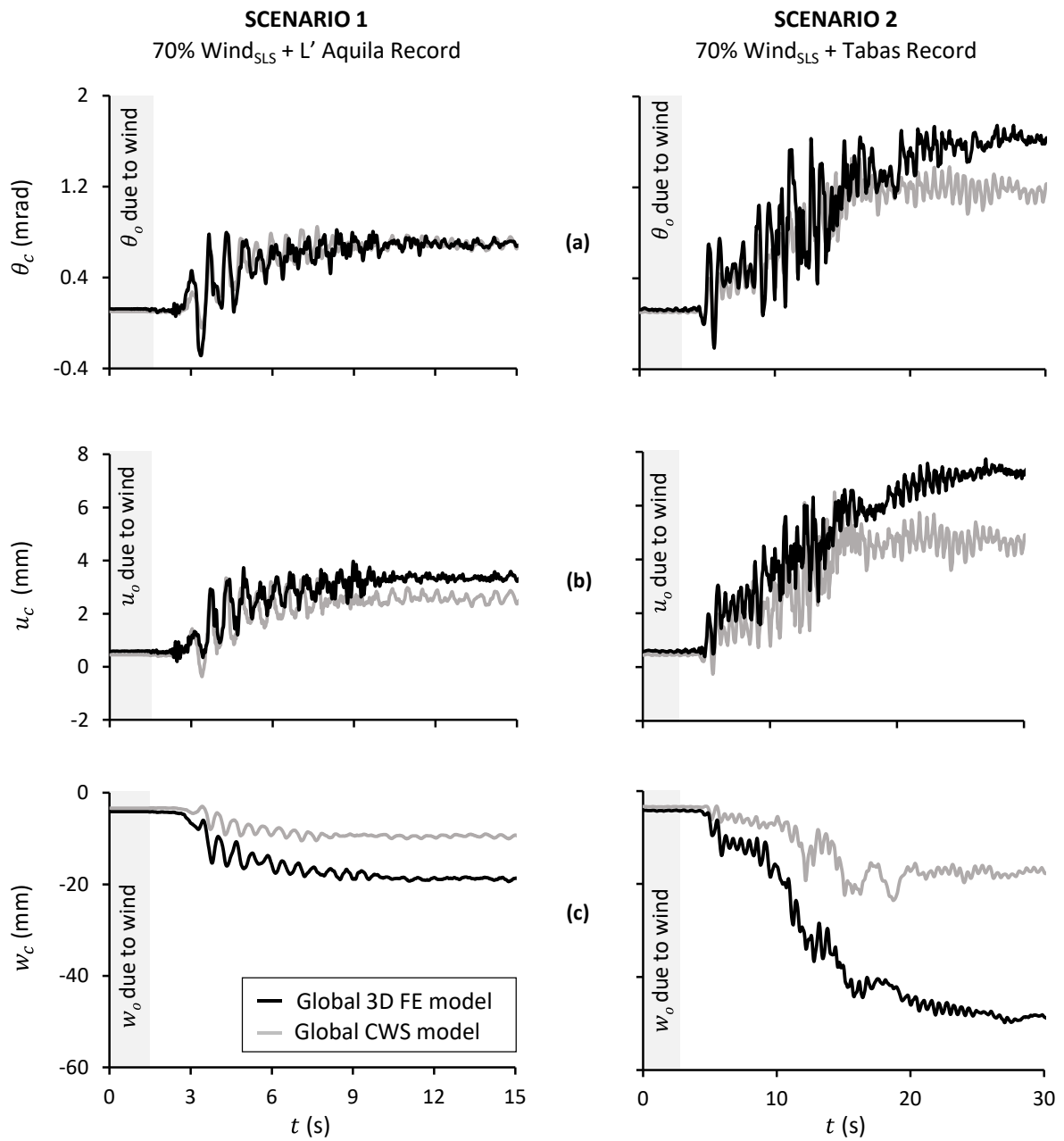


Figure 3.10. Comparison of the global CWS and 3D FE models for Scenarios 1 and 2. Time histories of: (a) leeward caisson rotation θ_c ; (b) leeward caisson horizontal displacement u_c ; and (c) leeward caisson settlement w_c .

3.5. Co-seismic caisson settlements

Generation mechanism

As highlighted in the previous discussion, seismically excited caissons may experience increased settlements that exceed those experienced in non-seismic load cases. To illuminate the factors contributing to this striking deformation pattern, we analyze herein the single 3D FE model under two alternative loading scenarios (**Fig. 3.11**):

- Caisson bearing an initial static load of $V_w = 9.2\text{MN}$ is subjected to seismic shaking (applied at the model base), idealized by a Tsang-type pulse (a modulated sinusoid) having a predominant frequency of $f_E = 1.5\text{Hz}$ and peak acceleration $a = 0.4g$.
- Caisson bearing the same initial static load V_w is subjected to dynamic cyclic loading $V_{dyn}(t)$ of frequency $f_E = 1.5\text{Hz}$, applied at the caisson head. The amplitude of V_{dyn} is appropriately chosen to result in the same level of shear stress and strain as the seismic excitation (at the soil elements of the caisson shaft).

The results are shown for two characteristic elements in the middle of the caisson shaft, one on the left (1) and a second (2) on the right (**Figs. 3.11a; 3.11b**). As evidenced by the stress-strain loops of **Fig. 3.11c**, the two loading scenarios are equivalent in shear stresses and shear strains at these representative locations.

Figure 3.12 compares the two loading scenarios in terms of shear strain (γ_{xz}) time histories at the two characteristic soil elements (**Fig. 3.12a**), shear strain contours (**Fig. 3.12b**), and caisson settlement time histories (**Fig. 3.12c**). To focus on the dynamic (cyclic or shaking) part of the response, the shear strains imposed by the initial vertical load V_w have been subtracted from the respective time-histories and contour plots of **Fig. 3.12**. Although the caisson is subjected to the same level of γ_{xz} there is a distinctive difference between the two loading scenarios (**Fig. 3.12a**). The time history of γ_{xz} of the two soil elements is identical in the case of cyclic loading, which is not the case for the seismic scenario where the two elements demonstrate a phase shift in their response. This difference is further elucidated when comparing the shear strain contours of **Fig. 3.12b**. Once again, during cyclic loading, the two elements can be seen to sustain symmetric straining for the cyclic loading scenario: at times t_1 and t_2 (corresponding to a positive and a negative peak of V_{dyn}), the two elements experience the same shear strain ($\gamma_{V,1} = \gamma_{V,2}$). The vertical displacement of the caisson is

directly correlated to the direction of the imposed cyclic load V_{dyn} . When $V_{dyn} < 0$ (pull out) the caisson settles, moving back upwards when $V_{dyn} > 0$ (compression). As shown in **Fig. 3.12c**, this leads to the accumulation of settlement only when the caisson is subjected to compressive V_{dyn} .

In the shaking scenario, the developing shear strains γ_{xz} are due to the coupled effect of shearing γ_V caused by the vertical static load V_w , and shearing γ_E due to the vertically propagating shear waves. At $t = 0$ (initiation of shaking), the two elements display the same shearing due to vertical loading ($\gamma_{V,1} = \gamma_{V,2}$). However, at $t = t_1$, the kinematically induced (by the propagating shear waves) shear strain mandates an anti-symmetric deformation pattern (**Fig. 3.12b**, bottom): the shear strain of element 1 (left) is reduced, while that of element 2 (right) is increased: $(\gamma_V + \gamma_E)_1 < (\gamma_V + \gamma_E)_2$. The opposite pattern is observed at $t = t_2$. As a result, the two opposite sides of the caisson (left and right) experience different shear stress at any time t , as imprinted in the observed phase difference of γ_{xz} (**Fig. 3.12a**). This leads to a ‘rocking’ response of the caisson, which leans towards the left or the right during subsequent acceleration cycles, thereby accumulating settlement both for negative and positive loading peaks. As a result, a pronounced difference appears in the accumulated settlement, which reaches $w = 17$ mm for the shaking scenario, as opposed to $w = 4$ mm for cyclic loading (**Fig. 3.12c**).

Naturally, the rate of settlement accumulation will depend (among other factors) on the specific characteristics of the excitation (i.e., its amplitude and frequency content) and the mean (V_w) and maximum value of the bearing load of the caisson V_{dyn} . These very effects are further elaborated in the remaining part of Section 3.5. The following subsection demonstrates the effect of the non-constant vertical load on the mechanics of seismic settlement accumulation, while ‘*The effect of earthquake motion variability*’ considers the seismic performance of a single caisson under multiple earthquake records (assuming that all other model parameters remain constant) and investigates the correlation of maximum permanent settlement to characteristic ground motion parameters.

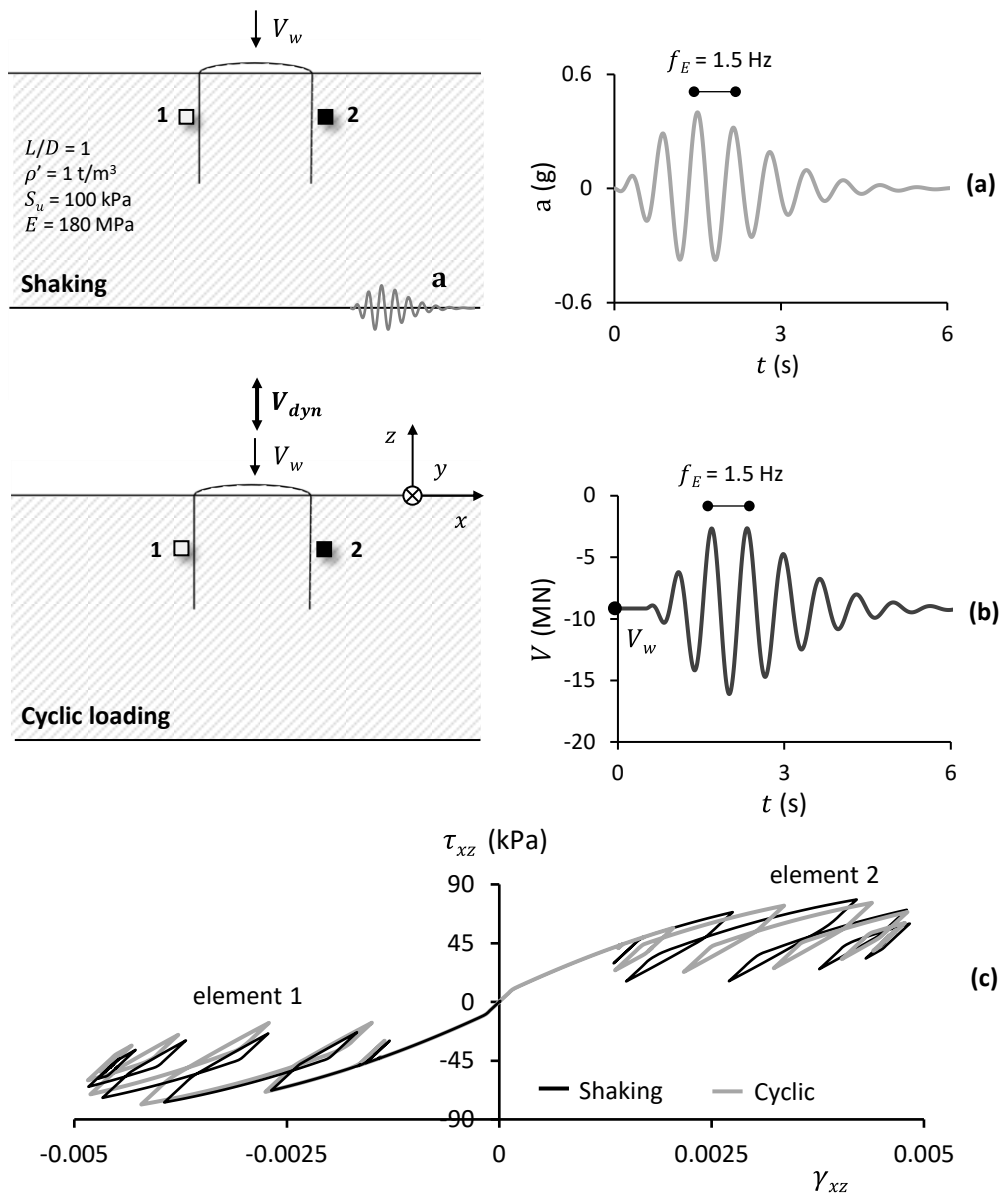


Figure 3.11. Investigation of mechanisms controlling the seismic response of caissons in clay: (a) the shaking scenario, (b) the cyclic scenario, and (c) comparison of shear stress – shear strain loops at two characteristic soil elements (1 and 2).

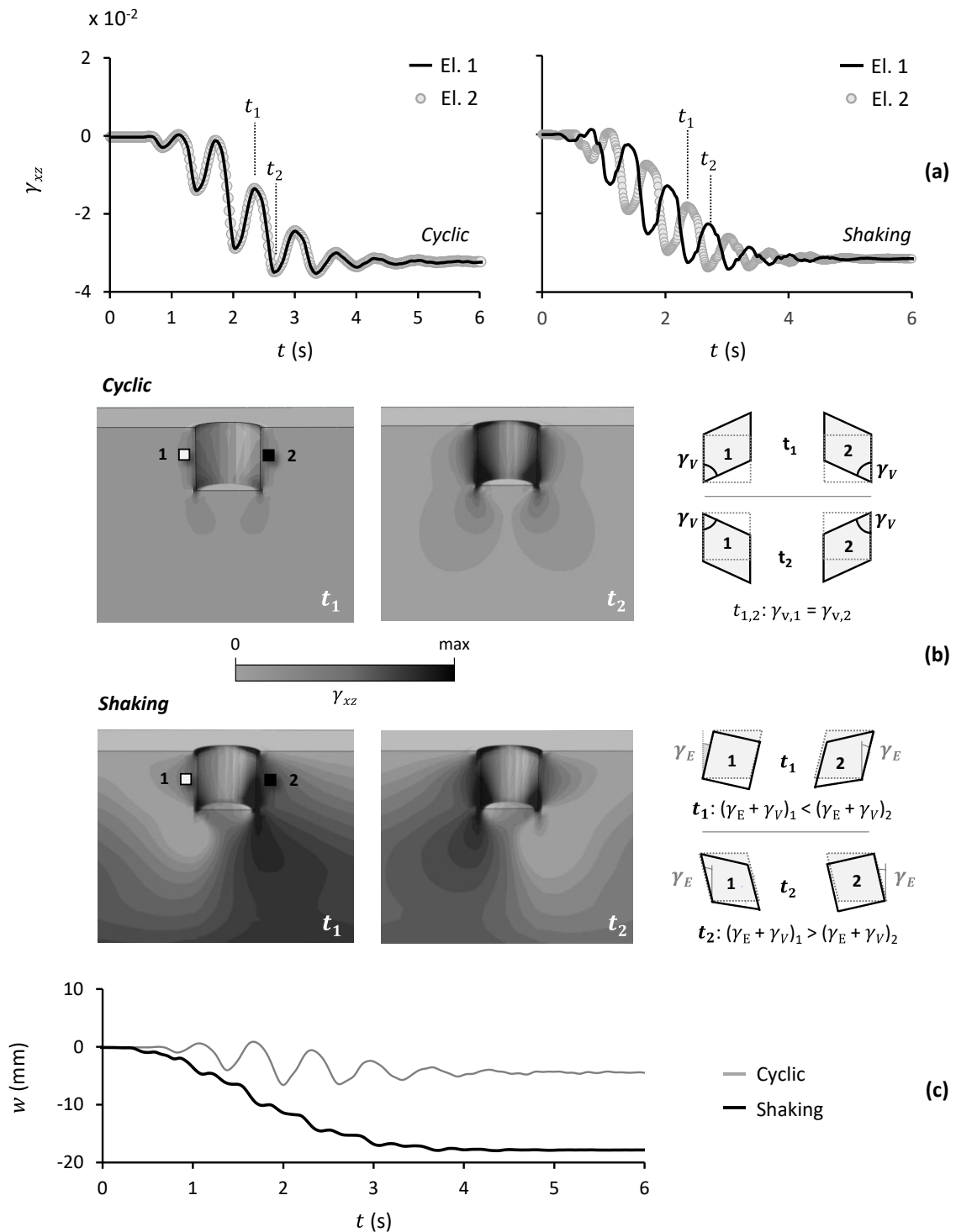


Figure 3.12. Comparison of cyclic loading to seismic shaking scenarios in terms of: (a) shear strain (γ_{xz}) time histories at two characteristic soil elements (1 and 2); (b) shear strain contours at times t_1 and t_2 , along with a schematic illustration of the shearing mechanism at caisson sides; and (c) caisson settlements.

The effect of non-constant V

In the previous section, it was tacitly assumed that, simultaneously with the seismic loading (shaking scenario), the caisson is subjected to a constant axial load V_w that corresponds to the load acting on the leeward leg of the jacket due to wind loading (W). In reality, however, the axial forces developing on the jacket legs during shaking are not constant. A preliminary set of 3D FE analyses was therefore performed to quantify the effect of non-constant V on the caisson settlement (**Fig. 3.13**). To this end, the settlement computed using the global 3D FE model under combined ($W + E$) loading is compared to the single 3D FE model subjected to the same seismic excitation but assuming a constant vertical load V_w .

The comparison is performed for medium (L'Aquila 2009) and large-intensity shaking (Takatori, Kobe 1995). In **Fig. 3.13a**, the results are shown for the L'Aquila record combined with an increased wind thrust $1.2W_{SLS}$ (i.e., exceeding SLS by 20%), generating a ratio of maximum seismic axial load to initial vertical load $V_{max}/V_w = 1.6$ (while $V_w = 9.16 \text{ MN}$). The assumption of constant vertical load V_w leads to an appreciable underestimation of the settlement w by 23%. The same wind load, combined with the stronger Takatori record, yields $V_{max}/V_w = 1.7$ and to a slight increase of the underestimation of w by 25% (**Fig. 3.13b**). The same seismic excitation (Takatori) combined with a reduced wind load $0.7W_{SLS}$ ($V_w = 7.07 \text{ MN}$), yields an increased $V_{max}/V_w = 1.86$ and much smaller underestimation of w by a mere 5% (**Fig. 3.13c**). It may, therefore, be concluded that the underestimation of settlement is mainly related to the value of V_w , and to a lesser extent, to V_{max} .

The effect of earthquake motion variability

It is generally accepted that the seismic performance (also referred to as damage potential) of nonlinear systems is strongly dependent on the earthquake excitation's particular characteristics, commonly referred to as Intensity Measures (IMs). To name a few: the frequency content, the maximum acceleration, the duration, and the important cycles of the excitation will eventually determine the level of accumulated settlement. As a result, attempting to correlate damage potential with any single IM introduces significant uncertainty [Padgett et al., 2008; Garini & Gazetas, 2013]. Correlations may be improved when combining different IMs. For example, Anastasopoulos et al. [2015] and Sakellariadis et al. [2018] successfully correlated seismic performance indices of motorway bridges with statistically significant IMs, combining FE simulations with advanced econometric modelling.

Similarly, in Marin et al. [2019], the correlation between input motions and co-seismic displacements of slopes was shown to be markedly improved by matching the relative significant duration (RSD), the Arias Intensity (I_A), and the spectral acceleration (SA) to characterize and select input motions.

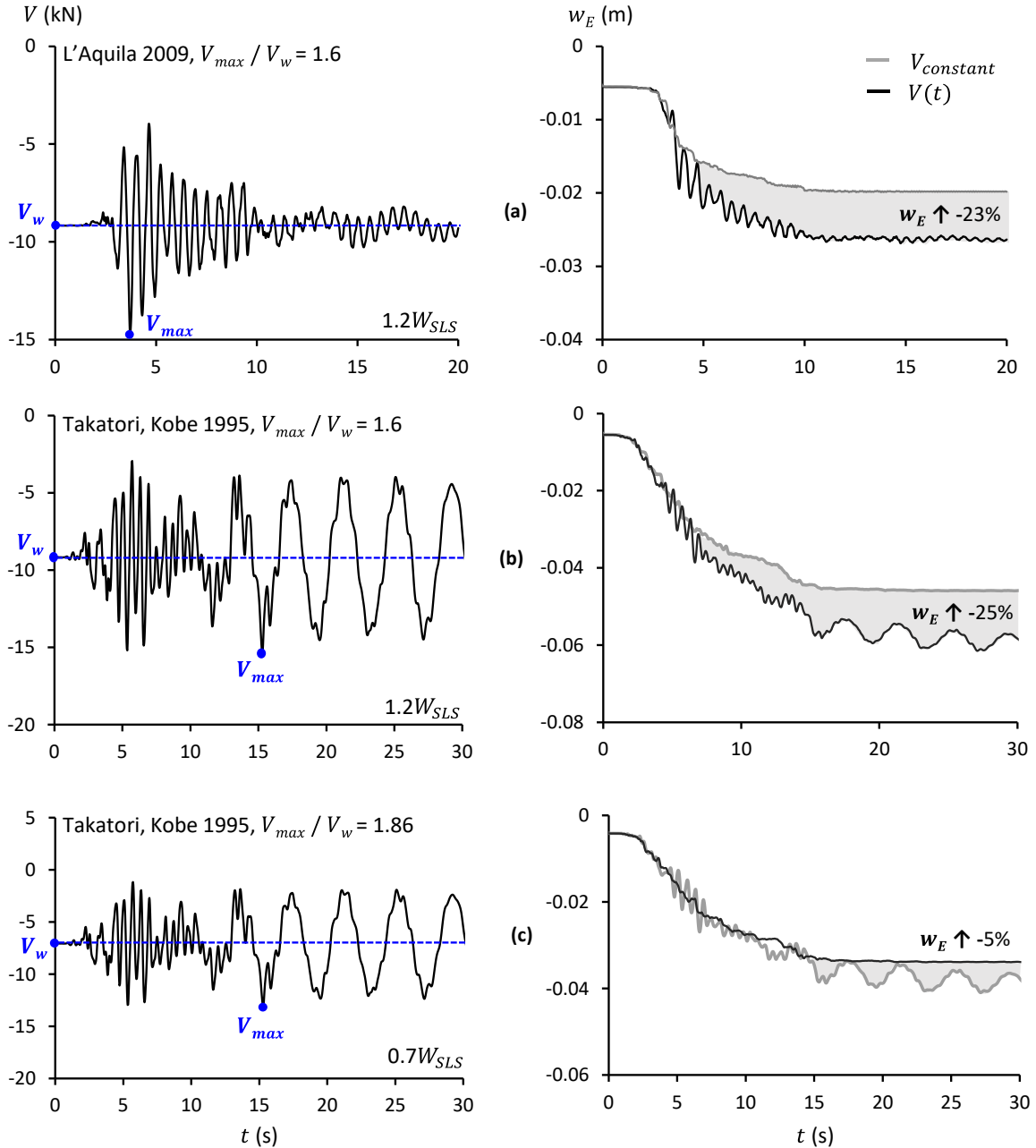


Figure 3.13. Comparison of settlement time histories (w_E) for constant vertical load $V = V_w$ to those of the global 3D FE model (non-constant V): (a) medium-intensity shaking (L'Aquila 2009) with $V_{max}/V_w = 1.6$ ($0.7W_{SLS}$); (b) large-intensity shaking (Takatori, Kobe 1995) with $V_{max}/V_w = 1.7$ ($1.2W_{SLS}$); and (c) the same excitation but with $V_{max}/V_w = 1.86$ ($0.7W_{SLS}$).

Building on these findings, the current study employs a similar deterministic approach based on FE modelling to assess the efficacy of a double-parameter correlation for the estimation of the seismic settlement of caissons in which the first parameter is a targeted site response spectrum and the second, the Arias Intensity. For demonstration purposes, the single 3D FE model is here excited by an ensemble of input motions (derived from real parent accelerograms) that have been pre-processed to match a reference spectrum: the EC8 Type Soil-C design spectrum assuming peak ground acceleration $PGA = 0.35$ g. An initial static load V_w is applied to the model prior to seismic shaking. The geometry and material parameters of the single 3D FE model are modified in this section to correspond to an example $L = D = 4.5$ m caisson, founded on a uniform clay stratum of $S_u = 75$ kPa and $E_o = 134.5$ GPa. The computed permanent seismic displacements are plotted against the Arias Intensity (I_A) of the respective matched motions to derive a linear correlation.

Parent accelerograms

The ensemble of 22 real accelerograms is selected from international ground motion databases (e.g., the PEER Strong Ground Motion Databases¹⁰). **Table 3.5** summarizes their key characteristics, including the moment magnitude (M_w), Peak Ground Acceleration (PGA) and soil type according to EC8. The rationale behind the records' selection is two-fold:

- Ground motions recorded on similar site conditions as the design earthquake were preferred (soil type B or C) to allow compatibility with the spectrum.
- The selected motions are intended to cover a wide range of frequency content (especially in the period range $T = 0.01 - 4$ s) to allow for the smooth application of Method B, which requires the median spectrum to fit the target EC8 spectrum without a change in the motions' frequency content.

Two different matching strategies have been implemented to derive spectrum-compatible input motions:

Method A: One-by-one spectrum matching (Fig 3.14a): Spectrum-compatible input motions across the entire range of periods $T = 0.01 - 4$ s are produced, either by generating artificial waveforms based on published intensity envelopes [Hou, 1968; Liu, 1969; Saragoni & Hart,

¹⁰ <https://peer.berkeley.edu/peer-strong-ground-motion-databases>

1973] or through direct mathematical manipulation of real records in the frequency domain. In the second case, the physical characteristics of the seismic motion (e.g., number of cycles) are retained, rendering the technique more appealing than artificial motion generation. The SeismoMatch software is used to produce the spectrum-compatible records of Method A [Seismosoft, 2020]. The application adjusts accelerograms to match a specific target response spectrum using the algorithm proposed by Al Atik & Abrahamson [2010].

Table 3.5. Key characteristics of the selected ground motions.

Record No.	Event	Station	M_w	Soil Type	PGA (g)	Method B scaling factor
1	San Salvador, US, 1986	NGI (180)	5.7	C	0.392	1.5
2	Northridge, US, 1994	Jensen (292)	6.7	B	0.424	1.6
3	Kocaeli, Turkey, 1999	Yarimca (060)	7.4	B	0.268	2.0
4	Loma Prieta, US, 1989	Gilroy #2 (000)	6.9	C	0.367	2.0
5	Loma Prieta, US, 1989	Treasure Island (000)	6.9	C	0.0855	4.0
6	San Fernando, California, US, 1971	Pacoima dam (254)	6.6	B	1.160	0.6
7	Tabas, Iran, 1978	Tabas	7.4	B	0.836	0.5
8	Lefkada, Greece, 2003	Lefkada (Long. Dir.)	6.2	C	0.348	1.6
9	Kobe, Japan, 1995	Takatori (000)	6.9	C	0.611	1.0
10	Imperial Valley, El Centro, US, 1940	El Centro (270)	6.9	C	0.215	2.4
11	Erzincan, Turkey, 1992	Erzincan (Station 95)	6.7	C	0.481	0.6
12	Lytle Creek, US, 1970	Wrightwood - 6074 Park	5.3	B	0.143	0.7
13	Northern Calif-03, US, 1954	Ferndale City Hall	6.5	C	0.162	0.7
14	Superstition Hills-02, US, 1987	El Centro Imp. Co cent.	6.5	C	0.340	0.8
15	Whittier Narrows-01, US, 1987	Brea Dam	6.0	B	0.171	0.7
16	Morgan Hill, US, 1984	Anderson Dam	6.2	B	0.416	0.6
17	Irpinia, Italy, 1980	Brienza	6.9	B	0.175	2.0
18	Laquila, Italy, 2009	IT.ACIV	6.3	B	0.657	1.0
19	Friuli 3 rd Shock, Italy, 1976	E.FRC	6.5	B	0.332	1.7
20	Emilia-Romagna, Italy, 2012	Mirandola	6.1	C	0.264	1.2
21	ChiChi, Taiwan, 1999	TCU052	7.7	C	0.350	1.2
22	Iquique, Chile, 2014	GO01	8.2	B	0.361	1.2

Method B: Median spectrum match (Fig. 3.14b): Although Method A is widely used in practice, the motions generated through one-to-one spectrum matching are often criticized for being unrealistic. Since the design spectrum represents an envelope of possible spectral accelerations rather than an actual seismic event, one-to-one spectrum matching leads to a distorted frequency content. For this reason, performance-based assessment methods (e.g.,

ATC-58) often require a more realistic description of the seismic excitation. This requirement is met by Method B, which aims to match the response spectrum on average while preserving the frequency content and the physical characteristics of each of the original motions. This may be considered a more natural process, mimicking the way the design spectra have been developed. In this simpler approach, a set of seismic records is scaled one by one only in terms of amplitude without altering their frequency content. The procedure involves several iterations (performed in Excel VBA environment), where the scaling factors are readjusted until the best fit of the median to the target spectrum is obtained (i.e., the residual between the median and the target spectrum is below a pre-specified limit.). The scaling factors that resulted in the best fit of the median to the target spectrum during the amplitude-based scaling of Method B are tabulated in **Table 3.5**.

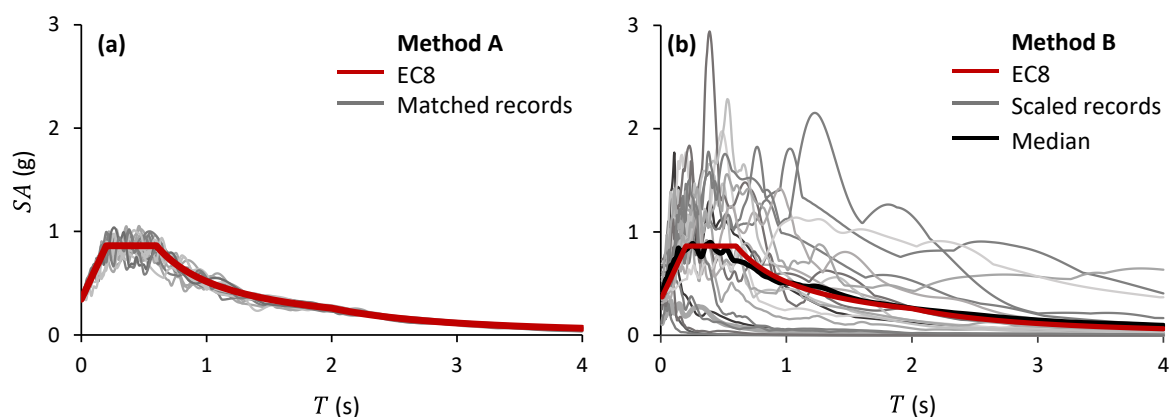


Figure 3.14. Records matching the EC8 design acceleration spectrum (Type C) employing two different approaches: (a) Method A, and (b) Method B.

Seismic settlement – I_A correlation

Figure 3.15 plots the final seismic caisson settlement (w_E) for Method A records against the Arias Intensity I_A (Arias, 1970), which is defined as:

$$I_A = \frac{\pi}{2g} \int a_{ff}(t)^2 dt \quad (3.16)$$

where $a_{ff}(t)$ stands for the acceleration time history at the free field.

It should be clarified that the proposed charts correspond to permanent caisson settlements. The final caisson settlement w_E utilized for the charts' construction corresponds to the summation of incremental settlements Δw occurring during consecutive acceleration cycles.

Such a response is in accordance with the results of the previous subsection (*'Generation mechanism'*), where a single caisson is shown to incrementally accumulate inelastic settlements during subsequent cycles of the idealized Tsang-type excitation.

As shown in **Fig. 3.15**, for the examined EC8-compatible motions ($PGA = 0.35g$), the results fit very well a linear equation of the form:

$$w_E = \beta \times I_A + \delta \quad (3.17)$$

with coefficients $\beta = 0.0036$ and $\delta = 0.0044$. The success of the statistical fit is confirmed by the satisfactory $R^2 = 0.99$.

The linearity observed in the derived regression equations is considered valid for the $w_E - I_A$ range examined herein. The trend is directly correlated with the fact that I_A is proportional to the integral of the squared acceleration $a_{ff}(t)$, meaning that it implicitly incorporates the effect of acceleration amplitude, frequency content, and the number of cycles, which are primarily responsible for the observed accumulation of settlements. Furthermore, the linear trend is also the result of the following:

- The undrained shear strength S_u and rigidity ratio E_o/S_u of the clay stratum are constant variables in the examined problem. The resulting expressions would entail a level of nonlinearity in the case of sand materials that experience densification or sensitive clays that experience cyclic degradation phenomena.
- The soil-caisson seismic response is essentially symmetric, i.e., an identical response is expected in both loading directions during the applied seismic SV waves. The derived linear correlations would probably be less successful (i.e., having a lower correlation coefficient) in the case of systems with non-symmetric response, such as retaining walls or slopes.

Data points using Method B are also plotted in the same figure (black dots). It is interesting to note that, although the caisson is subjected here to 22 seismic motions of different PGA , frequency content and number of cycles, the linear correlation between w_E and I_A is essentially maintained. A new (not identical, but similar) linear regression equation is derived for Method B ($\beta = 0.0028$ and $\delta = 0.0044$), yielding $R^2 = 0.94$. The statistical correlation is lower than the one of Method A, but the same data points (22 motions) now span over a larger range of I_A . It is worth observing that for the common range of I_A (0.1 – 3 m/s), the two

methods yield very similar results, confirming the robustness of the developed prediction equations. The small difference between the two methods suggests that linear regression equations produced with one method can be used to predict the permanent caisson settlement as a function of a combination of I_A and the design spectrum, regardless of the employed spectral matching technique (Method A or B).

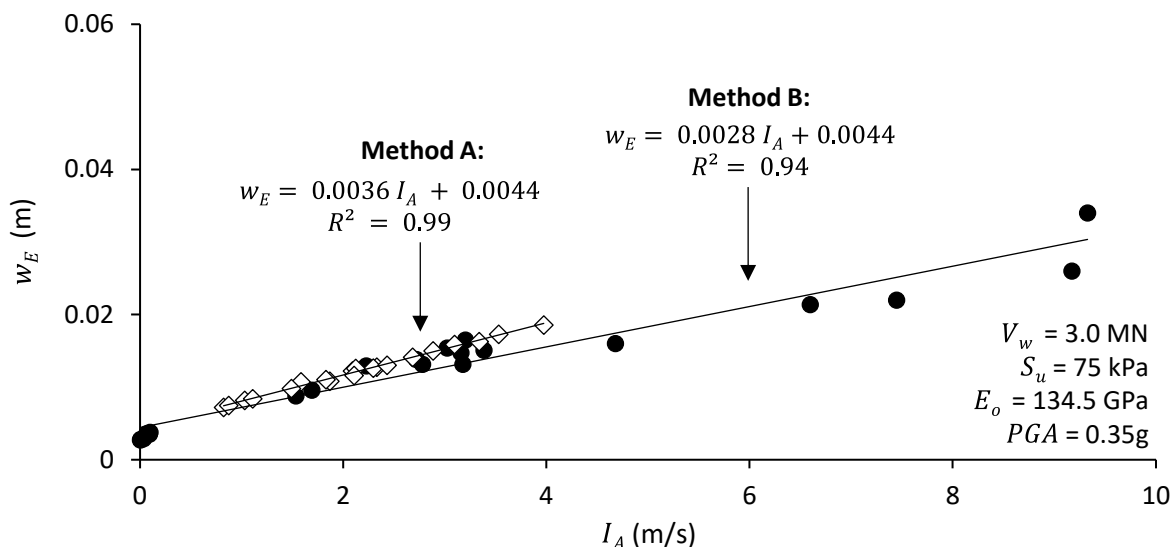


Figure 3.15. Correlation of caisson seismic settlement w_E with the Arias Intensity (I_A): comparison of Methods A and B.

Figure 3.16 offers a close-up of the effect of PGA on the developed linear regression curves. Case 1 in **Fig. 3.16a** corresponds to the results of Method A presented in **Fig. 3.15** (for $PGA = 0.35g$). For Case 2, the same analyses were conducted, but with the seismic motions re-manipulated to match the EC8 spectrum with lower $PGA = 0.24g$. Interestingly, the derived relation between w_E and I_A is insensitive to PGA (**Fig. 3.16a**). This confirms the efficiency of the proposed combination of spectrum matching and I_A in deriving good correlations with caisson settlement w_E . Such a trend is not present when considering other intensity measures instead of I_A , such as the Relative Significant Duration (RSD). The measure is defined as:

$$RSD = \int_0^{\infty} [H(A_r(t) - 0.05) - H(A_r(t) - 0.95)] dt \quad (3.18)$$

where: $H()$ is the Heaviside step function, and $A_r(t) = I_A(t)/I_{A,max}$. The RSD incorporates the effect of motion duration, as it practically indicates the time within which 5 – 95% of the signal's energy/intensity is released. **Fig. 3.16b** indicates that results are sensitive to different

PGA levels when plotted against the RSD , while the statistical significance of linear equations is additionally reduced (lower values of R^2 are observed).

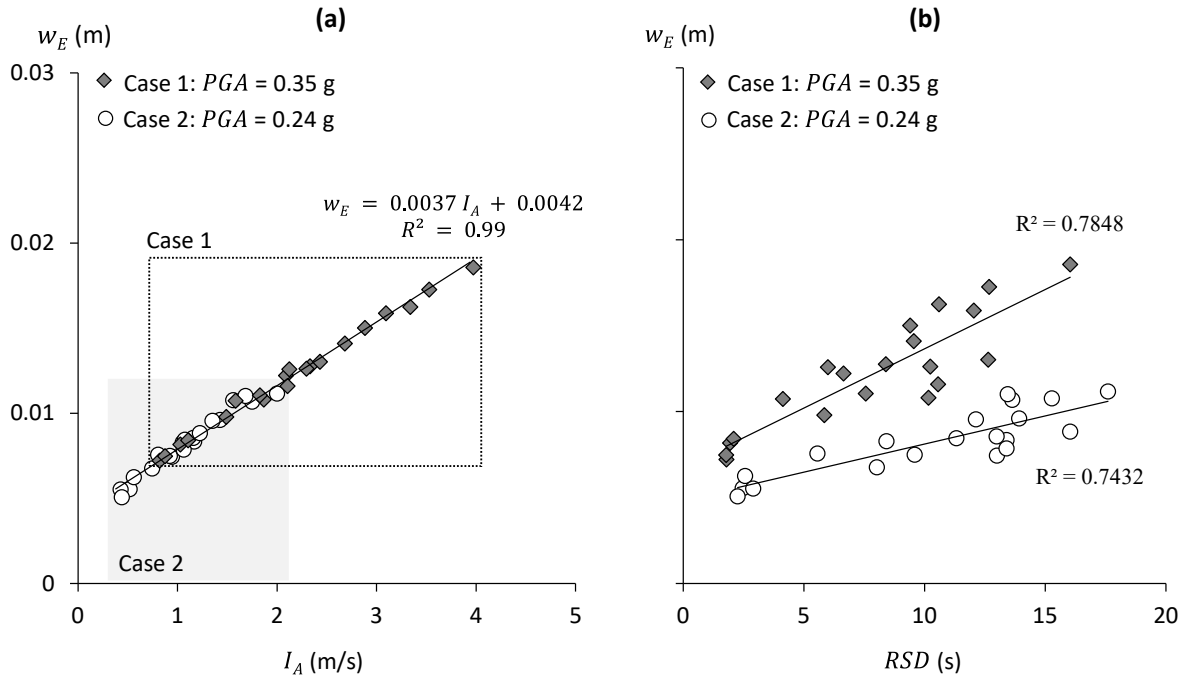


Figure 3.16. Correlation of caisson settlement (w_E) with (a) the Arias Intensity (I_A); and (b) the Relative Significant Duration (RSD) using Method A spectrum-compatible seismic motions: The effect of PGA .

3.6. Simplified approach for the preliminary assessment of permanent seismic settlements in SBJ OWTs

The study attempts to generalize the case-specific findings presented in the previous section and propose dimensionless expressions for the preliminary estimation of seismically induced settlements in various suction caisson configurations. To this end, we first employ a formal dimensional analysis of the caissons' performance in clayey soils to derive families of self-similar problems [Makris & Black, 2004]. Then, for each set of self-similar caisson configurations, we derive a single master line that correlates the Arias Intensity with the dimensional seismically induced settlement of any member of the self-similar family using the methodology of section 'The effect of earthquake motion variability'.

The dimensional problem

The dimensional analysis employs the single 3D FE model subjected to concurrent axial and seismic loading. Under this loading, the caisson settlement is a function of 8 variables:

$$w_E = f(V_w, D, L, S_u, E_o, \rho, PGA, f_E) \quad (3.19)$$

where: PGA and f_E are the peak ground acceleration and mean frequency of the same, arbitrary shape ground motion. The effect of earthquake motion variability on caisson response is introduced later on using the derived linear regression equations. According to the Vaschy-Buckingham Π -theorem of dimensional analysis [Buckingham, 1914], Eq. (3.19) can be re-arranged in (8–3) dimensionless Π -products, where 3 is the minimum number of reference dimensions (length, mass, time) necessary for the description of the physical variables:

$$\frac{w_E}{D} = f\left(\frac{V_w}{S_u D^2}, \frac{L}{D}, \frac{E_o}{S_u}, \frac{f_E}{R}, \frac{S_u}{PGA \rho L}\right) \quad (3.20)$$

where: $R = \sqrt{E_o / \rho D L}$.

Parameters $\frac{E_o}{S_u}$, $\frac{V_w}{S_u D^2}$, $\frac{f_E}{R}$ and $\frac{S_u}{PGA \rho L}$ are hereafter termed soil rigidity ratio, vertical capacity ratio, frequency ratio and soil strength mobilization index. A detailed description and validation of the dimensional formulation may be found in Antoniou et al. [2019].

Response charts

For the derivation of dimensionless settlement charts, the caisson dimensions are varied within a reasonable range for the jacket foundation under consideration, i.e., $L = D = 3 - 9$ m. The examined clay profiles correspond to Soil Type C (i.e., deep deposits of stiff clay with thickness from several tens to many hundreds of meters, according to the EC8 site classification scheme), having undrained shear strength that varies between $S_u = 70 - 250$ kPa while the shear wave velocity is within the range of $V_s = 180 - 360$ m/s. The FE model is excited with the seismic records of Method A, and aggregated results are plotted in **Fig. 3.17** in the form of linear master lines correlating the dimensionless settlement w_E/D with Arias Intensity I_A . Each chart corresponds to a family of self-similar caissons for which the dimensionless variables of Eq. 20 are set equal to predetermined values (that aim to cover a realistic, although not exhaustive, ensemble of possible caisson configurations). Following the discussion of **Fig. 3.16**, which demonstrated that spectrum-compatible records of different PGA may be represented by the same $w_E/D - I_A$ regression formula, in this set of analyses, the strength mobilization index $\frac{S_u}{PGA \rho L}$ is replaced by the non-dimensional $\frac{S_u}{\rho L}$ ratio. It is also

clarified that the charts of **Fig. 3.17** assume constant vertical load V_w acting concurrently with seismic loading to represent the wind-induced bearing load on the supports of the jacket. It is therefore advised that the derived dimensionless settlement is multiplied by a factor $q = 1.1$ to 1.3 (depending on the level of $V_w/S_u D^2$ and the intensity of seismic shaking) to account for the effect of non-constant V_w (as discussed in section 'The effect of non-constant V ').

For this parametric study, we have assumed constant L/D and E_o/S_u ratios, and have parametrically investigated the effect of the remaining three dimensionless variables within the following applicable range:

- L/D , the embedment ratio, is set equal to 1 (which corresponds to the most typical caisson configuration for multi-pod installations)
- E_o/S_u , the soil rigidity ratio, is assumed equally to 1800 (which is a typical rigidity ratio for stiff clay profiles)
- $V_w/S_u D^2$, the mean vertical capacity ratio, varies between 2.0 and 3.0. The lower vertical capacity ratio is representative of the mean loading of suction caissons under SLS conditions; the higher value is an estimate of the average dimensionless vertical load of the leeward caisson near extreme wind, representative of the rare event of an earthquake occurring amidst a storm.
- $S_u/\rho L$ varies between 5.0 and 8.3. The lower bound is representative of soil/caisson systems with reduced soil strength mobilization, i.e., development of larger permanent deformations under the same vertical capacity ratio.
- f_E/R lies within 0.032 – 0.045 when $\frac{S_u}{\rho L} = 8.3$ and 0.050 – 0.058 when $\frac{S_u}{\rho L} = 5.0$. This particularly small flexibility of the $\frac{f_E}{R}$ variable should not be a surprise for such an overconstrained problem. The nominator f_E (i.e., the mean record frequency) may only slightly vary around a mean value of (~ 1.8 Hz) – since the ensemble of applied seismic motions has to conform with the EC8 Type Soil-C design spectrum, and the denominator R is constrained by the caisson dimensions ($L = D = 3 - 9$ m), the minimum acceptable undrained shear strength for a Soil-C profile and the $\frac{S_u}{\rho L}$ ratio.

The example caisson employed for the analyses of Section 3.5 ($L = D = 4.5$ m, $S_u = 75$ kPa, E_o

= 134.5 GPa) corresponds to the lower $\frac{f_E}{R}$ bound for $\frac{S_u}{\rho L} = 8.3$; its dimensionless response is characterized by Eqs. [i] and [i_a] in **Fig. 3.17a**.

The parameters of all linear regression equations presented in **Fig. 3.17** are tabulated in **Table 3.6**, which also includes the mean average percentage error (*MAPE*) for each equation:

$$MAPE = \frac{1}{n} \sum_{i=1}^n |PE_i| \quad (3.21)$$

where:

$$PE = 100\%[(w_E/D)_i - (\widehat{w_E/D})_i]/(w_E/D)_i \quad (3.22)$$

is the percentage error for observation *l* of the predicted with the linear regression equation dimensionless settlement $(\widehat{w_E/D})_i$, to the FE-computed dimensionless settlement $(w_E/D)_i$. As summarized in **Table 3.6**, the *MAPE* of the derived regression equations ranges from 1.8% to 3.9%, which is considered a success.

As should be expected, **Fig. 3.17** indicates that an increase in load ratio $V_w/S_u D$ leads to the increase of w_E/D (comparison between **Fig. 3.17a**, left and **Fig. 3.17a**, right). The same holds true for a decrease in parameter $\frac{S_u}{\rho L}$, which indicates lower mobilized soil shear strength. The decrease in frequency ratio $\frac{f_E}{R}$ also results in slightly augmented dimensionless settlement for the examined systems; however, this difference is diminished in the case of $\frac{S_u}{\rho L} = 5.0$, due to the quite narrow $\frac{f_E}{R}$ band.

Implications for foundation design

According to the current state of practice [e.g., DNV-OS-J101, 2014], the permanent foundation rotation should not exceed 0.25° (0.0044 rad) for the continuation of operations. For a jacket structure founded on suction caissons, of relevance is the jacket rotation (θ_j), which is generated by the differential settlement between leeward and windward legs. Based on the settlement accumulation patterns presented within the paper, it may be assumed that the leeward caisson's residual settlement dominates the jacket rotation. To this end, it is possible to correlate θ_j to a threshold settlement at the leeward leg, considering zero residual settlements at the windward leg. The latter comprises a reasonable assumption, considering that the initial settlement of the windward leg (due to the dead weight of the superstructure)

is counterbalanced by the uplift displacement experienced due to the application of wind and seismic loading. For a realistic OWT jacket structure (for the size of the caissons examined herein), this results in a settlement threshold $w_{lim} = 55$ mm, or $w_{lim}/D = 0.006$ in dimensionless terms, for a $D = L = 9$ m caisson. Based on the results of **Fig. 3.17**, it may safely be concluded that a single seismic event is hardly ever expected to threaten the operability of a jacket OWT, except for the highly improbable case of a strong earthquake occurring amid a storm for caissons with low $\frac{S_u}{\rho L}$ ratios (**Fig. 3.17b**, right). However, the sustained seismic settlement and the resulting permanent θ_j will unavoidably reduce the remaining operational life of the OWT. For example, a seismic event of $I_A = 3$ m/s may lead to approximately $w_E/D = 0.0045$ for a caisson with $\frac{S_u}{\rho L} = 5.0$ under normal environmental loads (**Fig. 3.17b**, left). Therefore, the remaining threshold for settlement accumulation due to long-term environmental cyclic loading will be significantly diminished: $w_{rem}/D = w_{lim}/D - w_E/D = 0.006 - 0.0045 = 0.0015$.

Table 3.6. Parameters of the linear regression equations $w_E/D - I_A$ presented in Fig. 3.17.

Eq.	PGA (g)	f_E/R	E_o/S_u	$V_w/S_u D^2$	R^2	β	δ	MAPE (%)
[i]	0.35	0.045	1800	2.0	0.98	0.0006	0.0009	3.9
[ii]	0.35	0.045	1800	3.0	0.99	0.0011	0.0013	2.6
[iii]	0.35	0.058	1800	2.0	0.99	0.0013	0.0011	3.4
[iv]	0.35	0.058	1800	3.0	0.99	0.0023	0.0014	2.9
[i _a]	0.35	0.032	1800	2.0	0.99	0.0008	0.001	1.8
[ii _a]	0.35	0.032	1800	3.0	0.99	0.0014	0.0014	1.9
[iii _a]	0.35	0.051	1800	2.0	0.99	0.0015	0.0011	2.9
[iv _a]	0.35	0.051	1800	3.0	0.99	0.0026	0.0015	2.3

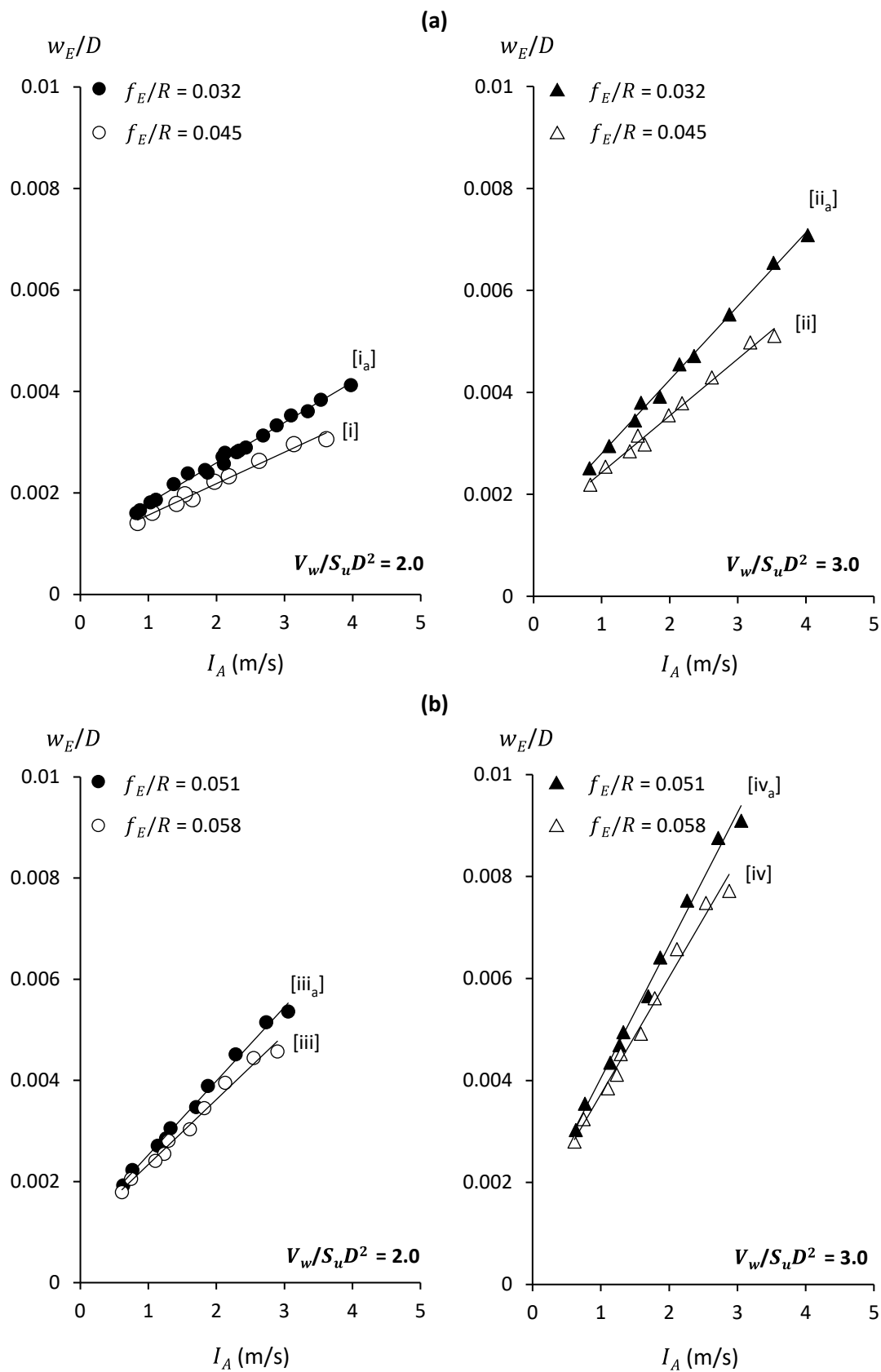


Figure 3.17. Dimensionless caisson response charts for Method A and $E_0/S_u = 1800$: (a) $\frac{S_u}{\rho L} = 8.3$, (b) $\frac{S_u}{\rho L} = 5.0$.

Use & limitations of the developed regression equations

It is acknowledged that a different or richer dataset of ground motions may slightly change the constants of the derived regression equations. However, it is not expected to essentially affect the observed linear trends for the examined problem. The methodology is validated across the entire range of common I_A values, while the selected ground motions incorporate all primary parameters affecting the investigated problem: acceleration amplitude, frequency content, and number of cycles.

The presented linear regression equations should be treated with caution for sites that do not match the environmental and soil parameters or the foundation configuration examined herein. This includes 4-pod SBJs on a uniform clay stratum founded on $L/D = 1$ caissons under a specific range of wind loads (applicable to the examined Mediterranean Sea site or any similar site in terms of environmental load conditions) and soil rigidity ratios (stiff clays). Moreover, the charts' application is limited to $S_w/\rho L$ between 5.0 – 8.3, and the associated frequency ratio (f_E/R) range.

Despite their undeniable limitations, the value of the response charts lies in the underlying methodological framework rather than the regression equations per se. In this context, the same methodology may be employed with more sophisticated soil constitutive models to derive prediction equations for the same or any other type of caisson configuration.

3.7. A hybrid approach for the seismic assessment of SBJ OWTs

A hybrid methodology for performance-based seismic assessment of SBJ offshore wind turbines is proposed, combining the nonlinear CWS modelling technique and seismic settlement prediction using the derived linear regression equations. The hybrid methodology comprises eight consecutive steps:

Step 1. Define the design acceleration response spectrum (EC8 or equivalent site-specific spectrum).

Step 2. Estimate the Aria's intensity (I_A) (mean and standard deviation) at the reference site, using regression formulas that correlate I_A to earthquake magnitude, distance from the fault, and the local soil conditions [e.g., Peláez et al. 2005; Lee et al. 2012; Chousianitis et al. 2014].

Step 3. Generate an ensemble of spectrum-compatible seismic motions (Method A or B).

Step 4. Define the mean environmental loads acting on the OWT (Wind, Wave loads) pertinent to the loading combination ($W + E$), as well as the soil conditions (E_o, S_u) at the site of reference.

Step 5. Subject the global CWS model to pure environmental loading and compute the axial load V_w and the respective dimensionless term $V_w/S_u D^2$ at the leeward and windward legs. The proposed model captures soil-structure interaction (SSI) effects, in contrast with fixed-base superstructure models or further simplified models where SSI effects are taken into account by replacing the substructure with a set of elastic springs that correspond to the vertical (K_V), lateral (K_H) and rocking (K_R) soil-caisson stiffness. On the cost of accuracy, users may replace the proposed model with a simpler one to compute V_w .

Step 6. Subject the global CWS model to combined environmental and seismic loading (using the motions of Step 3) and compute the horizontal displacement u and rotation θ of individual caissons. Due to the lower model accuracy regarding the calculation of seismically induced deformations, it is advised that results are used for preliminary assessment only. Step 6 is redundant if the interest lies solely in the estimation of the jacket rotation θ_j (i.e., the rotation stemming from the differential settlement of the caissons). In this case, users should directly move to Step 7.

Step 7. Use the spectrum-compatible linear regression equations to preliminary assess the seismic settlement w_c at the (critical) compressive leg (for the $V_w/S_u D^2$ calculated in Step 5, the E_o/S_u ratio that best describes the site conditions and a reasonable range of I_A , compatible with the seismological profile of the area of interest).

Step 8. Estimate the jacket rotation $\theta_j \approx w_c/B$ and compare against threshold values.

3.8. Conclusions

The paper has developed a simplified performance-based assessment technique for SBJ OWTs founded in clay under the combined action of wind (W) and earthquake (E) loading. Using an example of an 8 MW jacket-supported OWT installed at 60 m depth in the Adriatic Sea, system performance was assessed employing a detailed 3D FE model of the soil–foundation–structure (SFS) system (global 3D FE model). After deriving insights on system performance,

the global 3D FE model was used as a *benchmark* to assess the efficiency of an enhanced Winkler-based ‘Caisson-on-Winkler-Soil’ (CWS) model. Soil–suction caisson interaction is represented by nonlinear hysteretic elements, capturing residual deformations and hysteresis. The proposed CWS model offers physical coupling between vertical and moment loading by introducing distributed vertical hysteretic elements along the caisson shaft, simultaneously contributing to vertical and moment shaft resistance.

The CWS model was shown to offer a very good prediction of the $H-M$ failure envelope in the most relevant first quadrant of $H-M$ space, where the loads are acting in the same direction. It was subsequently employed to predict the response of the Jacket OWT subjected to transient VHM loading generated by the combined action of a steady wind force and seismic excitation. Subjected to external inertia loading, the CWS model successfully predicted the nonlinear dynamic response of the caisson, matching well with the *benchmark*. The leeward caisson's residual settlement was shown to be critical for design, as it controls jacket rotation θ_j .

The global CWS model was shown to capture wave propagation effects imposed by the non-uniform free-field deformation pattern. However, when subjected to seismic loading at the base, it was unsuccessful in predicting caisson settlements (horizontal displacements and rotations were less affected). The caisson was shown to be subjected to a *dual shearing* mechanism due to: (i) *kinematic* loading by vertically propagating S-waves; and (ii) *inertial* loading from the superstructure. The simplified CWS model cannot capture such a *dual-shearing mechanism* since the horizontal hysteretic elements are *not coupled* to the vertical ones. This is an inherent limitation of any *uncoupled* analysis.

The 3D FE model of a single caisson (single 3D FE model) was used to shed light on the mechanisms controlling permanent caisson deformations. In stark contrast to cyclic inertia loading, where the caisson accumulates settlement only when subjected to compressive loads, the combination of *kinematic* and *inertia* (coupled) loading leads to an anti-symmetric deformation pattern. The developing shear strains are due to the *coupled* effect of shearing γ_V caused by the initial vertical load V_w , and shearing γ_E due to the vertically propagating shear waves. While γ_V is constant, the fluctuation of γ_E leads to a ‘rocking’ response, due to which the caisson accumulates settlement both for negative and positive load peaks.

Recognizing the inability of the simplified CWS model to predict seismic settlements realistically, the single 3D FE model was used to develop settlement prediction equations for the critical leeward caisson. A methodology is proposed to derive meaningful correlations of co-seismic caisson settlement (w_E) with statistically significant Intensity Measures (IMs). First, spectrum-compatible input motions are generated, following two alternative strategies: (a) Method A – one-by-one spectrum matching, manipulating actual records in the frequency domain; and (b) Method B – median spectrum matching, manipulating the records only in amplitude. Then, the spectrum-compatible motions were used to conduct a numerical study with the single 3D FE model, the results of which were used to derive linear regression equations, correlating w_E with I_A . The efficiency of the method was demonstrated using an example $L/D = 1$ caisson, subjected to 22 seismic records, scaled to match the EC8-Type C spectrum, using both spectrum-matching techniques. The results were shown to be relatively insensitive to the spectrum-matching technique, with the goodness-of-fit R^2 ranging from 0.94 to 0.99.

A parametric study was then conducted, based on a formal dimensional analysis, which correlated the seismic foundation response with five dimensionless Π -products relevant to the caisson geometry (L, D), the soil properties (ρ, E_o, S_u), the initial (deadweight + wind) vertical load (V_w), and the earthquake characteristics (PGA, f_E). The dimensionless permanent caisson settlement (w_E/D) was presented as a function of I_A in the form of response charts, dependent on the derived dimensionless products. The fluctuation of the vertical load (V_w) during shaking was shown to increase the accumulation of caisson settlements by 10 – 30% (compared to the assumption of constant V_w). Yet, the increase is primarily dependent on the dimensionless load ratio $V_w/S_u D^2$ (i.e., the average wind thrust at the onset of the earthquake).

Finally, a hybrid step-by-step method was outlined, facilitating the performance-based assessment of SBJ OWTs. The method employs the simplified CWS model to calculate the VHM loads and approximately estimate horizontal displacements and rotations at the caissons, followed by a preliminary assessment of caisson settlements using the correlations of w_E/D with I_A , on the basis of spectrum-compatible input motions.

Acknowledgement

This research has received funding from the Hellenic Foundation for Research and Innovation and the General Secretariat for Research and Technology (GSRT) under Grant Agreement 974.

Appendix 3A

The geometric details of the jacket structure supporting the examined 8MW turbine are illustrated in **Fig. 3.A1** and **Table 3.A1** [Von Borstel & Vobeck, 2016].

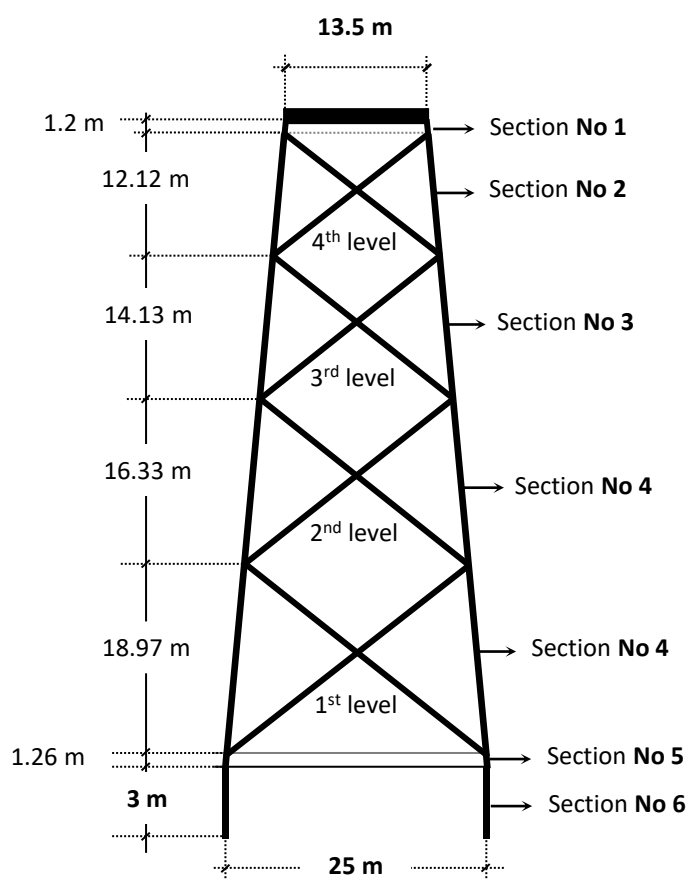


Figure 3.A1. Geometric properties of the examined jacket structure.

Table 3.A1. Section properties of the examined jacket structure.

	Braces				Main tubulars					
	1 st level	2 nd level	3 rd level	4 th level	Section No 1	Section No 2	Section No 3	Section No 4	Section No 5	Section No 6
D (mm)	965	813	711	610	1525	1525	1525	1525	1525	1525
t (mm)	21	21	21	21	51	30	35	40	83	45

Notation

a	Acceleration
a_{tower}	Acceleration at the turbine tower top
$a_{surface}$	Acceleration at the soil surface
A	Area
A_r	Arias Intensity ratio
B	Jacket width
C_{dash}	Dashpot coefficient
C	Initial modulus of the kinematic hardening constitutive model
D	Caisson diameter
D_{tower}	Diameter of the turbine tower
d_{rotor}	Rotor diameter
E	Earthquake load
$E_{o,ns}$	Small-strain stiffness of hysteretic elements
E_o	Small-strain soil stiffness
E_{steel}	Young's modulus of steel
$E_{ur,ns}$	Unloading/Reloading modulus of hysteretic elements
F	Yield surface of the kinematic hardening constitutive model
f_E	Predominant seismic frequency
f_{cyc}	Cyclic force
f_{max}	Ultimate strength of hysteretic elements
f_{yield}	Steel yield stress
G	Soil shear modulus
H	Horizontal load
H_b	Horizontal resistance at the caisson base
H_o	Pure horizontal caisson capacity
H_{shaft}	Horizontal resistance at the caisson shaft
$H_{shaft,n}$	Horizontal shear traction on the caisson sides parallel to the loading direction
$H_{shaft,s}$	Passive & active reaction on the caisson sides perpendicular to the loading direction
H_{tower}	Height of the turbine tower
I_A	Arias' Intensity
J	Relative soil-caisson rigidity ratio
k_e	Uniaxial elastic stiffness of hysteretic elements

$k_{x,n}$	Distributed normal horizontal stiffness
$k_{x,s}$	Distributed frictional horizontal stiffness
k_z	Distributed shaft vertical stiffness
K_{HH}	Caisson lateral stiffness
K_{MH}	Caisson coupled swaying-rocking stiffness
K_{MM}	Caisson rocking stiffness
$K_{b\theta}$	Rotational stiffness of the caisson base
K_{bx}	Lateral stiffness of the caisson base
K_{bz}	Vertical stiffness of the caisson base
L	Length
M	Moment load
M_b	Moment resistance of caisson base
M_{shaft}	Moment resistance of caisson shaft
$M_{shaft,y}$	Shaft resisting moment generated by vertical shear stresses on the shaft
$M_{shaft,x}$	Shaft resisting moment generated by horizontal stresses
M_o	Pure moment caisson capacity
N_{cH}	Uniaxial horizontal capacity factor
$N_{cH,base}$	Local horizontal capacity factor at the caisson base
$N_{cH,shaft}$	Local horizontal capacity factor at the caisson shaft
N_{cM}	Uniaxial moment capacity factor
$N_{cM,base}$	Local moment capacity factor at the caisson base
$N_{cM,shaft}$	Local moment capacity factors at the caisson shaft
N_{cV}	Uniaxial vertical capacity factor
$N_{cV,base}$	Local vertical capacity factor at the caisson base
$N_{cV,shaft}$	Local vertical capacity factor at the caisson shaft
PGA	Peak ground acceleration
PI	Clay plasticity index
RSD	Relative significant duration
S_u	Undrained shear strength
t_{tower}	Thickness of the turbine tower
t_w	Caisson skirt thickness
$T_{1.n}$	First natural period of the OWT system
T_E	Predominant earthquake period
u	Horizontal caisson displacement

V	Vertical load
V_b	Vertical resistance of caisson base
V_o	Pure vertical caisson capacity
V_s	Shear wave velocity
V_{shaft}	Vertical resistance of caisson shaft
V_w	Static vertical load on the leeward caisson leg, corresponding to dead loads & wind load
W	Wind load
W_{SLS}	Wind load at SLS conditions
w	Vertical caisson displacement
w_c	Vertical displacement of the compressive (leeward) jacket leg
w_t	Vertical displacement of the tensile (windward) jacket leg
x	Horizontal in-plane direction
y	Horizontal out-of-plane direction
z	Vertical direction
a_0	Dimensionless frequency
\mathbf{a}	Backstress tensor in the kinematic hardening constitutive model
β	Scalar coefficient of the linear regression equations
γ	Scalar coefficient of the kinematic hardening constitutive model
γ_{xz}	Shear strain in the $x - z$ plane
γ_V	Shear strain due to vertical loading
γ_E	Shear strain due to seismic loading
δ	Scalar coefficient of the linear regression equations
$\Delta(\omega)$	Dynamic stiffness coefficient
θ	Caisson rotation
θ_j	Rotation of the jacket structure
ν	Poisson's ratio
ρ	Material density
σ_{Mises}	Mises stress
σ_y	Maximum yield stress at saturation
σ_o	Maximum stress at zero plastic strain
τ_{xz}	Shear stress in the $x - z$ plane
ω	Angular frequency
$\dot{\mathbf{a}}$	Evolution law of the backstress tensor \mathbf{a}
$\underline{\mathbf{s}}$	Deviatoric stress tensor of the kinematic hardening constitutive model

References

- ABAQUS 6.14. (2014). Standard user's manual. Dassault Systèmes Simulia Corp., Providence, RI, USA.
- Al Atik, L., & Abrahamson, N. (2010). An improved method for nonstationary spectral matching. *Earthquake spectra*, 26(3), 601-617.
- Alati, N., Failla, G., & Arena, F. (2015). Seismic analysis of offshore wind turbines on bottom-fixed support structures. *Philosophical Transactions of the Royal Society A: Mathematical, Physical and Engineering Sciences*, 373(2035), 20140086.
- Anastasopoulos I., Theofilou M. (2016), "Hybrid foundation for offshore wind turbines: environmental and seismic loading", *Soil Dynamics and Earthquake Engineering*, 80: 192–209.
- Anastasopoulos, I., Anastasopoulos, P. C., Agalianos, A., & Sakellariadis, L. (2015). Simple method for real-time seismic damage assessment of bridges. *Soil dynamics and earthquake engineering*, 78, 201-212.
- Anastasopoulos, I., Gelagoti, F., Kourkoulis, R. and Gazetas, G. (2011). Simplified Constitutive Model for Simulation of Cyclic Response of Shallow Foundations: Validation against Laboratory Tests, *Journal of Geotechnical and Geoenvironmental Eng.*, ASCE, 137 (12): 1154-1168.
- Anoyatis, G., & Mylonakis, G. (2012). Dynamic Winkler modulus for axially loaded piles. *Geotechnique*, 62(6), 521-536.
- Antoniou, M., Gelagoti, F., Kourkoulis, R., Georgiou, I., Karamanos, S. A. (2019). Seismic response of jacket wind-turbines: Dimensional analysis of foundations and SSI. *Proceedings of the 2nd International Conference on Natural Hazards & Infrastructure (ICONHIC2019)*. June 2019, Crete, Greece.
- API (2010). API Recommended Practice 2A-WSD - Planning, Designing, and Constructing Fixed Offshore Platforms. *American Petroleum Institute*.
- Arias, A. (1970). A measure of earthquake intensity. In: *Hansen RJ*, editor. Cambridge: MIT Press, p.438–83.
- Assimaki, D., & Gazetas, G. (2009). A simplified model for lateral response of large diameter caisson foundations —Linear elastic formulation. *Soil Dynamics and Earthquake Engineering*, 29(2), 268-291.
- Bransby M.F., Yun G. (2009). The undrained capacity of skirted strip foundations under combined loading. *Géotechnique* 59 (2), 115–125.
- Buckingham, E., (1914). On physically similar systems; illustrations of the use of dimensional equations. *Physical Review*, 4(4), 345.
- Byrne, B. W., & Hously, G. T. (2004). Experimental investigations of the response of suction caissons to transient combined loading. *Journal of geotechnical and geoenvironmental engineering*, 130(3), 240-253.
- Chousianitis, K., Del Gaudio, V., Kalogeras, I., & Ganas, A. (2014). Predictive model of Arias intensity and Newmark displacement for regional scale evaluation of earthquake-induced landslide hazard in Greece. *Soil Dynamics and Earthquake Engineering*, 65, 11-29.

- De Risi, R., Bhattacharya, S., & Goda, K. (2018). Seismic performance assessment of monopile-supported offshore wind turbines using unscaled natural earthquake records. *Soil Dynamics and Earthquake Engineering*, 109, 154-172.
- Det Norske Veritas. (2014). Offshore Standard DNV-OS-J101, Design of Offshore Wind Turbine Structures. Det Norske Veritas, Høvik.
- Fu, D., Gaudin, C., Tian, Y., Cassidy, M.J., Bienen, B. (2017). Uniaxial capacities of skirted circular foundations in clay. *Journal of Geotechnical and Geoenvironmental Engineering*, 143(7).
- Garini, E., & Gazetas, G. (2013). Damage potential of near-fault records: sliding displacement against conventional "Intensity Measures". *Bulletin of Earthquake Engineering*, 11(2), 455-480.
- Gazetas, G. (1991). Formulas and charts for impedances of surface and embedded foundations, *Journal of Geotechnical Engineering*, ASCE, 117 (9): 1129–1141
- Gazetas, G., Dobry, R., & Tassoulas, J. L. (1985). Vertical response of arbitrarily shaped embedded foundations. *Journal of geotechnical engineering*, 111(6), 750-771.
- Gelagoti, F., Georgiou, I., Kourkoulis, R., & Gazetas, G. (2018). Nonlinear lateral stiffness and bearing capacity of suction caissons for offshore wind-turbines. *Ocean Engineering*, 170, 445-465.
- Gerolymos, N., & Gazetas, G. (2006a). Development of Winkler model for static and dynamic response of caisson foundations with soil and interface nonlinearities. *Soil Dynamics and Earthquake Engineering*, 26(5), 363-376.
- Gerolymos, N., & Gazetas, G. (2006b). Static and dynamic response of massive caisson foundations with soil and interface nonlinearities—validation and results. *Soil Dynamics and Earthquake Engineering*, 26(5), 377-394.
- Gerolymos, N., & Gazetas, G. (2006c). Winkler model for lateral response of rigid caisson foundations in linear soil. *Soil Dynamics and Earthquake Engineering*, 26(5), 347-361.
- Gerolymos, N., Gazetas, G., (2005). Nonlinear lateral response of caisson foundations. *Proceedings of the 1st Greece-Japan Workshop on Seismic Design, Observation. Retrofit of Foundations*, Athens, Greece, pp. 125
- Giannakos, S., Gerolymos, N., Gazetas, G. (2012). Cyclic lateral response of piles in dry sand: finite element modeling and validation. *Comput. Geotech.* 44, 116–131.
- Gourvenec S., Barnett S.(2011). Undrained failure envelope for skirted foundations under general loading. *Géotechnique* 261(3), 263–270.
- Guo, W. D. (2000). Vertically loaded single piles in Gibson soil. *Journal of geotechnical and geoenvironmental engineering*, 126(2), 189-193.
- Hou, S. (1968). Earthquake simulation models and their applications, *Research Report R68-17*. Cambridge, Massachusetts: Dept. of Civil Eng. Massachusetts Institute of Technology.
- Hung, LC., Kim S.R. (2012). Evaluation of vertical and horizontal bearing capacities of bucket foundations in clay. *Ocean Engineering*, 52, 75 - 82.

- Katsanos, E. I., Thöns, S., & Georgakis, C. T. (2016). Wind turbines and seismic hazard: a state-of-the-art review. *Wind Energy*, 19(11), 2113-2133.
- Kaynia, A. M. (2019). Seismic considerations in design of offshore wind turbines. *Soil Dynamics and Earthquake Engineering*, 124, 399-407.
- Keawsawasvong S., Ukritchon B. (2016). Finite element limit analysis of pull-out capacity of planar caissons in clay. *Comput. Geotech.* 75, 12–17.
- Kim, D. H., Lee, S. G., & Lee, I. K. (2014). Seismic fragility analysis of 5 MW offshore wind turbine. *Renewable energy*, 65, 250-256.
- Lee, C. T., Hsieh, B. S., Sung, C. H., & Lin, P. S. (2012). Regional Arias intensity attenuation relationship for Taiwan considering V_{s30} . *Bulletin of the Seismological Society of America*, 102(1), 129-142.
- Liu, S. C. (1969). Autocorrelation and power spectral density functions of the Parkfield earthquake of June 27, 1966. *Bulletin of the Seismological Society of America*, 59(4), 1475-1493.
- Makris, N., & Black, C. J. (2004). Dimensional analysis of rigid-plastic and elastoplastic structures under pulse-type excitations. *Journal of engineering mechanics*, 130(9), 1006-1018.
- Mana, D.S.K., Gourvenec, S., Randolph, M., Hossain, M.S. (2012). Failure mechanisms of skirted foundations in uplift and compression. *Int. J. Phys. Modell. Geotech.*12 (2), 47–62.
- Mardfekri, M., & Gardoni, P. (2013). Probabilistic demand models and fragility estimates for offshore wind turbine support structures. *Engineering Structures*, 52, 478-487.
- Marin, A., Truffer, P. L., & Anastasopoulos, I. (2019). Combined-intensity-measures matching approach for improved performance-based design of slopes. *Soil Dynamics and Earthquake Engineering*, 126, 105763.
- Mavrakos, S., (2016). Med-Ocean data and hydrodynamic loading for the North Sea and the Mediterranean Sea location. JABACO Development of Modular Steel Jacket for Offshore Windfarms, Deliverable 1.1.
- Mo, R., Kang, H., Li, M., & Zhao, X. (2017). Seismic fragility analysis of monopile offshore wind turbines under different operational conditions. *Energies*, 10(7), 1037.
- Mylonakis, G., Nikolaou, A., & Gazetas, G. (1997). Soil–pile–bridge seismic interaction: kinematic and inertial effects. Part I: soft soil. *Earthquake Engineering & Structural Dynamics*, 26(3), 337-359.
- Novak, M., Aboul-Ella, F., & Nogami, T. (1978). Dynamic soil reactions for plane strain case. *Journal of the Engineering Mechanics Division*, 104(4), 953-959.
- O'Rourke, M. J., & Dobry, R. (1982). Spring and dashpot coefficients for machine foundations on piles. *Special Publication*, 78, 177-198.
- Padgett, J. E., Nielson, B. G., & DesRoches, R. (2008). Selection of optimal intensity measures in probabilistic seismic demand models of highway bridge portfolios. *Earthquake engineering & structural dynamics*, 37(5), 711-725.

- Peláez, J. A., Delgado, J., & Casado, C. L. (2005). A preliminary probabilistic seismic hazard assessment in terms of Arias intensity in southeastern Spain. *Engineering Geology*, 77(1-2), 139-151.
- Pender, M. J. (1993). Aseismic pile foundation design analysis. *Bulletin of the New Zealand Society for Earthquake Engineering*, 26(1), 49-160.
- Randolph, M. F. & Wroth, C. P. (1978). Analysis of deformation of vertically loaded piles. *J. Geotech. Engng ASCE* 104, No. 12, 1465–1488.
- Sakellariadis, L., Agalianos, A., & Anastasopoulos, I. (2018). Simplified method for real-time seismic damage assessment of motorway bridges: Transverse direction — Accounting for abutment stoppers. *Earthquake Engineering & Structural Dynamics*, 47(6), 1496-1521.
- Saragoni, G., & Hart, G. C. (1973). Simulation of artificial earthquakes. *Earthquake Engineering & Structural Dynamics*, 2(3), 249-267.
- Schaumann, P., and Böker, C. (2005). Can Tripods and Jackets Compete With Monopiles?, *Contribution to Copenhagen Offshore Wind*, Copenhagen, Denmark, Oct. 26–28, 2005.
- Seidel, M. (2007). Jacket Substructures for the REpower 5M Wind Turbine. *European Offshore Wind Conference and Exhibition*, Berlin, Germany, Dec. 4–6, 2007.
- Seismosoft (2020). SeismoMatch - A computer program for spectrum matching of earthquake records. Available from URL: www.seismosoft.com.
- Skau, K. S., Grimstad, G., Page, A. M., Eiksund, G. R., & Jostad, H. P. (2018). A macro-element for integrated time domain analyses representing bucket foundations for offshore wind turbines. *Marine Structures*, 59, 158-178.
- Skau, K. S., Jostad, H. P., Eiksund, G., & Sturm, H. (2019). Modelling of soil-structure-interaction for flexible caissons for offshore wind turbines. *Ocean Engineering*, 171, 273-285.
- Suryasentana, S. K., Byrne, B. W., Burd, H. J., & Shonberg, A. (2018). An elastoplastic 1D Winkler model for suction caisson foundations under combined loading. In *Numerical Methods in Geotechnical Engineering IX, Volume 2: Proceedings of the 9th European Conference on Numerical Methods in Geotechnical Engineering (NUMGE 2018)*, June 25-27, 2018, Porto, Portugal (p. 973). CRC Press.
- Swiss Re (2017). Wind farms: Harvesting energy on shaky grounds and in stormy seas. Report. Swiss Reinsurance Institute.
- Trifunac, M. D., & Brady, A. G. (1975). A study on the duration of strong earthquake ground motion. *Bulletin of the Seismological Society of America*, 65(3), 581-626.
- Tsigginos, C., Gerolymos, N., Assimaki, D., & Gazetas, G. (2008). Seismic response of bridge pier on rigid caisson foundation in soil stratum. *Earthquake Engineering and Engineering Vibration*, 7(1), 33.
- Ukritchon B., Keawsawasvong, S. (2016). Undrained pull-out capacity of cylindrical suction caissons by finite element limit analysis. *Comput. Geotech.* 80, 301–311.
- Ukritchon B., Wongtoythong P., Keawsawasvong S. (2018). New design equation for undrained pull-out capacity of suction caissons considering combined effects of caisson aspect ratio, adhesion factor at interface, and linearly increasing strength. *Applied Ocean Research*, Volume 75, 1-14.

- Von Borstel, T. & Vobeck M. (2016). Preliminary design of reference offshore steel jackets for 8MW and 10MW wind turbines. JABACO Development of Modular Steel Jacket for Offshore Windfarms, Deliverable 1.3.
- Vucetic, M., & Dobry, R. (1991). Effect of soil plasticity on cyclic response. *Journal of Geotechnical Engineering*, 117(1), 89-107.
- Vulpe, C. (2015). Design method for the undrained capacity of skirted circular foundations under combined loading: effect of deformable soil plug. *Géotechnique* 65, No. 8, 669–683.
- Wagner, H., Baack, C., Eickelkamp, T., Epe, A., Lohmann, J., and Troy, S. (2011). Life Cycle Assessment of the Offshore Wind Farm Alpha Ventus. *Energy*, 36(5), pp. 2459–2464.
- Wang, W., Gao, Z., Li, X., & Moan, T. (2017a). Model test and numerical analysis of a multi-pile offshore wind turbine under seismic, wind, wave, and current loads. *Journal of Offshore Mechanics and Arctic Engineering*, 139(3).
- Wang, X, Yang, X, Zeng, X (2017b). Seismic centrifuge modelling of suction bucket foundation for offshore wind turbine. *Renew Energy*:114.
- WindEurope (2020). Wind Energy in Europe in 2019 - Trends and statistics. *Technical Report*. February 2020.
- Yun, G., & Bransby, M. F. (2007). The horizontal-moment capacity of embedded foundations in undrained soil. *Canadian Geotechnical Journal*, 44(4), 409-424.
- Zheng, X. Y., Li, H., Rong, W., & Li, W. (2015). Joint earthquake and wave action on the monopile wind turbine foundation: An experimental study. *Marine Structures*, 44, 125-141.

4. Offshore foundations in low-plasticity cohesive soils: Cyclic degradation experimental evidence and simplified numerical analysis

This chapter consists of the accepted version (following peer-review) of the following article: Antoniou, M., Gelagoti, F., Herzog, R., Kourkoulis, R., & Anastasopoulos, I. Offshore Foundations in Low-Plasticity Cohesive Soils: Cyclic Degradation Experimental Evidence and Simplified Numerical Analysis. *Ocean Engineering*.

Abstract

The paper studies the effect of soil strength and stiffness degradation on the undrained cyclic performance of offshore foundations in low-plasticity cohesive soil using 3D finite element modelling. Cyclic triaxial tests on reconstituted kaolin were conducted at the ETH Zurich laboratory, providing insights into key parameters affecting the degradation process. A simplified soil constitutive model accounting for cyclic degradation is developed and encoded in Abaqus via a user subroutine. The model is calibrated against experimental results and validated with published centrifuge model tests of monopiles under cyclic lateral loading. It is subsequently used to evaluate the performance of suction caisson foundations with different aspect ratios ($L/D=0.5$ and 2) under short-term cyclic and seismic loading. Due to its ductile resistance mechanism, the $L/D=0.5$ caisson exhibits superior performance under vertical cyclic loading in fast-degrading soil. Under inclined cyclic loading, the slower degradation rate of the $L/D=2$ caisson governs response, reversing the trend. Under seismic shaking, the degradation-induced resistance imbalance amplifies the irrecoverable settlements produced by kinematic shearing at the caisson sidewalls. For the fast-degrading soil examined, degradation is shown to increase the settlements by up to 50%.

4.1. Introduction

Cyclic loading may lead to significant changes in foundation response of more than an order of magnitude within the lifetime of an offshore wind turbine (OWT). The term *cyclic degradation* is commonly used to describe the decrease of soil stiffness and strength under undrained cyclic loading due to soil de-structuring and excess pore pressure accumulation that leads to effective stress relaxation [Andersen, 2009]. In contrast to fine-grained materials, which can only lose part of their initial strength and stiffness, cohesionless soils are more susceptible to such degradation, even sustaining a complete loss of their shear strength – a phenomenon termed *soil liquefaction* [Mortezaie & Vucetic, 2013]. In the case of cohesive soils, part of the degradation during repeated cyclic loading can be compensated by the increase of shear strength due to strain rate (or loading frequency) effects [Lefebvre & Pfendler, 1996; Einav & Randolph, 2005].

The severity of cyclic degradation is governed by the magnitude and number of load cycles [Matasovic & Vucetic, 1995; Andersen, 2009]. For fine-grained materials, laboratory testing indicates that the degradation rate is a function of the ratio of average to cyclic applied stress/strain [Andersen, 2009], the multidimensional nature of loading (when at least two stress components are out-of-phase; Cai et al., 2018; Matsuda et al., 2013), the loading frequency [Zhou & Gong, 2001; Mortezaie & Vucetic, 2013], the overconsolidation ratio [Zhou & Gong, 2001; Hanna & Javed, 2014], the plasticity and sensitivity of the soil material [Matasovic & Vucetic, 1995], and the overburden stress [Mortezaie & Vucetic, 2013; Hanna & Javed, 2014].

The reliable prediction of plastic deformation accumulation of OWT foundations subjected to cyclic loading is of the utmost importance, as it may adversely affect the service life of the entire installation. Cyclic degradation increases the complexity of such computations and the required computational effort, and therefore, only a few models have been proposed for numerical prediction of such deformations under the millions of environmental (wind and wave) load cycles sustained by OWTs [Jostad et al., 2014, 2015; Staubach et al., 2022]. Instead of analyzing the cyclic load history in the time domain, these models typically employ explicit processes to account for the effects of cyclic degradation on foundation performance (e.g., by decomposing the cyclic load history in constant amplitude load parcels to derive average cyclic response).

At the same time, understanding foundation performance under more extreme but short-duration dynamic events – such as earthquakes and storms – is also vital. Such events may entail disproportional risks for the OWT operation compared to the hundreds of thousands of lower-amplitude wind and wave cycles, especially given the high sensitivity and prominent cyclic degradation of natural cohesive soils in the offshore environment [O’Loughlin et al., 2020]. Due to the short-duration of such events, the loading is typically undrained, and therefore, cyclic consolidation effects cannot compensate for strength degradation. Recent studies have highlighted the potential for earthquake-induced damage on OWT foundations in seismically active regions, especially when the turbine is operational during the earthquake [e.g., Kourkoulis et al., 2014; Antoniou et al., 2022].

Extreme short-term cyclic events consist of a low to medium number of cycles, rendering time domain numerical analysis with conventional soil constitutive models applicable for assessing cyclic foundation performance. Indeed, several advanced, effective stress-based models have successfully been employed to simulate the degradation of cyclically-loaded undrained clay [e.g., Elia & Rouainia, 2016; Shi et al., 2018]. Despite their success, the application of such models in practice can be cumbersome due to their complexity and challenging calibration process. On the other hand, total stress-based models, where the soil is treated as a single-phase medium with undrained shear strength characteristics, have been shown to reasonably predict the (non-degrading) undrained cyclic behaviour of cohesive soils while significantly reducing the complexity in terms of parameter calibration [e.g., Anastasopoulos et al., 2011]. Towards this direction, Huang et al. [2021] and Shi et al. [2023] recently proposed the AUC-Clay (Anisotropic Undrained Cyclic Clay) model: a modified kinematic hardening model that considers the effect of strength and (cyclic shear stress-dependent) stiffness deterioration during cycling, along with the effects of soil anisotropy and small-strain stiffness. The AUC-Clay constitutive equations have been introduced in finite element (FE) analysis software, and the model has been shown to satisfactorily capture the degrading cyclic foundation response at the system level [Shi et al., 2023].

A similar approach is adopted in the present study to investigate the performance of offshore foundations subjected to short-term transient loading. A practical-simplified constitutive model is developed, combining isotropic/kinematic hardening with a Von Mises failure criterion and introducing cyclic stiffness and strength degradation through a simple (and thus readily applicable) user subroutine. A series of monotonic and cyclic (strain-

controlled) undrained triaxial tests on reconstituted kaolin were conducted at the ETH Zurich (ETHZ) laboratory to quantify the effect of key parameters on cyclic degradation and to allow for rigorous model calibration. The model is validated against published centrifuge model tests of a monopile subjected to cyclic lateral loading and subsequently used for the preliminary investigation of cyclic suction caisson performance under environmental and seismic loading. This novel foundation scheme has been increasingly used in the offshore industry due to its many advantages over conventional foundation systems (reduced carbon footprint, cost-effectiveness, and ease of installation). As the offshore wind industry expands further, suction caissons are expected to play an increasingly important role in the construction of offshore wind farms in challenging environments, calling for an improved understanding of their performance under complex site conditions and adverse loading scenarios.

The key contributions of the present study may be summarized as follows:

- (1) The developed soil model incorporates a newly introduced equation for the representation of soil stiffness degradation during cyclic loading, formulated on the basis of the conducted soil element tests and considered suitable for low plasticity soils similar to the one investigated herein.
- (2) The research extends beyond the development and calibration of the simplified numerical model in leveraging it as an efficient tool for the evaluation of the underlying mechanics governing the performance of suction caisson foundations of different aspect ratios under short-term vertical and inclined cyclic loading.
- (3) The study offers insights into the potential effects of cyclic degradation on the response of suction caissons in soft soils under earthquake loading, a hazard that has gained focus during the past few years due to its relevance for emerging offshore wind markets, such as Japan and Taiwan.

4.2. Experimental cyclic response of normally consolidated kaolin

Isotropically consolidated (monotonic and cyclic) undrained triaxial (CIU) tests were conducted at the ETHZ geotechnical laboratory (**Fig. 4.1**). The experimental campaign employs samples consolidated from Kaolin K1, a material classified as medium-plastic silt by Wichtmann & Triantafyllidis [2018]. Its physical properties are listed in **Table 4.1**.

Table 4.1. Physical properties of Kaolin K1.

Specific Gravity, G_s	Liquid Limit, w_L [%]	Plastic Limit, w_p [%]	Unit weight, γ_s [kN/m^3]
2.675	47.2	35	17.3

For specimen preparation, dry Kaolin powder was mixed with demineralized water to create a slurry of water content $w/w_L = 2.1$. The goal was to achieve pre-consolidated samples with a water content (w_c) near the liquid limit before inserting them into the triaxial device. To eliminate air from the slurry, the mixture was stirred under vacuum for 8 hours (**Fig. 4.1a**), then sealed and allowed to rest for 24 hours in a temperature-controlled environment to reach a homogeneous state.

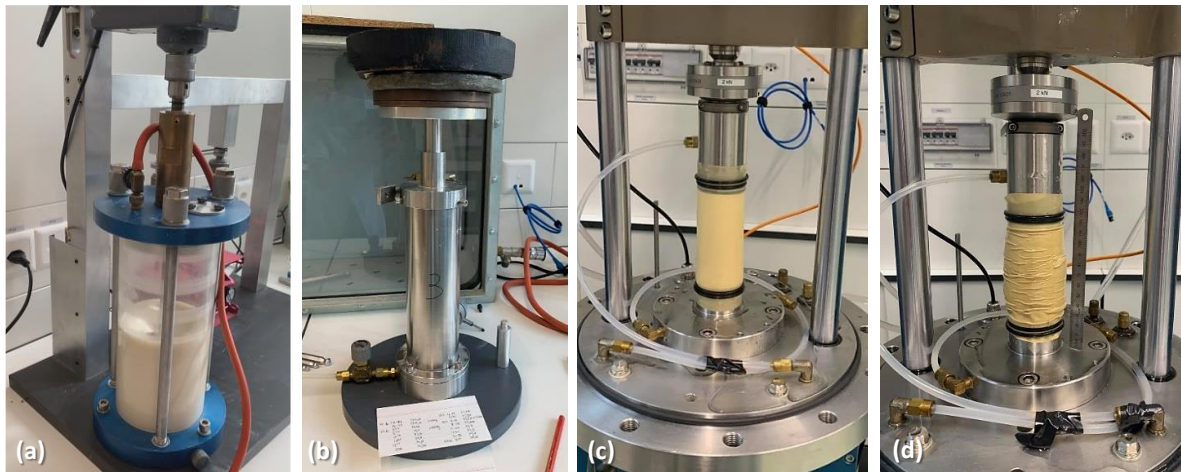


Figure 4.1. Kaolin CIU triaxial testing: (a) Kaolin powder mixed with demineralized water under vacuum; (b) 1D slurry consolidation; (c) sample positioned within the triaxial apparatus, ready for testing; and (d) sample at failure after a triaxial compression test.

During the 1D pre-consolidation stage (**Fig. 4.1b**), the maximum applied vertical stress ranged from 100 to 300 kPa, applied incrementally to the samples using the step loading method. Approximately 10 – 15 days were required to result in the reconstituted samples of diameter $D = 50$ mm and height $h \approx 100$ mm (**Fig. 4.1c**). The samples' water content was determined using the oven-drying method in accordance with ASTM D2216-10 standards (2010). The measured values, recorded upon completion of the pre-consolidation process, are listed in **Table 4.2**. It was observed that w_c slightly decreases as the applied vertical stress increases from 100 to 300 kPa. Although the uniformity of the samples was not directly measured (e.g., through compression tests on specimens from various parts of the samples or by dissecting samples into cubes to assess water content distribution), the consistency in sample

preparation was closely monitored by ensuring similar time-settlement curves between samples consolidated at the same pre-consolidation pressure. The samples' sensitivity, defined as the ratio of intact to fully remoulded undrained shear strength, was measured equal to $S_t = 11$ via fall cone tests, using a standardized 60g/60° (mass/tip) cone. In the triaxial apparatus, the samples were water-saturated with a back pressure of 500 kPa and consolidated to the initial mean effective stress level p'_o . A B-value test was conducted, ensuring $B > 0.95$ for all specimens. As summarized in **Table 4.2**, all tests were performed at an overconsolidation ratio of $OCR = 1$, corresponding to a normally consolidated soil material. A typical sample after testing can be seen in **Fig. 4.1d**.

Table 4.2. Program of cyclic and monotonic CIU tests conducted at the ETH geotechnical laboratory.

Test ID	p'_o (kPa)	\dot{s} (mm/min)	f (Hz)	Load type	h (mm)	ε_1^{ampl} (%)	OCR	w_c prior to triaxial testing (%)
				(Cyclic/ Monotonic]				
1a	100	0.6	0.005	C	101.2	0.5	1	52.1
2a	100	6	0.005	C	100.6	5	1	52.5
3a	150	0.6	0.005	C	101.4	0.5	1	49.9
4a	150	6	0.005	C	100.8	5	1	51.6
5a	150	25	0.02	C	102.7	5	1	50.4
6a	150	58	0.05	C	97.3	5	1	51.0
7a	300	0.6	0.005	C	98.9	0.5	1	47.2
8a	300	6	0.005	C	101.0	5	1	47.3
9a	150	0.006	-	M	99.4	-	1	51.2
10a	300	0.006	-	M	98.7	-	1	47.7

Monotonic tests

During monotonic testing (Tests 9a and 10a), the specimens were sheared with a displacement rate $\dot{s} = 0.006$ mm/min. The measured deviatoric stress $q = \sigma_1 - \sigma_3$ (where σ_1 and σ_3 are the major and minor principal stresses) versus the applied axial strain ε_1 is plotted in **Fig. 4.2a**, denoting a contractive response, which is typical for normally consolidated samples. The tests were stopped at axial strain $\varepsilon_1 = 15\%$, which corresponds to the failure strain of the sample, i.e., the strain where the maximum deviator stress $q_{max} = 2S_{uo}$ has been reached. Consistent with the literature [e.g., Bolton & Stewart, 1994; Gourvenec et al., 2009], we assume a linear correlation $S_{uo} = \kappa\sigma'_v$ of intact undrained shear strength S_{uo} with vertical effective stress σ'_v . The test results reveal a curve slope of $\kappa = 0.268$, as shown in **Fig. 4.2b**. This aligns well with

the range proposed by the semi-empirical equations of Gourvenec et al. [2009] and Bolton & Stewart [1994], which are based on T-bar penetration tests. For the correlation between p'_o and σ'_v , a coefficient of earth pressures at rest $K_o = 1$ is adopted, reflecting the isotropic consolidation of the specimens.

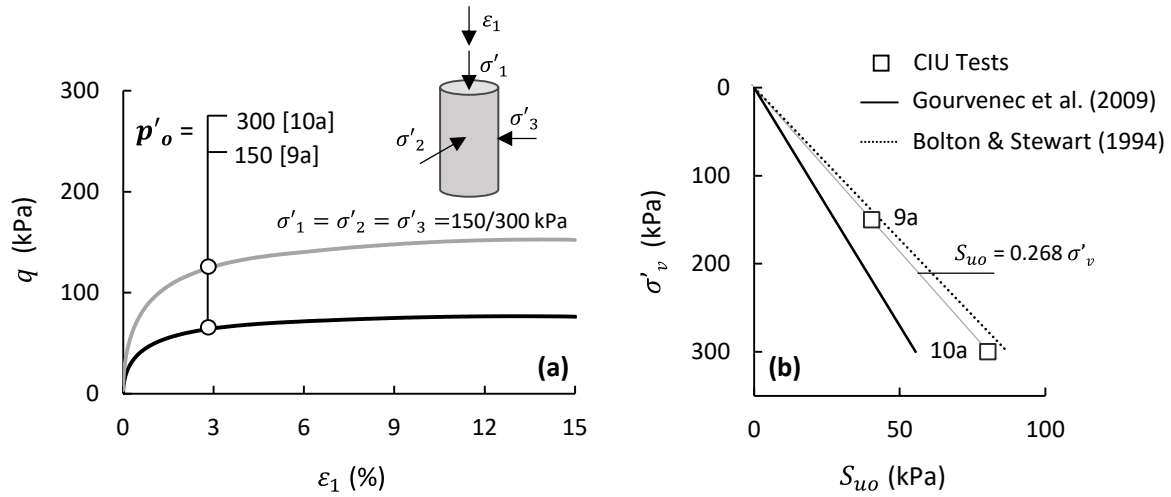


Figure 4.2. Monotonic triaxial CIU tests: (a) deviatoric stress q vs. axial strain ε_1 ; and (b) distribution of intact undrained shear strength S_{uo} with vertical effective stress σ'_v .

Cyclic tests

Eight undrained cyclic symmetric tests of constant vertical strain amplitude ε_1^{amp} and strain rate \dot{s} were performed (initial stress ratio $\eta_0 = q_0/p'_0 = 0$). The initial mean effective pressure p'_0 , vertical strain amplitude ε_1^{amp} , and loading rate \dot{s} were parametrically varied between tests to explore their effect on sample response. The experimental campaign does not examine the effect of the stress ratio η_0 or OCR , despite both of them reportedly affecting cyclic soil response [e.g., Andersen, 2015; Staubach et al., 2022]. Moreover, we do not explicitly estimate the threshold strain amplitude, below which no cumulative effects occur [Vucetic, 1994; Hsu & Vucetic, 2004; Hsu & Vucetic, 2006]. However, the threshold is known to decrease with decreasing PI and is considered to lie near the lower end of the 0.024–0.06% range proposed by Hsu & Vucetic [2006] for silts and clays with $PI = 14$ to 30. A test was stopped when the developed excess pore water pressure asymptotically reached the initial mean effective pressure p'_0 (indicating total loss of shear strength), or when the rate of excess pore pressure accumulation fell below 0.0002 kPa/cycle.

Typical test results (Test 8a) are shown in **Fig. 4.3**, which plots the decrease in deviatoric q and mean effective stress p' (**Fig. 4.3a**) and the accompanying increase in accumulated pore

water pressure u_{acc} (**Fig. 4.3b**) with the number of load cycles. The effective stress path, reminiscent of a fir tree, is very similar to that of sand experiencing liquefaction. **Figure 4.3c** depicts the deviatoric stress–axial strain ($q - \varepsilon_1$) loops for cyclic loading at a constant axial strain amplitude $\varepsilon_1^{amp} = 5\%$, highlighting the change in peak deviatoric stress q_N per cycle – a sign of stiffness and strength degradation due to accumulated plastic strain. It is evident from **Fig. 4.3c** that the sample displays higher deviatoric stress in compression than in tension (for example, compare the 1st quarter to the 3rd quarter of cycle 1) under the same cyclic strain amplitude. The trend is consistent in all cyclic tests. A similar behaviour – albeit to a smaller extent – is also observed in the limited, strain-controlled CIU tests on kaolin of Wichmann & Triantafillidis [2018]. It is attributed to the uniaxial loading history of the samples (1D consolidation during specimen preparation), which produces a certain degree of stress-induced cross-anisotropy during subsequent testing under isotropic conditions.

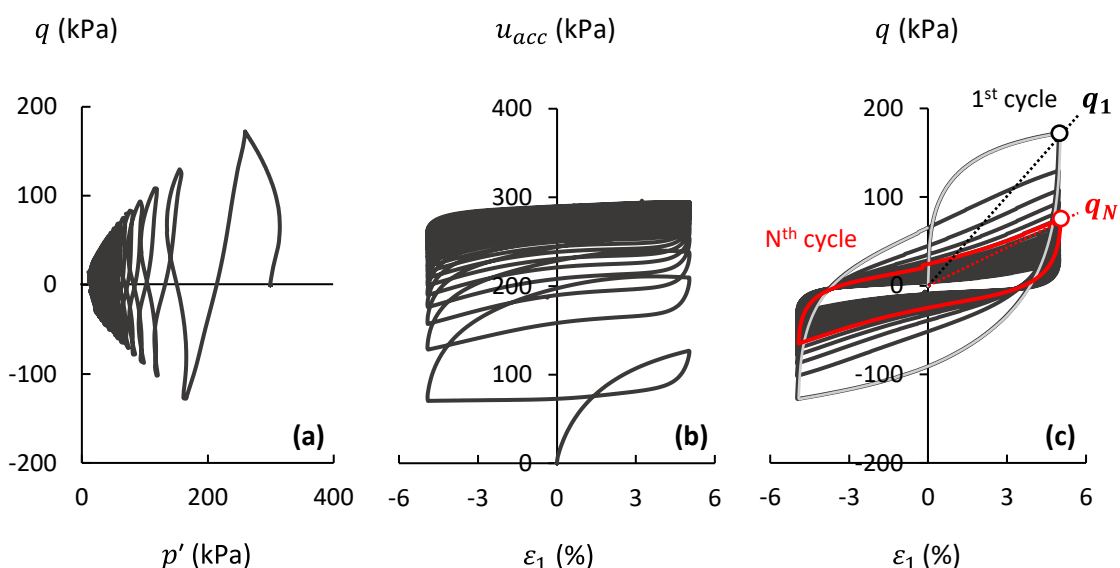


Figure 4.3. Test 8a [$p'_0 = 300$ kPa; $\varepsilon_1^{amp} = 5\%$; $\dot{s} = 6$ mm/min]: (a) deviatoric stress q vs. mean effective pressure p' ; (b) accumulated excess pore water pressure u_{acc} vs. axial strain ε_1 ; and (c) deviatoric stress q vs. axial strain ε_1 .

The effect of initial pressure p'_0

Tests 2a, 4a, and 8a were performed under the same load frequency ($f = 0.005$ Hz) and constant strain amplitude ($\varepsilon_1^{amp} = 5\%$), varying the consolidation pressure $p'_0 = 100, 150,$ and 300 kPa. The resulting loading rate was $\dot{s} = 6$ mm/min for all samples. The results are summarized in **Fig. 4.4** in terms of peak deviatoric stress q_N and pore water pressure u_{acc}/p'_0

ratio with the number of cycles N . Unless otherwise stated, q_N refers to the peak deviatoric stress in compression. At first glance, **Fig. 4.4a** indicates a similar rate of q_N decrease with load cycles at different p'_o levels. However, when the results are plotted in dimensionless terms, it becomes apparent that the increase of consolidation pressure favours the cyclic response of the sample by effectively reducing the rate of excess pore pressure accumulation (**Fig. 4.4c**), thus leading to a reduction of peak deviatoric stress (**Fig. 4.4b**). This observation agrees with the study of Mortezaie & Vucetic [2013], which reports a decrease in the cyclic degradation rate with the increase of vertical effective stress in cyclic strain-controlled simple shear tests on normally consolidated kaolin clay. The latter is attributed to the larger void ratio of samples at lower initial pressure, which translates to a larger capacity for volume reduction and, therefore, a potential for larger pore water pressure build-up under undrained conditions.

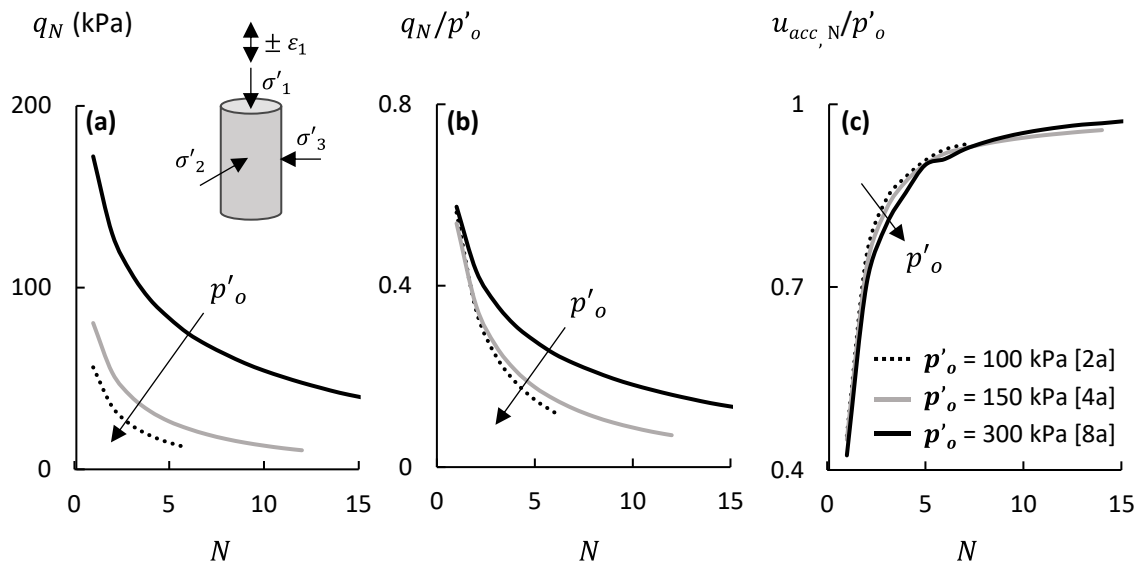


Figure 4.4. Variation of initial pressure p'_o during cyclic triaxial tests at $\epsilon_1^{amp} = 5\%$: (a) peak deviatoric stress q_N per load cycle N ; (b) dimensionless peak deviatoric stress q_N/p'_o per N ; and (c) dimensionless peak excess pore water pressure per cycle $u_{acc,N}/p'_o$ vs. N .

The effect of cyclic strain amplitude ϵ_1^{amp}

The influence of cyclic strain amplitude ϵ_1^{amp} on the cyclic degradation rate is shown in **Fig. 4.5** for tests conducted at $p'_o = 300$ kPa. The figure plots the variation of the peak deviatoric stress ratio q_N/q_o with the number of cycles N for various levels of applied cyclic strain amplitude $\epsilon_1^{amp} = 0.5, 1, 2, 5\%$. The black lines (corresponding to $\epsilon_1^{amp} = 0.5\%$ and 5%) refer to tests conducted in this study (Tests 7a and 8a, respectively), while the grey lines (C43, C44,

C45) correspond to strain-controlled tests conducted on the same material and initial pressure level by Wichtmann & Triantafillidis [2018]. Cross-examination with tests C43-C45 serves a dual purpose: (i) it confirms the quality of our tests through a direct comparison between Tests 8a and C45 conducted at the same level of $\varepsilon_1^{amp} = 5\%$, and (ii) it offers increased resolution to the observed response. As expected, a monotonically increasing relationship exists between the cyclic strain amplitude and the q_N/q_1 degradation rate with the number of cycles, an observation confirmed by previous studies investigating cyclic strength and stiffness degradation effects via strain-controlled cyclic tests in cohesive soils [e.g., Matasovic & Vucetic, 1995; Andersen, 2015].

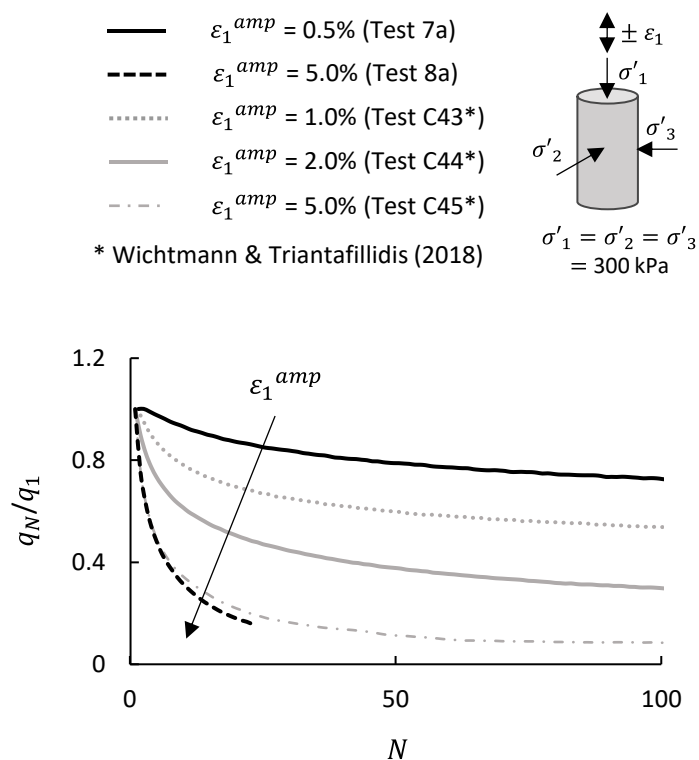


Figure 4.5. Peak deviatoric stress ratio q_N/q_1 vs. load cycle number N for $p'_o = 300 \text{ kPa}$ and various levels of cyclic strain amplitude ε_1^{amp} .

The effect of loading rate \dot{s}

The influence of loading rate on the initial deviatoric stress q_o and the cyclic degradation rate is examined via Tests 4a – 6a, all conducted at $p'_o = 150$ kPa (**Fig. 4.6**). Based on the relevant literature, the increase in loading rate has been shown to enhance the undrained shear strength of cohesive soils [Dayal & Allen, 1975; Biscontin & Pestana, 2001; Einav & Randolph, 2005] and reduce the rate of cyclic degradation [Ansal & Erken, 1989; Hanna & Javed, 2014]. According to Andersen [2015], this influence grows stronger with increasing soil plasticity. The displacement rates in Tests 4a – 6a (conducted at constant $\varepsilon_1^{amp} = 5\%$) vary from $\dot{s} = 6$ to 60 mm/min (corresponding to $f = 0.005$ to 0.05 Hz). An increase of initial deviatoric stress of 10 – 20% is observed for samples 4a – 6a compared to the monotonic Test 9a (**Fig. 4.6a**), which was loaded with $\dot{s} = 0.006$ mm/min (i.e., at least three orders of magnitude slower). Focusing on Tests 4a – 6a, the response is rather insensitive to \dot{s} , as also confirmed by **Fig. 4.6b**, which shows the evolution of peak deviatoric stress ratio q_N/q_1 with the N . The low dependence of cyclic degradation on \dot{s} is attributed to the low plasticity of kaolin and is in good agreement with the studies of Wichtmann & Triantafillidis [2018] and Staubach et al. [2022], who investigate such effects via stress-controlled cyclic tests under a lower range $\dot{s} = 0.01$ – 0.5 mm/min) on similar plasticity kaolin.

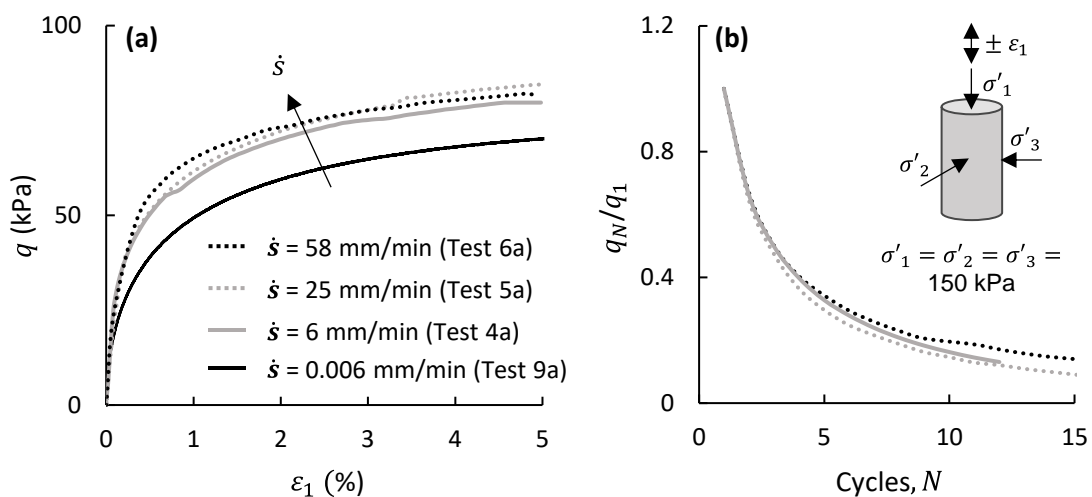


Figure 4.6. Loading rate effects: (a) deviatoric stress q vs. axial strain ε_1 in the 1st quarter of cycle 1 for Tests 4a, 5a, 6a, compared to monotonic soil response at $p'_o = 150$ kPa (Test 9a); and (b) peak deviatoric stress ratio q_N/q_1 vs. load cycle number N for Tests 4a, 5a, 6a.

4.3. A practical-simplified model for cyclic degradation in fine-grained soils

Based on the experimental observations and the literature consensus on the post-cyclic reduction of undrained stiffness and strength in cohesive soils, a simplified and practical model is formulated to describe the degradation of such materials under undrained cyclic loading. The proposed model is based on a simple isotropic/kinematic hardening constitutive model with a Von Mises failure criterion and associated flow rule [Armstrong & Frederick, 1966; Lemaitre & Chaboche, 1990], available in ABAQUS [2013]. The original model has been parameterized by Anastasopoulos et al. [2011] to simulate the undrained monotonic and cyclic response of clays under a total stress analysis framework and has been extensively validated and employed to analyze the behaviour of a variety of soil–structure systems under cyclic or seismic loading [e.g., Anastasopoulos et al., 2011; Zafeirakos et al., 2013; Kourkoulis et al., 2014; Tsinidis et al., 2014; Anastasopoulos & Theofilou, 2016; Antoniou et al., 2022]. The baseline model is briefly described before introducing the new modifications that account for undrained cyclic degradation.

Baseline model

The kinematic evolution of the yield surface in the stress space is defined through a function F :

$$F = f(\boldsymbol{\sigma} - \mathbf{a}) - \sigma_o \quad (4.1)$$

where: $\boldsymbol{\sigma}$ is the stress tensor; σ_o is the size of the yield surface; \mathbf{a} is the backstress tensor that defines the kinematic evolution of the yield surface in the stress space; and $f(\boldsymbol{\sigma} - \mathbf{a})$ is the equivalent Mises stress with respect to the backstress \mathbf{a} . As shown in **Fig. 4.7a**, the failure surface is centred around the origin of the stress space, indicating that it predicts isotropic strength (i.e., identical strength in triaxial compression, extension, and direct shear). The evolution of stress comprises two components: (a) an isotropic hardening component, which may describe the evolution of the yield surface size σ_o in function of equivalent plastic strain $\bar{\epsilon}^{pl}$; and (b) a nonlinear kinematic hardening component, which describes the translation of the yield surface in the stress space and is defined by the superposition of a purely kinematic term and a relaxation term that introduces nonlinearity [Gerolymos & Gazetas, 2005]. The evolution of the kinematic component of the model is defined as:

$$\dot{a} = C \frac{1}{\sigma_o} (\boldsymbol{\sigma} - \mathbf{a}) \dot{\boldsymbol{\varepsilon}}^{pl} - \gamma \mathbf{a} \dot{\boldsymbol{\varepsilon}}^{pl} \quad (4.2)$$

where: C is the kinematic hardening modulus (set as the small strain Young's modulus $C = E_o$); γ is a parameter determining the rate of decrease of the kinematic hardening with increasing plastic deformation; and $\dot{\boldsymbol{\varepsilon}}^{pl}$ is the equivalent plastic strain rate, calculated as $\dot{\boldsymbol{\varepsilon}}^{pl} = \sqrt{\frac{2}{3} \dot{\boldsymbol{\varepsilon}}^{pl} : \dot{\boldsymbol{\varepsilon}}^{pl}}$, where $\dot{\boldsymbol{\varepsilon}}^{pl}$ represents the rate of plastic flow. According to this evolution law, the centre of the yield surface must be contained within a cylinder of radius $\sqrt{2/3} C/\gamma$, while the yield surface is contained within a limiting surface of radius $\sqrt{2/3} \sigma_{max}$, where σ_{max} is the maximum yield stress associated with the undrained shear strength of the soil S_u . At large plastic strains, the magnitude of a approaches $a_s = C/\gamma$, and σ_{max} approaches $\sigma_o + a_s$. In most of its applications, parameter σ_o , which controls the initiation of nonlinear response, is defined as a fraction λ of the maximum yield stress, typically ranging from 0.1-0.3 [Anastasopoulos et al., 2011]. Based on the above, the plastic behaviour of the baseline model requires the definition of only three parameters: σ_{max} , E_o , and γ , with the latter being calculated as follows:

$$\gamma = \frac{C}{(\sigma_{max} - \sigma_o)} = \frac{E_o}{(1 - \lambda) \sigma_{max}} \quad (4.3)$$

The elastic material response is described by the small strain elasticity modulus E_o and the Poisson's ratio ν . The latter should be set to 0.49 to ensure negligible volume change under undrained conditions.

Modification to account for cyclic degradation

Similar to the work of Huang et al. [2021] and Shi et al. [2023], the proposed model considers strength and stiffness deterioration during cyclic loading via two reduction coefficients: b_s and b_e . The former accounts for the cyclic strain-softening effect on intact undrained shear strength S_{uo} , and is defined through the degradation relationship proposed by Einav & Randolph [2005]:

$$b_s = d_{rem} + (1 - d_{rem}) e^{-3\xi/\xi_{95}} \quad (4.4)$$

where: ξ is the accumulated plastic shear strain; $d_{rem} = 1/S_t = S_{u,rem}/S_{uo}$ ($S_{u,rem}$ = remoulded undrained shear strength); and ξ_{95} is the cumulative shear strain required to lead to 95%

reduction of the undrained shear strength (from peak to remolded), while typical values for marine clays range from 10 to 50 [Einav & Randolph, 2005].

The degradation of soil stiffness with plastic strain accumulation is introduced via the b_e multiplier, which is defined as:

$$b_e = b_{e,rem} + (1 - b_{e,rem}) e^{-3\xi^k/m} \quad (4.5)$$

where: k and m are material-dependent parameters; and $b_{e,rem}$ is the soil modulus degradation ratio E_{rem}/E_o at large plastic strains (E_o = intact Young's modulus, and E_{rem} = residual Young's modulus). Equation (4.5) is formulated based on the experimental results, following an exponential law similar to the one employed for the degradation of undrained shear strength. However, the exponent k suggests that b_e can simulate a faster (or slower) degradation of E with increasing strain accumulation compared to shear strength, which aligns well with existing experimental findings, such as those reported by Yasuhara et al. [2003], who observed a more pronounced reduction in Young's modulus with load cycles, particularly in low plasticity fine-grained soils. This implies a non-constant E/S_u ratio throughout cycling loading. Parameters k and m are functions of cyclic strain amplitude ε^{ampl} and initial mean effective stress p'_o , both earlier shown to influence the degradation rate. The formulations of $k = f(p'_o, \varepsilon^{ampl})$ and $m = f(p'_o, \varepsilon^{ampl})$ are provided later on.

In the modified model, henceforth referred to as VM-CD (Von Mises – Cyclic Degradation) model, the kinematic hardening parameters are calculated as:

$$C_d = b_e C \quad (4.6)$$

$$\gamma_d = \left(\frac{b_e}{b_s}\right) \gamma \quad (4.7)$$

where: C and γ were previously defined for the initial (pre-cyclic) state. Parameter b_s implies that the limit surface of the model shrinks with the increase of accumulated plastic shear strain, reaching a radius of $\sqrt{2/3} \sigma_{max,d} = \sqrt{2/3} b_s \sigma_{max}$, where σ_{max} is the maximum yield stress corresponding to the pre-cyclic state and $\sigma_{max,d}$ is the degrading maximum yield stress. At very large strains, a maximum (degrading) stress of $\sigma_{max,d} = b_s (\sigma_o + C/\gamma)$ is achieved. The initial yield surface is assumed to remain unchanged until cyclic loading initiates to avoid degradation during monotonic loading. A schematic illustration of the yield and limit surfaces of the modified model projected on the π -plane (principle stress space) is depicted in **Fig.**

4.7b. In its current form, the VM–CD model should not be expected to capture the experimentally observed cross-anisotropy effects, nor the potential variations in cyclic degradation rate due to the influence of varying amplitude average stresses prior to cyclic loading, leaving room for further improvement.

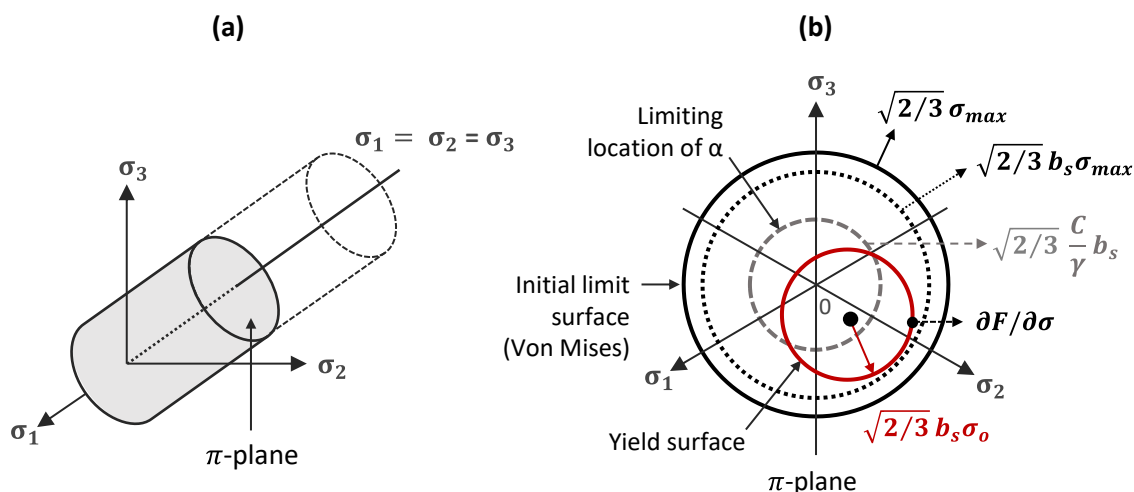


Figure 4.7. VM-CD model: (a) representation of the original Von Mises failure criterion in the principle stress space; and (b) projection of the yield and limit surfaces of the proposed modification on the π -plane.

Implementation in Abaqus

The model is encoded in Abaqus through a simple USDFLD user subroutine (Abaqus, 2013). A set of field variables (FVs) and solution-dependent state variables (SDVs) are defined for this purpose. Within the subroutine, FVs can be defined in function of any material point output quantity by calling the GETVRM utility routine and subsequently be used as artificial fields to modify material properties during the analysis. SDVs evolve with the analysis solution and are necessary when information from the current analysis increment must be remembered and employed in subsequent increments.

For the proposed model version, three FVs are employed. FV1 corresponds to parameter ξ , the accumulated equivalent plastic strain PEEQ at a material point during cyclic loading. FV2 represents the cyclic strain amplitude ε^{amp} , calculated as the maximum plastic cyclic strain magnitude PEMAG experienced by a material point up to the current increment. FV3 corresponds to the initial mean effective stress p'_o .

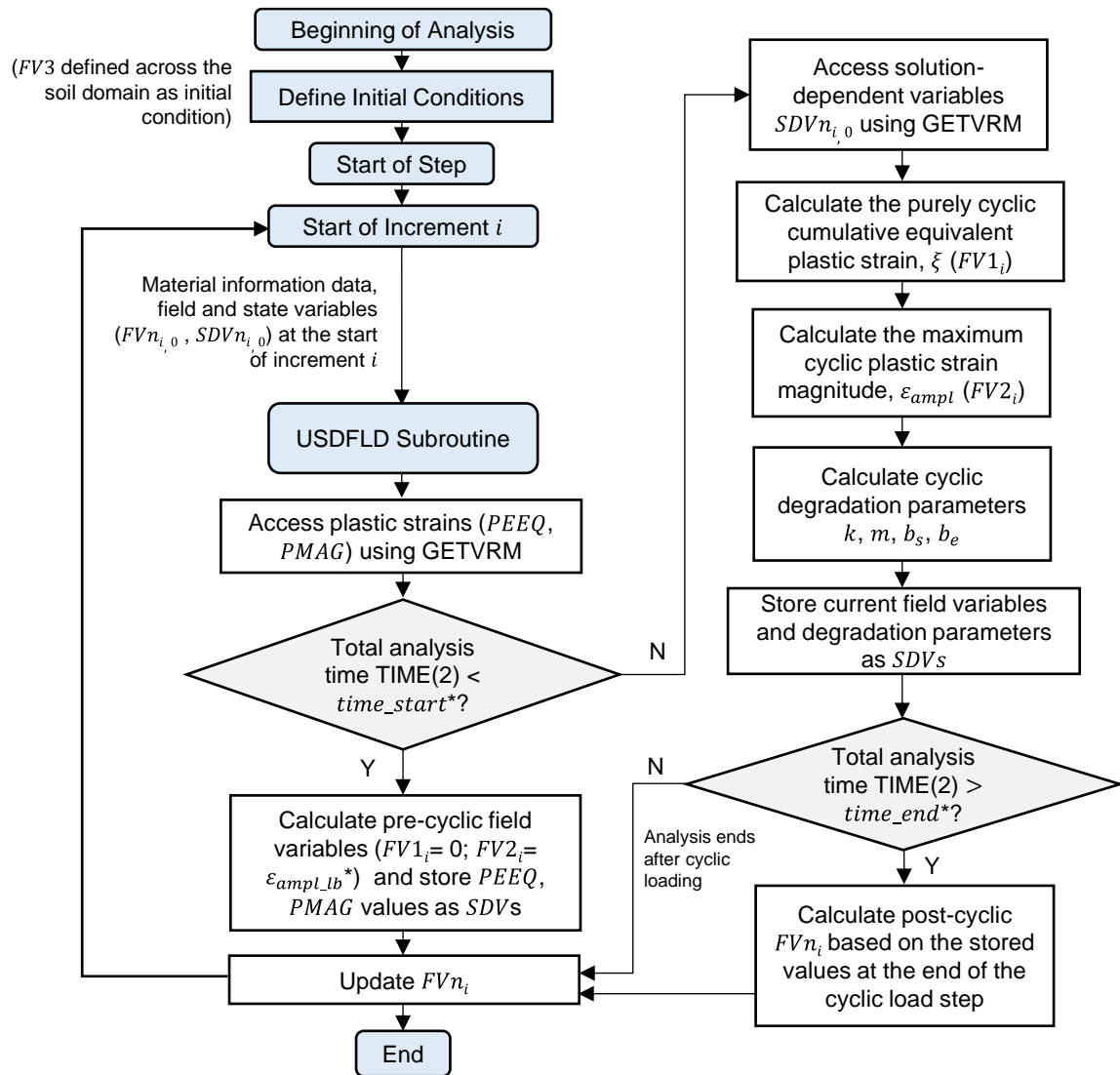
The strength and stiffness parameters of the VM-CD model are updated based on FVs 1 – 3 by relating the soil material with user-defined field variable dependencies stated in the material properties definition. At the beginning of each increment, FVs 1 – 3 are calculated over the entire soil domain and model parameters are updated following Eqs. (4.4) – (4.7). At the current increment, parameters ξ and ε^{ampl} are calculated based on the stored FV1 and FV2 from previous increments and the newly extracted (current increment) PEEQ and PEMAG. The temporally variable coefficients b_s and b_e , as well as parameters k and m are calculated and stored as SDVs for visualization purposes. The calculation procedure is summarized in the flowchart of **Fig. 4.8**, while an example of the developed USDFLD subroutine is provided as supplemental material in **Appendix 4A**.

Calibration against element tests

Coefficients b_s and b_e are calibrated against the previously discussed CIU triaxial experiments. Key triaxial test results that assisted the calibration process are summarized in **Table 4.3**, including the total number of test cycles (N_f), the peak deviatoric stress during the first and last cycle (q_1 and q_{N_f}), and the total accumulated strain at the end of each test (ξ_f). Coefficient b_s is independent of ε^{ampl} or p'_o , and therefore requires the definition of only two material parameters: d_{rem} and ξ_{95} (**Table 4.4**). The first is taken as $d_{rem} = 1/S_t = 0.09$, based on soil sensitivity measurements. The exact derivation of ξ_{95} would require penetration resistance tests, which were not conducted in the present study. Based on the nature of the examined soil (low-plasticity, normally consolidated, high cyclic degradation rate), $\xi_{95} = 10$ is assumed, lying at the lower bound of the range suggested by Einav & Randolph [2005], and found to fit well the CIU test results.

Table 4.3. Key triaxial test results used for model calibration.

Test ID	p'_o [kPa]	ε_1^{ampl} [%]	N_f	q_1 [kPa]	q_{N_f} [kPa]	ξ_f
1a	100	0.5%	324	31.5	11.3	6.5
2a	100	5.0%	10	56.1	5.8	2.0
3a	150	0.5%	275	42.5	21.3	5.7
4a	150	5.0%	14	79.7	7.5	2.8
7a	300	0.5%	334	93.0	57.1	6.6
8a	300	5.0%	24	172.2	26.1	4.8
C43	300	1.0%	568	99.8	40.9	23
C44	300	2.0%	363	101.9	19.0	29



* $time_start$ = start time of cyclic loading
 $time_end$ = end time of cyclic loading
 ϵ_{amp_lb} = lower-bound ϵ_{amp} value for which the model is calibrated

Figure 4.8. Calculation flow chart of the USDFLD subroutine used in the VC-MD model.

Figure 4.9 depicts the cyclic strain amplitude and pressure dependency of parameters k and m (Eq. 4.5). The markers refer to the k , m values that provide the best fit of Eq. (4.5) to the triaxial test results, while the lines to the derived relationships that express k and m in function of ε^{ampl} and p'_o :

$$k = a \varepsilon^{ampl} (p'_o/100)^{-c} + b (p'_o/100)^{-c} \quad (4.8)$$

$$m = \left[d (p'_o/100)^e \varepsilon^{ampl} \right]^{-f} \quad (4.9)$$

where: $a - f$ are positive material coefficients, calibrated to best fit the marker points (i.e., the best fit of Eq. 5 to the experimental data). For the specific calibration process, their values are tabulated in **Table 4.4**. Parameter m increases with decreasing ε^{ampl} and increasing p'_o , following a power law. Equation (4.9) conforms to the physically observed specimen response, indicating an increased ξ margin before the soil modulus reaches its residual value for lower levels of ε^{ampl} and higher p'_o . Both parameters should always yield positive values to comply with the requirements of Eq. (4.5): if k is zeroed, the effect of ξ in Eq. (4.5) is eliminated and b_e no longer obeys a degradation law, while if m is zeroed, Eq. (4.5) cannot be calculated. In the developed user subroutine, a lower and upper bound limit is set for the ε^{ampl} value (0.005 and 0.05, respectively, in accordance with the value range examined in the triaxial tests) to limit the range of parameters k and m within known boundaries and avoid unexpected material response.

Of course, Eqs. (4.8) and (4.9) should not be expected to apply for materials that exhibit a substantially different undrained cyclic response compared to the low-plasticity, normally consolidated soil tested herein. Moreover, their dependency on ε^{ampl} is derived based on test results at $p'_o = 300$ kPa, which provide four distinct points for calibration across the ε^{ampl} axis (**Fig. 4.9**). In the absence of more detailed experimental data, k and m can be assumed to display similar trends across all pressure levels.

Figure 4.10 plots the resulting calibrated strength, b_s (Eq. 4.4), and stiffness, b_e (Eq. 4.5) degradation coefficients of the VM-CD model in function of accumulated plastic strain ξ . Coefficient b_e (**Fig. 4.10a**) is plotted for two levels of mean effective stress ($p'_o = 100$ and 300 kPa) and cyclic strain amplitude ($\varepsilon^{ampl} = 0.5\%$ and 5%). Coefficient b_s (**Fig. 4.10b**) is insensitive to such variations, in accordance with the strength degradation model of Einav & Randolph [2005] employed herein.

Table 4.4. Cyclic degradation parameters of the VM-CD model used in the element test simulations.

Cyclic degradation parameters		
Parameter	Description	Value
d_{rem}	The reciprocal of soil sensitivity	0.09
ξ_{95}	The cumulative shear strain required to lead to 95% reduction of the undrained shear strength	10
$b_{e,rem}$	The soil modulus degradation ratio E_{rem}/E_o	0.10
k	Eq. (5) parameter	$f(p'_o, \varepsilon^{ampl})$
a		13.67
b	Material coefficients for the calculation of k	0.3919
c		0.4019
m	Eq. (5) parameter	$f(p'_o, \varepsilon^{ampl})$
d		0.2136
e	Material coefficients for the calculation of m	0.5429
f		0.5371
Baseline model		
Parameter	Description	Value
C_1	Kinematic hardening parameters for the 1 st backstress	$E_o = 220p'_o$
γ_1		800
C_2	Kinematic hardening parameters for the 2 nd backstress	$11p'_o$
γ_2		26.8
λ	The fraction of σ_o to the maximum yield stress	0.1

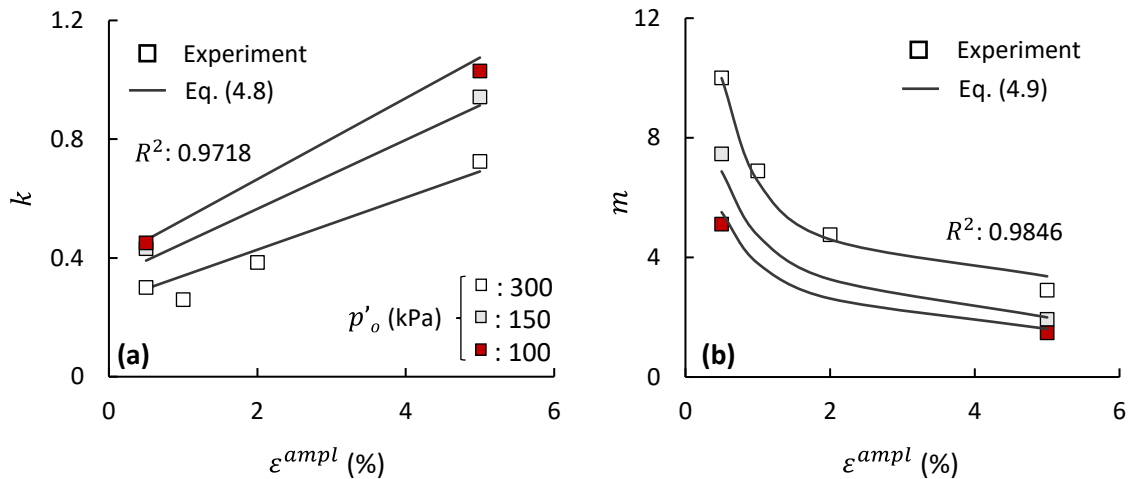


Figure 4.9. Parameters k and m calibrated against experimental data: (a) k (Eq. 4.8) in function of cyclic strain amplitude ε^{ampl} and initial mean effective pressure p'_o ; and (b) m (Eq. 4.9) in function of ε^{ampl} and p'_o .

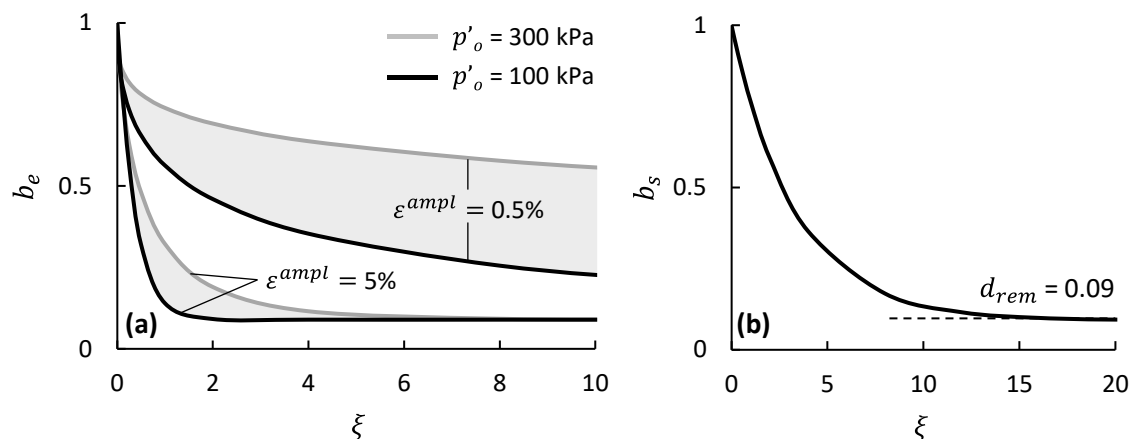


Figure 4.10. Calibrated stiffness and strength degradation coefficients of the VM-CD model: (a) b_e vs accumulated plastic strain ξ for two levels of mean effective stress ($p'_o = 100$ and 300 kPa) and two levels of cyclic strain amplitude ϵ^{ampl} (0.5% and 5%); and (b) b_s vs. accumulated plastic strain ξ .

Regarding the baseline model properties, the study simplistically adopts a small strain Young's modulus (E_o) equal to the secant modulus $E_{0.1}$ [Yasuhara et al., 2003], which corresponds to the deviator stress at 0.1% axial strain. A linear relationship with p'_o is assumed, fitted to the triaxial test results:

$$E_{0.1} = 220p'_o \quad (4.10)$$

The (pre-degradation) maximum yield stress $\sigma_{max} = f(p'_o)$ is correlated to the dynamic undrained shear strength to implicitly account for small-scale loading rate effects observed in the monotonic tests. The maximum deviator stress during cyclic loading is derived from the monotonic specimen response as:

$$q_{max,cyclic} = f_N q_{max,mono} = f_N(0.55p'_o) \quad (4.11)$$

where: $f_N = 1.2$ to account for the loading rate-induced strength increase (see also Section 4.2 for a detailed explanation of the rate-induced strength increase based on the performed experiments). Equation (4.11) serves as a practical means for incorporating the (limited) increase in undrained shear strength induced by loading rate, particularly applicable to low plasticity soils, such as the one examined herein. For high plasticity soils – which are notably sensitive to loading rate effects – the model should be adapted to include a strain-rate-dependent parameter that will account for the enhancement of undrained shear strength due to increased-rate cyclic loading, similar to the one proposed by Einav & Randolph [2005].

The VM-CD model response is compared to the soil element tests in **Figs. 4.11** and **4.12**, in terms of deviatoric stress – axial strain ($q - \varepsilon_1$) response, and peak deviatoric stress ratios q_N/q_1 in function of the number of load cycles N , for various pressure levels and cyclic strain amplitudes. The model parameters used in the simulations are summarized in **Table 4.4**.

The calibrated model reproduces the experimental results adequately well, both in terms of hysteretic stress-strain loops (**Fig. 4.11**) and in terms of strength and stiffness degradation rate (**Fig. 4.12**). Besides the careful calibration of parameters b_s and b_e , the model owns part of its success to the superposition of two kinematic hardening components (two backstresses) to control the (intact) nonlinear model behaviour, each covering a different range of plastic strain. The first (with coefficients $C_1 = E_o, \gamma_1 = 800$) captures the first cycle dynamic backbone curve for equivalent plastic strain $\bar{\varepsilon}^{pl} < 0.5\%$, while the second one (with coefficients $C_2 = 0.05C_1, \gamma_2 = 26.8$) controls the response for $\bar{\varepsilon}^{pl} \geq 0.5\%$. Other than that, the model cannot reproduce the anisotropy effects observed in the experimental results, becoming evident from the purely symmetric form of the numerically predicted stress-strain loops in **Fig. 4.11**.

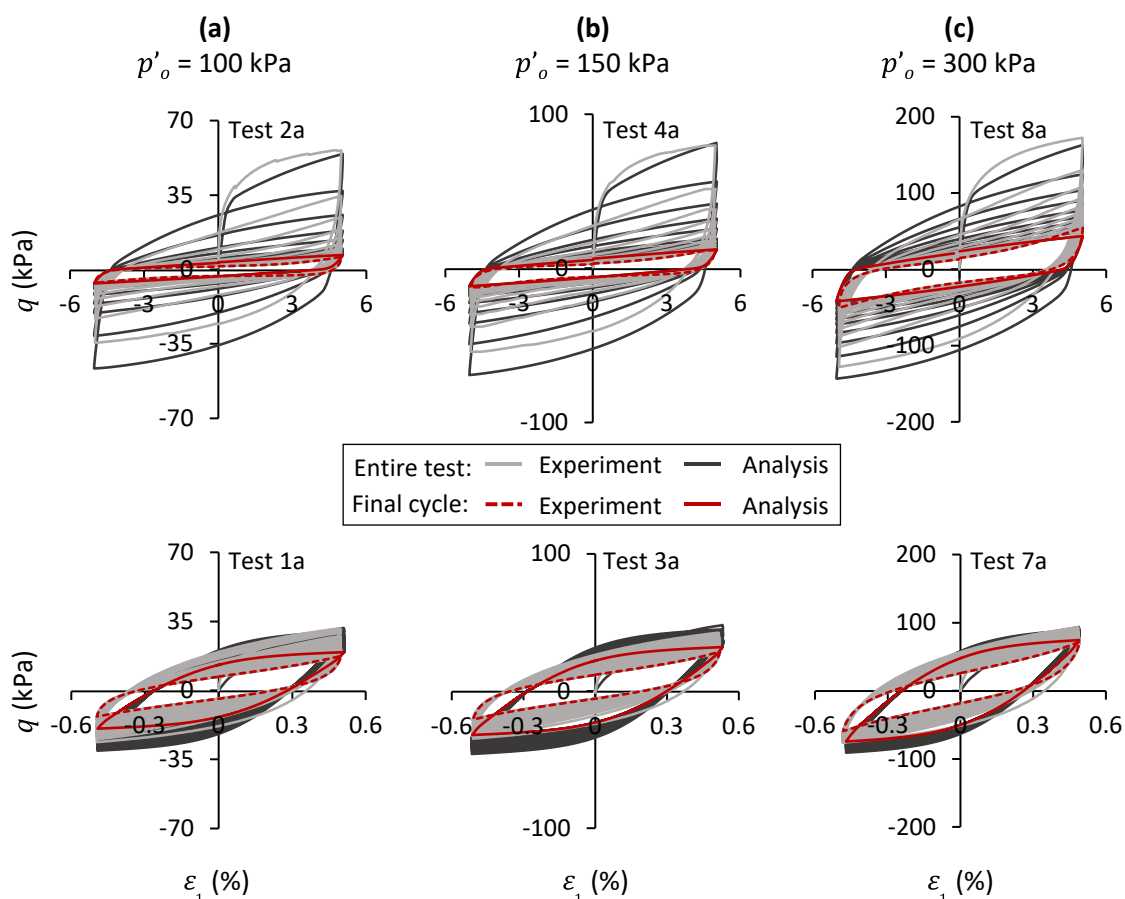


Figure 4.11. VM-CD model prediction vs. experimental results. Deviatoric stress – axial strain ($q - \varepsilon_1$) response for two vertical strain amplitudes $\varepsilon_1^{amp} = 5\%$ (top) and $\varepsilon_1^{amp} = 0.5\%$ (bottom) for three levels of initial mean effective stress: (a) $p'_o = 100$ kPa; (b) $p'_o = 150$ kPa; and (c) $p'_o = 300$ kPa.

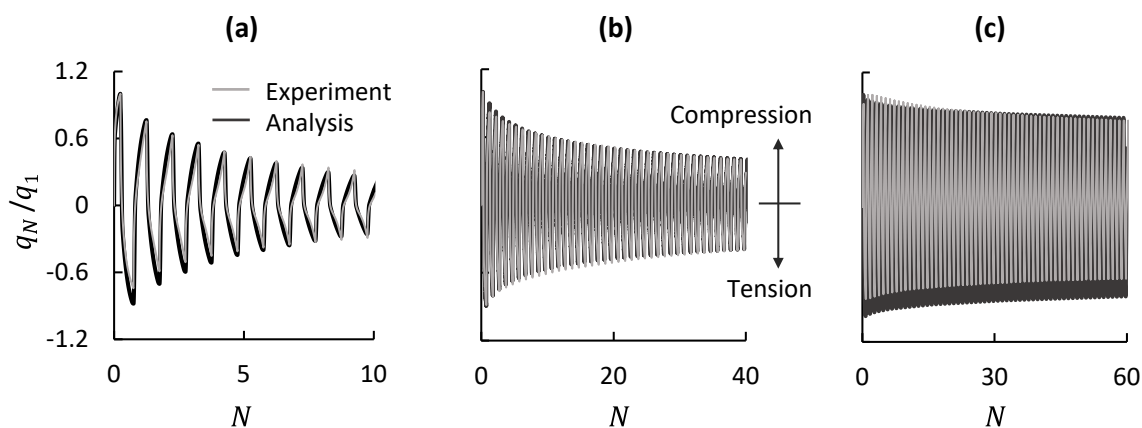


Figure 4.12. Peak deviatoric stress degradation ratio q_N / q_1 (for $p'_o = 300$ kPa) in function of the number of load cycles N and cyclic strain amplitude: (a) $\varepsilon_1^{amp} = 5\%$; (b) $\varepsilon_1^{amp} = 2\%$; and (c) $\varepsilon_1^{amp} = 0.5\%$.

4.4. Validation against cyclic centrifuge tests of a monopile

The model is validated against the centrifuge tests of Li [2019] on monopile foundations in normally consolidated Malaysian kaolin clay (**Table 4.5**). The tests were performed at a centrifuge acceleration of 50 g, measuring the response of a *semi-rigid* pile subjected to cyclic lateral loading. Detailed information on the facility and the experimental setup can be found in Li et al. [2020] and Shi et al. [2023]. The foundation comprises a long, solid section, steel pile of prototype diameter $D = 0.5$ m and length $L = 12$ m ($L/D = 24$), free to rotate at the top (free-head).

Table 4.5 Basic properties of Malaysian kaolin clay used in the Li [2019] centrifuge tests [Shi et al., 2023].

Property	Value
Unit weight, γ_s (kN/m^3)	16.4
Plastic limit, w_p (%)	35
Liquid limit, w_L (%)	74
Angle of internal friction, φ_r ($^\circ$)	25
Undrained shear strength profile, S_u (kPa)	$S_u(z) = 0.27 + 1.35z$

FE modelling

Figure 4.13a depicts the FE mesh for the *semi-rigid* pile and its key dimensions (in prototype scale). A similar mesh configuration has been developed for the *rigid* pile, not shown herein for the sake of brevity. Only half of the experimental setup is modelled, taking advantage of model symmetry. The steel piles are simulated with linear elastic continuum elements of $E = 200$ GPa, Poisson's ratio $\nu = 0.3$, and effective density $\rho' = 68.5$ t/m³. To minimize boundary effects, the distance of the pile to the lateral and bottom boundary is set to $14.5D$ and $8D$, respectively. To improve numerical accuracy, the mesh discretization is finer close to the pile. Following Shi et al. [2023], the soil-pile interface is modelled through frictional contact governed by Coulomb's law, with an appropriate friction coefficient $\mu = 0.4$. The horizontal displacement of the lateral model boundaries is restrained, along with the out-of-plane displacement at the plane of symmetry and the vertical displacement at the model base. Installation effects are not accounted for since the pile was jacked at 1g, and the centrifuge was subsequently spun up to 50g for several hours to allow for pore pressure dissipation and reduction of the installation influence on the initial soil state [Yu et al., 2020].

The soil is modelled as a one-phase medium using nonlinear hexahedral continuum elements (C3D8), employing the VM–CD constitutive model. Its submerged unit weight $\gamma_s' = 6.4 \text{ kN/m}^3$ and the lateral coefficient of earth pressures at rest is set to $K_o = 1 - \sin\phi = 0.577$. The undrained shear strength profile obeys the linear law of **Table 4.5**. Similarly to the previously discussed calibration procedure, we assume the superposition of two backstresses to control the (pre-degradation) nonlinear model behaviour with coefficients: $C_1 = E_o = 235p'_o = 800S_u$, $\gamma_1 = 1480$, $C_2 = 60p'_o$, $\gamma_2 = 162$. The intact soil strength and stiffness parameters are calibrated against the undrained monotonic triaxial tests of Duque et al. [2022] on Malaysian kaolin clay (**Fig. 4.13b**).

For the needs of the validation, we employ published laboratory tests to calibrate the degradation parameters for Malaysian kaolin clay, namely the undrained cyclic triaxial tests of Ho (2013) and the cyclic T-bar penetration test of Yu et al. (2018) (**Figs. 4.13c-d**). Equation (4.4) fits the curve of **Fig. 4.13d** for $d_{rem} = 0.33$, $\xi^T_{95} = 33.2$, and $\xi^T = 2N_{T-bar}\varepsilon_{\gamma,T}$, where N_{T-bar} are the T-bar cycles, $2\varepsilon_{\gamma,T} = 7.68$ is the maximum plastic shear strain accumulated during one cycle of T-bar penetration, i.e., two passes of the T-bar (Yu et al., 2018), and ξ^T_{95} is the maximum cumulative plastic shear strain required to cause a 95% reduction in shear strength due to the cyclic T-bar movement. For the simulations, parameter ξ^T_{95} is modified following the procedure proposed by Yu et al. [2018] to consider the different deformation mechanisms associated with soil-pile interaction and T-bar penetration. Consistently with its higher plasticity value [Poudel et al., 2019], Malaysian kaolin clay has lower sensitivity ($1/d_{rem} = 0.33 \approx 0.3$) compared to the kaolin tested at ETHZ. The material coefficients for Eqs. (4.8) and (4.9) are summarized in **Table 4.6** in comparison to those obtained for Kaolin K1 (Section 4.2). It is interesting to observe that the ‘power coefficients’ (i.e., b , c , e and f) are consistent across both materials, potentially suggesting that for soils with similar properties, they may be treated as constants in Eqs. (4.8) and (4.9). However, this hypothesis requires further experimentation to be fully confirmed. Furthermore, **Fig. 4.14** illustrates the range of parameters k and m for the two materials examined in this study. As observed, for the higher sensitivity Kaolin K1, k tends to increase, denoting a faster degradation of b_e , while the opposite occurs for parameter m , indicating a lower ξ margin for stiffness to reach its residual value. At the element level, the cyclic response of the calibrated VM–CD model compares well with the undrained triaxial tests of Ho [2013].

Table 4.6. Constants of Eqs. (4.8) and (4.9) calibrated for Malaysian kaolin clay, in comparison to the values obtained for Kaolin K1.

Constant	Malaysian kaolin clay	Kaolin K1	Constant	Malaysian kaolin clay	Kaolin K1
a	4.000	13.67	d	0.320	0.210
b	0.392	0.392	e	0.543	0.543
c	0.402	0.402	f	0.537	0.537

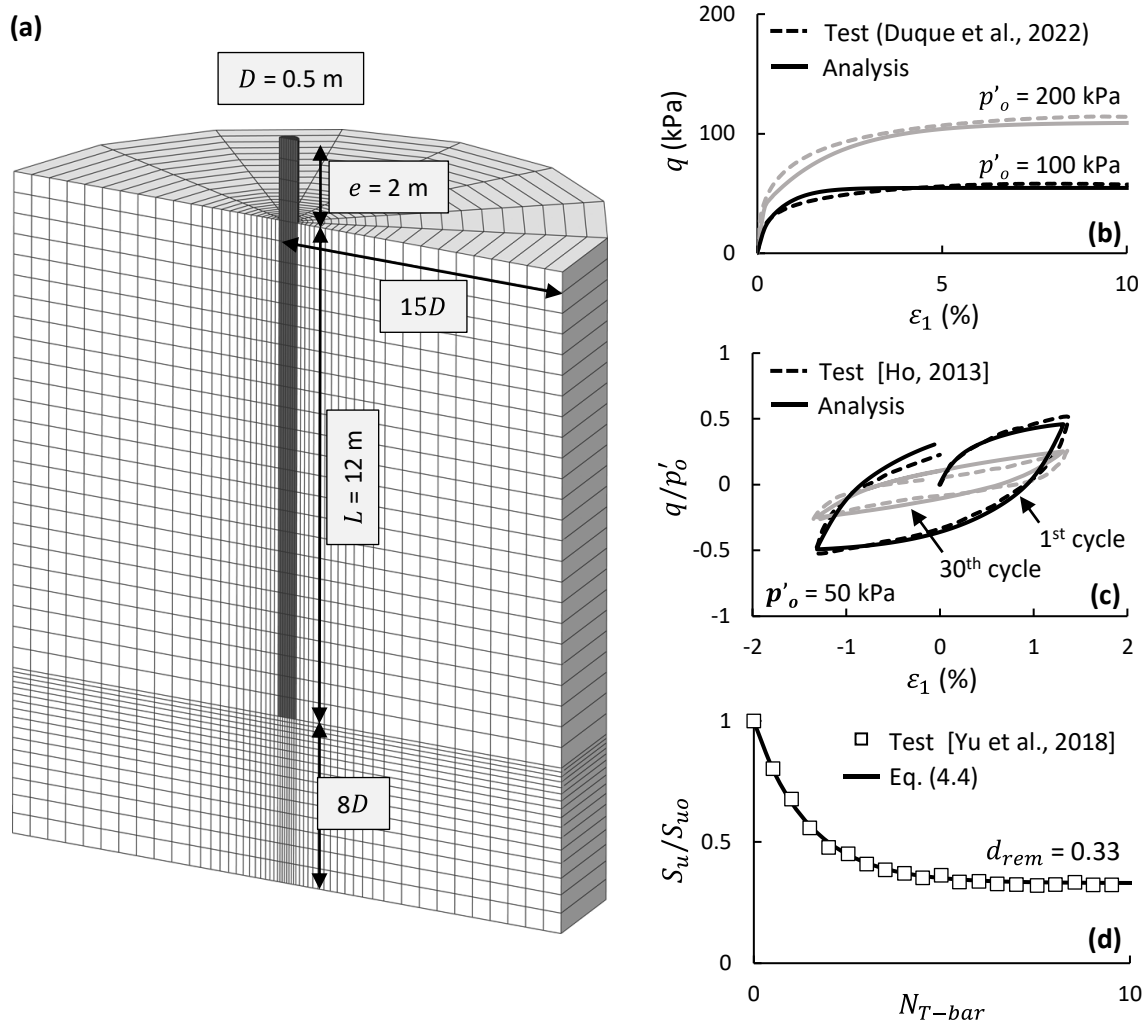


Figure 4.13. Validation against the centrifuge model tests of Li [2019]: (a) FE model of the pile-soil experimental setup (dimensions in prototype scale); (b) numerical prediction vs. undrained triaxial monotonic tests of Malaysian kaolin clay [Duque et al., 2023]; (c) numerical prediction vs. undrained triaxial cyclic tests at $p'_o = 50$ kPa [Ho, 2013]; and (d) adopted strength degradation S_u/S_{u0} with the number of T-bar penetration cycles [Yu et al., 2018].

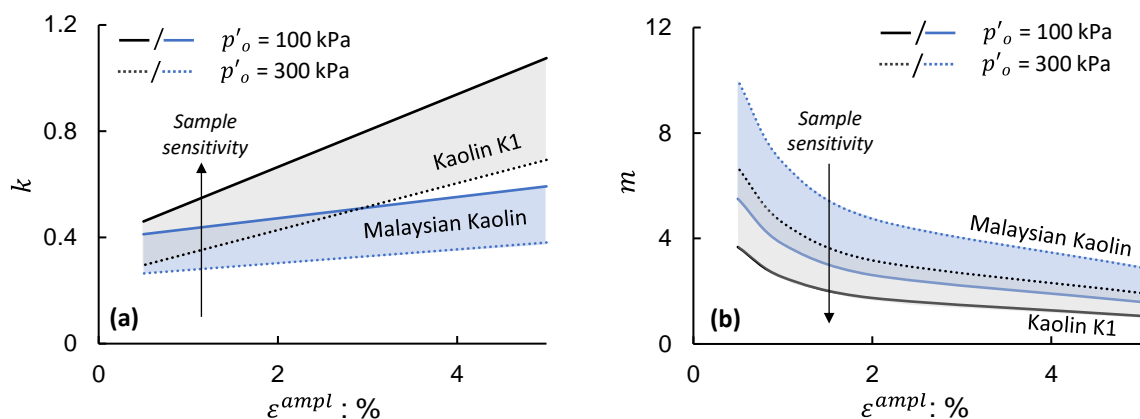


Figure 4.14. Range of parameters k and m for Kaolin K1 and Malaysian Kaolin clay.

Numerical prediction vs. experimental results

We compare the numerical predictions to the centrifuge test results both for the monotonic and the cyclic response of the pile under cyclic displacement of magnitude u_{max} . As in the tests, the lateral load is applied in a displacement-controlled manner at the pile head, at a distance $e = 2$ m above the mudline (prototype dimensions). The FE analysis is conducted in two consecutive steps: (a) static application of dead loads; and (b) static application of lateral displacement u in the case of monotonic loading or dynamic time history analysis of 15 lateral displacement cycles of $u_{max} = 0.05D$ or $0.1D$ in the case of cyclic loading.

The numerical prediction is compared to the centrifuge test results in **Figs. 4.15** and **4.16**. Focusing on monotonic pile response, **Fig. 4.15a** compares the analysis to the experiment in terms of dimensionless horizontal reaction force $H/S_{uo,av} DL$, where $S_{uo,av}$ is the average undrained shear strength at the pile mid-length (equal to 8.3 kPa), in function of dimensionless pile head displacement u/D . The analysis adequately predicts the pile resistance, both in terms of lateral capacity and stiffness.

Figure 4.15b plots the evolution of the dimensionless peak pile reaction force ($H_N/S_{uo,av} DL$) with the number of load cycles N for the cyclic loading tests. The numerical model effectively predicts the degradation of lateral resistance at both levels of u_{max} , confirming the VM-CD model's capability to capture cyclic foundation response in the presence of cyclic degradation. However, as revealed by the force-displacement loops of **Fig. 4.16**, the numerical model underestimates the hysteretic damping of the pile-soil system, especially for small displacement amplitudes (**Fig. 4.16a**, $L/D = 24$, $u_{max} = 0.05D$). The

experimental results exhibit a stiffer unloading response, which is not captured by the FE model.

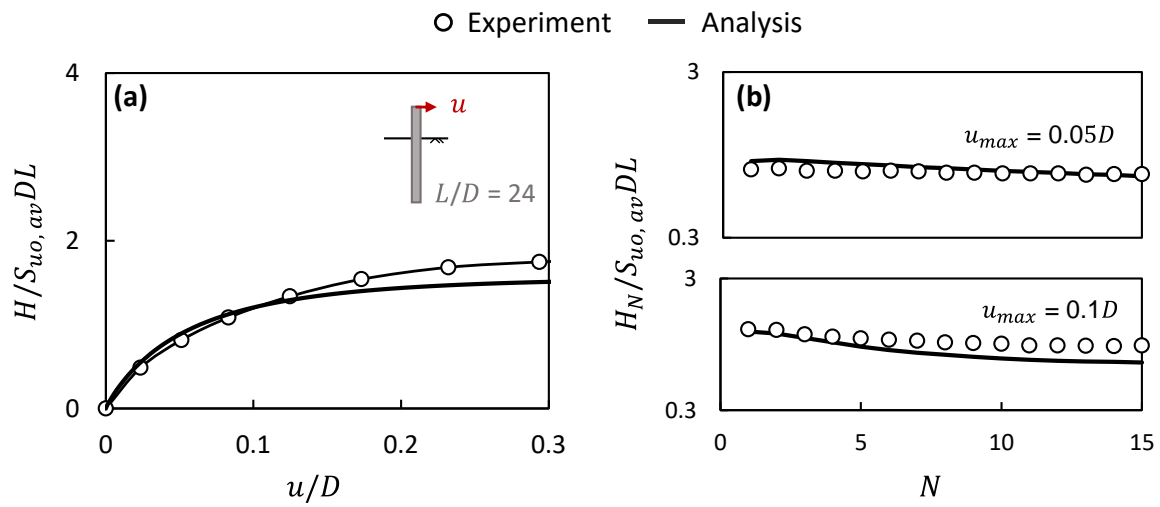


Figure 4.15. Numerical prediction vs centrifuge test results (Li, 2019): (a) dimensionless horizontal force-displacement response ($H/S_{u_o, av}DL - u/D$) under monotonic loading; and (b) degradation of peak dimensionless lateral reaction force ($H_N/S_{u_o, av}DL$) in function of load cycles N .

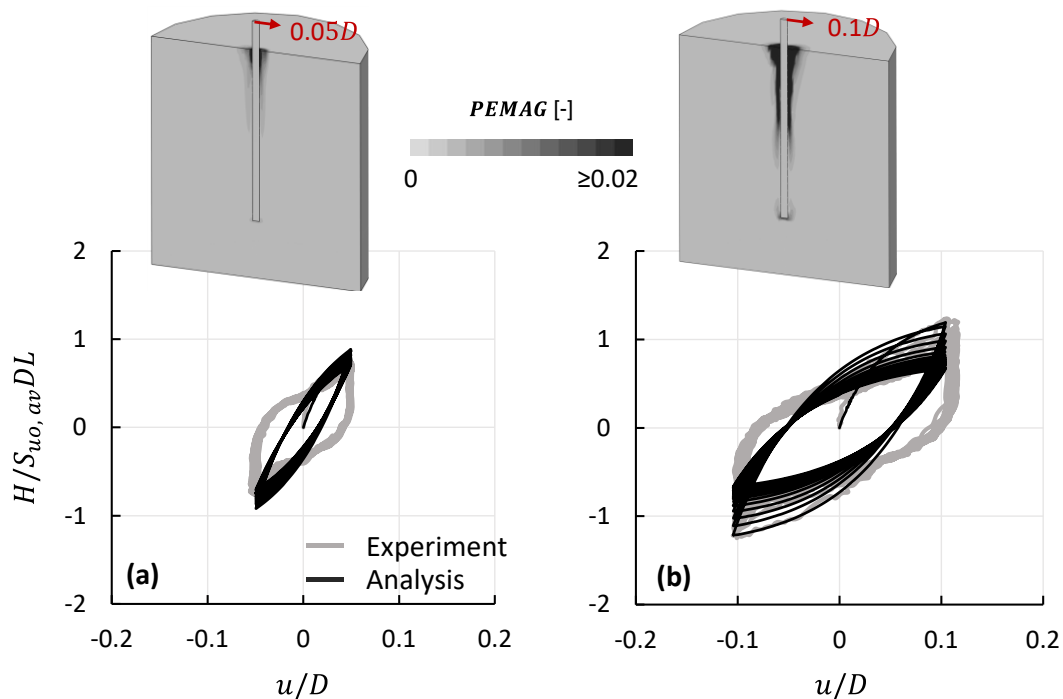


Figure 4.16. Numerical prediction vs centrifuge test results (Li, 2019). Dimensionless cyclic lateral force-displacement response ($H/S_{u_o, av}DL - u/D$) for the pile under: (a) $u_{max} = 0.05D$; and (b) $u_{max} = 0.1D$. Contours of plastic strain magnitude at the end of loading are plotted above the charts.

This discrepancy is attributed to the absence of a more sophisticated elastic model to characterize the nonlinear variation of soil stiffness at small strains. Shi et al. [2023] present a better comparison of the numerically computed damping against the same experiments, combining their AUC-Clay model with an intergranular strain elastic model to model stress-strain nonlinearity at small strains. With increasing cyclic amplitude, the nonlinearity of the soil-foundation system prevails, and the hysteresis loops grow (**Fig. 4.16b**, $L/D = 24$, $u_{max} = 0.1D$), thus diminishing the effect of small strain stiffness.

4.5. Suction caisson in sensitive cohesive soil: cyclic loading

The validated VM–CD model is employed to derive deeper insights into the cyclic performance of suction caisson foundations in soft soils of degrading stiffness and strength under environmental (wind and wave) cyclic and seismic loading. The most common application of suction caissons in the offshore wind industry is related to jacket-supported OWTs, where caissons are designed to resist environmental overturning moments through an axial push-pull mechanism. A more unconventional application for deep-sea installations was recently analyzed by Antoniou et al. [2019], involving a compliant OWT tower tethered to the ground via taut wires, which in turn are moored to the seabed by suction caissons (guyed system). Due to its efficiency, the industry is currently testing a similar idea¹¹ in the form of the FRP (fully restrained platform) foundation.

Consistent with these applications, we investigate suction caisson performance under vertical and inclined cyclic loading at the top, with the analyses reflecting loading conditions on individual caissons supporting a jacket structure or a guyed system, respectively. Particular focus is given to the effect of aspect ratio L/D on overall foundation performance and its sensitivity to cyclic degradation effects. Due to the relatively low aspect ratios encountered in this foundation type, even small variations of the L/D ratio may significantly alter the contribution of shaft and base resistance to the ultimate capacity of the caisson and, hence, the rate of accumulated deformations. Therefore, the scope of this investigation is twofold: (a) to assess the importance of accounting for cyclic degradation phenomena when assessing substructure (soil/foundation) deformations under cyclic/seismic loading, and (b) to weigh the

¹¹ <https://www.entrionwind.com/technology>

benefits between caissons of the same (static) safety factor, but of different geometry during the design of foundations in soils of degrading capacity.

Geometry and FE modelling

Two suction caisson configurations of varying geometry are parametrically examined: $L/D = 0.5$ and 2 , termed hereafter ‘shallow’ and ‘deep’, respectively. The caissons are embedded in a non-uniform stratum of normally consolidated kaolin, described by the calibrated and validated VM–CD model. Its submerged unit weight equals $\gamma_s' = 7.3 \text{ kN/m}^3$. The employed 3D FE model geometry is presented in **Fig. 4.17**, following the previously described principles. The steel suction caissons are assumed to be fully bonded to the soil (i.e., no separation or detachment is allowed), an assumption justified in the case of rapid seismic loading or storm surges, during which excess pore water pressures cannot dissipate, and passive suction is maintained beneath the caisson lid. The caissons are expected to display a ‘sealed’ failure mode [Randolph & House, 2002], comprising the end-bearing resistance of the bottom caisson area and the shearing resistance between the soil and the external caisson surface.

Cyclic loading at the caisson top: the effect of aspect ratio L/D

The examined caissons are subjected to vertical or inclined ($\varphi = 45^\circ$) cyclic loading, consisting of constant amplitude symmetric load cycles ($f = 0.1\text{Hz}$), attempting to provide an initial manifestation of the effect of L/D on foundation response. The adopted loading scenario serves well the purpose of this preliminary investigation; yet, understandably, it cannot be considered typical for OWT foundations under environmental loading, where a certain load asymmetry would be expected from the simultaneous action of complex wind and wave forces on the turbine tower. In order to isolate the effect of aspect ratio on foundation response, the dimensions are selected accordingly to provide very similar stiffness and resistance characteristics (i.e., the same safety factor) against static loading. The studied caisson diameter D , length L , and thickness t_w pertaining to each case are summarized in **Table 4.7**, along with their ultimate capacities under vertical or inclined loading (whichever is relevant).

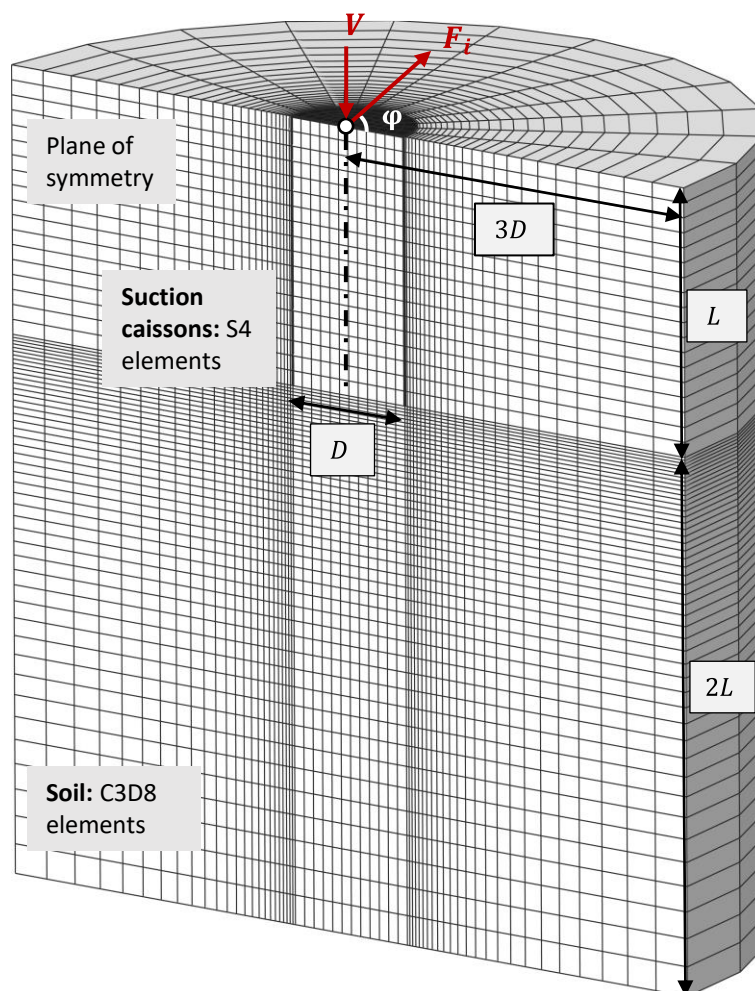


Figure 4.17. FE model discretization and key geometric properties for the suction caisson.

Table 4.7. Geometric properties and ultimate capacity of the *shallow* and *deep* caissons subjected to vertical and inclined cyclic loading.

Vertical cyclic loading, V ($\varphi = 0^\circ$)				
L/D	L (m)	D (m)	t_w (m)	V_{ult} (MN) ¹
0.5	4.5	9	0.1	4
2.0	10.26	5.13	0.055	4
Inclined cyclic loading, F_i ($\varphi = 45^\circ$)				
L/D	L (m)	D (m)	t_w (m)	F_{ult} (MN) ²
0.5	4.5	9	0.1	1.7
2.0	10.9	5.45	0.06	1.7

¹ Defined at vertical displacement $w = 0.45\text{m}$ ($0.05D$ and $0.09D$ for the $L/D = 0.5$ and $L/D = 2$ caissons, respectively).

² Defined at inclined displacement $v = 0.45\text{m}$ ($0.05D$ and $0.08D$ for the $L/D = 0.5$ and $L/D = 2$ caissons, respectively).

Response to vertical cyclic loading ($\varphi = 0^\circ$)

Results under axial loading of amplitude $V^{ampl} = 1\text{MN}$ (corresponding to a safety factor $SF_{V,c} = V_{ult}/V = 4$ for cyclic loading) are presented in **Figs. 4.18a** and **4.19**. **Figure 4.18a** compares the vertical force-displacement ($V - w$) loops of the shallow and deep caissons, while their settlement time histories are depicted in **Fig. 4.19a**. The case of no cyclic degradation is also included in **Fig. 4.19a** (dashed lines) in terms of maximum settlement w per load cycle. **Figure 4.19b** plots the evolution of effective safety factor $SF_{eff} = V_{post,N}/V$ for both caissons, denoting the reduced post-cyclic caisson capacity $V_{post,N}$ after N cycles of loading, in function of the applied cyclic load amplitude $V = 1\text{MN}$. The plotted points are the result of push-down analyses following $N = 0, 15, 30$ and 45 load cycles (see the grey-shaded plot, which presents the push-down curves of the deep caisson).

Not surprisingly (considering the fast degradation rate of the examined kaolin), the absence of degradation results in trivial deformation accumulation throughout the applied loading, denoting a quasi-elastic soil response that leads to a settlement $w \approx 10$ mm for both caissons at the end of loading. On the other hand, the plastic strain accumulation results in a decrease of the foundation secant stiffness and strength for the caissons in *degrading* soil, evident in the increasing inclination of the force-displacement hysteresis loops in **Fig. 4.18a** and the post-cyclic capacity curves of the deep caisson in **Fig. 4.19b**. This initially occurs at a somewhat slower rate for the $L/D = 2$ caisson due to the higher mean effective stress at deeper soil strata. At $N = 30$, the settlement reaches $w = 21$ mm and 18 mm for the deep and shallow caisson, respectively (**Fig. 4.19a**).

Past this point, significant deviations are observed for the two systems that are certainly worth discussing. While the shallow caisson continues accumulating settlement at a stable rate (**Fig. 4.19a**), the deep caisson displays an abrupt change in accumulation rate, with w reaching about 85 mm by the end of loading, compared to a mere 22 mm for the $L/D = 0.5$ caisson. The ‘swollen’ force-displacement loop of the deep caisson at $N = 45$ (**Fig. 4.18a**) is representative of the largely inelastic system response. This may appear counter-intuitive, as the $L/D = 2$ caisson reaches deeper into the soil, which should display a lower rate of cyclic degradation due to the larger mean effective stress.

The response can be explained, however, by the different contributions of shaft friction and base resistance to the ultimate axial capacity of the two caissons. Due to its shape, the

shallow caisson resists the vertical load mainly by the mobilized base resistance: let's consider simplistically that the shaft contributes $V_{shaft} = S_{u,av}(\pi DL) \approx 500$ kPa, where $S_{u,av}$ is the average shear strength at the caisson mid-length. With the base resistance being dominant, a rather ductile failure mode is expected [Chen & Randolph, 2005]. In contrast, the *deep* caisson mobilizes primarily shaft resistance (with an approximate $V_{shaft} \approx 1700$ kPa), and hence, a more brittle failure should be expected upon its exhaustion. Under the applied loading, shear zones tend to form first along the shaft due to the more brittle nature of this resistance mechanism. The soil along the caisson periphery is significantly impacted by cyclic degradation, which reduces its stiffness and strength upon plastic shear strain accumulation with every load cycle. Shaft resistance is eventually depleted for both caissons prior to the end of loading ($N = 50$), as revealed by the contour plots of parameter b_e after $N = 45$ cycles (**Fig. 4.21a**): the soil around the shaft displays more than 70% reduction of its initial stiffness. For the *deep* caisson, this occurs between $N = 30$ and 45, as implied by the reduction of the effective safety factor from $SF_{eff} = 4$ ($N = 0$) to 3 ($N = 30$), and eventually 1.8 at $N = 45$. The apparent capacity drop explains the sudden increase in settlement accumulation for the rest of the load package, as the caisson gradually loses more than half of its bearing capacity. For the $L/D = 0.5$ caisson, the loss of shaft resistance is not a major issue; the foundation continues to settle towards a more ductile failure mechanism, relying on its significant remaining base resistance (note that $SF_{eff} = 2.8$ after 45 load cycles, which implies the exhaustion of shaft resistance, as well as a slight reduction of base resistance).

Response to inclined cyclic loading ($\varphi = 45^\circ$)

The results for inclined loading are presented in **Figs. 4.18b** and **4.20**. The cyclic amplitude $F^{ampl} = 0.6$ MN corresponds to a lower safety factor ($SF_{I,c} = F_{i,ult}/F_i = 2.85$) compared to vertical cyclic loading, aiming to drive the caissons closer to failure and explore the developing failure mechanisms in view of soil degradation. In an actual taut-wire system, the wire pretension force would act on the foundation as an average inclined load prior to the application of cyclic actions (i.e., resulting in one-way cyclic loading). However, for the sake of simplicity, loading in this analysis series is also considered symmetric.

Figure 4.18b plots the inclined lateral force-displacement ($F_i - u$) response for both caissons up to cycle $N = 24$ (failure cycle for the low aspect ratio caisson), while **Fig. 4.20** displays the evolution of horizontal and vertical caisson displacement (u and w) with the

number of load cycles. Under such combined axial-lateral loading ($\varphi = 45^\circ$), the lateral mechanism prevails over the vertical one, being the critical mode of deformation for the examined caissons. Contrary to what was concluded in the case of vertical cyclic loading, the deep $L/D = 2$ caisson performs marginally better under inclined loading, sustaining three additional load cycles prior to failure (i.e., before displacements start increasing at an exponential rate). In both cases, the caissons primarily resist cyclic inclined loading by forming conical (active and passive) wedges at their sides. Consistent with previous studies [Randolph & House, 2002], an external base scoop is additionally developed at the base of the *deep* $L/D = 2$ caisson (**Fig. 4.21b**), with its centre of rotation between the bottom of the conical wedge and the caisson bottom. For the *shallow* $L/D = 0.5$ caisson, whose centre of rotation lies below the caisson base, the internal soil plug shears relative to the external soil, creating an inverted scoop mechanism around the centre of rotation.

The ductile load resistance mechanism for both configurations now favours the *deep* caisson, which enjoys a slower cyclic deterioration rate stemming from the higher mean effective stresses along its length. A certain asymmetry is observed in the force-displacement response of the *shallow* caisson near failure (**Fig. 4.18b**, cycle $N = 24$), explained by the fast degradation at large plastic strains and the fact that cyclic degradation initiates upon the first load reversal (which here occurs under positive loads). Due to this very characteristic, the soil is bound to display lower properties during the 1st quarter of cycle N (maximum positive load), compared to the 3rd quarter of cycle $N - 1$ (maximum negative load), an effect that becomes more pronounced when the accumulated strains are large enough to produce a considerable decrease of soil stiffness and strength within the course of one load cycle. As a result, lower soil properties lead to more significant deformation towards the positive side, i.e., the direction of the first load reversal.

Comparison with the FE analyses in *non-degrading* soil confirms the dominant effect of strength and stiffness degradation (**Fig. 4.20**, dashed lines). Under the 50 cycles of applied loading, the caissons behave elastically, with no signs of displacement accumulation and maximum lateral/vertical displacements $u \approx 17$ mm and $w \approx 4$ mm, respectively. For soils exhibiting significant degradation, such as the one examined herein, cyclic foundation safety factors should be selected to limit straining below a threshold strain amplitude where no cumulative effects occur.

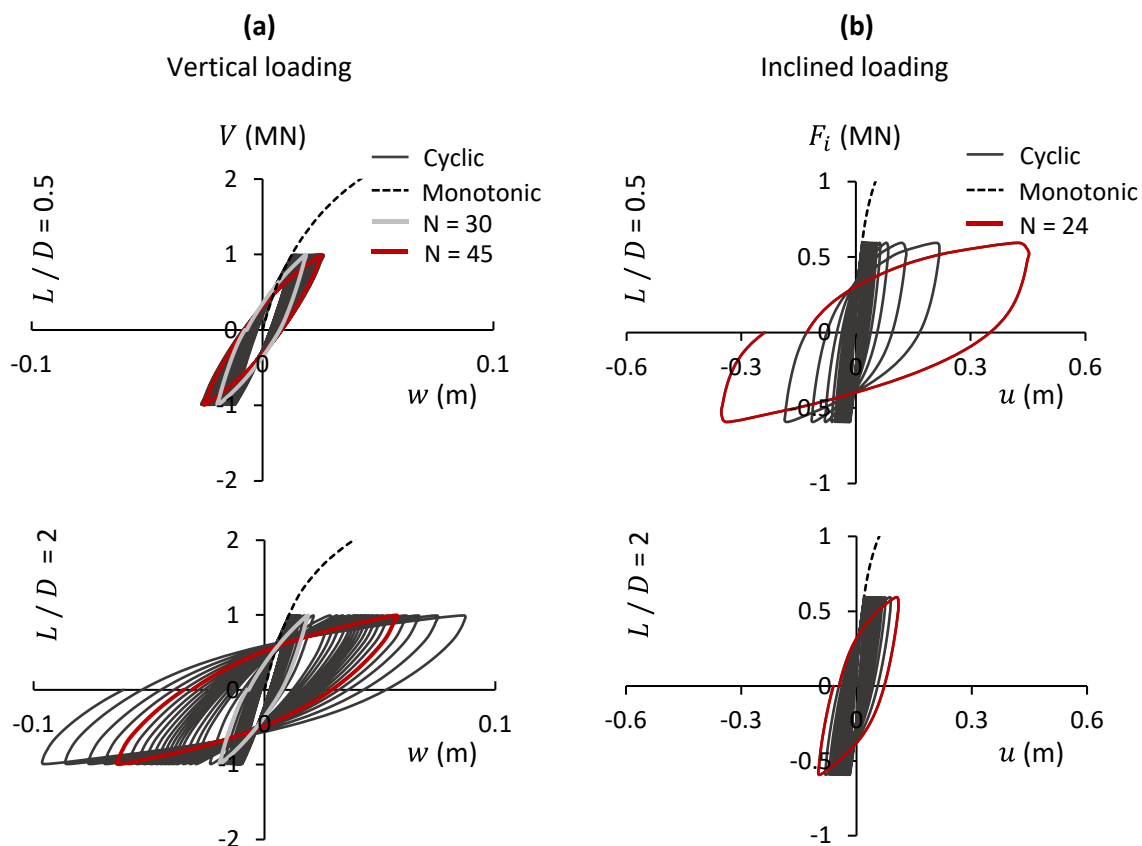


Figure 4.18. The effect of caisson aspect ratio (L/D) for vertical and inclined cyclic loading: force-displacement response for the $L/D = 0.5$ (top) and $L/D = 2$ (bottom) caissons subjected to: (a) vertical; and (b) inclined loading.

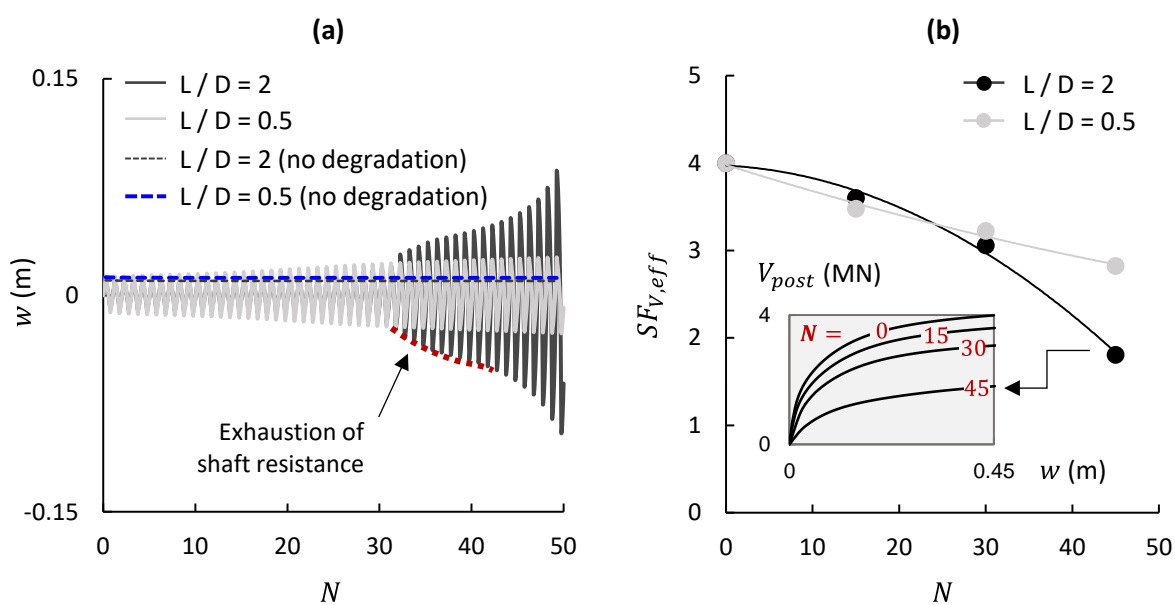


Figure 4.19. Effect of caisson aspect ratio (L/D) under vertical cyclic loading: (a) vertical displacement w and (b) effective safety factor $SF_{V,eff}$ vs. the number of load cycles N .

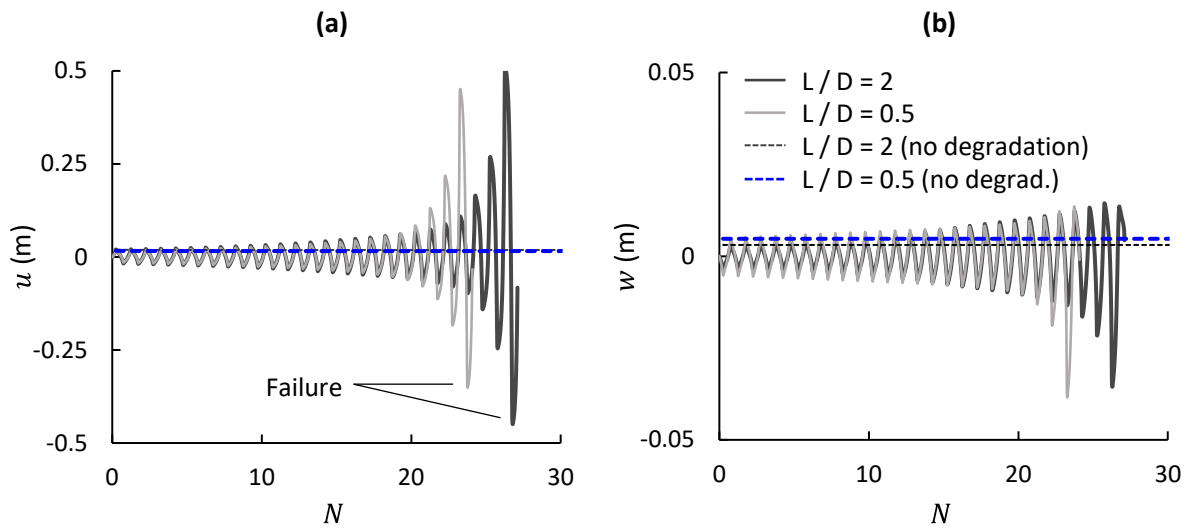


Figure 4.20. Effect of caisson aspect ratio (L/D) under inclined cyclic loading: (a) horizontal displacement u ; and (b) vertical displacement w vs. the number of load cycles N .

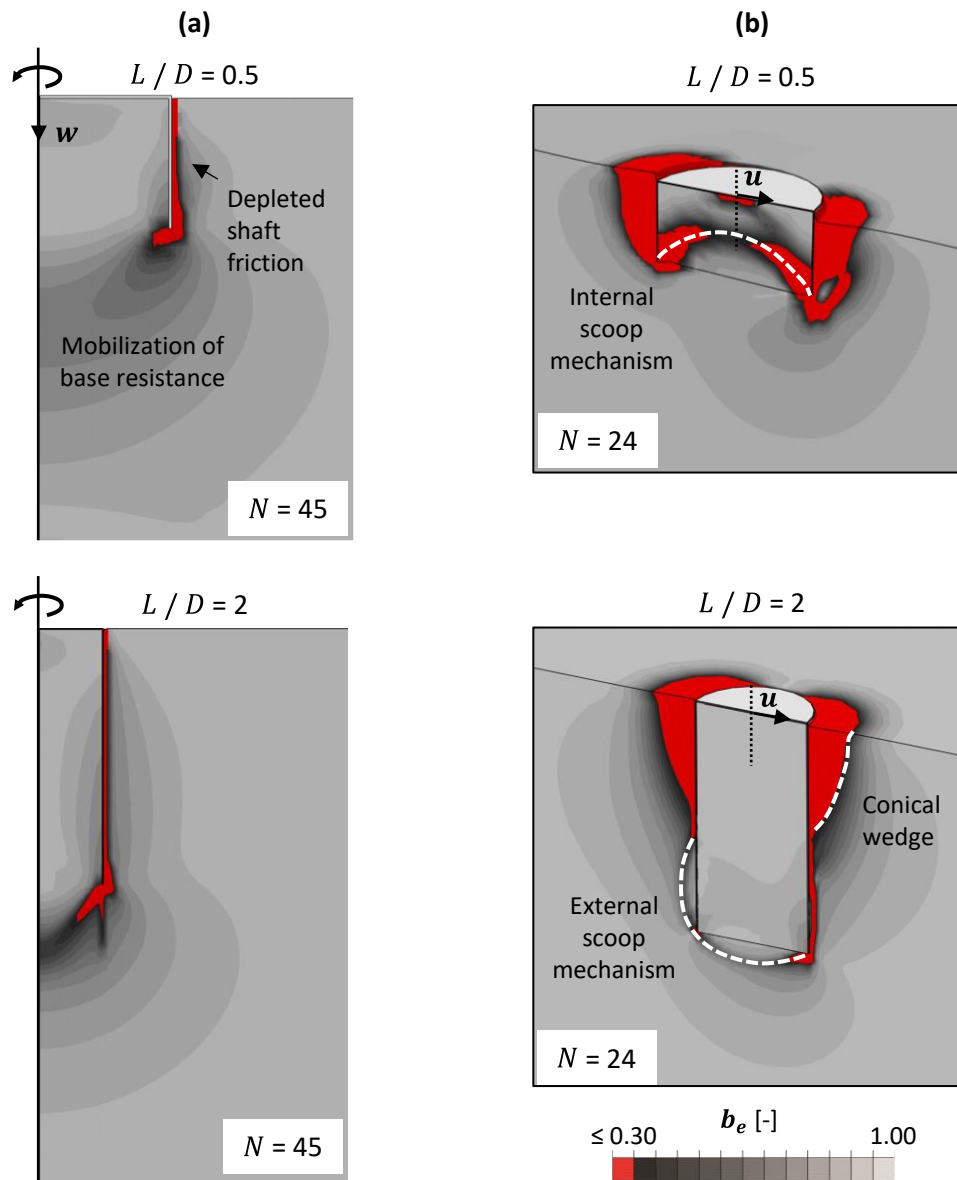


Figure 4.21. The effect of caisson aspect ratio (L/D) under vertical and inclined cyclic loading: (a) contours of degradation parameter b_e after $N = 45$ cycles of vertical loading; and (b) contours of degradation parameter b_e after $N = 24$ cycles of inclined loading.

4.6. Suction caisson in sensitive cohesive soil: seismic loading

Two loading scenarios are considered to investigate the seismic vulnerability of suction caissons given the discussed soil degradation phenomena:

A. Caissons under seismic loading in degrading soil, simulating the case of an earthquake striking during parked OWT conditions. The caissons are subjected to seismic shaking (applied at the model base), idealized for simplicity by a Tsang-type pulse of predominant frequency $f_E = 1.1\text{Hz}$ and peak ground acceleration $a = 0.1g$ (**Fig. 4.22a**).

B. Caissons under seismic loading in non-degrading soil: The loading assumptions are identical to Scenario A, yet soil degradation is not accounted for, allowing us to quantify its effect in comparison to Scenario A.

The boundary conditions are modified for the dynamic time history analyses (**Fig. 4.22b**). Appropriate kinematic (MPC) constraints are imposed at the lateral boundaries to simulate free-field soil response (i.e., a rigid disc is created at each level by applying kinematic constraints between the node on the central axis and each peripheral node). Dashpot elements are introduced at the model base to reproduce radiation damping. The damping coefficient is calculated as:

$$C_{dash} = \rho V_s A \quad (4.12)$$

where: ρ is the material density; V_s is the shear wave velocity; and A the effective dashpot area. The shear wave velocity is set to $V_s = 300\text{ m/s}$, assuming that the simulated soil stratum overlies a significantly stiffer formation. A Rayleigh damping $\xi_R = 2\%$ is adopted to ensure viscoelastic response under low strain amplitudes.

The soil profile is amended in this analysis series to reflect an inhomogeneous kaolin stratum of undrained shear strength $S_{uo} = S_{uo,surf} + \kappa\sigma'_v$, where $S_{uo,surf} = 27\text{ kPa}$ is the shear strength at mudline. This assumption allows for avoiding extended acceleration cut-offs due to soil plastification close to the ground surface, where the soil stiffness and strength are low and degradation rates are quite high, aiming to keep the focus on the assessment of variations in foundation performance under the examined seismic scenarios. It is acknowledged that the adopted trapezoidal strength profile is more typical of an overconsolidated soil rather than the normally consolidated kaolin, for which the VM-CD model is calibrated, suggesting that the analysis results may overpredict the developed

foundation deformations in such profiles. In the context of the comparative study performed herein, such an assumption is not expected to affect the qualitative nature of the derived conclusions. The geometry and ultimate axial capacity of the $L/D = 0.5$ and 2 caissons in the amended soil profile are summarized in **Table 4.8**. Once again, the foundations are designed to have the same static safety factor and similar elastic behaviour under vertical loading, considering the latter as the critical (environmental) design load for caissons supporting jacket OWTs.

Table 4.8. Geometric properties and ultimate capacity of the *shallow* and *deep* caissons under seismic loading.

L/D	L (m)	D (m)	t_w (m)	V_{ult} (MN)
0.5	4.5	9	0.1	20
2.0	11.6	5.8	0.06	20

Response to earthquake loading

The analysis is performed in two consecutive steps. Gravitational loading is applied in the first step, followed by seismic loading in the second step. The acceleration time history at the free-field ground surface is depicted in **Fig. 4.22a** for the shallow caisson under Scenario A, being almost identical to that of Scenario B. The applied input motion reaches the surface with a delay, reflecting the time required for the seismic waves to propagate through the simulated soil stratum, while a slight amplification is observed ($a = 0.14g$), attributed to the natural frequency of the soil lying close to the dominant frequency of the seismic motion.

Figure 4.22 (c-d) plots the settlement-rotation ($w - \theta$) response of the foundations subjected to Scenarios A and B. Both caissons are strongly affected by degradation effects (Scenario A), sustaining significant irrecoverable settlements (**Fig. 4.22c**): $w = 57$ mm and $w = 24$ mm for the shallow and deeply embedded caissons, respectively. This is in contrast with observations made in previous studies [e.g., Kourkoulis et al., 2014], where suction caissons in stiffer clay profiles were shown to behave almost elastically under seismic loading when environmental actions were disregarded (deformations experienced during one seismic load cycle were ultimately recovered during the next). In the case examined herein, the inherently soft soil profile and the fast cyclic degradation rate lead to an increasing trend in permanent deformations. The caissons' loading resistance decreases from one loading cycle to another, thus introducing a type of 'asymmetry', which, along with the kinematically-induced shearing

at the caisson sides, results in a *rocking*-dominant foundation response and the development of residual settlements. The latter is evident in the shape of the settlement-rotation curves of **Fig. 4.22c**, which imply that the caissons lean towards the left or right during subsequent load cycles, thereby accumulating settlement (i.e., sinking) during both negative *and* positive acceleration peaks. The settlement accumulation mechanism is similar – yet less detrimental – to that described in Antoniou et al. [2022] for suction caissons subjected to combined environmental and seismic loading. The *rocking* motion is more pronounced in the case of the *deep* caisson, as evidenced by the increased rotation $\theta = 2.5$ mrad, compared to 0.7 mrad of the *shallow* caisson. This is explained by its greater embedment depth, which implies larger induced (lateral) differential displacements due to the kinematic response of the soil stratum. Contours of plastic soil strains at the end of loading are illustrated in **Fig. 4.23a** for the degrading soil scenario (Scenario A).

Despite being comparable in terms of vertical safety factor SF_v , the two caissons exhibit a considerably different performance in degrading soil (Scenario A), with settlement buildup being more than 50% lower in the case of the *deep* caisson. To a limited extent, this is attributed to the marginally lower axial flexibility of the *shallow* caisson. However, the discrepancy is predominantly the result of kinematically-induced stressing, which does not solely engage axial caisson resistance. Under the *rocking* motion, the $L/D = 2$ caisson engages its horizontal side resistance (passive/active soil state), in addition to vertical shearing on the sides and the base resistance, resulting in increased dissipation of seismic energy from the side soil and a gradual, more ductile sequence in soil plasticity (i.e., a more diffuse soil plastification mechanism), which leads to the development of overall lower residual settlement. The $L/D = 2$ caisson displays twice as high L rotational resistance compared to the *shallow* one ($M_{ult, L/D=2} = 46$ MN $>$ $M_{ult, L/D=0.5} = 22.5$ MN at $\theta = 10$ mrad), thereby safely sustaining the larger induced rotations.

Non-consideration of cyclic degradation (Scenario B) results to a 50% decrease in permanent settlements ($w < 25$ mm in both cases, **Fig. 4.22d**) and significantly less soil yielding in the vicinity of the caissons (**Fig. 4.23b**). The observed settlement difference is, of course, expected to diminish for soils with less abrupt strength and stiffness degradation (e.g., soils of higher plasticity). Even so, the presented results serve as preliminary evidence of the need to account for cyclic degradation effects in the seismic assessment of offshore foundations,

especially for soils of low strain-rate dependency that cannot benefit from the enhancement of undrained shear strength during high-frequency shaking.

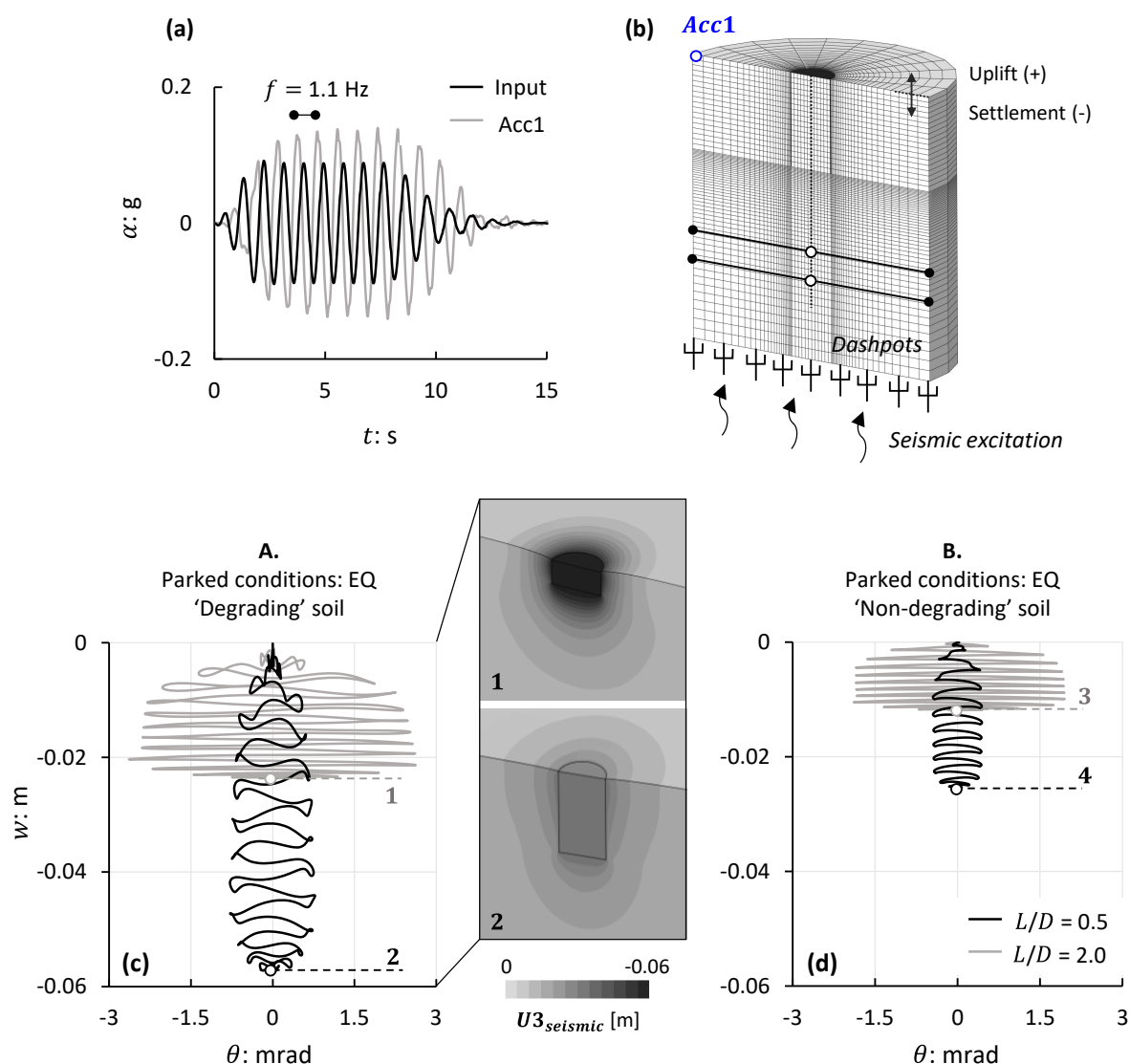


Figure 4.22. Seismic loading: (a) input motion ($a_{max} = 0.1g$) compared to the free-field acceleration (Acc1); (b) modified FE model boundaries for the dynamic time history analyses; (c), (d) settlement-rotation ($w - \theta$) curves of the shallow and deep caissons during seismic loading under: (a) Scenario A; and (b) Scenario B. The contours of seismic soil-foundation vertical deformation ($U3_{seismic}$) at the end of shaking are illustrated for Scenario A.

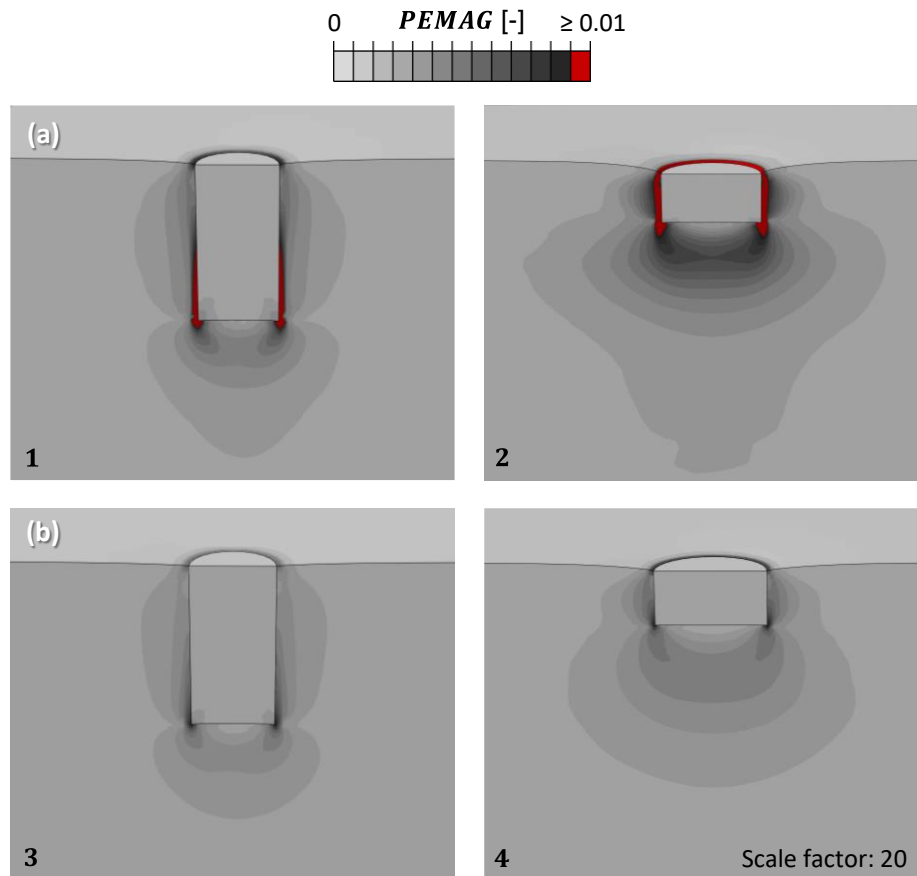


Figure 4.23. Contours of plastic strain magnitude at the end of seismic loading for: (a) Scenario A (points 1 – 2 in Fig. 22); and (b) Scenario B (points 3 – 4 in Fig. 4.22).

4.7. Study Limitations

The following study limitations are recognized and are outlined here as recommendations for future work:

- (1) The presented model is developed and validated on the basis of bi-directional, symmetric tests. Although we anticipate reasonable performance under conditions of limited load asymmetry, additional testing is required to validate this assumption. Moreover, the formulation of the model may need to be adapted to ensure optimal performance under strongly non-symmetric (unidirectional) cyclic loading. To confirm the model's broader applicability under such scenarios, comparisons against centrifuge model tests should be performed. The latter is envisaged as part of our ongoing research on the subject by utilizing the recently established ETHZ geotechnical centrifuge center to perform one-way cyclic tests on suction caissons embedded in Kaolin K1.

- (2) The model does not account for cross-anisotropy effects or the nonlinear variation in soil stiffness at small strains. Moreover, the current formulation of Eqs. (4.8) and (4.9) – which empirically correlate the stiffness degradation parameter b_e to the loading parameters ξ , p'_{o} and e^{amp} – is tailored for normally consolidated soils with similar characteristics to the kaolin materials examined in this study (Kaolin K1 and Malaysian Kaolin). Their broader applicability to cohesive materials of different characteristics and/or other cyclic loading modes remains to be verified.
- (3) The influence of OCR and loading rate (for higher plasticity soils) on cyclic degradation could be further explored and incorporated into the model's framework.
- (4) The significance of the deformation accumulation trends identified in Sections 4.5 and 4.6 should be further explored under more realistic soil conditions (i.e., natural soils instead of reconstituted materials) and for foundation configurations representative of the design loads for mega-size turbines.
- (5) Once the model's applicability to non-symmetric loading is established, the performance of suction caissons under short-term transient loading should be further explored under representative load scenarios that more accurately mirror the asymmetric loading conditions met in offshore environments (arising from the combined impact of complex wind and wave forces, or the simultaneous action of environmental and seismic loads on turbine structures).

4.8. Conclusions

The paper developed a practical-simplified model to study the effect of strength and stiffness degradation on the short-term cyclic performance of OWT foundations in sensitive cohesive soils. The model is encoded in Abaqus through a simple user subroutine by modifying a total stress-based constitutive model to account for shear strength and stiffness degradation with accumulated plastic cyclic shear strain via two material-dependent coefficients. A series of undrained cyclic triaxial tests were performed on low-plasticity, normally consolidated kaolin to better understand the key parameters affecting cyclic degradation and allow for model calibration. Consistent with the literature, the tests reveal a dependency of the cyclic degradation rate on the mean effective stress (p'_{o}) and the level of applied cyclic strain amplitude (e^{amp}), yet trivial correlation with the loading rate ($\dot{\delta}$).

Based on the experimental results, a simple exponential relationship was developed to describe the stiffness degradation parameter b_e in function of the accumulated plastic shear strain ξ , p'_o and e^{amp} . The Einav & Randolph [2005] formula is employed for the correlation of ξ with parameter b_s , which describes the strain-softening effect of cyclic loading on undrained shear strength. With a single set of material constants, the model was shown to sufficiently capture triaxial test results; alas, it cannot reproduce the experimentally observed anisotropy.

The model was subsequently validated against centrifuge model tests of a *semi-rigid* monopile subjected to lateral cyclic loading in normally consolidated Malaysian kaolin clay [Li, 2019]. Upon re-calibration against relevant laboratory tests, the FE model was shown to predict the degradation of pile reaction force with load cycles reasonably well. However, the hysteretic system damping is underestimated at small strains due to the lack of a more accurate representation of the nonlinear small-strain soil stiffness.

Despite its limitations, the model was shown to yield promising results and was employed thereafter for a preliminary examination of the cyclic and seismic response of suction caisson foundations in kaolin. Comparisons between caissons of the same static safety factor, yet different L/D (0.5 and 2) indicate that the *shallow* caisson performs better when subjected to vertical cyclic loading in fast-degrading soil. This is due to the dissimilar contribution of the brittle shaft resistance and the ductile base resistance mechanisms to the caissons' load-bearing mechanism. Cyclic degradation compels rapid consumption of the brittle shaft resistance under only a few cycles of axial loading. With a $\sim 50\%$ reduction of total vertical capacity, the *deep* caisson was shown to display an abrupt increase in settlement accumulation rate. In contrast, the *shallow* caisson continues to deform in a controlled, ductile manner due to the larger contribution of its remaining base capacity. The trend is reversed under inclined cyclic loading, where both configurations exhibit a ductile load resistance mechanism, and the response is governed by the slower deterioration rate of the $L/D = 2$ caisson.

Under seismic shaking, the degradation-induced resistance imbalance amplifies the irrecoverable settlements produced by kinematic shearing at the caisson sidewalls, with the foundation displaying a rocking-dominated response, where irrecoverable settlement develops during both negative and positive acceleration cycles. Opposite to the trends observed during the vertical cyclic loading case, the settlement build-up under seismic shaking

is significantly lower for the *deep* ($L/D = 2$) caisson, which engages its side resistance and the slower degradation rates along its depth to resist the seismically induced shear. The results indicate approximately 50% settlement reduction in the absence of cyclic degradation effects.

Understandably, the reported difference in short-term cyclic foundation performance under *non-degrading* and *degrading* soil conditions is case-specific (material dependent) and is expected to diminish in the case of lower-sensitivity, natural soils. Nevertheless, it raises concerns regarding the safety of OWT under cyclic and seismic loading, highlighting the need for further research towards rational determination of cyclic offshore foundation capacities.

Acknowledgement

The authors would like to thank Prof. Maosong Huang of Tongji University, Shanghai, China, for providing the centrifuge test data in digitized form.

Appendix 4A

```
subroutine usdfld(field,statev,pnewdt,direct,t,celent,time,dtime,
1 cmname,orname,nfield,nstatv,noel,npt,layer,kspt,kstep,kinc,
2 ndi,nshr,coord,jmac,jmtyp,matlayo,laccflg)
C
include 'aba_param.inc'
C
character*80 cmname,orname
character*8 flgray(15)
dimension field(nfield),statev(nstatv),direct(3,3),t(3,3),time(2),
& coord(*),jmac(*),jmtyp(*)
dimension array(15),jarray(15)
C
REAL, PARAMETER :: CONST1 = 0.09 ! d_rem value
REAL, PARAMETER :: CONST2 = 10 ! ksi_95 value
REAL, PARAMETER :: CONST3 = 0.4019 ! c coefficient
REAL, PARAMETER :: CONST4 = 13.67 ! a coefficient
REAL, PARAMETER :: CONST5 = 0.392 ! b coefficient
REAL, PARAMETER :: CONST6 = 0.2136 ! d coefficient
REAL, PARAMETER :: CONST7 = 0.5429 ! e coefficient
REAL, PARAMETER :: CONST8 = 0.5371 ! f coefficient
REAL, PARAMETER :: CONST9 = 0.10 ! be_rem value
REAL, PARAMETER :: CONST10 = 0.005 ! lower bound limit of strain amplitude
REAL, PARAMETER :: CONST11 = 0.05 ! upper bound limit of strain amplitude
C -----
C Define start and end time of cyclic load step
REAL :: time_start, time_end
time_start = 1 ! Replace with cyclic load step start time
time_end = 200 ! Replace with cyclic load step end time
C -----
C Call and read current plastic principal strains
call getvrm('PE',array,jarray,flgray,jrcd,
&jmac, jmtyp, matlayo, laccflg)
C
Peeq=ARRAY(7)
Pmag=ARRAY(8)
C -----
C Check if TIME(2) is before, within, or after the cyclic loading timestep
IF (TIME(2) .LT. time_start) THEN
C
STATEV(1) = Peeq
STATEV(2) = Pmag
C
```

```
FIELD(1)=0
FIELD(2)=CONST10
C -----
  ELSEIF (TIME(2) .LE. time_end) THEN
C
  PeeqC=ABS(Peeq-STATEV(1))
  StrainIncr=PeeqC-STATEV(3)
  FIELD(1)=StrainIncr+STATEV(4)
C
C  Call and read current SDVs
  call getvrm('SDV',array,jarray,flgray,jrcd,
&jmac, jmtyp, matlayo, laccflg)
C
  PmagMax=ARRAY(5)
  PmagC=Pmag-STATEV(2)
  PmagFinal=MAX(PmagC,PmagMax)
C
  IF (PmagFinal .LT. CONST10) THEN
    FIELD(2)=CONST10
  ELSEIF (PmagFinal .GT. CONST11) THEN
    FIELD(2)=CONST11
  ELSE
    FIELD(2)=PmagFinal
  ENDIF
C -----
  Bs=CONST1+(1-CONST1)*(2.71828**((( -3)*FIELD(1))/CONST2))
  ParK=(CONST4)*((FIELD(3)/100)**(-CONST3))*FIELD(2)+(CONST5)*((FIELD(3)/100)**(-
CONST3))
  ParM=(CONST6)*((FIELD(3)/100)**(CONST7))*(FIELD(2)**(-CONST8))
  Be=CONST9+(1-CONST9)*(2.71828**((( -3)*FIELD(1)**ParK))/ParM)
C
  STATEV(3)=PeeqC
  STATEV(4)=FIELD(1)
  STATEV(5)=PmagFinal
  STATEV(6)=FIELD(2)
  STATEV(7)=ParK
  STATEV(8)=ParM
  STATEV(9)=Be
  STATEV(10)=Bs
  STATEV(11)=StrainIncr
C
  ELSE
C
  FIELD(1)= STATEV(4)
```

```
FIELD(2)= STATEV(6)
C
ENDIF
C-----
C If error, write comment to .DAT file:
IF(JRCD.NE.0)THEN
WRITE(6,*) 'REQUEST ERROR IN USDFLD FOR ELEMENT NUMBER ',
& NOEL,'INTEGRATION POINT NUMBER ',NPT
ENDIF
C
return
end
```

Notation

a	Backstress tensor
\dot{a}	Evolution of the kinematic component in the baseline constitutive model
A	Area
a_s	Value of backstress α at large strains
$b_{e,rem}$	Soil modulus degradation ratio at large plastic strains
b_e	Stiffness degradation coefficient
b_s	Undrained shear strength degradation coefficient
C	Kinematic hardening modulus
C_d	Degrading kinematic hardening modulus in the VM-CD model
C_{dash}	Dashpot damping coefficient
D	Diameter
d_{rem}	Opposite of soil sensitivity ($1/S_t$)
e	Load eccentricity
E	Young's modulus
$E_{0.1}$	Secant Young's modulus corresponding to 0.1% axial strain in the triaxial tests
E_o	Soil Young's modulus at small strains
E_{rem}	Residual soil Young's modulus
F	Von Mises model failure surface
f	Frequency
f_E	Dominant seismic frequency
f_N	Coefficient that accounts for the loading rate-induced soil strength increase
$F_{i,ult}$	Ultimate inclined caisson capacity
F_i	Inclined force
h	Height
H	Horizontal force
k	Material-dependent parameter influencing the soil modulus degradation
I_P	Plasticity index
K_o	Coefficient of earth pressures at rest
L	Length
m	Material-dependent parameter influencing the soil modulus degradation
M_{ult}	Ultimate rotational caisson resistance
N	Cycle number
N_{T-bar}	Cycle number in cyclic T-bar penetrometer tests
OCR	Overconsolidation ratio

p'	Mean effective stress
p'_o	Initial mean effective stress in triaxial tests
$PEMAG$	Magnitude of computed plastic strains
q	Deviatoric stress
q_{max}	Maximum deviatoric stress
q_0	Initial deviatoric stress in triaxial tests
q_N	Peak deviatoric stress at cycle N of a triaxial test
q_1	Peak deviatoric stress at cycle 1 of a triaxial test
$q_{max,cyclic}$	Maximum deviator stress in cyclic triaxial tests
$q_{max,mono}$	Maximum deviator stress in monotonic triaxial tests
\dot{s}	Strain rate
S_t	Soil sensitivity
$S_{u,rem}$	Remoulded undrained shear strength
$S_{uo, av}$	Average undrained shear strength at the foundation mid-length
$S_{uo,surf}$	Intact undrained shear strength at the soil surface
S_{uo}	Intact undrained shear strength
$SF_{I,c}$	Safety factor against cyclic inclined load
$SF_{V,c}$	Safety factor against cyclic vertical load
SF_V	Safety factor against static vertical load
t	Time
t_w	Caisson thickness
u	Horizontal displacement
u_{acc}	Accumulated pore water pressure
u_{max}	Cyclic horizontal displacement amplitude
V	Vertical force
V_{av}	Average vertical force
V_s	Shear wave velocity
V_{shaft}	Caisson shaft resistance
V_{ult}	Ultimate vertical caisson capacity
w_C	Water content
w_L	Liquid limit
w_P	Plastic limit
z	Depth
C_1, γ_1	Kinematic hardening parameters of the first VM-CD model backstress
C_2, γ_2	Kinematic hardening parameters of the second VM-CD model backstress
$\sigma_1, \sigma_2, \sigma_3$	Principal stresses

a, b, c	Positive material constants included in the definition of parameter k
d, e, f	Positive material constants included in the definition of parameter m
α	Acceleration
γ	Parameter determining the rate of kinematic hardening decrease with increasing plastic deformation in the baseline constitutive model
γ_d	Parameter determining the rate of kinematic hardening decrease with increasing plastic deformation in the VM-CD model
γ_s	Unit weight
γ_s'	Effective unit weight
ε_1	Axial strain
ε^{ampl}	Cyclic plastic strain amplitude
$\dot{\varepsilon}^{pl}$	Equivalent plastic strain rate
$\bar{\varepsilon}^{pl}$	Equivalent plastic strain
ε_1^{ampl}	Cyclic axial strain amplitude
η_0	Initial stress ratio in triaxial tests
θ	Rotation
κ	Slope of the linear $S_{uo} - \sigma'_v$ curve
λ	Fraction of initial yield stress to maximum yield stress in the combined hardening constitutive model (σ_o/σ_{max}).
μ	Friction coefficient in a Coulomb-type friction law
ν	Poisson's ratio
ξ_{95}	Cumulative shear strain required to cause 95% undrained shear strength reduction (from peak to remoulded)
ξ^T_{95}	Maximum cumulative plastic shear strain required to cause 95% soil strength reduction due to the cyclic T-bar movement
ξ_R	Rayleigh damping
ξ^T	Accumulated plastic shear strain in cyclic T-bar tests
ξ	Accumulated plastic shear strain
ρ'	Effective density
σ	Stress tensor
σ'_v	Vertical effective stress
$\sigma_{max,d}$	Degrading maximum yield stress in the VM-CD model
σ_{max}	Maximum yield stress in the baseline constitutive model
σ_o	Initial size of the yield surface in the baseline constitutive model
φ_r	Angle of internal friction
φ	Load angle

References

- Abaqus, User's Manual (2013). Version 6.13, Dassault Systèmes Simulia Corp., Providence, RI.
- Anastasopoulos, I., & Theofilou, M. (2016). Hybrid foundation for offshore wind turbines: Environmental and seismic loading. *Soil dynamics and earthquake engineering*, 80, 192-209.
- Anastasopoulos, I., Gelagoti, F., Kourkoulis, R., & Gazetas, G. (2011). Simplified constitutive model for simulation of cyclic response of shallow foundations: validation against laboratory tests. *Journal of Geotechnical and Geoenvironmental Engineering*, 137(12), 1154-1168.
- Andersen, K. H. (2009). Bearing capacity under cyclic loading—offshore, along the coast, and on land. The 21st Bjerrum Lecture presented in Oslo, 23 November 2007. *Canadian Geotechnical Journal*, 46(5), 513-535.
- Andersen, K. H. (2015). Cyclic soil parameters for offshore foundation design. In *Frontiers in offshore geotechnics III* (ed. V. Meyer), pp. 5–82. Leiden, the Netherlands: CRC Press/Balkema
- Andersen, K.H. and Jostad, H.P. (1999). Foundation design of skirted foundations and anchors in clay, Proc. Annual Offshore Technology Conf., Houston, Paper OTC 10824.
- Ansal, A. M., & Erken, A. (1989). Undrained behavior of clay under cyclic shear stresses. *Journal of Geotechnical Engineering*, 115(7), 968-983.
- Antoniou, M., Gelagoti, F., & Anastasopoulos, I. (2019). A compliant guyed system for deep-sea installations of offshore wind turbines: Concept, design insights and dynamic performance. *Soil Dynamics and Earthquake Engineering*, 119, 235-252.
- Antoniou, M., Kourkoulis, R., Gelagoti, F., & Anastasopoulos, I. (2022). Simplified method for performance-based seismic design of suction caissons supporting jacket offshore wind turbines. *Soil Dynamics and Earthquake Engineering*, 155, 107169.
- Armstrong, P. J., & Frederick, C. O. (1966). A mathematical representation of the multiaxial Bauschinger effect (Vol. 731). Berkeley, CA: Berkeley Nuclear Laboratories.
- ASTM International (2010). *ASTM D2216, Standard Test Methods for Laboratory Determination of Water (Moisture) Content of Soil and Rock by Mass*, ASTM International, West Conshohocken, PA, USA, 2010.
- Biscontin, G., & Pestana, J. M. (2001). Influence of peripheral velocity on vane shear strength of an artificial clay. *Geotechnical Testing Journal*, 24(4).
- Boltton, M. D., & Stewart, D. I. (1994). The effect on propped diaphragm walls of rising groundwater in stiff clay. *Géotechnique*, 44(1), 111-127.
- Cai, Y., Wu, T., Guo, L., & Wang, J. (2018). Stiffness degradation and plastic strain accumulation of clay under cyclic load with principal stress rotation and deviatoric stress variation. *Journal of Geotechnical and Geoenvironmental Engineering*, 144(5), 04018021.
- Chen, C., Xu, G., Zhou, Z., Kong, L., Zhang, X., & Yin, S. (2020). Undrained dynamic behaviour of peaty organic soil under long-term cyclic loading, Part II: Constitutive model and simulation. *Soil Dynamics and Earthquake Engineering*, 129.

- Chen, W., & Randolph, M. F. (2005, October). Centrifuge tests on axial capacity of suction caissons in clay. In Proceedings, International Symposium on Frontiers in Offshore Geotechnics (pp. 243-249).
- Dayal, U., & Allen, J. H. (1975). The effect of penetration rate on the strength of remolded clay and sand samples. *Canadian Geotechnical Journal*, 12(3), 336-348.
- Duque, J., Roháč, J., Mašín, D., & Najser, J. (2022). Experimental investigation on Malaysian kaolin under monotonic and cyclic loading: inspection of undrained Miner's rule and drained cyclic preloading.
- Einav, I., & Randolph, M. F. (2005). Combining upper bound and strain path methods for evaluating penetration resistance. *International journal for numerical methods in engineering*, 63(14), 1991-2016.
- Elia, G., & Rouainia, M. (2016). Investigating the cyclic behaviour of clays using a kinematic hardening soil model. *Soil Dynamics and Earthquake Engineering*, 88, 399-411.
- Gerolymos, N., & Gazetas, G. (2005). Phenomenological model applied to inelastic response of soil-pile interaction systems. *Soils and Foundations*, 45(4), 119-132.
- Gourvenec, S., Acosta-Martinez, H. E., & Randolph, M. F. (2009). Experimental study of uplift resistance of shallow skirted foundations in clay under transient and sustained concentric loading. *Géotechnique*, 59(6), 525-537.
- Hanna, A. M., & Javed, K. (2014). Experimental investigation of foundations on sensitive clay subjected to cyclic loading. *Journal of geotechnical and geoenvironmental engineering*, 140(11), 04014065.
- Hanna, A. M., & Javed, K. (2014). Experimental investigation of foundations on sensitive clay subjected to cyclic loading. *Journal of geotechnical and geoenvironmental engineering*, 140(11), 04014065.
- Ho, J. (2014). Cyclic and post-cyclic behaviour of soft clays (Doctoral dissertation, PhD thesis, National University of Singapore).
- Hsu, C. C., & Vucetic, M. (2004). Volumetric threshold shear strain for cyclic settlement. *Journal of geotechnical and geoenvironmental engineering*, 130(1), 58-70.
- Hsu, C. C., & Vucetic, M. (2006). Threshold shear strain for cyclic pore-water pressure in cohesive soils. *Journal of Geotechnical and Geoenvironmental Engineering*, 132(10), 1325-1335.
- Huang, M., Liu, L., Shi, Z., & Li, S. (2021). Modeling of laterally cyclic loaded monopile foundation by anisotropic undrained clay model. *Ocean Engineering*, 228, 108915.
- Jostad, H.P., Grimstad, G., Andersen, K.H. & Sivasithamparam, N. (2015). A FE procedure for calculation of cyclic behaviour of offshore foundations under partly drained conditions. Proc., Int. Symp. on Frontiers in Offshore Geotechnics, ISFOG, Oslo, Norway.
- Jostad, H.P., Grimstad, G., Andersen, K.H., Saue, M., Shin, Y. & You, D. (2014). A FE procedure for foundation design of offshore structures – applied to study a potential OWT monopile foundation in the Korean Western Sea. *Geotech. Engrg. J. of SEAGS & AGSSEA*, Vol. 45 (4), Dec 2014.

- Kourkoulis, R. S., Lekakakis, P. C., Gelagoti, F. M., & Kaynia, A. M. (2014). Suction caisson foundations for offshore wind turbines subjected to wave and earthquake loading: effect of soil–foundation interface. *Géotechnique*, 64(3), 171-185.
- Lefebvre, G., and Pfendler, P. (1996). Strain rate and preshear, effects in cyclic resistance of soft clay. *Journal of Geotechnical Engineering*, ASCE, 22(1): 21–26.
- Lemaitre, J., & Chaboche, J. L. (1994). *Mechanics of solid materials*. Cambridge university press.
- Li, S. (2019). Total-loading EMSD method and the behavior of laterally loaded single pile in clay (Doctoral dissertation, Ph. D. thesis, Tongji University).
- Li, S., Yu, J., Huang, M., & Leung, C. F. (2020). Application of T-EMSD based py curves in the three-dimensional analysis of laterally loaded pile in undrained clay. *Ocean Engineering*, 206, 107256.
- Matasović, N., & Vucetic, M. (1995). Generalized cyclic-degradation-pore-pressure generation model for clays. *Journal of geotechnical engineering*, 121(1), 33-42.
- Matsuda, H., Nhan, T. T., & Ishikura, R. (2013). Prediction of excess pore water pressure and post-cyclic settlement on soft clay induced by unidirectional and multi-directional cyclic shears as a function of strain path parameters. *Soil Dynamics and Earthquake Engineering*, 49, 75-88.
- Mortezaie, A. R., & Vucetic, M. (2013). Effect of frequency and vertical stress on cyclic degradation and pore water pressure in clay in the NGI simple shear device. *Journal of Geotechnical and Geoenvironmental Engineering*, 139(10), 1727-1737.
- O’Loughlin, C. D., Zhou, Z., Stanier, S. A., & White, D. J. (2020). Load-controlled cyclic T-bar tests: a new method to assess effects of cyclic loading and consolidation. *Géotechnique letters*, 10(1), 7-15.
- Poudel, S., Karki, R., & Acharya, I. P. (2019). Comparative Study of Sensitivity and Thixotropic Behavior of Various Clayey Soil Using Unconfined Compression and Lab Vane Shear Test. In *Proceedings of IOE Graduate Conference*.
- Randolph, M. F., & House, A. R. (2002). Analysis of suction caisson capacity in clay. In *Offshore Technology Conference*. OnePetro.
- Sachan, A., & Penumadu, D. (2007). Effect of microfabric on shear behavior of kaolin clay. *Journal of geotechnical and geoenvironmental engineering*, 133(3), 306-318.
- Shi, Z., Buscarnera, G., & Finno, R. J. (2018). Simulation of cyclic strength degradation of natural clays via bounding surface model with hybrid flow rule. *International Journal for Numerical and Analytical Methods in Geomechanics*, 42(14), 1719-1740.
- Shi, Z., Liu, L., Huang, M., Shen, K., & Wang, B. (2023). Simulation of cyclic laterally-loaded piles in undrained clays accounting for soil small-strain characteristics. *Ocean Engineering*, 267, 113268.
- Staubach, P., Machaček, J., Tafili, M., & Wichtmann, T. (2022). A high-cycle accumulation model for clay and its application to monopile foundations. *Acta Geotechnica*, 17(3), 677-698.

- Tsinidis, G., Pitilakis, K., & Trikalioti, A. D. (2014). Numerical simulation of round robin numerical test on tunnels using a simplified kinematic hardening model. *Acta Geotechnica*, 9, 641-659.
- Vucetic, M. (1994). Cyclic threshold shear strains in soils. *Journal of Geotechnical engineering*, 120(12), 2208-2228.
- Wichtmann, T., & Triantafyllidis, T. (2018). Monotonic and cyclic tests on Kaolin: a database for the development, calibration and verification of constitutive models for cohesive soils with focus to cyclic loading. *Acta Geotechnica*, 13(5), 1103-1128.
- Yang, Q. J., Gao, Y. F., Kong, D. Q., & Zhu, B. (2019). Centrifuge modelling of lateral loading behaviour of a “semi-rigid” Mono-pile in soft clay. *Marine Georesources & Geotechnology*, 37(10), 1205-1216.
- Yu, J., Leung, C. F., Huang, M., & Goh, S. C. J. (2018). Application of T-bar in numerical simulations of a monopile subjected to lateral cyclic load. *Marine Georesources & Geotechnology*, 36(6), 643-651.
- Zafeirakos, A., Gerolymos, N., & Drosos, V. (2013). Incremental dynamic analysis of caisson–pier interaction. *Soil Dynamics and Earthquake Engineering*, 48, 71-88.
- Zhou, J., & Gong, X. (2001). Strain degradation of saturated clay under cyclic loading. *Canadian Geotechnical Journal*, 38(1), 208-212.

5. Conclusions & Outlook

Abstract

This chapter summarizes the key findings and contributions of this dissertation, in addition to the individual conclusions drawn at the end of each chapter. Moreover, the main limitations of this study are clearly stated, and an outlook with suggestions for future research is offered.

5.1. Synopsis and key conclusions

This dissertation comprised five chapters, summarizing the conducted work on the numerical modelling of offshore wind turbines (OWT) foundations in cohesive soils under dynamic (seismic and environmental cyclic) loading, considering the effects of soil cyclic degradation and Soil-Foundation-Structure Interaction (SFSI). Since the majority of relevant research focused on the dynamic performance of monopod OWT structures (founded on monopiles or monopod suction caissons), this work studied the behaviour of two alternative foundation types suitable for transitional water depths (40 – 60m), where monopod solutions are no longer economically efficient or technically feasible: a guyed support structure and a jacket foundation, both founded by means of suction caissons. The problem was analyzed with the aid of nonlinear 3D FE analyses in Abaqus.

Guyed tower support structure: Design insights & seismic response considerations

The guyed tower support structure comprises a compliant monotower connected at its base to a shallow footing with a pier-pin connection. The latter ensures that no overturning moment is transmitted to the tower foundation while bending at the lower tower sections is significantly reduced, allowing for material savings. The OWT tower is supported in four directions by 45° pretensioned cables, extending from a single connection point on the tower (just below the rotor blades) to suction anchors at the seabed. A 3D soil-foundation-superstructure model was developed in Abaqus, using as a benchmark a 10 MW OWT installed at 50m water depth in the seismically active region of the Adriatic Sea. The efficiency of the employed soil constitutive model to simulate the undrained pullout capacity of suction caissons in clay was validated against the numerical study of Zdravkovic et al. [2001] for load angles ranging from $0^\circ \leq \beta \leq 90^\circ$ (horizontal to vertical pull-out loading). The proposed foundation design (including the cables, the suction caissons, and the shallow foundation) was initially examined against SLS and ULS loading conditions to confirm satisfactory response under design environmental (wind and wave) loading. The seismic response of the entire system was subsequently analysed under design-level seismic shaking (10% probability in 50 years) at the assumed OWT location. The key take-aways and recommendations derived from this part of the study can be summarized as follows:

- The selected cable pretension (T_0) should be sufficiently low to eliminate the necessity for massive anchors, yet large enough to guarantee no-slack conditions at the leeward cables under ULS conditions and stabilize the nonlinear taut cable response [Davenport, 1959]: it was shown that upon increase of the horizontal displacement at the connection point, the pretensioned cables quickly transition from a sagged static equilibrium to a stretched profile, thereby enhancing their horizontal stiffness $K_{c,st}$, which asymptotically approaches the axial stiffness of an elastic rod.
- Contrary to the resonance concerns raised in relevant design standards, the analyses revealed satisfactory dynamic performance, even when the system does not follow the widely used 'soft-stiff' design, which mandates the 1st natural frequency of the structure to remain between the 1P and 3P frequency range (where 1P/3P = the frequencies of mechanical vibrations at the hub level). The validity of this finding should be verified with additional fatigue calculations for critical steel joints/connections of the examined structure.
- Following design recommendations, the study conservatively ignored the existence of passive suction below the lid during SLS conditions (due to the sustained, low-frequency nature of applied loading), which decreased the inclined pullout resistance and stiffness of suction caissons by 65% and 30%, respectively, in comparison with the '*perfectly sealed*' conditions assumed during extreme ULS loading (e.g., during a storm). This very conservative assumption was the one that controlled the design of suction caissons.
- Parametric analyses with respect to the padeye position indicated that when located at the top edge of the caisson, the foundation's pull-out capacity and small-strain stiffness (considering '*perfectly sealed*' conditions, i.e., during ULS conditions) can be increased by 55% and 35%, respectively, in comparison to placement at the caisson centerline. Two distinct caisson failure mechanisms were revealed: a rotational one in the case of 'centerline' loading, with an asymmetric deep scoop developing around the caisson, and an – almost purely – translational one in the case of loading at the top caisson edge, which better exploits the stiffness and capacity reserves of the soil-foundation system.
- The observed translational mechanism (with the padeye located at the caisson edge) is not maintained during SLS loading. Under '*unsealed*' conditions, two different caisson failure mechanisms develop: The first one – associated with the mobilization of shaft friction

along the caisson skirt – is responsible for the vertical resistance R_z . The second – demonstrated in the form of a passive wedge on the caisson sidewall – evolves more gradually and is associated with the horizontal resistance R_x . With increasing inclined displacement at the edge of the caisson, the resisting moment M_x (offered by R_x) eventually overtops the counter-balancing moment M_z (offered by R_z), with this moment imbalance being responsible for non-trivial caisson rotations during SLS conditions.

- Based on analysis of the SFS system under concurrent environmental and seismic loading, the seismic performance of the guyed substructure is deemed satisfactory; the residual rotations due to shaking at the cables' connection point are zero at the end of shaking. The suction anchors performed in an (almost) elastic manner under seismic shaking, being subjected to minor pullout displacements. This highlights the conservatism of current codes on the design of suction caissons: by completely ignoring the beneficial effect of suction for SLS conditions, we end up with oversized foundations which perform 'quasi-elastically' even when subjected to extreme loading.
- With the progression of seismic shaking, the pretension gradually decreases on both cable lines due to the accumulation of plastic deformations (settlements) at the central tower foundation. The settlements of the central footing should be minimized to avoid such an effect, either by over-designing the shallow foundation or by considering an embedded foundation alternative.
- Although the decrease in mean cable tension during shaking almost led to a condition of 'tension zeroing' on the lee-ward cable for one of the examined seismic events, the momentary nature of this occurrence did not lead to any structural instability – at least for the load cases examined.

Suction Bucket Jacket foundations: Response mechanisms & simplified seismic assessment

A detailed numerical analysis of the seismic response of jacket-supported OWTs founded in clay was conducted using the same numerical principles. With the aid of a detailed 3D SFS model, the study commenced with an illustrative example of the deformations (vertical and horizontal displacement and rotation) exerted on the suction caissons of a reference 8MW jacket-supported OWT under combined wind and earthquake (W+E) loading. Subsequently, the advantages and limitations of simplified Winkler-based methodologies to predict the response were discussed through the development of an enhanced 'Caisson-on-Winkler-soil'

(CWS) model. The model is based on the 4-spring Winkler model of Gerolymos & Gazetas [2006a; 2006b; 2006c] and Assimaki et al. [2009] for cylindrical suction caissons, extended to incorporate the coupling of vertical – horizontal – moment (*VHM*) loading and the nonlinear hysteretic soil behavior under dynamic loading. By introducing distributed vertical hysteretic elements along the caisson shaft that simultaneously contribute to the vertical and horizontal caisson resistance, the model offers physical coupling between vertical and moment loading. Its response was evaluated against rigorous 3D FE models of the OWT system, while the primary mechanisms that govern the accumulation of permanent caisson settlements for SBJs under this loading combination were highlighted. Finally, a hybrid simplified method was presented for the seismic performance assessment of suction caissons supporting SBJ OWTs. The method proposes the combined use of (a) the CWS model for the calculation of *VHM* loads on the caissons and the estimation of horizontal displacements and rotations; and (b) a set of dimensionless regression equations developed on the basis of parametric FE analyses, which estimate the accumulated co-seismic caisson settlements as a function of environmental loading parameters, caisson geometry, and the seismic characteristics of the problem. The key conclusions and contributions of this part of the study can be summarised as follows:

- Under the W+E load combination, the residual settlement of the leeward suction caisson was shown to be critical for the design as it controls the jacket rotation, θ_j .
- Under external inertial loading (generated by the W+E load combination on the jacket structure), the CWS model successfully predicted the nonlinear dynamic response of the caissons, both in terms of permanent deformation and accumulation rate. However, it was unable to successfully predict the seismically accumulated settlements of the leeward suction caisson (and hence, the global rotation of the jacket structure) when the OWT was subjected to seismic loading at its base, although the transient horizontal displacements and rotations, and the wave propagation effects imposed by the non-uniform free-field deformation pattern were captured in a satisfactory manner.
- With the aid of 3D numerical analyses on a single suction caisson, it was revealed that the accumulation of caisson settlements under purely inertial (e.g., environmental cyclic loading) and coupled inertial and kinematic loading (e.g., when wind and earthquake forces act concurrently) is governed by two different mechanisms. Under *cyclic inertial loading*,

settlement is only accumulated when the caisson is subjected to compressive loading. Conversely, under the combination of *kinematic* and *inertial* loading, the caisson exhibits an anti-symmetric deformation pattern, attributed to shear strains developing from two sources: shearing γ_V caused by the wind-induced vertical load V_w , and shearing γ_E resulting from vertically propagating shear waves. The fluctuation in γ_E resulted in 'rocking' response for the caisson, causing it to lean left or right during consecutive acceleration cycles, accumulating settlement both during negative and positive load cycles. This *dual-shearing mechanism* is not captured by the proposed CWS model because the stressing of horizontal and vertical hysteretic elements is not coupled.

- Settlement prediction equations were developed (specific to the response of the critical windward caisson) based on a 3D FE model of an $L/D = 1$ caisson and a set of 22 spectrum-compatible seismic motions. The formulated linear regression equations correlate the caisson settlement (w_E) with the Arias Intensity (I_A) of the surface ground motion and were shown to remain relatively unaffected by the spectral matching technique of input seismic motions (i.e., one-by-one matching of each record or median match of the records set to the target EC8 spectrum).
- A formal dimensional analysis correlated the permanent seismic caisson settlement with five dimensionless Π -products relevant to the caisson geometry (L, D), the soil properties (ρ, E_o, S_u), the initial vertical load (V_w) due to the OWT deadweight and the wind load, and the earthquake characteristics (PGA, f_E). The dimensionless caisson settlement (w_E/D) was presented as a function of Arias Intensity (I_A) in settlement response charts, dependent on the derived dimensionless products.
- It was demonstrated that the fluctuation of vertical load acting at the top of the caisson foundation during shaking increases the accumulated settlement by 10 to 30% compared to the prediction provided by response charts, where it is simplistically assumed that the vertical load remains constant and equal to the average wind thrust V_w acting on the foundation at the beginning of the earthquake; the increase is revealed to be primarily related to the amplitude of V_w .

Cyclic degradation effects: Laboratory testing and numerical insights on the dynamic performance of suction caissons

The previously described soil constitutive model was modified via two material-dependent coefficients (b_s and b_e , respectively) to account for shear strength and stiffness degradation. The developed 'VM-CD' model was encoded in Abaqus through a user subroutine, offering a simple yet practical method for deriving preliminary insights on the short-term cyclic performance of OWT foundations in sensitive cohesive soils. A series of strain-controlled, undrained two-way cyclic triaxial tests was performed on low-plasticity, normally consolidated kaolin. The tests assisted in understanding the key parameters affecting cyclic degradation for the examined material and were used afterwards to calibrate the constitutive model. Following validation against published centrifuge tests of a semi-rigid monopile subjected to lateral cyclic loading, the model was exploited to examine the cyclic and seismic response of suction caissons in kaolin. The key conclusions and contributions of this part of the study can be summarised as follows:

- Based on laboratory testing, it was shown that the cyclic degradation rate of kaolin increases with the decrease of mean effective stress (p'_o) and the increase of applied cyclic strain amplitude (e^{amp}), while it is minimally affected by the loading rate ($\dot{\epsilon}$). The test results are in good agreement with previous experimental campaigns on cohesive materials of similar characteristics [e.g., Wichtmann and Triantafyllidis, 2018; Matasovic & Vucetic, 1995; Mortezaie & Vucetic, 2013].
- Based on the experimental results, a simple exponential relationship was introduced to describe the stiffness degradation parameter b_e in function of the accumulated plastic shear strain ξ , the mean effective stress p'_o and the amplitude of applied cyclic strain e^{amp} . Parameter b_s was correlated to ξ using the published formula proposed by Einav & Randolph [2005]. Upon calibration, the 'VM-CD' model was shown to sufficiently capture the two-way, symmetric triaxial test results with a single set of material constants, being, however, unable to reproduce the experimentally observed soil anisotropy.
- The simulation of monopile centrifuge tests revealed that the simplified model reasonably predicts the degradation of pile reaction force with load cycles. Nevertheless, the hysteretic system damping is underestimated at small strains due to the lack of a more accurate representation of the nonlinear small-strain soil stiffness.

- Considering cyclic degradation, comparisons between caissons of the same static safety factor yet different aspect ratios ($L/D = 0.5$ and 2) indicated that the $L/D = 0.5$ caisson performs better when subjected to vertical cyclic loading at its top. This is attributed to the dissimilar contribution of shaft and base resistance mechanisms to the caissons' load-bearing mechanism. Cyclic degradation leads to the rapid consumption of brittle shaft resistance under only a few cycles of axial loading, which translates to a $\sim 50\%$ reduction of total vertical capacity for the $L/D = 2$ caisson and an abrupt increase in settlements. In contrast, the $L/D = 0.5$ caisson continues to deform in a controlled, ductile manner due to the larger contribution of its remaining base capacity.
- The trend is reversed under inclined cyclic loading, where both caisson configurations exhibit a ductile load resistance mechanism, and the response is governed by the slower deterioration rate of the $L/D = 2$ caisson (owing to its larger embedment depth, associated with increased p'_o levels).
- Under seismic actions, the degradation-induced resistance imbalance amplified the irrecoverable settlements produced by kinematic shearing at the caisson sidewalls and was shown to increase the developed foundation settlements by approximately 50% compared to non-degrading soil conditions.
- Opposite to the trends observed during the vertical cyclic loading case, the settlement build-up under this load combination is significantly lower for the $L/D = 2$ caisson, which engages its side resistance and the slower degradation rates along its depth to resist the seismically induced shearing.

5.2. Limitations and outlook

Aiming to focus on the fundamental mechanisms that influence the dynamic/seismic response of the examined systems, the problem was idealised to some extent. The key limitations of the study, along with recommendations for further research, are summarised below:

- Soil behaviour is described by a total-stress-based constitutive model that treats the soil as a one-phase medium of undrained shear strength S_u , and does not explicitly account for the development of excess pore water pressures. The assumption is reasonable for the rapid cyclic loading investigated herein when cohesive soils are expected to behave in an undrained manner. However, a more sophisticated, effective-stress model could be employed in the future to examine (a) the effect of soil consolidation on the post-seismic

foundation response (i.e., when the developed pore water pressures dissipate) and (b) the behaviour of cohesive soils during lower-frequency environmental loading, where the soil may behave in a partially drained manner, and the installation suction may not be maintained below the lid.

- Metocean loads have been represented simplistically throughout the study – either as quasi-static loads (e.g., wind load acting on the rotor) or as sinusoidal load time histories. However, wind and waves are natural phenomena occurring in a stochastic, irregular manner. More realistic time-domain simulations for both loading types would allow us (a) to investigate the impact of environmental load variability in the overall response of the support structures under purely environmental and/or combined environmental and seismic loading and (b) to confirm, with higher confidence, our findings about the satisfactory performance of the guyed support structure, when the design does not follow the commonly adopted ‘soft-stiff’ approach and resonance concerns arise.
- An alternative embedded foundation to the shallow footing supporting the guyed OWT described in Chapter 2 should be examined, and its design should be optimized to provide a resilient, cost-efficient solution that minimizes tower settlements and ensures the system's structural stability. A proof-of-concept study on the seismic performance of the system in the ETHZ centrifuge facility could assist in this direction.
- The seismic assessment methodology for Suction Bucket Jackets, outlined in Chapter 3, could be extended to account for cyclic degradation effects and the variability of axial load at the top of the caissons.
- The simplified constitutive model presented in Chapter 4 should be extended to account for the effect of the initial stress ratio (and potentially other contributing soil parameters) in response. Despite our presumption that the model will perform adequately within a range of low initial stress values (denoting asymmetric loading), its formulation should be evaluated and potentially adjusted to ensure suitability under strongly asymmetric (one-way) cyclic loading. Centrifuge testing or a more advanced constitutive model that can capture cyclic degradation phenomena should be employed to validate the model's response at the system level under such loading conditions.
- The significant effect of cyclic degradation in the response of suction caissons reported in Chapter 4 is material-specific and may be augmented due to the sensitive nature of the

employed laboratory material (kaolin). There is a need to explore further the importance of such effects on natural cohesive soils of the offshore environment.

References

- Assimaki, D., & Gazetas, G. (2009). A simplified model for lateral response of large diameter caisson foundations —Linear elastic formulation. *Soil Dynamics and Earthquake Engineering*, 29(2), 268-291.
- Einav, I., & Randolph, M. F. (2005). Combining upper bound and strain path methods for evaluating penetration resistance. *International journal for numerical methods in engineering*, 63(14), 1991-2016.
- Gerolymos, N., & Gazetas, G. (2006a). Development of Winkler model for static and dynamic response of caisson foundations with soil and interface nonlinearities. *Soil Dynamics and Earthquake Engineering*, 26(5), 363-376.
- Gerolymos, N., & Gazetas, G. (2006b). Static and dynamic response of massive caisson foundations with soil and interface nonlinearities—validation and results. *Soil Dynamics and Earthquake Engineering*, 26(5), 377-394.
- Gerolymos, N., & Gazetas, G. (2006c). Winkler model for lateral response of rigid caisson foundations in linear soil. *Soil Dynamics and Earthquake Engineering*, 26(5), 347-361.
- Mašín, D. (2014). Clay hypoplasticity model including stiffness anisotropy. *Géotechnique* 64(3): 232-238.
- Matasović, N., & Vucetic, M. (1995). Generalized cyclic-degradation-pore-pressure generation model for clays. *Journal of geotechnical engineering*, 121(1), 33-42.
- Mortezaie, A. R., & Vucetic, M. (2013). Effect of frequency and vertical stress on cyclic degradation and pore water pressure in clay in the NGI simple shear device. *Journal of Geotechnical and Geoenvironmental Engineering*, 139(10), 1727-1737.
- Suryasentana, S. K., Byrne, B. W., Burd, H. J., & Shonberg, A. (2018). An elastoplastic 1D Winkler model for suction caisson foundations under combined loading. In *Numerical Methods in Geotechnical Engineering IX, Volume 2: Proceedings of the 9th European Conference on Numerical Methods in Geotechnical Engineering (NUMGE 2018)*, June 25-27, 2018, Porto, Portugal (p. 973). CRC Press.
- Wichtmann, T., & Triantafyllidis, T. (2018). Monotonic and cyclic tests on Kaolin: a database for the development, calibration and verification of constitutive models for cohesive soils with focus to cyclic loading. *Acta Geotechnica*, 13(5), 1103-1128.
- Zdravković, L., Potts, D. M., & Jardine, R. J. (2001). A parametric study of the pull-out capacity of bucket foundations in soft clay. *Geotechnique*, 51(1), 55-67

CURRICULUM VITAE
ANTONIOU MARIA
Doctoral Candidate



EDUCATION

2018 – present: Doctoral Candidate (external), Swiss Federal Institute of Technology in Zurich (ETH Zurich), Switzerland.

Provisional Doctoral Thesis: ‘Next-generation offshore wind turbine foundations under seismic and environmental dynamic loading’ | Supervisors: Prof. Dr. Ioannis Anastasopoulos, Dr. Rallis Kourkoulis

2013 – 2014: MSc in Geotechnical and Offshore Engineering (1-year program), University of Dundee (UoD), United Kingdom – Distinction awarded.

MSc Thesis: ‘Numerical analysis of a guyed support structure for next generation offshore wind turbines in deep waters.’ | Supervisor: Prof. Dr. Ioannis Anastasopoulos

2007 – 2013: Diploma in Civil Engineering (5-year curriculum, equivalent to Master 300 ECTS), National Technical University of Athens (NTUA), Greece – GPA: 8.49 /10

Specialization: Geotechnical Engineering

Diploma Thesis: ‘Numerical and experimental analysis of an innovative stiffness and energy dissipation system (INSTED–FUSEIS) considering soil–structure interaction.’ | Supervisors: Prof. Dr. George Gazetas, Prof. Dr. Ioannis Anastasopoulos, Dr. Phaedon Karydakis

PROFESSIONAL ACTIVITY

2022 – present: Principal Consultant, GRID Engineers, Greece

2020 – 2022: Marie Skłodowska-Curie Research Fellow as part of the INSPIRE Innovative Training Network, ETH Zurich, Switzerland

2016 – 2020: Consultant, GRID Engineers, Greece

2015 – Present: Associate, Innovation Center on Natural Hazards & Infrastructure, Greece

PROFESSIONAL EXPERIENCE

Consulting Projects

2023 – Present: Support for the development of practical sectoral guidance on climate resilience proofing [Client: European Investment Bank (EIB)]

2023 – Present: Transport network planning and analysis decision-support tool for South Asia [Client: World Bank, USA]

2023 – Present: Technical guidance note for disaster and climate resilient transport [Client: World Bank, USA]

2022: Seismic loss assessment for the Aluminium of Greece and Protergia energy plants [Client: Mytilineos SA, Greece]

2021 – Present: An interactive tool for the appraisal & planning of interventions to enhance resilience of transport networks [Client: National Technical Institute of Standards and Technology (NIST), USA]

2021: Framework for infrastructure resilience and post-hazard response for the Federal Highway administration, USA [Client: WSP / FHWA, USA]

2020: Disaster risk assessment and optimization of resilience for Olympia Odos motorway PPP project [Client: Vinci Concessions SA, Greece]

2019: Intelligent Cement in Drilling Operations, Implementation Phase [Client: TXIS, USA]

2017: MOREAS MOTORWAY - Earthquake Probable Maximum Loss Assessment [Client: Moreas SA, Greece]

2017: AEGEAN MOTORWAY - Earthquake Probable Maximum Loss Assessment [Client: Aegean Motorway SA, Greece]

Research Projects

2022 – Present: ReCharged: Climate-aware Resilience for Sustainable Critical and interdependent Infrastructure Systems enhanced by emerging Digital Technologies', funded by EU- H2020.

2019 – 2023: INSPIRE: 'Innovative Ground Interface Concepts for Structure Protection', funded by EU - H2020.

2018 – 2021: AGNES: 'Life-cycle Assessment of Next Generation OWTs under Extreme Environmental Loading', funded by the Hellenic Foundation for Research and Innovation (R&D).

2019 – 2020: Shaking Tunnel Vision Project: Investigation of the performance of concrete tunnel linings under repeated dynamic loading. Supported by the Newton Fund, the Global Challenge Research Fund (GCRF) and the Higher Education Funding Council for England (HEFCE), and led by the University of Leeds, UK.

2017 – 2018: 'New Geotechnical Systems for deep-sea installations of offshore wind-turbines', in co-operation with ETH, Zurich, Switzerland.

2015 – 2018: JABACO: 'Development of Modular Steel Jacket for Offshore Windfarms', European Research Fund for Coal and Steel, funded by EU-H2020.

2013 - 2014: THALIS: 'Contemporary Evaluation Methodology of Seismic Vulnerability and Upgrade of Port Facilities', funded by General Secret. for Research and Technology, Greece.

JOURNAL PUBLICATIONS

Antoniou, M., Gelagoti, F., Herzog, R., Kourkoulis, R., & Anastasopoulos, I. Offshore Foundations in Low-Plasticity Cohesive Soils: Cyclic Degradation Experimental Evidence and Simplified Numerical Analysis. *Ocean Engineering* (submitted for peer-review).

Antoniou, M., Alvertos, A., Sapountzakis, E. J., Anastasopoulos, I. (2023). Application of the Extended KDamper to the seismic protection of bridges: Design optimization, nonlinear response, SSI and pounding effects. *Journal of Earthquake Engineering*, doi: 10.1080/13632469.2023.2250463.

Kapasakalis, K., Mantakas, A., Kalderon, M., **Antoniou, M.**, & Sapountzakis, E. J. (2023). Performance Evaluation of Distributed Extended KDamper Devices for Seismic Protection of Mid-Rise Building Structures. *Journal of Earthquake Engineering*, 1-26.

Antoniou, M., Mantakas, A., Nikitas, N., & Fuentes, R. (2023). A numerical case study on the long-term seismic assessment of reinforced concrete tunnels in corrosive environments. *Journal of Rock Mechanics and Geotechnical Engineering*, 15(3), 551-572.

Antoniou, M., Kourkoulis, R., Gelagoti, F., & Anastasopoulos, I. (2022). Simplified method for performance-based seismic design of suction caissons supporting jacket offshore wind turbines. *Soil Dynamics and Earthquake Engineering*, 155, 107169.

Antoniou, M., Nikitas, N., Anastasopoulos, I., & Fuentes, R. (2020). Scaling laws for shaking table testing of reinforced concrete tunnels accounting for post-cracking lining response. *Tunnelling and Underground Space Technology*, 101, 103353.

Antoniou, M., Gelagoti, F., & Anastasopoulos, I. (2019). A compliant guyed system for deep-sea installations of offshore wind turbines: Concept, design insights and dynamic performance. *Soil Dynamics and Earthquake Engineering*, 119, 235-252.

CONFERENCE PAPERS

Antoniou, M., Gelagoti, F., Anastasopoulos, I. (2023). Cyclic degradation of low-plasticity cohesive soils: Experimental evidence and simplified numerical analysis at the soil-foundation level. In the 9th *Hellenic Conference on Geotechnical Engineering*, 4-6 October, Athens, Greece (accepted for publication).

Antoniou, M., Kourkoulis, R., Gelagoti, F., Anastasopoulos, I. (2021). Suction Caissons as Multipod OWT Foundations in Clay: Investigation of Loading Rate Effects. In *International Conference on Offshore Mechanics and Arctic Engineering* (Vol. 85192). American Society of Mechanical Engineers.

Antoniou, M., Kourkoulis, R., Gelagoti, F., Anastasopoulos, I. (2021). A Guyed Support Structure for OWT Installations in Intermediate Water Depths. In *ISOPE International Ocean and Polar Engineering Conference* (pp. ISOPE-I). ISOPE.

Antoniou, M., Gelagoti, F., Kourkoulis, R., Georgiou, I., Karamanos, S.A. (2019). Seismic response of jacket wind-turbines: Dimensional analysis of foundations and SSI. In *Proceedings of the 2nd International Conference on Natural Hazards and Infrastructure (ICONHIC2019)*, Crete, Greece, June 23-26, 2019.

Antoniou, M., Gelagoti, F., Anastasopoulos, I. (2018). Seismic Performance of a Novel Guyed System for the Support of Offshore Wind-Turbines. In *Proceedings of the 16th European Conference on Earthquake Engineering (16ECEE)*, Thessaloniki, Greece, June 18-21, 2018.

Anastasopoulos, I., Loli, M., **Antoniou, M.**, Knappett, J., Brennan, A., Gazetas, G. (2015). Centrifuge testing of multi-block quay walls. In *SECED 2015 conference: Earthquake risk and engineering towards a resilient world* (pp. 766-777).

DISSEMINATION & OUTREACH

2020 – 2023: Key team member of the organisation of the 9th International Congress on Environmental Geotechnics, held in June 2023, in Chania, Greece.

2015 – present: Key Organizing Team Member of the 1st, 2nd and 3rd International Conferences on Natural Hazards & Infrastructure held in Crete and Athens, Greece.

IT SKILLS & LANGUAGES

Software for Engineering Applications: Abaqus, QGIS, Plaxis, Seismosignal, Slide, AutoCAD

Software (Other): MS Office Suite, Adobe Illustrator, Adobe InDesign

Computing: Matlab

Languages: Greek (native), English (Cambridge Proficiency, C2 level), German (Goethe-Zertifikat, B2 level)

HONORS/AWARDS

September 2014: Nomination of the MSc Dissertation ‘Numerical analysis of a guyed support structure for next generation offshore wind turbines in deep waters’ for the Master’s Degree Dissertation Prize 2014 of the British Geotechnical Association (September, 2014).

September 2013: Bodossaki Foundation scholarship for the postgraduate studies at the University of Dundee, during the academic year 2013-2014.

August 2013: Scottish Funding Council (SFC) scholarship for the postgraduate studies at the University of Dundee, during the academic year 2013-2014.

June 2007: Award from OTE-Cosmote telecommunications company for the excellent performance in the Greek National Exams of 2007.

June 2007: Award from the bank Eurobank Ergasias S.A. for the highest general mark (19.6/20) in the 3rd Public Senior School of Rethymno, during the academic year 2006 – 2007.

October 2006: Ministry of Education award for the highest general mark (19.8/20) in the Prefecture of Rethymno, during the academic year 2005-2006.